Microfabricated rubidium dielectric barrier discharge light sources for portable atomic clocks

THÈSE N^{O} 5702 (2013)

PRÉSENTÉE LE 12 AVRIL 2013

À LA FACULTÉ DES SCIENCES ET TECHNIQUES DE L'INGÉNIEUR
LABORATOIRE DES MICROSYSTÈMES POUR LES TECHNOLOGIES SPATIALES
PROGRAMME DOCTORAL EN MICROSYSTÈMES ET MICROÉLECTRONIQUE

ÉCOLE POLYTECHNIQUE FÉDÉRALE DE LAUSANNE

POUR L'OBTENTION DU GRADE DE DOCTEUR ÈS SCIENCES

PAR

Vinu LALGUDI VENKATRAMAN

acceptée sur proposition du jury:

Prof. P.-A. Farine, président du jury
Prof. H. Shea, directeur de thèse
Dr D. Briand, rapporteur
Prof. G. Mileti, rapporteur
Prof. A. Weis, rapporteur

ÉCOLE POLYTECHNIQUE
FÉDÉRALE DE LAUSANNE

Suisse
2013

Abstract

Miniature (<few cm^3) atomic clocks, with their high time precision (higher than 10^{-9} fractional frequency instability) capabilities, are needed to improve the performance of many portable applications such as GPS receivers. Compact (100-1000 cm^3) Rb vapor-cell double-resonance (DR) clocks could not be miniaturized mainly because it's optical pumping component: the inductively-coupled glass-blown rubidium (Rb) discharge lamp (several cm^3), had many limitations including high-power consumption (several Watts) and non-planar hard-to-integrate geometry. Today's miniature atomic clocks therefore use a laser diode (VCSEL) as the light source, which are compact, energy efficient, and operate at low power. However, they have several undesirable characteristics including a strong temperature dependence of the output wavelength, and ageing effects. A miniature mm-scale Rb plasma light source could avoid these disadvantages of a laser diode and extend the inherent advantages of a Rb discharge lamp (intrinsically correct Rb D line wavelengths and very low-frequency drifts with time) to a miniature DR clock. A microfabricated (1 cm x 1 cm x 0.3 cm) planar miniature Rb dielectric barrier discharge (DBD) light source was developed for this purpose, as part of the MACQS project (funded by the Swiss National Science Foundation), and the characterization, optimization and performance evaluation of such light sources for optical pumping in atomic clocks and magnetometers are presented here in this thesis. The primary objective of this research is to evaluate the potential of planar mm-scale Rb light sources: to produce at least 10 μW of the Rb D line (with <0.2% optical power fluctuations) when the power consumption is less than tens of mW, and have a lifetime of at least several years to be useful in a miniature optical pumping application. This research is the first to report a Rb plasma discharge from a miniature microfabricated cell.

The optimum operating conditions, including the electrode material (Al, In, ITO) and electrode geometry, buffer gas pressure (Ar, He, N_2 from 2 to 100 mbar), drive frequency (2-500 MHz) and the cell temperature (25 °C to 180 °C), were experimentally determined to enable an optically stable and low-power consuming lamp operation. Series LC-resonant RF drive circuits were developed to transfer maximum power to the capacitively-coupled Rb lamp-cell by impedance matching it to a 50 Ω source at all desired drive frequencies. A total optical power of 140 μW was obtained when coupling less than 20 mW to the discharge cell, with up to 15 μW and 9 μW on the Rb D2 and D1 lines respectively. The Rb lamp was operated continuously for 6 months and it was observed to function well without any significant degradation in its performance. The lamp operating conditions were found to be optimal when the electron oscillation amplitude becomes approximately equal to the discharge gap length, as a suitable trade-off between the lamp's power consumption, optical stability and optical power efficiency was achieved in this condition. Preliminary optical pumping tests using the Rb lamp, performed by building a magnetometer test setup are also presented here.

The optimized lamp performance results show the high potential of miniature microfabricated Rb light sources to operate with high stability and low input power, enabling a new class of very compact atomic clocks and quantum sensors.

Keywords: atomic clocks, rubidium, dielectric barrier discharge, microfabrication, anodic bonding, rf plasma, solder sealing, double-resonance

Résumé

Les horloges atomiques miniaturisées (<quelques cm^3), avec leur précision élevée (instabilité de fréquence fractionnaire de moins de 10^{-9}), sont requises pour améliorer les performances de nombreuses applications, telles les récepteurs GPS. Les horloges cellules à vapeur de rubidium (Rb) à double résonance (DR) compactes (100-1000 cm^3) existant actuellement ne peuvent être miniaturisées principalement à cause de leur composante de pompage optique. Cette composante, une lampe à couplage inductif en verre soufflé à décharge de rubidium a de nombreuses limitations, notamment une haute consommation d'énergie (plusieurs Watts) et une géométrie non planaire difficile à intégrer et mesurant plusieurs cm^3. Les horloges atomiques miniatures d'aujourd'hui utilisent plutôt comme source de lumière des diodes laser (VCSEL) car elles sont compactes, économes en énergie et fonctionnent à faible puissance, bien qu'elles aient plusieurs caractéristiques indésirables, dont une longueur d'onde ayant une forte dépendance à la température et des effets de vieillissement. Une source de lumière à plasma de Rb miniature (de l'ordre du mm) pourrait éviter ces inconvénients et permettre à une horloge miniature de profiter des avantages d'une lampe à décharge de Rb, dont la longueur d'onde intrinsèquement correcte des lignes D de Rb ainsi qu'une très basse dérive de fréquence.

Dans le cadre du projet MACQS (financé par le Fonds National Suisse), une source micro-usinée (1 cm x 1 cm x 0.3 cm) de décharge à barrière diélectrique de Rb (DBD) a donc été élaboré pour pompage optique dans des horloges atomiques ou magnétomètres. La caractérisation, l'optimisation et la performance de cette source sont présentées dans cette thèse. L'objectif principal de cette recherche est de développer une source de lumière Rb qui peut répondre à une exigence de durée de vie de plusieurs années et d'identifier les conditions de fonctionnement correspondant à une sortie d'au moins 10 μW de la ligne D du Rb, avec moins de 0.2% de fluctuations de puissance optique de moins d'une seconde, tout en minimisant la puissance d'entrée à la source (idéalement moins de quelques dizaines de mW). Ce travail de recherche présente pour la première fois d'une cellule micro-usinée Rb décharge de plasma.

Les conditions de fonctionnement optimales, y compris le matériel (Al, In, ITO) et la géométrie de l'électrode, la pression du gaz tampon (Ar, He, N_2 2 à 100 mbar), la fréquence d'entraînement (2-500 MHz) et la température de la cellule (25 °C à 180 °C), ont été déterminés expérimentalement pour permettre une consommation de faible puissance et une opération de la lampe optiquement stable. Des circuits de résonance LC en série ont été développés pour transférer le maximum de puissance aux lampes harmonisés à une impédance de 50 Ω, pour une opération efficace à toutes les fréquences désirées. Une puissance optique totale de 140 μW fut obtenue en couplant moins de 20 mW à la cellule de décharge, allant jusqu'à 15 μW et 9 μW sur les lignes D2 et D1 du Rb, respectivement. La lampe Rb fut opérée de façon continue pour six mois, les résultats indiquant que la lampe pourrait fonctionner de façon fiable sans dégradations significative de performance. Des résultats préliminaires de tests de pompage optique de la cellule, effectués à l'aide d'un montage d'essai de magnétométrie sont aussi présentés.

La performance démontrée de la lampe optimisée montre le grand potentiel de ces sources micro-usinée de lumière étant capables d'opérer avec une grande stabilité et permettant la création d'une nouvelle catégorie d'horloges atomiques très compactes et de capteurs quantiques.

Mots-clés: horloges atomiques, rubidium, décharge à barrière diélectrique, microfabrication, collage anodique, plasma RF, soudure étanche, double résonance

Acknowledgements

Science is a belief system, propelled by the unquenchable human curiosity, which has a structure so impenetrable, inimitable and transparent that it is destined to dominate the foreseeable future of human life. A Ph.D. in one of its fields is the best opportunity to experience this marvel from so many new perspectives that one wouldn't even know existed. I am truly happy and honored to have gained considerable insight in this winning movement, which I could not have done without the continuous support of my mentors, colleagues, friends and family. I hope the knowledge I gained will help my life contribute to the immortality of science.

I am highly indebted and thankful to my thesis director, Prof. Herbert Shea, for giving me the opportunity to work at the LMTS - a lab with excellent infrastructure and working spirit, for mentoring and giving me excellent research advices throughout these years, for always asking me enough questions to get me pondering and craving for answers, for his patience in dealing with my delays in writing documents and for his inspirational interest in science and developing technology.

I thank Prof. Farine Pierre-André, Prof. Gaetano Mileti, Dr. Danick Briand and Prof. Antoine Weis for kindly accepting to be the members of the thesis jury for my PhD exam.

I gratefully thank-

Dr. Christoph Affolderbach for all the research advises, mentoring efforts and lengthy discussions which were crucial in moving this research forward, for setting up various pumping demonstration experiments at LTF and for always using a helpful attitude towards research.

Prof. Gaetano Mileti for co-ordinating the MACQS project, for including me in the research visit to NIST, Boulder and for encouraging me to achieve higher goals in my research. Matthieu Pellaton for this help with the lock-in amplifier setup.

Dr. Yves Pétremand for his collaborative work, for the microfabricated cells and the electrode depositions, which were most important for this project.

Dr. Thomas Maeder and Fabrizio Vecchio for their collaboration on the research involving LTCC packaging, screen-printing and solder-sealing and letting me use their research facilities at LPM. I also thank Fabrizio for all the research discussions and the joyful times.

The Swiss National Science Foundation for funding this project and all the MACQS project members for their support and research discussions on the atomic clock development.

The SNF R'Equip program for the funding of the high speed data acquisition test bench.

Dr. Patrick Carazzetti and Philip Moser for their previous work on miniature plasma light sources which acted as strong references and helped laying a strong foundation to this research.

It was a pleasure to work with all my LMTS work colleagues: Kaustav Ghose, Samin Akbari, Joao Gomes, Caglar Ataman, Luc Maffli, Simon Dandavino, Tobias Bandi, Subha Chakraborty, Jun Shintake, Samuel Rosset, Seun Araromi and Alexandre Poulin, and I thank them for all the

fun times together, leisure discussions, hiking trips and for sharing ideas and experiences with me. Special appreciation and thanks to Myriam Poliero for all the help and support over the years.

I also would like to thank the people and colleagues of SAMLAB for sharing their research equipment and also for all the fun times: Prof. Nico de Rooij, Dr. Danick Briand, Dr. Alexandra Homsy, Dr. Peter Van der Wal, Dr. Wilfried Noell, Karine Frossard, Rahel Straessle, Dara Bayat, Michael Canonica, Jerome Courbat, David de Koninck, Rokhaya Gueye, Don Isarakorn, Pattanaphong Janphuang, Fabio Jutzi, Robert Lockhart, Giorgio Mattana, Frederic Loizeau, Francisco Molina Lopez, Jason Ruan, Sara Talaei, Andres Vasquez and Yexian Wu.

Finally, I would like to thank all my friends and family for their unconditional support through my years of study. I thank my parents, L.S. Venkatraman and Ranjini Venkatraman, for the limitless freedom, love and support they have offered me from the beginning. I thank my wife, Deepta Sridhar, for her unconditional love and patience and for holding me to the ground during all the crazy times.

Contents

Abstract ---------- **iii**

Résumé ---------- **iv**

Acknowledgements ---------- **v**

Contents ---------- **vii**

List of figures ---------- **x**

List of tables ---------- **xvii**

List of abbreviations ---------- **xviii**

Chapter 1 Introduction ---------- **1**

1.1 Double-resonance atomic clocks ---------- 3

1.2 Current state-of-the-art portable vapor-cell atomic clocks ---------- 4

1.3 Miniature atomic clocks and quantum sensors (MACQS) project ---------- 5

1.4 Thesis objectives and report structure ---------- 6

Chapter 2 Electrically-induced plasma discharge emission ---------- **10**

2.1 Gas discharge plasmas ---------- 10

2.2 Excitation phenomena in gases ---------- 11

2.2.1 Motion of particles in a gas ---------- 12

2.2.2 Types of collisions ---------- 14

2.2.3 Electron energy distribution ---------- 14

2.3 Electrically induced discharges ---------- 16

2.4 Electrical breakdown in a steady (DC) electric field condition ---------- 19

2.5 Electrical breakdown in an alternating electric field condition ---------- 23

2.6 Overview of discharge drive options ---------- 27

2.7 Dielectric barrier discharge light source design ---------- 29

2.7.1 Dielectric barrier discharges ---------- 29

2.7.2 Types of DBDs ---------- 30

Chapter 3 Miniature DBD cell development ---------- **32**

3.1 Rb light source – size and performance requirements ---------- 32

3.1.1 Physical properties of Rb ---------- 33

3.1.2 Buffer gas and pressure conditions ---------- 34

3.2 Rb cell fabrication techniques ---------- 36

3.2.1 Glass-blown Rb discharge lamps ---------- 36

3.2.2 Miniature Rb vapor cell fabrication methods – state-of-the-art ---------- 37

3.3 Novel Rb cell fabrication technique by solder-sealing ---- 42
3.3.1 Rb solder-cell design and development---- 43
3.3.2 Rb dispensing in liquid alkane and sealing method---- 45
3.3.3 Hermeticity tests---- 45
3.4 List of fabricated cells used as light sources---- 47
3.5 Electrode deposition for Rb DBD cells ---- 48
Chapter 4 Electrical drive circuitry for the miniature Rb DBD lamp ---- 51
4.1 RF drive design concepts for a CCP discharge cell---- 51
4.1.1 Electromagnetic wave propagation model---- 51
4.1.2 The electrostatic approximation ---- 53
4.1.3 RF input power options for driving the Rb lamp---- 53
4.1.4 Elements of RF drive design ---- 55
4.2 LC resonant drive circuit for the Rb DBD lamp---- 59
4.2.1 Drive circuit - input stage ---- 59
4.2.2 Drive circuit - LC stage---- 60
4.3 Electrical modeling of the Rb DBD lamp---- 68
Chapter 5 Electrical and optical characterization of the Rb DBD lamp ---- 73
5.1 Experimental test setup for Rb DBD lamp characterization ---- 73
5.2 A functional miniature Rb DBD lamp---- 79
5.3 Electrode geometry optimization ---- 81
5.4 RF input characterization of the Rb DBD lamp ---- 82
5.4.1 Effects of input RF power on discharge emission ---- 82
5.4.2 Effects of drive frequency on the light source performance ---- 85
5.4.3 Power coupled to the discharge gap ---- 88
5.4.4 Impedance mismatch conditions ---- 90
5.5 Optical power and stability of the Rb DBD lamp ---- 92
5.6 Temperature tests and Rb self-absorption ---- 93
5.6.1 Rb red-mode transition at high cell temperatures ---- 94
5.6.2 Breakdown power versus cell temperature ---- 95
5.7 Lifetime and reliability studies---- 96
5.8 LTCC integrated Rb DBD lamp module---- 99
Chapter 6 Experiments and simulations for optimizing discharge gap parameters --103
6.1 Plasma characterization at different discharge gap conditions---- 103
6.1.1 Discharge gap experiments – test setup ---- 104

6.1.2 Electrical equivalent model ---- 105
6.1.3 Plasma discharge characterization results ---- 105
6.2 COMSOL plasma discharge simulations ---- 110
6.2.1 COMSOL plasma model ---- 111
6.2.2 Simulation results ---- 112
Chapter 7 Optical pumping experiments ---- 117
7.1 Magnetometer optical pumping ---- 117
7.1.1 Background: atomic clock DR experiment ---- 117
7.1.2 Atomic double-resonance magnetometry ---- 119
7.1.3 Magnetometer test setup ---- 120
7.1.4 Signal noise reduction using FM ---- 122
7.2 Optical pumping results ---- 123
7.2.1 Rb D1 laser pumping test ---- 123
7.2.2 Optical pumping tests with Rb discharge lamps ---- 124
Chapter 8 Conclusions ---- 128
8.1 Summary ---- 129
8.2 Thesis contributions ---- 131
8.3 Outlook ---- 132
Appendix: COMSOL simulation data ---- 134
Bibliography ---- 136
Curriculum Vitae ---- 145
List of publications ---- 146

List of figures

Figure 1.1: The different types of atomic clocks classified according to size, power, cost and performance. Picture sources: [L-R]: NIST, HP Inc., Spectratime SA, Symmetricom Inc., Laptech Inc. Data source: [1].....1
Figure 1.2: A schematic illustration of the double-resonance interrogation technique to produce the high-precision time signal.....3
Figure 1.3: Photographs of high-performance (XPRO, Symmetricom), compact (LCR-900, Spectratime) and chip-scale (SA.45s, Symmetricom) Rb vapor-cell atomic clocks.....4
Figure 1.4: An example VCSEL used by Serkland et. al. [9] and a typical Rb discharge lamp with an excitation coil around it to ignite an inductively-coupled plasma.....4
Figure 1.5: A schematic representation of the envisioned miniature Rb DR atomic clock showing all the microfabricated components and the electronics inside a package volume within few cm^3.6
Figure 1.6: A microfabricated Rb DBD light source, with the LC drive circuit, emitting discharges when driven with radio-frequency power.....8
Figure 2.1: Some examples of plasma discharge light sources: (a) a common neon sign, Source: perma-laboratories.com (b) fluorescent light tubes Source: best-b2b.com and (c) plasma TV which uses at least several thousand plasma discharge cells for the display.....10
Figure 2.2: A schematic and simplistic illustration of a plasma state consisting of a non-negligible density of charged entities in a gas.....11
Figure 2.3: A schematic model of a Ne atom (example) with electrons distributed in the various orbitals held by the positively charged proton centric nucleus at different energy levels. Source: Lawrence Berkeley National Laboratory.....12
Figure 2.4: A schematic representation of an electron impact collision with a gas atom leading to different possible atomic transitions after collision depending on the incoming electron's kinetic energy, E_e [23].....12
Figure 2.5: An illustration of an electron avalanche effect resulting in Townsend discharges and an electrical breakdown for an applied DC field condition.....19
Figure 2.6: A voltage versus current plot of all low-density plasma discharge regimes (Townsend, glow and arc discharge). Operating in the normal glow discharge regime is ideal for light source applications [35].....20
Figure 2.7: Paschen curves for various gases [30] plotted based on the experimentally derived model.....22
Figure 2.8: Photographs of interdigitated electrodes patterned on silicon, before and after igniting and sustaining a DC discharge for 1 hour. Both electrodes were eroded with the cathode being severely eroded due to the heavy ion bombardment.....22
Figure 2.9: General behaviour of the breakdown field required versus the operating drive frequency normalized to the DC value (for a constant p.d and buffer gas) for mm-scale discharge lengths. The different discharge drive techniques and their typical drive power requirements for igniting and sustaining discharges are also illustrated. This graph is only for understanding the overall trend of the breakdown field versus drive frequency and the exact values vary with the gas type, (p.d) and other conditions.....27
Figure 2.10: (a) A 13.56 MHz capacitive coupled plasma reactor, Source: PAL, University of Texas, Dallas (b) An inductively-coupled plasma torch, Source: Elemental analysis, Inc. (c) a

micro-coil inductively-coupled plasma generator for ionizing applications [57], (d) a capacitively coupled micro-plasma generator for gas chromatography applications [64]. 28
Figure 2.11: Typical DBD configurations where design type (c) is a useful sealed cell solution for the rubidium discharge light source. 29
Figure 2.12: Typical DBD applications: (a) Ozone generation using DBD reactors, (b) schematic of the ozone generation in each DBD tube, (c) a plasma TV display containing DBD micro-light sources, (d) a schematic of the plasma display panel showing the DBD cells [73]. Image source for (a), (b), (c): Jose Lopez, Dielectric barrier discharge, ozone generation and their applications, 2008. 30
Figure 2.13: The plasma discharge in a DBD cell can be divided into two primary groups of DBDs - volume and surface microdischarges, along with diffuse glow discharges which are better described by diffusion theory. Volume discharges also include the filamentary discharges and streamers which occur at certain input conditions (usually low frequency and/or high electric field conditions). 30
Figure 3.1: Cross-sectional schematic view of the miniature DBD cell where d=2mm and D=5mm for most of the anodic bonded cells used in this research. 32
Figure 3.2: Envisioned integration of our light source in a miniature double-resonance clock with the optional Rb isotope filter. 32
Figure 3.3: Energy level diagram of the Rb atom showing all probable excitation and decay transitions and the corresponding discharge emission wavelengths. The D lines are shown in red. Source: www.chem.purdue.edu 33
Figure 3.4: (a), (b) Photographs of a glass-blown Rb cell developed at LTF, Neuchâtel and the Rb ICP lamp with the cell placed inside an excitation coil. (c) A compact Rb DR clock (Spectratime), showing a conventional glass-blown lamp emitting light to a resonance cell. 37
Figure 3.5: The expected Rb self-absorption temperature calculated based on 1:1000 ratio of Rb vapor to Ar atoms in the discharge volume. 37
Figure 3.6: A miniature Rb cell fabricated by the glass-blowing technique [103]. 38
Figure 3.7: A schematic illustration of cell fabrication based on silicon etching and anodic bonding. A Si wafer (a) with holes etched through it (b) is anodically bonded to a piece of glass (c). It is then filled with alkali atoms and buffer gas (d), and a second piece of glass is bonded on top (e) to form a robust, hermetically sealed vapor cell (f) [94]....38
Figure 3.8: The anodic bonding process showing the formation of the depletion layer and the interfacial electrostatic field. The oxygen anions migrate to the positively charged Si to form a permanent bond....39
Figure 3.9: Microfabrication process flow of the Rb light source showing Rb dispensing and hermetic sealing of the buffer gas+Rb vapor cell. Steps 1 and 2 are performed at wafer level and steps 3 and 4 are completed at chip level. 40
Figure 3.10: Process to enclose Rb in wax micropackets. By Radhakrishnan et al. 41
Figure 3.11: Schematic of the bonding procedure of two solder-layer deposited glass substrates and the cross-sectional view of a bonded cell. 43
Figure 3.12: The illustration of the solder-bonding setup using four springs for a balanced compressive force, L-shaped pieces for alignment of the rectangular substrates, walls to submerge the dispensed Rb in liquid alkane and a 300 °C capacity heater with temperature control. 44

Figure 3.13: Photographic illustration of some screen-printed glass substrates for bonding. An example of a substrate with a bad wetting solder/metallization layer combination is also shown. 44
Figure 3.14: Rb dispensing and storage in a pool of dodecane (liquid alkane). The Rb is dispensed using a micropipette on the cell inside a walled platform to keep the Rb submerged even after removal from the dodecane pool.....45
Figure 3.15: (a) Drilling a hole through the glass substrate using an ultrasonic drill, (b) a miniature pressure sensor, (c) a drilled glass substrate, (d) an integrated sensor and substrate.....46
Figure 3.16: The pressure of the cell plotted during and after the cell is sealed. While the cell was found to be sealed, there was a slight increase in cell pressure with time which could be leak or because of outgassing.....46
Figure 3.17: An absorption spectrum of a sealed cell obtained from FTIR spectroscopy showing the presence the N_2O and confirming hermeticity.....46
Figure 3.18: Illustration of In solder deposition. 48
Figure 3.19: 200 nm Al thin film electrode deposited using the evaporation technique (concept schematic). 49
Figure 3.20: 100 nm ITO thin film electrode deposition by physical vapor deposition (concept schematic). 49
Figure 4.1: The schematic of the electromagnetic wave propagation model with the orthogonal electric and magnetic field components. 52
Figure 4.2: Simplified DBD cell model as a capacitive load with parallel-electrodes. The RF wavelength diagram is only for understanding and is not to scale. 53
Figure 4.3: (a) Electrical equivalent model of a crystal oscillator with the (b) typical impedance spectrum versus frequency. 54
Figure 4.4: Schematic of the ideal rf input power supply to the Rb cell-load. 54
Figure 4.5: The rf drive design schematic showing the input and LC stage of the drive circuit. ..55
Figure 4.6: The transmission line and its characteristic impedance model. 56
Figure 4.7: Electrical model of a high-frequency capacitor with parasitics.....56
Figure 4.8: Electrical model of a high-frequency inductor with parasitics.....57
Figure 4.9: Maximum power transfer and maximum power efficiency versus impedance for a purely real load [145]. 58
Figure 4.10: A simplified LC series resonant circuit with the capacitive cell load. 58
Figure 4.11: The measured impedance spectrum of the cell with and without PCB (Figure 4.12) calibration showing its high capacitive reactance at frequencies <200 MHz. 59
Figure 4.12: A schematic representation of the LC-stage and the series LC resonant circuit configuration. 60
Figure 4.13: A photograph of the PCB for the Rb-cell and the LC stage components for impedance matching.....60
Figure 4.14: Concept of a Smith chart with the infinities of both resistance and reactance meeting at the centre-right of the circular plot. The 50 Ω load point is at the centre.....61
Figure 4.15: Impedance matching example showing the addition of components to match the cell-load to 50 Ω at 13.56 MHz and the corresponding change in the Smith chart (refer Figure 4.14) 61

Figure 4.16: A photograph of the LC stage PCB with a Rb discharge cell (with In electrodes) fixed on to a PCB along with the soldered matching LCR components. It is impedance matched to 50 Ω at 13.56 MHz with an output BNC connection. 62
Figure 4.17: A 50 Ω matched LC stage with a Al electrode Rb cell and using only an series inductor and a parallel capacitor. A schematic of this circuit is also shown for reference. 62
Figure 4.18: The electrical circuit model of the LC stage load based on which the impedance equation (4.12) is calculated. This load is connected to a transmission line with an inductance L_t in series and capacitance C_t in parallel. 64
Figure 4.19: An example curve fit (red) using the equivalent circuit model for the recorded impedance spectrum data (blue) for a drive circuit operation at 20.7 MHz. 65
Figure 4.20: The R^2 values recorded from the respective curves fitted for various drive circuits with impedance matched LC resonant frequencies between 2-500 MHz 65
Figure 4.21: An example PSPICE circuit for the 20.7 MHz drive circuit showing the s_{11} plot and LC stage circuit parts and the voltage markers 66
Figure 4.22: The plot of the voltage across the cell versus frequency and $V_{Cce} = Q_{rp.}$ 67
Figure 4.23: The plot of Qrp versus frequency for impedance matched Rb-cell CN3 with Al electrodes. 67
Figure 4.24: A high-frequency RF transformer for driving cell voltage. 68
Figure 4.25: Cross-sectional view of the microfabricated Rb light source with circuit notations. On the right, equivalent circuit of the Rb light source (without matching circuit) with the discharge current modeled as a voltage-controlled current source, I_g. L_g is the parasitic inductance induced in the gap after electrical breakdown. 70
Figure 5.1: A schematic illustration of the test and measurement setup showing the four sections used for device characterization. The red lines are 50 Ω BNC coaxial cables, green lines are GPIB cables and black lines are standard laboratory cables/wires. The LC-stage was placed inside a electromagnetically shielded enclosure (Pomona box) or a Faraday cage whenever necessary. 74
Figure 5.2: Test PCBs for powering and heating Rb-cells placed on a 500 μm Al_2O_3 layer. 76
Figure 5.3: The heaters H1, H2 and H3 used in this research showing the active heating area on top of which the Rb cell with the Al_2O_3 spacer is placed. 76
Figure 5.4: Some mounts and stages developed using milling POM and PTFE for the lamp experiments. 77
Figure 5.5: The output of the RF amplifier when set initially to 1 W output. It was controlled using a PID feedback loop through LabVIEW to avoid the observed drifts in forward power... 79
Figure 5.6: An LC-stage circuit showing an ignited microfabricated Rb light source, with Indium ring electrodes, emitting a visible glow discharge. 79
Figure 5.7: Optical spectrum showing the Rb D lines measured from cells: CN1 (a) and CN3 (b) at different cell temperatures. 80
Figure 5.8: The total optical power and Rb D2 line power emitted by CN1 at different cell temperatures. 80
Figure 5.9: Comparison of Rb and Ar line intensity variations with temperature. 80
Figure 5.10: The various electrode configurations used in this research where the electrodes are drawn to the cell scale on the left. The ring inner diameter is 4.5 mm and outer diameter is 6 mm. 81

Figure 5.11: The measured breakdown power and capacitance values of CN2 for different electrode configurations at ~5 MHz. 82
Figure 5.12: The comparison of the power consumption of the CN2 cell with Al and In electrodes (EL6) to produce 10 μW of Rb D2 output. More than 50% improvement in the power consumption is achieved with Al electrodes over In at the >10 MHz drive range.....83
Figure 5.13: The measured optical power from CN1 at two regions of operation: 13.5 MHz diffusion controlled breakdown (red) and 4.2 MHz drift-dominated breakdown (blue). Measured cell temperatures at some relevant data points are mentioned for reference. 83
Figure 5.14: The measured input power (black) at breakdown and the calculated breakdown voltage (blue) of CN3 (with EL6 electrodes) at different drive frequencies between 2-500 MHz. A_e is the electron oscillation amplitude. 85
Figure 5.15: The calculated collision frequency and the electron mean free path for different pressures of Argon at 300 K and 12 eV electron temperature. 86
Figure 5.16: Plots of measured P_{op} and calculated P_g for CN3 when driven at 25 MHz at different input power values....88
Figure 5.17: Ratio of the measured optical power, P_{op} and the calculated P_g for the same cell when emitting a total optical power of 100 μW (400-1000 nm range). 89
Figure 5.18: The calculated values of the power incident on the cell, P_e and the voltage and power coupled to the gap, V_g and P_g respectively for CN3 at breakdown in the 2-500 MHz range. 89
Figure 5.19: The measured optical power and electrical powers at different input frequency values starting from the initial impedance matched value at 15.7 MHz. 91
Figure 5.20: The measured Rb D2 optical power from CN3 and CN1 at different drive frequencies for an input power of 700 mW. 92
Figure 5.21: The change in the number of the volume, diffuse and surface discharges with increase in the magnitude of different input conditions. The test range for each condition within which these observations are valid is mentioned. Lower VDs and SDs lead to higher optical stability but higher breakdown power. 93
Figure 5.22: The spectrum of the emitted light from the Rb lamp-cell during the red-mode operation. 94
Figure 5.23: The measured breakdown power values for CN0 and CN1 at different cell temperatures. 95
Figure 5.24: The measured optical power and forward and reflected electrical powers to the LC-stage of the Rb DBD lamp lifetime test. The lamp was initially set to emit 100 μW of optical power (corresponding to 25 μW from the position of measurement. The lamp was still fully functional after the test. 97
Figure 5.25: CN2 after the lifetime test showing a slightly brownish thin layer of Rb on the inner dielectric wall indicating possible Rb diffusion in the Pyrex walls. 98
Figure 5.26: Dark craters observed on the inner Pyrex wall after several months of plasma operation in CN6. The surface discharges formed on liquid Rb droplets are the most likely cause. 98
Figure 5.27: The LTCC integrated Rb mini-lamp module at operation (lamp powered at 25 MHz). 99
Figure 5.28: The schematic of the LTCC module operation and test setup. 100

Figure 5.29: Cell temperature and Rb D2 optical power measured during a continuous run of 5 hours. Lamp drive frequency: 25 MHz, forward power: 1.1 Watts. 100
Figure 6.1: The photograph of the pressure chamber and the schematic of the discharge gap experiment setup inside which the ITO coated Pyrex substrates were aligned in parallel inside a pressure-controlled chamber to ignite DBDs by connected the ITO electrodes to rf power. ... 103
Figure 6.2: Photographs of an example bases with the milled slots, with different separation lengths, where the Pyrex substrates are placed. 104
Figure 6.3: Cross-sectional view of the discharge gap ITO coated substrates. On the right, equivalent circuit of these substrates (without matching circuit) with the discharge current modelled as a voltage-controlled current source, I_{dg}. 104
Figure 6.4: An ignited discharge between the ITO coated Pyrex substrates viewed through the optical window 105
Figure 6.5: Input electrical breakdown power, P_{in}, of three different buffer gases for different pd conditions at (a) 4.42 MHz, (b) 75.7 MHz and at 465.2 MHz. Measured data points are marked but line plots were chosen only for convenient understanding. 106
Figure 6.6: Top and side view photographs of observed discharge behavior at different pressures of Ar. 107
Figure 6.7: Optical power fluctuations (sub-second) observed in the discharge gap setup, as a function of drive frequency/(*pd*) ratio. 108
Figure 6.8: The optical power measured above the optical window for the different buffer gases at various drive frequencies for P_{in}=1W. 108
Figure 6.9: Side-view photographs of the observed plasma in the discharge gap at different frequencies and Argon pressures for a 2 mm discharge gap length and P_{in}=1 W. The increase in the diffuse glow discharge is observed at lower pressures while a decrease in the number of dielectric barrier discharges can be seen at higher drive frequencies. 109
Figure 6.10: Experimentally measured optical spectrum of the CN10 cell at 100 °C showing the observed Rb lines and their corresponding transitions. All other spectral lines correspond to Ar or Cs impurities. 110
Figure 6.11: The normalized Rb line intensities in the 400-1000 nm range from both measured and simulated data corresponding to CN10 at 100 °C. The values were found to be closely matched. 111
Figure 6.12: A surface plot of the electron density and the electron temperature from a 1-D discharge gap simulation with the input parameters: 2 MHz, 150 V, 373 K and 30 mbar Argon. 112
Figure 7.1: The DR atomic clock test setup (photograph and schematic) to test the optical pumping characteristics of the microfabricated Rb light source at LTF, University of Neuchâtel. 117
Figure 7.2: The drop in optical power versus distance from the light source surface. The focal length and diameter are in millimetres. The measured data points are marked and line plots were chosen for easier understanding. 118
Figure 7.3: The Rb energy levels, hyperfine splitting and the Zeeman splitting in the presence of a magnetic field [185]. 119
Figure 7.4: Representation of the ground and excited states of Rb atoms in the presence of a static magnetic field and the transitions induced by pumping these atoms with circularly polarized light [186]. 120

Figure 7.5: The magnetometer test setup schematic showing the vertical stack configuration of the various components..... 121
Figure 7.6: A photograph of the realized magnetometer test setup with the vertically aligned cage system using milled POM parts..... 121
Figure 7.7: The FM of the rf field technique to produce a high SNR pumping signal and avoid the influence of optical power fluctuations on the signal detection. 122
Figure 7.8: The modified magnetometer test setup placed inside a triaxial Helmholtz coil shield stage for the Rb D1 laser pumping test..... 123
Figure 7.9: The pumping test results using a Rb D1 laser showing the Rb absorption signals. The DC current through the DC field coils shown correspond to 85 μT, 65 μT and 48 μT DC fields respectively. The intensity (Y-axis) values correspond to the voltage measured across a 100 kΩ resistor connected to the photodetector. 124
Figure 7.10: The pumping signal when the optical power of the Rb D1 laser was 10 μW. A detectable magnetometer signal without the rf field FM technique can be understood to be around 10 μW..... 124
Figure 7.11: The pumping signal recorded using the LIA (R output) and the rf field FM technique from a nat. Rb ICP lamp at a DC magnetic field of 25 μT..... 125
Figure 7.12: The measured ^{85}Rb pumping signals at 110 kHz at different cell temperatures. When the AC heater was switched on, the signal was highly attenuated or almost vanished possibly due to the field inhomogeneities introduced by the heater..... 125

List of tables

Table 2.1: Different types of collisions in a gaseous system and the resulting atomic transitions [23], [24]. 13
Table 2.2: Different types of wall collisions in a finite gaseous system leading to electron emissions [30]. 15
Table 3.1: List of the desired performance and geometry requirements of the light source for portable optical pumping applications. 33
Table 3.2: Values of a, b and η_{max} of some inert gases and Rb for ionization efficiency calculations. 35
Table 3.3: Visual observations and comparisons of the different metallization–solder combinations on 1 mm thick glass substrates. 44
Table 3.4: The list of microfabricated cells used in this research and their properties. 47
Table 4.1: List of electrical notations of the different powers and voltages used in this report. 68
Table 5.1: The slope values (linear regression and keeping intercept zero) of the Pop function of Pin, when Pin is less than 5 W, for different cells at the diffusion and drift dominated regions. .84
Table 5.2: The experimentally observed fr values for different cells where the breakdown voltage was minimum. The estimated ν values for Ar, assuming 300 K and 12 eV electron temperature, are also mentioned for reference. 87
Table 5.3: The different calculated power losses for CN3 along with the measured input power, Pin and power coupled to the gap, Pg, at electrical breakdown condition for different resonant drive circuits. 90
Table 5.4: The measured input power values at different drive frequencies for the three cells when they were observed to transcend to the red mode. The accuracy of the drive frequency values is ±1 MHz. 95
Table 6.1: The electron properties in the discharge gap recorded for a 30 mbar Ar and 2 mm discharge gap length with an input voltage of 150 V at different drive frequencies. 113
Table 6.2: The electron properties in the discharge gap recorded for an input voltage of 150 V at 13 MHz for different Argon pressures at a 2 mm discharge gap length. 113
Table 6.3: The electron properties in the discharge gap recorded for an input voltage of 150 V with 30 mbar Ar and 2 mm discharge gap length for different secondary electron emission coefficients of the inner dielectric walls. 114
Table 6.4: The electron properties in the discharge gap with 30 mbar Ar and a 2 mm discharge gap length with different input voltages when the drive frequency is 13 MHz. 114
Table 6.5: The simulated electron properties on reducing the discharge gap length when the drive frequency is 13 MHz, 150 V input voltage and 30 mbar Ar buffer gas pressure. 115

List of abbreviations

CCP	-	Capacitively Coupled Plasma
CPT	-	Coherent Population Trapping
DBD	-	Dielectric Barrier Discharge
DR	-	Double Resonance
EM	-	Electro Magnetic
ESR	-	Equivalent Series Resistance
ICP	-	Inductively Coupled Plasma
ITO	-	Indium Tin Oxide
LIA	-	Lock In Amplifier
LTCC	-	Low Temperature Co-fired Ceramic
PID	-	Proportional-Integral-Derivative
POM	-	Polyoxymethlylene
RF	-	Radio Frequency
SNR	-	Signal to Noise Ratio
VCSEL	-	Vertical Cavity Surface Emitting Laser
VNA	-	Vector Network Analyzer
p.d	-	product of buffer gas pressure (p) and discharge gap length (d)

Chapter 1 Introduction

Time is one of the most obviously perceivable dimensions and yet one of the hardest quantities to define without circularity. Time, along with space, defines human life, history, present, future, power, speed, change and all discernible entities. It is mainly because of its easily perceivable nature and its ability to enable comprehensible communications that the Euclidean space-time perspective (and the more general space-time continuum) has remained the dominant perception among humans. Most humans have evolved with this perception, understanding and accepting the circular nature of its dimensions' definitions, and quantifying it to the level of precision and accuracy as needed. A time precision of a day or so might still be acceptable for some cases, for example, say a postal delivery, and it is expressible through several means including a simple verbal form of communication. But for an application such as the now ubiquitous GPS (Global Positioning System) receiver, a time precision of less than one billionth of a second might be required to accurately give the user's position on earth. There are several existing and emerging device technologies, such as quartz oscillators and MEMS-based micro-resonators, that can potentially realize such a high-precision time signal which is communicable through electrical means – the most accurate and precise device till date being the atomic clock.

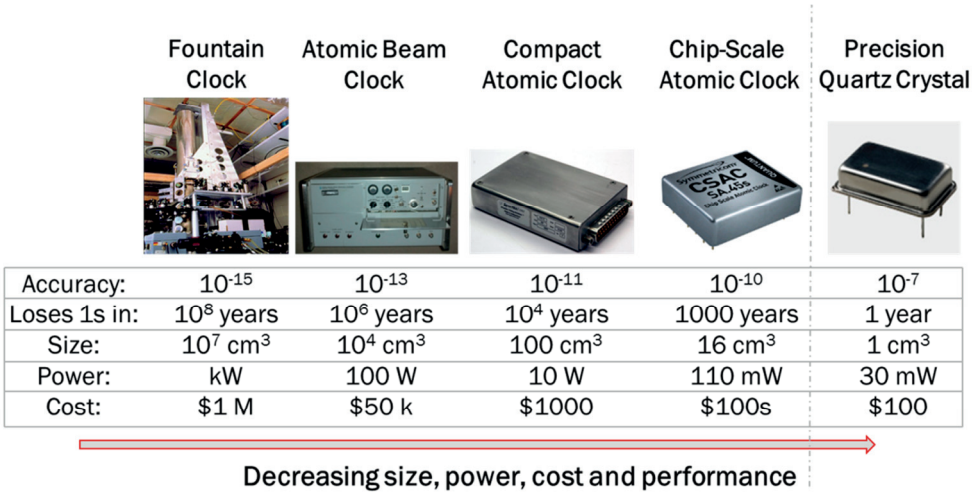

Figure 1.1: The different types of atomic clocks classified according to size, power, cost and performance. Picture sources: [L-R]: NIST, HP Inc., Spectratime SA, Symmetricom Inc., Laptech Inc. Data source: [1].

Atomic clocks monitor and manipulate atomic transitions to use the transition frequencies as references to produce a high precision time signal (more details in section 1.1). Today there exist several varieties of atomic clocks that exploit different atomic transition frequencies, atom/ion containment methods, and interrogation schemes for the realization of highly accurate and stable frequency references. Their frequency instability (Allan deviation) and accuracy generally scales inversely with total clock size. For example, atomic fountain clocks (the primary Cs fountain frequency standard) provide the most accurate frequency references (clock uncertainty down to less than 10^{-15}) but occupy volumes of several m^3 and consume hundreds of watts of power. On the other side of the size-scale are the compact vapor-cell ^{87}Rb Double-Resonance (DR) microwave frequency standard (overall volumes of 100-1000 cm^3), that bring the benefits of atomic clocks to applications where mass, volume, and power consumption of the clock are an issue, e.g. navigation systems [2], network synchronization and digital communication systems

[3]. Even smaller miniature and chip-scale atomic clocks have volumes of a few cm^3 and lower, and consume <100 mW of power are now emerging from research to applications, in response to a large demand for portable or remote operations [4]. Alkali metals like Rb or Cs are preferred for atomic clocks because of their single valence electron and a relatively simple atomic energy structure when compared to other elements, which is important for a straight-forward interrogation.

The compact Rb vapor-cell DR clocks use light emitted by a Rb discharge lamp for optical pumping and detection of the atomic transitions (explained in section 1.1). [A minimum of few μW on the Rb D1 or D2 line is required from the lamp for detectable optical pumping in DR clocks (experimentally determined)] These Rb discharge lamps [5], are typically spherical (5-10 mm diameter), glass-blown cells filled with a few hundred μg of Rb and a few mbar of a starter/buffer gas for easier ignition of the plasma, which is inductively coupled by an external coil. These lamps operate very well for compact clocks due to the intrinsically correct light frequency for optical pumping (Rb lines), technical simplicity, slow frequency drift (aging), and long lifetime. However, they cannot be used for miniature and chip-scale atomic clocks due to their high power consumption (several Watts), large size and non-planar geometry which prevent compact integration (chip-stack configuration, for example) and portable operation requirements [6]. Hence, the DR approach has been a challenge for chip-scale clocks [3] and the Coherent Population Trapping (CPT) approach was widely chosen [7], [8], [9] where a VCSEL (vertical cavity surface emitting laser diode) [10] is used to create a coherent "dark state" in the atomic sample [11]. The CPT technique also avoids the necessity of a microwave cavity which makes it easier to achieve such ultra-compact sizes. Some studies have been published on the realization of chip-scale clocks using DR or non-CPT methods but they also employ VCSELs [12], [13].

While VCSELs offer several advantages including compact size (~mm^3), planar substrates, easy integration with other microfabricated components, and low power consumption (few mW), they have several undesirable characteristics including a strong temperature dependence of the output D line wavelength, ageing effects [3], long-term reliability concerns (prone to failures caused by events such as ESD) [14] and availability issues. Rb plasma discharge lamps intrinsically produce the D lines and their wavelengths are not dependent on temperature. They are also known to have a linear frequency aging of less than 10^{-13}/day [15], with an average Rb diffusion rate (main performance-limiting mechanism) of 50 years into the glass walls of mm-scale lamps [16]. Hence, a mm-scale planar low-power Rb plasma discharge light source would avoid these limitations of the VCSELs and would extend the inherent advantages of Rb discharges and hence the DR technique to miniature atomic clocks.

This thesis presents the development and characterization of a microfabricated (1x1x0.3 cm^3) planar Rb capacitively-coupled dielectric barrier discharge light source that can be used for stable optical pumping in miniature DR atomic clocks and quantum sensors. The microfabricated light sources were experimentally tested within a wide range of input conditions including drive frequency, input power, electrode material and geometry, buffer gas pressure, temperature and discharge gap length to identify the suitable operating conditions for a low-power operation. A stable optical power of 10 μW with less than 0.2% fluctuations (in the seconds scale) on the Rb D2 line was achieved when the power consumed by the Rb cell was less than 19 mW. The light source was also demonstrated to operate without any functional problems for at least six

months, emitting a stable 100 µW of total optical power at 100 °C (corresponds to 6 µW of Rb D2 line power). They are thus found to be stable and robust, showing high potential towards enabling a new class of highly compact atomic clocks and quantum sensors.

This research was part of an overarching project: 'Miniature atomic clocks and quantum sensors', funded by the Swiss National Science Foundation, where the primary objective was to study and develop the physics package of a miniature double-resonance atomic clock (refer section 1.3 for more details).

The following sections in this chapter details: **(1)** the basic concepts of the primary target application of this research – the Rb DR atomic clock and **(2)** the current state-of-art miniature atomic clocks and Rb discharge lamps. Separate sections summarizing the thesis objectives and the structure of this thesis report, and the overarching project details are included in this chapter.

1.1 Double-resonance atomic clocks

The principle of operation of an atomic clock is to exploit an atomic resonance as a reference to stabilize the frequency of a quartz oscillator.

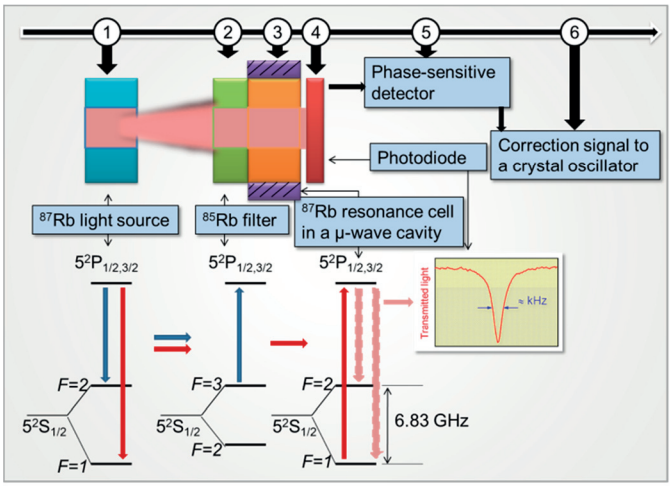

Figure 1.2: A schematic illustration of the double-resonance interrogation technique to produce the high-precision time signal.

In a double-resonance (DR) Rb atomic clock [17], this resonance is the "clock" transition between the two ground-state hyperfine levels of ^{87}Rb, at a microwave frequency near 6.83 GHz ($5^2S_{1/2}$ state, $|F=2, mF=0\rangle$ to $|F=1, mF=0\rangle$), detected on atoms maintained in a small Rb resonance cell, as shown in Figure 1.2. Pumping light from a lamp or laser resonant with the Rb D1 or D2 line (795.0 nm or 780.2 nm, respectively) illuminates the cell and creates a ground-state polarization in the atoms. The clock transition is then detected by applying a microwave field to the atoms via a microwave-cavity placed around the cell, and the resonance manifests itself as a narrow dip in pump-light power transmitted through the cell versus microwave frequency. The frequency of a voltage-controlled quartz oscillator is locked to this dip using phase-sensitive detection and the continuous phase-correction voltage helps actualize a highly precise time/frequency signal from the quartz oscillator. As it can be seen from Figure 1.2, a ^{85}Rb filter cell can be used to filter out the ($5^2S_{1/2}$ state, $|F=2, mF=0\rangle$ to $5^2P_{1/2,\,3.2}$ states) spectral

line from the ^{87}Rb lamp, to create the necessary nonthermal population distribution (imbalance) in the ^{87}Rb $5^2S_{1/2}$ states in the resonance cell. This is because the ^{85}Rb's F=3 state naturally happens to be degenerate with the ^{87}Rb's F=2 state and hence enables this easy filtering. For this reason, Rb is preferred over Cs for double-resonance clocks.

1.2 Current state-of-the-art portable vapor-cell atomic clocks

Portable vapor-cell atomic clocks can be roughly divided into three categories primarily based on size: high-performance atomic clocks (package volume: ~1000 cm^3, typical fractional frequency stability: 10^{-14} to 10^{-13} $\tau^{1/2}$), compact atomic clocks (100-300 cm^3, 10^{-13} to 10^{-11} $\tau^{1/2}$), and miniature or chip-scale atomic clocks (few cm^3-tens of cm^3, 10^{-11} to 10^{-10} $\tau^{1/2}$) (Figure 1.3) [18], [7].

Figure 1.3: Photographs of high-performance (XPRO, Symmetricom), compact (LCR-900, Spectratime) and chip-scale (SA.45s, Symmetricom) Rb vapor-cell atomic clocks.

Most miniature/chip-scale atomic clocks (MACs/CSACs), reported so far use the coherent population trapping (CPT) interrogation technique, as mentioned earlier, where a VCSEL (Figure 1.4) is used for Rb optical pumping. The smallest and most low-power consuming CSAC reported so far was developed and optimized by researchers at NIST [19], where the physics package occupies a volume of 12 mm^3, with 195 mW of power consumption to give a short-term frequency stability of $4\text{x}10^{-11}$ $\tau^{1/2}$. In the higher size scale, a 10 cm^3, ~200 mW power consuming MAC with a short-term stability of $4\text{x}10^{-10}$ $\tau^{1/2}$ was reported by Lutwak et. al. [18] for military communication applications. These are laboratory or non-commercial standards while the only commercial CSAC/MAC, available since 2011, was developed by Symmetricom where the reported timing accuracy is around 10^{-10} $\tau^{1/2}$ with an overall package volume of 16 cm^3 and a power consumption of 110 mW. These are the current state-of-the-art miniature and chip-scale clocks.

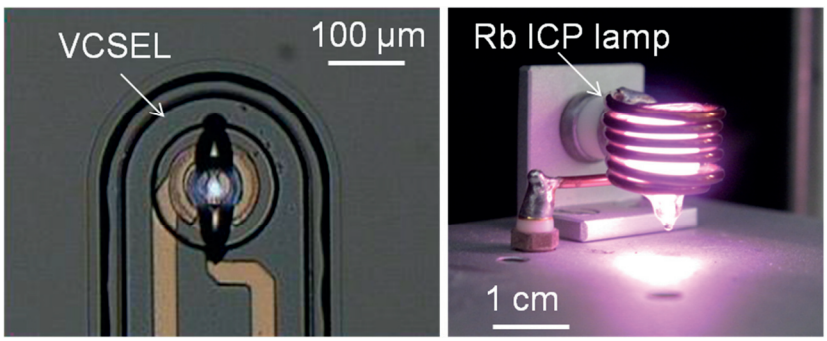

Figure 1.4: An example VCSEL used by Serkland et. al. [9] and a typical Rb discharge lamp with an excitation coil around it to ignite an inductively-coupled plasma.

This research reports on a miniature Rb discharge lamp for use in a miniature DR clock. The current commercially available DR clocks using a discharge lamp are typically compact-size clocks, for example, the LCR-900 by Spectratime, which is 74x77x40 mm^3 in size, consuming around 10 W of power with a short-term frequency stability of $1x10^{-11}$ $\tau^{1/2}$. The Rb discharge lamps typically used in these clocks are inductively-coupled glass-blown lamps, similar to the one shown in Figure 1.4. They are typically spherical, consume several Watts of power and require excitation coils around the cell making them unsuitable for miniature clocks. However, these are the current and existing state-of-the-art DR clocks and Rb discharge lamps and this research aims to extend the benefits of DR clocks and the discharge lamps to the miniature scale.

1.3 Miniature atomic clocks and quantum sensors (MACQS) project

The research work presented in this report was part of an overarching project called the MACQS project where the objective was to develop and study the key building blocks that are required for the realization of miniature DR atomic clocks and quantum sensors. The project started on July 1st, 2009 and was funded by the Sinergia project fund of the Swiss National Science Foundation. One of the key notes of this project is its multi-disciplinary approach; involving scientific teams specialized in the fields of atomic physics, microwave engineering, micro fabrication, material science, and photonics, brought together to exchange the know-how of different disciplines and work on this novel application.

The envisioned miniature DR Rb atomic clock, planned in this project, is shown in Figure 1.5 and consists of a microfabricated Rb plasma light source, an optional micro-fabricated ^{85}Rb filter, a micro-fabricated Rb resonance cell which is enclosed by a miniaturized microwave cavity, and a photodetector. The Rb plasma light source intrinsically emits at the correct wavelengths, Rb D1 and D2 lines, as required for optical pumping in a Rb clock, after excitation, when Rb atoms decay from the $5^2P_{1/2,\ 3/2}$ states back to the ground state $5^2S_{1/2}$. The different excitation methods and the physics involved are discussed in detail in the following chapters.

Research partners from five laboratories participated in this project:

(1) Laboratoire Temps-Fréquence (LTF), University of Neuchâtel,

(2) Sensors, Actuators and Microsystems Laboratory (SAMLAB), EPFL,

(3) Microsystems for Space Technologies Laboratory (LMTS), EPFL,

(4) Laboratory of Electromagnetics and Acoustics (LEMA), EPFL,

(5) Laboratory of Microengineering for Manufacturing (LPM), EPFL

All laboratories worked together towards reaching the miniature DR atomic clock package (represented in Figure 1.5) while each lab had their own responsibilities and research focuses. LTF were the project coordinators, focusing on studies of the atomic physics aspects for miniature atomic clocks, in particular on laser and microwave DR spectroscopy in microfabricated alkali vapor cells. SAMLAB worked on the development of miniature Rb cells including both anodically bonded and low-temperature Indium bonded Rb vapor cells for discharge light source and resonance cell applications. The primary focus of LEMA was on designing and developing a miniature microwave cavity required to sustain the double-resonance in the Rb DR clock. LPM worked on developing a packaging solution for the miniature clock,

creating heating and microwave components and also worked on developing low-temperature hermetic sealing techniques for Rb vapor cells.

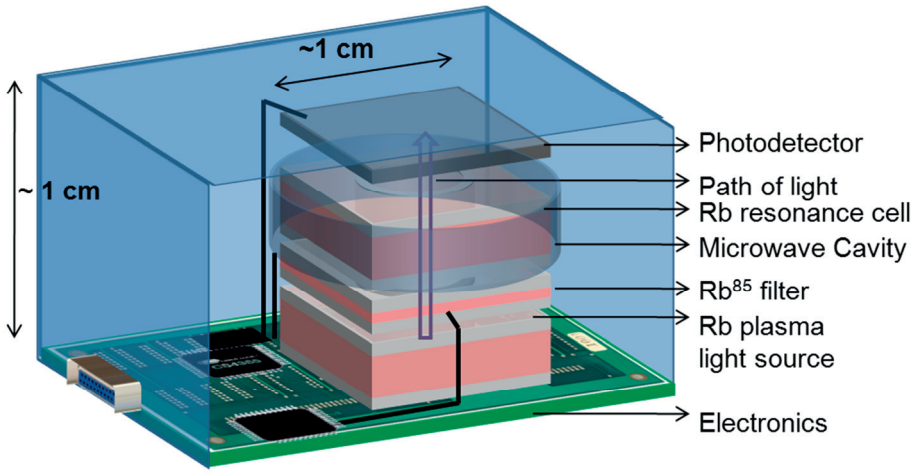

Figure 1.5: A schematic representation of the envisioned miniature Rb DR atomic clock showing all the microfabricated components and the electronics inside a package volume within few cm^3.

The main research focus of LMTS was to develop a microfabricated Rb discharge light source for the target Rb DR clock and the work done towards achieving this goal is presented here in this thesis. The LMTS worked in collaboration with the other labs: SAMLAB provided with the miniature Rb vapor cells for the lamp design (microfabrication by Dr. Yves Pétremand), LTF (Dr. Christoph Affolderbach) helped with the lamp optical pumping tests with their expertise and resources for such tests, aspects of lamp and clock designs and many spectroscopical studies throughout the project, and LPM (Fabrizio Vecchio and Dr. Thomas Maeder) assisted with their manufacturing technology resources to collaborate on developing low-temperature Rb hermetic sealing techniques and LTCC-integrated lamp modules.

This research project not only focused on a fully integrated miniature atomic clock, but also on more innovative and prospective scientific studies on selected relevant topics and challenges that may lead to separate and more product-oriented developments. The developed building blocks may also constitute the basic components of other quantum sensors (atomic magnetometers, atomic gyroscopes, etc.) and future quantum communication systems. This project is of high significance to several communities including timing and frequency, communications and to portable technologies in general as its impact could possibly pave the way towards a new generation of miniature and highly reliable atomic clocks and quantum sensors.

1.4 Thesis objectives and report structure

The aim of this research is to develop a low-power miniature rubidium plasma light source for optical pumping in miniature or chip-scale atomic clocks.

- The device needs to be easily integrable with the other components of the miniature DR atomic clock and hence desired to be planar, with a size equal to or less than 10 x 10 x 3 mm^3, for a simple stack configuration of components.
- The power consumption of the light source needs to be less than tens of mW and preferably as low as possible.

- A minimum of 5 μW optical power on one of the Rb D lines with less than 0.2% short-term fluctuations is required for stable optical pumping and an acceptable clock performance.
- The device needs to be robust with a minimum lifetime of several years.

The scientific objectives of this research:

- To study the physics behind plasma discharge emission from a mm-scale light source and identify the optimal operating conditions for maximum Rb D line emission
- To develop a power-efficient rf circuitry to drive the planar light source and identify the steps that can be taken to minimize power losses
- To develop an electrical model of the Rb light source and drive circuit to calculate the power coupled to the discharge gap and estimate the output Rb D line power for a given set of cell and input conditions
- To experimentally observe and understand the effects of buffer gas, pressure, input frequency and other discharge gap parameters on the performance of the Rb light source

The design and development of miniature Rb light sources, followed by the characterization and optimization of the developed microfabricated Rb dielectric barrier discharge light source, to achieve these thesis objectives, are reported in the following chapters and a brief outline of the chapters are mentioned below for reference.

Chapter 2 gives the introduction to the physics of plasma discharges, the phenomenon of impact excitations leading to discharge emissions and the methods to achieve a high magnitude of these emissions by applying alternating (RF-AC) electric fields. Using the RF-AC approach, the electrodes can be placed outside the discharge gap. This would enable a longer device lifetime, as the predominant lifetime limiting process of electrode erosion from electron and ionic bombardment is avoided.

The importance of adding a low-pressure buffer gas to a Rb vapor cell to enable a low electrical breakdown power, and the suitable gases and pressure ranges for the first prototype are reported. A literature survey outlining the available drive design options for the light source are discussed. The conceptually ideal frequency for the lowest breakdown power for a mm-scale light source is identified to be in the range when the transit time of electrons in the applied alternating electric field starts to get higher than half the time period of the applied field cycle. This corresponds to a drive frequency in the 1-50 MHz range for an optimal low-pressure buffer-gas filled Rb light source with a discharge gap in the few mm length scale. An external and parallel electrode geometry (dielectric barrier discharge or DBD design) to ignite a capacitively-coupled plasma (CCP) discharge was chosen for the planar mm-scale gap cell fabrication and characterization.

Chapter 3 reports on the miniature rubidium DBD cell design, fabrication and development. The exact cell requirements including cell geometry, materials and pressure for achieving the desired performance are discussed. The explosive properties of Rb with air or water make it challenging to hermetically seal Rb in an optically-transparent miniature cell. The current state-of-the-art miniature Rb vapor cell fabrication techniques are reported including the anodic bonding technique used to fabricate the cells used in this research. The suitable cell gap

conditions for a high Rb light output and a low breakdown power are analyzed based on kinetic theory and the ionization properties of different gases reported in literature. This study was important for determining an educated set of starting conditions for developing the first prototype of Rb vapor cells. A novel low-temperature (<140 °C with 58Bi42Sn) Rb dispensing and solder-sealing technique is reported, which was developed in collaboration with Dr. Thomas Maeder and Mr. Fabrizio Vecchio at LPM, EPFL for producing mm-scale planar Rb vapor cells. The electrode deposition methods used in this research are also discussed including a full list of cells used for characterization experiments.

Figure 1.6: A microfabricated Rb DBD light source, with the LC drive circuit, emitting discharges when driven with radio-frequency power.

Chapter 4 reports on the rf drive circuit development for the Rb DBD cell. The drive circuit needed to achieve a high voltage amplification across the lamp-cell with the lowest power input, allowing for a Rb D line output for at least few μW with ideally tens of mW (or lower) power consumption. The developed LC series resonant drive circuits for voltage amplification across the Rb cell and impedance matching of the cell-load to the source to 50 Ω at all desired frequencies between 2-500 MHz, are discussed. An electrical model of the Rb cell and the load-impedance models in MATLAB [20] and PSPICE [21], developed to calculate the voltage and power coupled to the discharge gap and the different power loss mechanisms, are also discussed.

Chapter 5 reports on the performance of the developed miniature Rb DBD lamp (Figure 1.6) at different operating conditions observed by experimentally varying different input variables (electrical power and frequency, electrode material and geometry, cell pressure and temperature) within an identified range of interest, and using different electrical and optical experimental characterization techniques. The effect of temperature, the observed red-mode transitions and also the observed lifetime and reliability characteristics of the Rb lamp are reported.

Chapter 6 reports on the experiments and simulations performed towards the optimization of the discharge gap parameters for improving the light source performance. The electrical breakdown power and the optical stability characteristics for different buffer gases, pressures and discharge gap lengths are reported. Visual observation of DBDs and rf discharges at different input conditions are reported. The developed COMSOL [22] simulation model and the observed electron properties including electron density, electron temperature at relevant operating conditions are reported and discussed.

Chapter 7 reports on the preliminary optical pumping tests conducted using a custom-built magnetometer test setup to demonstrate the optical pumping ability of the Rb DBD lamp. The test setup and its components are explained and the pumping results obtained from inductively-coupled Rb lamps on a microfabricated Rb resonance cell are also reported.

Chapter 8 gives the summary of all the observed results and the conclusions identified from this research, discussing the high potential of this Rb light source for the next generation of miniature atomic clocks.

Chapter 2 Electrically-induced plasma discharge emission

The primary thesis objective is to develop a stable and low-power consuming miniature rubidium discharge light source and hence, it is important to understand the physics behind efficient discharge emission. The basic concepts of discharge emission, relevant to this work, are discussed in this chapter, starting with a description of single atomic events, followed by statistical processes, electrically induced discharges and high frequency discharges. Single atomic events explain the fundamental processes governing the discharge physics while the statistical processes act as useful monitors for designing and developing a discharge light source. Electrical breakdown and the theoretical effects of the electrical frequency and gas conditions on the discharge behavior are discussed, finally arriving at the idea of dielectric barrier discharge light sources. The main goal of this chapter is to help the reader understand the fundamental concepts and logic behind choosing the rubidium discharge light source design (discussed in the next chapter).

While the basic concepts discussed in this chapter can be found in several books, the primary references for this chapter are [23], [24], especially for sections 2.2-2.5.

Plasma discharge light sources

Plasma discharges have been commonly used in several light source applications, including the prevalent neon lamps and fluorescent tubes (Figure 2.1). In the miniature scale, the best examples are the plasma television panels where millions of micro plasma-cells filled with buffer gas and phosphors are ignited to create the necessary output light combinations for displays Figure 2.1c. Some plasma excimer light sources are also used for medical and skin treatments [25]. Most of the commercial plasma light sources are electrically-powered at various frequencies and exploit the impact ionization process for a high power efficiency output and the use of phosphors for high photon efficiency. Here, in this research, a similar approach (no phosphors necessary) using the impact ionization process is implemented and the fundamental physics approach needed for developing a power-efficient rubidium discharge emission from a mm-scale light source is discussed in the following sections.

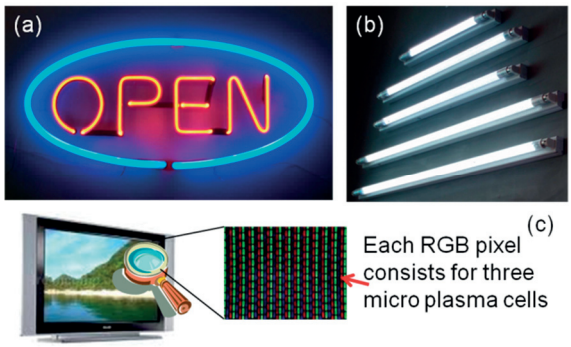

Figure 2.1: Some examples of plasma discharge light sources: (a) a common neon sign, Source: perma-laboratories.com (b) fluorescent light tubes Source: best-b2b.com and (c) plasma TV which uses at least several thousand plasma discharge cells for the display.

2.1 Gas discharge plasmas

Gas discharge plasma or low-temperature plasma is the type of plasma state that is used for rubidium discharge emission in the light sources in this research and hence they are introduced in this section starting with the definition of the plasma state. The plasma state, often referred to as the fourth state of matter, is essentially a gas containing a non-negligible amount of ionized

species (Figure 2.2). More specifically, when a gas contains roughly more than 1 ppm of ionized species or charge carriers, like electrons and ions, it can be said to be in the plasma state. The ionization degree can vary from 1 ppm (partially ionized gas) to 100% (fully ionized gas). There are several ways to classify the plasma state, based on temperature, degree of ionization, density of ionized species and electromagnetic properties. The most fundamental classification is based on the temperature of the plasma: **(1)** high-temperature or fusion plasmas, **(2)** low-temperature or gas discharge plasmas. High temperature plasmas are ubiquitous being responsible for almost all the visible radiation emitted from stars. They are said to be in thermal equilibrium and can also be generated in tokamaks using magnetic fusion reactions [26]. Thermal equilibrium implies that the temperature of all species (electrons, ions and neutral species) is the same. Low-temperature or gas discharge plasmas, on the other hand, correspond to a relatively low degree of ionization and can be classified into LTE (local thermal equilibrium) or non-LTE plasmas. Only the gas discharge plasma is discussed further in this study. The word 'discharge' originates from 'electrical discharges' – the term used to describe any flow of electric charge through a gas or liquid.

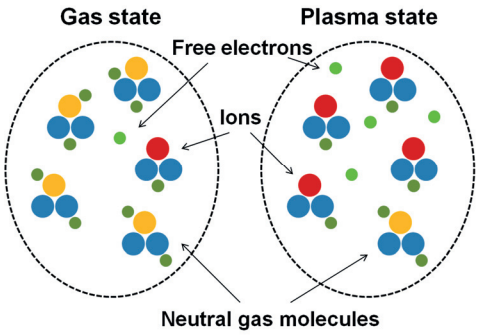

Figure 2.2: A schematic and simplistic illustration of a plasma state consisting of a non-negligible density of charged entities in a gas.

Local thermal equilibrium (LTE) denotes that the temperature of all plasma species are the same in localized areas in the plasma. While many parameters play a role in determining this property, the gas pressure and the length of plasma interactions can be used to narrow down and understand the overall physics of the gas discharge plasma. A high gas pressure (for an infinite length of plasma interactions) implies many collisions between the various plasma species leading to an efficient energy exchange between the various plasma species leading closer to equal temperatures and an LTE plasma. Lower the gas pressure, lower collisions leading to higher differences in temperatures of plasma species and a non-LTE plasma. Now, for a finite length of plasma interactions (bound by glass walls for instance), when the gas pressure is low enough for the collision mean free path to become comparable to this finite length, the plasma reaches highly non-LTE conditions with a significant amount of energy and plasma species lost to walls. Designing conditions for sustaining LTE discharges are typically useful for any application that requires heating [27], [28] but is not necessary for discharge light sources or other non-heating applications [29] as other parameters like power consumption and geometry dictate the discharge conditions. But as LTE discharges are more stable and homogeneous, design conditions can be chosen to work closer towards the LTE domain while meeting the performance requirements of the discharge device.

2.2 Excitation phenomena in gases

Direct experimental evidence from the scattering of particles and electrons by thin foils, and from the diffraction of X-rays, and indirect evidence from the spectra of the elements, leads to the conclusion that an atom consists of a central positive charge, the nucleus, surrounded by

electron clouds, the whole structure being electrically neutral. An example schematic of a Neon atom is shown in Figure 2.3. Almost the entire mass of the atom is concentrated in the nucleus, the mass of the electrons being negligible in comparison. The electron clouds extends over a geometrical region (sphere of radius in the order of Angstroms in the case of an s-orbital, lobes in the case of p-orbitals and higher), centered about the nucleus. This region consists mostly of empty space, within which there are constantly varying electric fields but it appears electrically neutral outside the sphere. This structure, when placed in a sufficiently strong electric field, can be disrupted by displacing the electrons which leads to either exciting or polarizing/ionizing the atom. In this section, some relevant concepts required to understand the excitation phenomena in gas atoms are discussed.

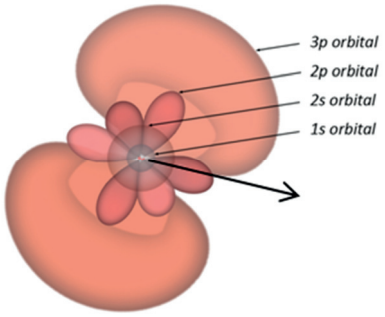

Figure 2.3: A schematic model of a Ne atom (example) with electrons distributed in the various orbitals held by the positively charged proton centric nucleus at different energy levels. Source: Lawrence Berkeley National Laboratory.

2.2.1 Motion of particles in a gas

Gas atoms in a system can be excited to higher energy states by supplying energy to the atoms. This can be done through several external means including thermal excitation by increasing the temperature of the system or by accelerating charged species by applying an electric field. Irrespective of the external source of energy, the energy is scattered and distributed among the gaseous entities in the system via collisions and hence it is important to understand the physics of particles in motion. Here, the fundamental atomic events involving the motion of particles or species (both charged and neutral) are discussed using the kinetic theory of gases and the quantum mechanical model of an atom. Assuming all particles are hard spheres, the effective cross-section area of collision, A_c, of two particles of radii r1 and r2, can be given by, $A_c = \pi.(r1 + r2)^2$.

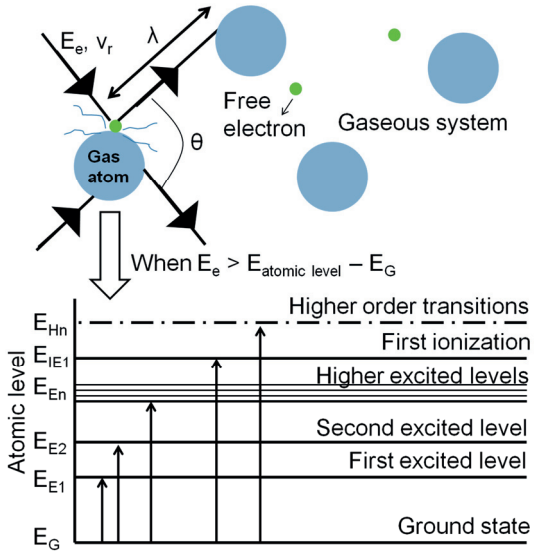

Figure 2.4: A schematic representation of an electron impact collision with a gas atom leading to different possible atomic transitions after collision depending on the incoming electron's kinetic energy, E_e [23].

When there is only one type of gas atoms with diameter d or when there are several types of gas atoms in significant proportions with d being the diameter of the largest atom, the atomic collision cross-section would be $A_c = \pi.d^2$. The mean free path, λ, which is defined as the distance between two collisions in a gas, of an atom can be given by [30]:

$$\lambda = \frac{\text{total distance travelled by the atom}}{\text{number of collisions}} = \frac{L}{\sqrt{2}.A_c.L.n} = \frac{1}{\sqrt{2}.\pi.n.d^2} \qquad (2.1)$$

where L is the total distance travelled by the atom and n is the number of atoms in a unit volume. The √2 factor is because the average velocity of the atoms is defined as the root mean square velocity and hence the average root mean square number of collisions, considering that all atoms are always moving, is increased by √2. This formula (2.1) also applies to ions as they are only negligibly lighter than the mass of an atom. Depending on the charge carrier and the amount of charge, they can have shorter mean free paths due to electrostatic forces and this is sometimes compensated using a small numerical factor.

Table 2.1: Different types of collisions in a gaseous system and the resulting atomic transitions [23], [24].

No.	Type of atomic interaction	Remarks
1	Elastic collisions where the kinetic energy is conserved within the colliding species	All collisions involving only elastic scattering of the colliding species after collision.
2	Elastic momentum transfer collisions	Usually between same species where there is a momentum transfer but the total kinetic energy is conserved within the colliding entities.
3	Atomic excitation by electron collisions	When the energy of the electrons exceeds the excitation potential of the atom. In the collision, however, the linear momentum and angular momentum about the common centre of mass must be conserved.
4	Atomic excitation by collisions with neutral atoms and ions	Same physics as 3 but occurs when atoms collide with accelerated ions or neutral atoms with high kinetic energy
5	Multiple excitation, energy pooling collisions and auto-ionization collisions	When more than one electron in an atom are raised to higher atomic energy levels, the total energy of the doubly excited atom can be more than the first ionization energy (IE1) of the atom, leading to ionization, or if less than IE1 leading to higher state excitation.
6	Atomic ionization by electron collisions	When the colliding electron has a higher kinetic energy than the ionization potential of the atom
7	Multiple ionization	When an ion collides with an electron with higher kinetic energy than the atom's higher ionization potentials (IE2 to remove the second electron)
8	Ionization of excited atoms	When an excited atom collides with an entity with kinetic energy more than the difference between IE1 and the excited level.
9	Inelastic collisions between atoms and ions	Momentum transfer collisions between atoms or ions leading to ionization or charge transfer between ions and neutral atoms
10	Penning ionization	Ionization when an excited atom collides with a neutral atom with ionization energy less than the internal energy of the excited atom, with any surplus energy carried away by the released electron. This type of collision can also be called superelastic.
11	Photo-excitation and photo-ionization	A photon on energy hν can be absorbed by an atom or molecule, exciting it to a higher state. If this energy is >IE1 of the atom, then this results in ionization.
12	Electron attachment	Electrons colliding with certain atoms can become attached, forming negative ions. The probability of attachment is greatest for electrons with low energy (~1 eV) as they are easier to be held by the atomic field.

If particles having a random velocity, v_r, have a mean free path, λ, the number of collisions each particle makes with the gas atoms/molecules per second (or the collision frequency), ν, is: $\nu = v_r/\lambda$ (Figure 2.4). There are fundamentally three types of collisions: **(1)** elastic collisions where the total kinetic energy of the colliding species is the same after collision, **(2)** elastic

momentum transfer collisions and **(3)** inelastic momentum transfer collisions. The momentum transfer collisions with atoms can possibly lead to any of the following three atomic processes: **(1)** ionization, **(2)** excitation or **(3)** recombination and electron attachment. The collision frequency for momentum transfer, ν_m, is the frequency at which an electron loses all its momentum in collisions, and can be given by $\nu_m = \nu_{.}(1 - \cos(\theta))$ where θ is the scattering angle of collision [30]. In order to understand the physics behind atomic/molecular excitation and discharge emission, the different types of collisions and the related atomic processes are discussed briefly below.

2.2.2 Types of collisions

The types of collisions in a gas are classified based on the involved species and the result of the collision (shown in Table 2.1) [23], [24]. This set of collisions considered here covers all the important types of atomic transitions that can result from two gaseous entities colliding in a system. This is especially relevant for the results discussed in section 6.2.2.

For a finite gaseous system, there are walls which play an important role in determining the discharge physics of the system as the gaseous entities interact with the wall material. Table 2.2 shows the primary surface processes involved in a gas system due to wall collisions and these are especially relevant to the results discussed in section 6.2.2. Surface processes play an important role in determining the discharge physics in the system when there are significant amount of electrons reaching and interacting with the walls. When the wall is a metal, all surface processes considered here are relevant while for dielectric or insulating walls, field and thermionic emission can be considered negligible for low-field applications like discharge light sources. The dominant surface process is the secondary electron emission, whose yield depends on the dielectric material used.

An atom in an excited state, before it collides with another entity, can decay back to its ground state by emitting a quantum of energy equal to the energy difference between the ground and excited state. For a rubidium discharge lamp, it is important to maximize the quantum of rubidium decay transitions necessary for the clock transition, to achieve a high power output of the required discharge wavelength. In order to do that, it is useful to consider the overall statistical processes in the system rather than single atomic events, to avoid the high computational complexities and also for the immediate significance of statistical parameters for developing the discharge light source parameters. **Single atomic events govern the discharge physics, but it is impossible to understand the system behavior by following these single events as all the species are widely distributed in their energies [23]. Hence, a statistical model is used for this purpose and is discussed in the next section.**

2.2.3 Electron energy distribution

The statistical electron energy distribution functions including the electron temperature and electron density are useful parameters to easily characterize and estimate the lamp discharge emission properties. The most important statistical factor is the energy distribution of the electrons. This is because the electron mean energy is usually considerably greater than that of the gas atoms/molecules or ions and their distributions vary appreciably with gases and applied field conditions. However, ions, because of their large mass and rapid energy loss properties due

to elastic collisions, have a Maxwellian distribution of velocities similar to that of the neutral atoms [23].

Table 2.2: Different types of wall collisions in a finite gaseous system leading to electron emissions [30].

No.	Type of wall interaction	Remarks
1	Field emission	The application of a sufficiently large electric field can change the shape of the potential barrier from a rectangle to a triangle and allow for an electron in the potential well to escape through the barrier to a free state of the same potential energy. The typical minimum electric field required for this emission is around 10^6 V/m.
2	Secondary electron emission	When electrons strike a solid surface, a fraction of them are reflected with hardly any loss of energy, but the majority penetrate the structure of the solid causing the emission of secondary electrons. The ratio between the total number of ejected electrons and the number of incident primary electrons is called the secondary electron emission coefficient, δ. δ rises with the energy of the primary electrons reaching a maximum value (at several hundred eV for most substances). δ value is usually between 1 and 2 for most glasses.
3	Thermionic emission	The electrons in a material (especially metal) are distributed in the energy bands according to the Fermi-Dirac law and as the temperature increases, a few electrons can achieve sufficient energy to overcome the potential barrier at the surface and leave the solid.
4	Photoelectric emission	Electrons are ejected when photons with sufficient energy strike the surface, their maximum kinetic energy dependent on the frequency of the incident light (hν). The photoelectric yield, γ, depends on the surface properties including surface roughness, angle of incidence and state of polarization of the light.
5	Electron emission due to bombardment of ions, excited and neutral atoms	The primary mechanism involved in electron emission due to ion bombardment is the distortion of the potential barrier of the surface atoms due to its local electric field, giving the electrons in the upper Fermi level to tunnel through the barrier. The kinetic energies of the ions have been observed to have only a marginal effect in increasing the emission yield. However, neutral atoms can eject electrons from the surface only if they have sufficient kinetic energy before collision.
6	Electron attachment	Electrons can also temporarily attach to the surface atoms if they have a very low kinetic energy being held by the local field of the surface atoms. However, a strong external electric field would usually dominate the electron movement, hence reducing the probability of electron attachment.

The electron energy distribution can be determined by the steady-state rate at which the number of electrons in a particular energy level is either **(1)** increased by slower free electrons gaining energy from the field and/or by faster electrons having lost different amounts of energy in elastic and inelastic collisions or **(2)** decreased by the electrons in this group losing momentum/energy through collisions. In steady-state conditions, the gain and loss of energy are equal and a constant energy distribution can be given by [23],

$$\frac{dn}{n} = f(\varepsilon).d\varepsilon \tag{2.2}$$

where dn/n is the fraction of electrons having energies in the range of ε to (ε+dε) and f is used to denote a function. There are broadly two types of electron energy distribution functions, either of which can be used to compute the energy distribution depending on the gas properties: **(1)** Druyvesteyn and **(2)** Maxwellian. Druyvesteyn is the energy distribution function when the only electron energy losses are by elastic collisions (assuming a constant electron mean free path), while the Maxwellian distribution applies when collisions between electrons (mutual repulsion) are dominant and responsible for the energy distribution. Both distributions are given below [23]:

$$\text{Druyvesteyn: } \frac{dn}{n} = \sqrt{\frac{\varepsilon}{\bar{\varepsilon}}}.e^{-0.55(\varepsilon/\bar{\varepsilon})^2}.d\left(\frac{\varepsilon}{\bar{\varepsilon}}\right); \text{ Maxwellian: } \frac{dn}{n} = \frac{2}{\sqrt{\pi}}.\sqrt{\frac{\varepsilon}{\bar{\varepsilon}}}.e^{-\varepsilon/\bar{\varepsilon}}.d\left(\frac{\varepsilon}{\bar{\varepsilon}}\right) \qquad (2.3)$$

where $\bar{\varepsilon}$ is the mean electron energy. It has been found that the Maxwellian distribution is usually a good approximation in molecular gases because of the widely distributed excitation levels of the gas up to the ionization potential [23]. For a given gas type, pressure and applied field conditions, the average electron energy would be low due to the molecules easily absorbing energy from electrons in a wide range of energies through inelastic losses. However, in noble gases, where the excitation levels are much closer to the ionization potential, the average electron energy is much higher than in molecular gases for the same input conditions (applied field and gas pressure). **Hence, the Druyvesteyn distribution becomes a closer approximation for these gases which can easily form metastable excited states close to the ionization potential of the gas.** Higher order approximations can also be included (Townsend-Ramsauer effect [24]) to take into the account the varying electron mean path with electron energy, but are not necessary for developing a discharge light source.

For the maxwellian distribution, the 'electron temperature', T_e, can be defined as [24]:

$$\bar{\varepsilon} = \frac{3}{2}kT_e = \frac{1}{2}m\overline{v_r^2} \qquad (2.4)$$

where k is the Boltzmann constant and v_r is the random velocity of an electron. The electron temperature or the mean electron temperature represents the mean energy of the electron energy distribution in a system. The overall transport phenomena, that is, drift and diffusion of the gas, depend on the mean electron temperature while the ionization and excitation processes depend more on the number of electrons in the high energy tail (electrons with energies higher than the respective ionization and excitation potentials). **Due to this reason, the excitation phenomenon is always directly proportional but a slow varying function of the overall mean electron temperature.**

2.3 Electrically induced discharges

Plasma discharges ignited and sustained by an applied electric field (implemented in this research) are electrically-induced discharges. Gas discharge emission (or rubidium vapor discharge emission here) in a system can be instigated by various forms of external energy, for example, by increasing the gas temperature or through chemical ignition. In fact, even without any external energy, statistics would show that a negligible amount of rubidium atoms emit

discharges even at room temperature without any external power. However, what is needed is a steady-state high power emission of these discharges with the minimum external power consumption and size requirements. Sustained or steady-state discharge emission by increasing the temperature would mean that the system needs to be heated to several thousands of Kelvin. In fact, the only efficient method to meet the performance requirements of the miniature light source is by using an external source of electrical energy. In this section, the basic concepts behind electrically induced discharges are discussed to define the electrical breakdown phenomenon and sustained discharge emission.

All charged entities in a system can be influenced and accelerated by an external electric field. In a gas, there are always some free electrons present (currently accepted reason for this being due to cosmic radiation) that can be accelerated by applying a force ($F = e.E$ where e is the electron charge and E is the applied electric field) due to the applied field. These accelerated electrons in turn transfer their momentum to the atoms through collisions. When the magnitude of the applied electric field is increased, the mean electron temperature increases and the collisions with atoms can lead to atomic excitation and ionizations. Ionization leads to the separation of the charge in the atom, creating two separate charge carriers: an ion and an electron after collision. With an increasing electric field, more ionization processes take place leading to the creation of large amounts of charge carriers with high momentum. At a specific value of the field, the gain in the electron density caused by ionization becomes equal to the loss of electrons by diffusion, recombination or attachment. **In other words, an electron at least makes one ionizing collision to create at least one other free electron before getting lost through recombination or other processes. This value of the field corresponds to the 'electrical breakdown' of the gas, after which a self-sustained discharge emission is possible.**

Based on kinetic theory and experimental observations by researchers over time, electrical breakdowns have been classified broadly into: **(1) drift-dominated breakdown** and **(2) diffusion-controlled breakdown.** Considering a plasma volume confined by parallel plate electrodes (also applicable when the electrodes are covered with dielectric material) separated by a discharge gap length, d (Figure 2.5). To reach a steady-state plasma discharge emission, new charged particles (electrons and/or ions) have to be permanently generated in the plasma volume by applying a suitable electric field, and compensate all the loss processes of charged particles. When the discharge of the charged particles at the dielectric/electrode surface is the dominant loss process compared to the recombination of the charged particles in the discharge gap or the walls, the eventual electrical breakdown is said to be drift-dominated or drift-controlled where the charged particle losses are partially compensated by the release of secondary electrons from the dielectric/electrode surface. When the dominant loss process is the ambipolar diffusion and recombination of charged particles in the discharge gap/walls, the eventual electrical breakdown is said to be diffusion controlled [31]. A complete set of defining these breakdown conditions can be found in [24], and the relevant details are briefly mentioned below.

Electron drift velocity

Electrons moving through a gas in random directions with a wide distribution of velocities, when subjected to an electric field, E, has superimposed upon its random motion, a slow drift in the centre of the cluster in the direction of the field. The average drift velocity, v_d, can be derived to

a first approximation by calculating the momentum gained by an electron along a free path in the field direction and assuming that the entire momentum is destroyed in a collision [23]. Averaging over all lengths and directions of free paths, the drift velocity can be given as [23]:

$$v_d = \frac{e.\lambda_e.E}{m.v_r} = \frac{e.E}{m.\nu} = \mu_e.E \qquad (2.5)$$

where λ_e is the electron mean free path, m is the mass of the electron, v_r the random velocity, ν the collision frequency and μ_e is termed the electron mobility. This equation (2.5) is a close approximation as an exact derivation of the drift velocity would require knowledge of the exact electron energy distribution of the specific case and the variation of the electron mean free path with energy. **One important note: higher gas pressure would mean a lower mean free path and the drift velocity is inversely proportional to the gas pressure and directly proportional to the applied field intensity.**

The drift of ions can be derived but is not of much significance to the light source design. This is because the ion has a relatively huge mass compared to the electron and hence almost ends up staying near the vicinity of neutral gas molecules long enough to polarize them. The resultant attractive force not only shortens the free path of the ion, but also causes a continuous exchange of momentum and this significantly reduces the drift velocity [23]. Hence, ion mobility or drift velocity is of significance only in very low field and frequency conditions and therefore considered negligible in all other cases.

Electron diffusion coefficient

All entities/particles in the gaseous state move about in random continuously colliding and exchanging momentum. If the number density of these particles is not uniform, the region of high particle density will transfer more momentum in the direction of regions with lower particle density than in the other directions. Hence, there results a net force on the particles driving them towards the region of low density and subsequently the current density under these conditions can be given by: $J = -D.\nabla n$, where n is the particle density and D is the diffusion coefficient. Using well-known kinetic theory methods, the D values have been derived for both ions and electrons: $D = \lambda.v_r/3$ where λ and v_r values of the respective ion or electron can be used [23]. As expected, the diffusion coefficient of the electrons are much higher than that of ions due to their smaller mass, longer mean free path and substantially larger random velocities.

In a gaseous discharge system, for a given intensity of an applied electric field, both drift and diffusion phenomena take place, where the dominance of one over the other depends primarily on the input electrical polarity switching frequency and the gas type and pressure. However, both phenomena can be treated independently for conditions where the drift velocity is smaller or comparable to the random velocity. In these conditions, the electron energy distribution and the electrical breakdown can be said to be diffusion controlled with the whole set of electrons moving (or oscillating depending on the input) with a drift velocity. **When the applied field intensity is very high, the drift velocity is much greater than the random velocity leading to drift-dominated electron distribution and temperature.**

In summary, when the applied field and pressure conditions are such that a significant number of charged particles reach and discharge on the electrode/dielectric surface, the breakdown is **drift-dominated.** When most of the charged particles discharge through recombining collisions in the discharge gap or walls, the breakdown is **diffusion controlled.**

2.4 Electrical breakdown in a steady (DC) electric field condition

The electrical breakdown in the presence of a DC electric field is discussed and reviewed in this section for the light source design. The concepts reported in this section are also of fundamental importance to this research and for understanding the high-frequency discharges, discussed in the next section. The glow discharge regime, achieved after initiating electron avalanches and the Townsend breakdown, is the preferred operating regime for a light source due to its highly stable light output and low power consumption. The physics involved in these processes, the Paschen's law, which has been widely used to estimate the breakdown power, and some details on the DC plasma lamp prototype developed at LMTS, prior to this research, are discussed in this section.

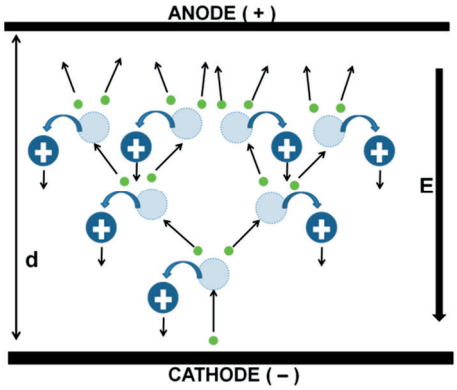

Figure 2.5: An illustration of an electron avalanche effect resulting in Townsend discharges and an electrical breakdown for an applied DC field condition.

The electrically induced discharge mechanisms, discussed so far in this section 2.3, fully apply to a gaseous system under a steady or DC electric field. High-power steady-state discharge emission from atoms is possible after the gas volume reaches the electrical breakdown condition (defined earlier). The external field (or voltage) required to initiate this breakdown is termed the breakdown field, E_{br} (or the breakdown voltage, V_{br}) and this value is used to understand the voltage and hence the power required to initiate a plasma discharge in a given set of conditions. $E_{br} = V_{br}/d$ (d – discharge gap length). The terms starting potential or ignition potential, usually used in discharge lamp literature, are also synonymous with breakdown voltage. Here, in this section, the primary processes initiating an electrical breakdown, and the reported (by past researchers) breakdown characteristics for different gas conditions when in a steady field are discussed briefly.

When a DC field is applied and increased on a gas present between two electrodes, breakdown of the gas happens at a certain value and can be understood as the state when a conducting path is fully established through the gas and across the electrodes. The observable effects of breakdown are either **(1)** a jump or sudden change in the current flow through the electrodes or **(2)** the sudden emission of light radiation from the initiated plasma discharge. The exact definition condition for breakdown varies widely with the type of application. **For lamp applications, breakdown is defined as the state when the plasma starts to emit light radiation and continues to do so as long as the applied electric field is sufficient enough to sustain it (or a self-sustained discharge).** The breakdown voltage is recorded using the effect (2) in this research, and usually there is always visible radiation from most gas discharge plasmas and hence can be observed by the naked eye.

Electron avalanche and Townsend discharges

The precursor to a DC field breakdown is an electron avalanche (shown in Figure 2.5). It denotes a process of multiplication of electrons in a series of impact ionizations (ionization of an atom on collision with other gaseous entities, usually an electron). When a strong field is applied on a gas (when mean free path < distance between electrodes), free electrons will collide with the gas atoms/molecules, which will result in more charge separations and thus more electrons. This electron multiplication is termed the electron avalanche and the degree of multiplication is given by the multiplication factor, M [24]:

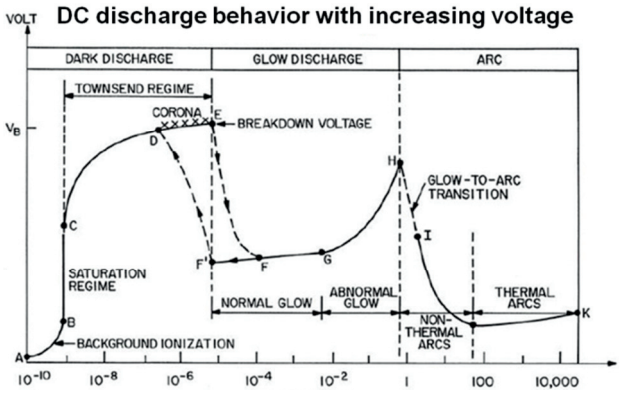

Figure 2.6: A voltage versus current plot of all low-density plasma discharge regimes (Townsend, glow and arc discharge). Operating in the normal glow discharge regime is ideal for light source applications [35].

$$M = \frac{1}{1 - \int_{x1}^{x2} \alpha . dx} \qquad (2.6)$$

where α is the ionization coefficient or the Townsend coefficient, x1 and x2 are the positions where the multiplications are measured between. The current of the electrons leaving the cathode, I_0, is increased by a factor (α.d), where d is the distance between the electrodes, to give the expression for the current flowing through the electrodes, I [32]:

$$I = I_0 . e^{\alpha . d} \qquad (2.7)$$

This expression (2.7) is used to describe, what is called the Townsend discharge, which can be sustained over a limited range of gas pressure and field intensity. With an increasing field strength, the discharge behavior changes to a relatively unstable corona discharge region. The corona discharge occurs when the gradient of the electric field around a conductor (the electrode) is high enough to form a conductive region, but not high enough to cause an electrical breakdown [33]. Coronas can be understood as localized plasma discharges occurring at highly ionized regions in the gas volume due to the presence of local high field gradients [34]. Hence, it is sometimes possible to visually observe very-low-power light radiation, usually near the metal electrodes, before an eventual breakdown at higher field strength.

Glow discharges

The glow discharge regime is the most suitable operation regime for a light source operation due to its diffuse light output and low sustaining power requirements. Figure 2.6 [35] shows the changing DC discharge behavior with increasing voltage/field strength. There will be marked change in discharge behavior up on further increasing the field strength to enter the glow discharge regime with a stable self-sustained emission of visible discharges. DC electrical breakdown usually refers to this point when the glow discharge regime begins and the term

Townsend breakdown is used to refer to the first flow of non-negligible current across the electrodes on increasing field strength (Figure 2.6). After a DC breakdown, the primary process responsible for maintaining a self-sustained discharge is the secondary electron emission from the electrodes. The condition for initiating a self-sustaining discharge (found by Townsend), also called the transition condition, is (γ is the Townsend second ionization coefficient) [32]:

$$\alpha.d = \ln\left(\frac{1}{\gamma}+1\right) \tag{2.8}$$

The glow discharge regime covers a wide range of discharge behaviors and can be classified into three distinct regions: **(1)** sub-normal glow discharge, **(2)** normal or homogeneous glow discharge and **(3)** abnormal glow discharge. For lamp applications, it is important to stay in the homogeneous glow discharge regime for two important reasons: **(1)** lowest power consumption to output a given optical power, and **(2)** stable emission region. As seen from the Figure 2.6, increasing the field beyond a certain value will lead to electric arcing and eventual rupturing of the electrodes due to the high current flow. So, if an increase in the optical power output is desired from the plasma, increasing the input power (and hence the field strength) would reach an upper limit and is also undesirable for a low-power lamp application. However, other parameters including gas pressure and the discharge gap length can be modified to achieve higher power emission and possibly higher power efficiency.

Paschen's law

The Paschen's law [36] is a set of equations that gives as output the expected DC breakdown voltage for the given set of input discharge gap conditions. The law essentially states that the breakdown characteristics of a gap are a function of the product of the gas pressure p and the gap length d. The product (p.d) is a measure of the number of collisions an electron makes by crossing the gap. For air, and gaps on the order of a millimeter, the breakdown is roughly a linear function of the gap length: V = 0.03 p.d + 1.35 kV [37]. The general expression of the Paschen's law is given by:

$$V_{br} = \frac{a.(p.d)}{\ln(p.d)+b} \qquad \text{where } b = \ln\left(c \Big/ \ln\left(1+\frac{1}{\gamma}\right)\right) \tag{2.9}$$

where constants a, b and c depend on the gas composition and γ is the secondary electron coefficient of the electrode material. Figure 2.7 shows the experimentally reported Paschen curves for some common gases (N_2 compatible with Rb). With increase in gas pressure, the mean free path of an electron reduces resulting in many collisions before reaching the anode. Each collision randomizes the electron direction hence reducing the influence of the applied electric field in accelerating the electrons. Hence, when the electron mean free path is less than the discharge length, d, increasing the pressure would increase the voltage required for breakdown. However, when the pressure or d is reduced to such an extent that the mean free path is more than d, the electron undergoes too few ionizing collisions and hence again requires a higher voltage to compensate for the reduced electron density. Hence, there is a breakdown minimum that can be seen in Figure 2.7 that happens at this conjuncture.

Many other factors have an effect on the breakdown of a gap, such as radiation, particles (dust), electrode shape and surface irregularities and hence the use of this law is very limited, especially to sub-mm scale discharge lengths (where strong field inhomogeneities due to surface roughness start to dominate the discharge mechanisms). Paschen's law reflects the Townsend breakdown mechanism in gases, that is, a cascading of secondary electrons emitted by collisions in the gap. Typically, the Townsend mechanism (and by extension Paschen's law) apply for (p.d) products less than 1.3 kPa×m [37]. For alternating field conditions, researchers have reported that the breakdown voltage is dependent on both (p.d) and only d (same p.d but varying d) [38]. Hence, this law acts only as a preliminary reference for the miniature lamp development and completes the relevant characteristics of discharges in a DC field condition which are later used for comparison of results and analysis of the light source performance.

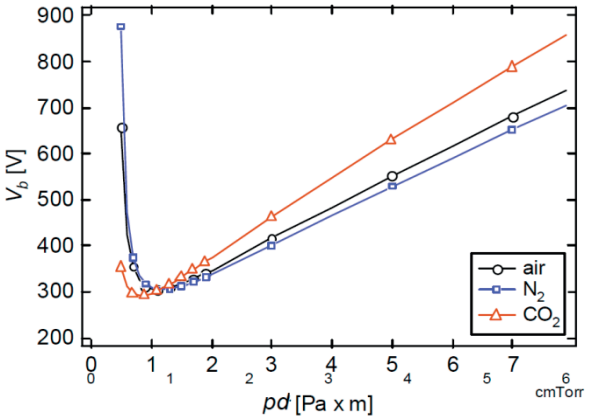

Figure 2.7: Paschen curves for various gases [30] plotted based on the experimentally derived model.

DC discharge design for miniature light sources

DC discharge designs have been widely used for many applications such as mass spectrometry [39], chemical depositions [40], gas chromatography [41] and for light sources [42]. Most of the DC discharge light sources use phosphor-coated dielectric walls to increase the efficiency of light output and it is estimated that more than 80% of the world's artificial light are from fluorescent DC discharge tubes [34]. However, a DC discharge design for the miniature lamp has one crucial problem: electrode erosion by plasma discharges. Figure 2.8 shows the results of a DC discharge experiment performed at LMTS, EPFL by P. Moser (fabrication by P. Carazzetti). An interdigitated electrode design [43], with 5 µm spacing and Al electrodes patterned on silicon, was supplied with DC power (350 V and 0.087 mA) to ignite and sustain a (100 mbar Ar) DC gas discharge for 1 hour. The cathode layer was later observed to be highly eroded (as shown in Figure 2.8) due to the high ionic bombardment. This severely limits the lifetime of the device and hence also eliminates the fundamental DC discharge design for the Rb discharge light source.

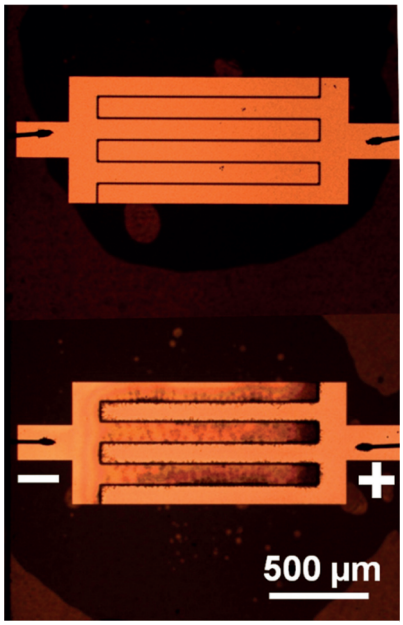

Figure 2.8: Photographs of interdigitated electrodes patterned on silicon, before and after igniting and sustaining a DC discharge for 1 hour. Both electrodes were eroded with the cathode being severely eroded due to the heavy ion bombardment.

The first design requirement for the miniature light source is that the electrodes should not be in contact with the discharges, or in lamp terminology: an electrodeless lamp. In the simple case that the electrodes are covered with insulating material, there are no more any metal electrodes for secondary electron emission and an eventual breakdown. One efficient

way here is to switch the polarity of the field continuously and quickly with time to accelerate and oscillate the electrons in the discharge volume; making ionizing collisions with atoms to generate electron avalanches and eventually an electrical breakdown. However, the discharge physics (and hence the light source performance) varies drastically when switching the polarity, or changing the frequency of switching (or the AC field frequency), gas conditions or the discharge length. In the next section, the discharge behavior versus these parameters is discussed, which would help narrow down the fundamental cell-design parameters to set a mature starting range for the rubidium light source design. The gas and input conditions can then be experimentally varied to determine the performance scale and hence the preferred range of operation for the light source (reported in sections 5.4.3 and 6.1.3).

2.5 Electrical breakdown in an alternating electric field condition

Here in this section, the different parameters associated with the AC and high-frequency electrical breakdown are discussed which are necessary for understanding and eventually determining the optimum frequency conditions (experimental results in section 5.4.2) for achieving a low-power consuming device with a long lifetime.

The excitation and ionization processes in a gas subjected to an alternating electric field (AC field of any finite frequency) differ significantly from those in a steady or DC field. The first significant difference is the fact that the charge carriers need not be swept out of the discharge volume on to the walls (provided the frequency is high enough). Hence, due to the lower losses in space-charge, lower fields might be necessary to initiate an electrical breakdown and hence favorable for the discharge light source design. The second significant difference is that the breakdown is lesser dependent on secondary processes like secondary electron emission, which play a crucial role in determining DC breakdown conditions. The third difference and one of the biggest advantages of an alternating field plasma ignition is that, the walls can be insulators and hence the equilibrium density of ionization in the discharge volume is highly controlled.

The factors that determine the field strength required for breakdown, and hence the current and electron density of the discharge are: **1)** gas pressure (p), **2)** electrical frequency or drive frequency ($\omega=2.\pi.f$) and **3)** discharge length (d) and **4)** volume (V). The gas pressure determines the electron mean free path and also the initial collision frequency. It is now necessary to differentiate the various set of conditions in which different physical processes and parameters become important and identify the preferred range of conditions for the light source design:

(1) *Very low pressure,* $\lambda_e > d$ *and any drive frequency* [23]: the electrons hit the walls more often than they hit gas molecules and hence secondary effects at the walls control breakdown. Under these conditions, the secondary electron emission coefficient, δ, of the insulating wall determines the breakdown potential, V_{br}, required (higher the δ, lower the V_{br}).

(2) *Medium or high pressure,* $\lambda_e < d$ *and low drive frequency* $\nu >> f$ [23]: the electrons make many collisions for each oscillation of the electric field and drift as a cluster in phase with the field. This condition can be further divided into two sub-groups: (a) if the frequency is sufficiently high, the amplitude of oscillation may be less than the discharge length. In this case, new charge carriers are formed mainly by ionizing collisions and the main loss mechanism is through diffusion into the walls. (b) at lower frequencies and larger amplitudes of oscillation, the entire

cluster of electrons is driven to the walls in each half cycle of the field. Hence, in this (b) case, secondary wall processes start to play a crucial role in determining the breakdown and discharge behavior.

(3) *Medium or high pressure, λ_e < d and high drive frequency ν << f* [23]: the electrons make many collisions of small amplitude between collisions with gas molecules. In such conditions, a cluster of electrons would appear to have no drift motion, spreading outwards only by diffusion. There are wide range of conditions between 2 and 3 in which the applied frequency and collision frequency is almost equal but no marked change in the mechanism (or a peak or trough for example) has been observed at this point. However conceptually, the lowest breakdown field condition should be when $\nu = f$ [30], [23] which can be seen in the discussion in 2.4.2.

(4) *Any pressure and very high frequency, λ_e << d* [23]: in this case, the electrons are no longer under the influence of an electric field but are under that of a standing wave with oscillatory electric and magnetic components, distributed in space in a manner determined by the frequency of the field and the discharge cell geometry. These conditions usually correspond to the microwave frequency range of operation.

Motion of electrons in an alternating electric field

An electron, with an initial velocity, v_0, starting at a point (x=0) and at time (t=0) in the direction of an applied uniform electric field, E, has an equation of motion [23]:

$$m.\frac{d^2x}{dt^2} = e.E_0.\sin(\omega t + \varphi) \tag{2.10}$$

where E_0 is the electric field component, φ is the phase angle of the field – both at t=0, and ω is the angular drive frequency (ω = 2.π.f). Integrating with the boundary condition that $dx/dt = v_0$ at t=0 gives the velocity, v, at time, t:

$$v = v_0 + \frac{e.E_0}{m.\omega}(\cos\varphi - \cos(\omega t + \varphi)) \tag{2.11}$$

The displacement, x, in the direction of the field can be calculated from equation (2.11) and given by:

$$x = \left(v_0 + \frac{e.E_0}{m.\omega}.\cos\varphi\right).t + \frac{e.E_0}{m.\omega^2}[\sin\varphi - \sin(\omega t + \varphi)] \tag{2.12}$$

As it can be seen from equation (2.12), there is a steady drift at a uniform speed (first term in equation 2.12) in the direction of the original velocity. The second term in 2.12 is the sinusoidal oscillation of the electron, whose amplitude is proportional to E/f^2 and is superimposed on the drift motion of the electrons. The significance of this equation is that, it shows an electron moving without hitting any gas molecules will not absorb any power from the field. This is because, the oscillatory velocity component is always 90° out of phase and the drift component (first term) will, in alternate half cycles, absorb energy from the field and return to it. Hence, when the gas pressure is very low or when the frequency is too high (case **(1)** discussed in the

previous page), such that there are very less number of collisions, the breakdown potential needed will be very high.

For the case **(2)**, when the electron collides many times during a half-cycle, that is, when the gas pressure is not too low or the frequency not too high, there is higher gain of energy from the field by the electrons. Considering electron elastic collisions, which are the fundamental type of collisions in the initial low-field conditions, the phase of the electron's motion is changed after collision with only a small fraction of its initial kinetic energy being lost on collision (~2m/M, m – mass of electron, M – mass of colliding entity). Thus, the steady electron motion is changed on collision to a random motion, after which it can gain energy from the field getting influenced slowly back to steady motion in the direction of the field. This showcases one of the main differences in DC and alternating field discharges where collisions are the dominant energy loss mechanism in DC, while collisions are the dominant energy gain mechanism in AC. However, collisions are also loss mechanisms (via excitations and ionizing collisions) and sometimes the dominant loss mechanism in AC as well but as no energy can be absorbed by the discharge volume without collisions, it is an important point of consideration for a light source design.

The energy of the electron that is gained from the applied field is much higher than the energy lost in an elastic collision with the gas atoms/molecules due to the change in phase after collision [23]. In this way, the energy of a swarm of electrons can increase until an appreciable number of them are fast enough to excite or ionize the gas molecules through momentum transfer collisions. In these conditions, it is convenient to consider the motion of an average electron representative as a cloud or cluster of electrons as it would be too complicated to consider single electron motions. The electrons gain momentum from the field and lose it by colliding with gas molecules. This net gain in momentum can be represented as a force given by [23]:

$$m.\frac{dv_d}{dt} = e.E_0 \sin \omega t - g.v_d \tag{2.13}$$

where g is the frictional factor of collision energy loss in an electron. The drift velocity is more relevant here than the electron's random velocity since it represents a cloud of electrons. The value for the factor g has been derived by past researchers using different theories where there are different initial assumptions and hence has various definitions. For example, collision theory assumes that an electron loses all its momentum in any direction on collision and in this case g would be equal to m/τ where τ is the average time of flight of an electron between collisions (or $\tau = 1/\nu$). Experimental observations have shown that the value was close to the m/τ at electron temperatures less than about 8 eV (for λ_e<d and a maxwellian electron energy distribution), slightly decreasing with an increase in the electron temperature above 8 eV [24]. For lamp applications, the mean electron temperatures are typically < 20 eV and hence m/τ is an acceptable approximation for the value of the frictional factor.

From equation (2.13), the drift velocity can be derived to a simplified expression [24]:

$$v_d = \frac{e.E_0}{m}.\frac{\sin(\omega t - \varphi)}{\sqrt{\nu^2 + \omega^2}} = \frac{dx}{dt} \quad \text{where} \quad \tan\varphi = \frac{\omega}{\nu} \tag{2.14}$$

On integrating equation (2.14), the expression for the displacement, x, can be given by [24]:

$$x = \frac{e.E_0}{m.\omega}.\frac{\cos(\omega t - \varphi)}{\sqrt{\nu^2 + \omega^2}} + const \tag{2.15}$$

The electron current of the high-frequency discharge is $J = n.e.v_d$ which can be calculated by substituting v_d from equation (2.14) [n – electrons/unit volume]. It can be noted that the drift velocity and hence the current lags behind the applied field by the phase angle φ. The instantaneous power, P_{abs}, absorbed by the discharge volume from the field is also equal to the product of the voltage across the electrodes, V_e, and the current through the discharge volume, I_e. Also, $I_e = J.A$ [A – surface area of the discharge volume] and $V_e = E.d$ [d – discharge length]. Hence, P_{abs} can be given by [24], [23]:

$$\begin{aligned} P_{abs} &= V_e.I_e = E.J.A.d = (E_0.\sin\omega t).\left(\frac{n.e^2.E_0}{m}.\frac{\sin(\omega t - \varphi)}{\sqrt{\nu^2 + \omega^2}}\right).V \\ &= \frac{n.V.e^2.E_0^2}{2m}.\frac{(\cos\varphi - \cos 2\omega t)}{\sqrt{\nu^2 + \omega^2}} \Rightarrow \left[\overline{P_{abs}} = \frac{n.V.e^2.E_0^2}{2m}.\frac{\nu}{\nu^2 + \omega^2}\right] \end{aligned} \tag{2.16}$$

The steady state power absorbed is given in equation (2.16) using equation (2.14) and the fact that the time averaged mean value of cos2ωt is zero. Here, it can be seen that higher the drive frequency, lower is the power that can be gained by the electrons for a given gas pressure and applied field strength. Moreover, there are many more relevant remarks that can be made on the expected breakdown characteristics versus the drive frequency and (p.d) based on the derived set of expressions, which are discussed succinctly in the following sub-section.

Breakdown behavior versus gas pressure and drive frequency

Based on the model described in this chapter and the expressions derived in this section, it is possible to comment on the expected behavior of the breakdown voltage against the gas pressure and drive frequency for a given discharge length. For a given drive frequency where the electron oscillation amplitude, A_e, is less than the discharge length, d, at high pressure (many collisions per oscillation), the electrons gain a small amount of energy ($E.\lambda_e$) along a free path and lose it in elastic collisions. As pressure increases, the energy gained per mean free path decreases. However, to maintain the minimum ionization rate to ignite a breakdown, a higher breakdown voltage is required (nearly proportional to $1/\lambda_e$). But, when the pressure is decreased, the breakdown voltage will reduce until one of the two critical conditions is reached – **(1)** $A_e > d$ or **(2)** $A_e < \lambda_e$, after which it will increase. In the first case, when the number of gas molecules gets low, an electron makes too few ionizing collisions before diffusing to the walls – thus requiring a higher breakdown voltage to compensate the number of ionizing collisions. The second type of critical condition is when the pressure is so low that the mean free path is higher than the electron oscillation amplitude. This would drastically increase the breakdown voltage due to the marginal number of ionizations per half cycle.

At appreciably high drive frequencies, a reduction in pressure could first lead to the condition in which the electron makes many oscillations in the field before colliding with a gas molecule (where the gas pressure is high enough to make ionizing collisions before diffusing into walls). As the electron oscillates at 90° out of phase with the field, the average energy gained by the

electron is zero. Hence, as the field becomes lesser effective in transferring energy to the discharge volume, much higher field strengths are required to maintain the rate of ionization for breakdown. Researchers have reported in the past that, the breakdown field at high pressure ($\nu >> f$) will have a very low dependence on the drive frequency, whereas at very low pressure ($\nu << f$), it will be proportional to the frequency for a given pressure. The minimum field condition occurs when $\nu \approx f$.

2.6 Overview of discharge drive options

So far, it is understood that for the light source design, the electrodes need to be insulated and hence an alternating electric field that can transfer energy to the electrons in the discharge gap volume is needed, whose frequency is to be decided based on the gas atoms, pressure, discharge length, electrode and wall properties, to realize low power consumption and stable operation. From various literature surveys [44], [45], [46], the expected electrical breakdown field versus drive frequency was identified and Figure 2.9 is a contribution of this research towards miniature light source developments.

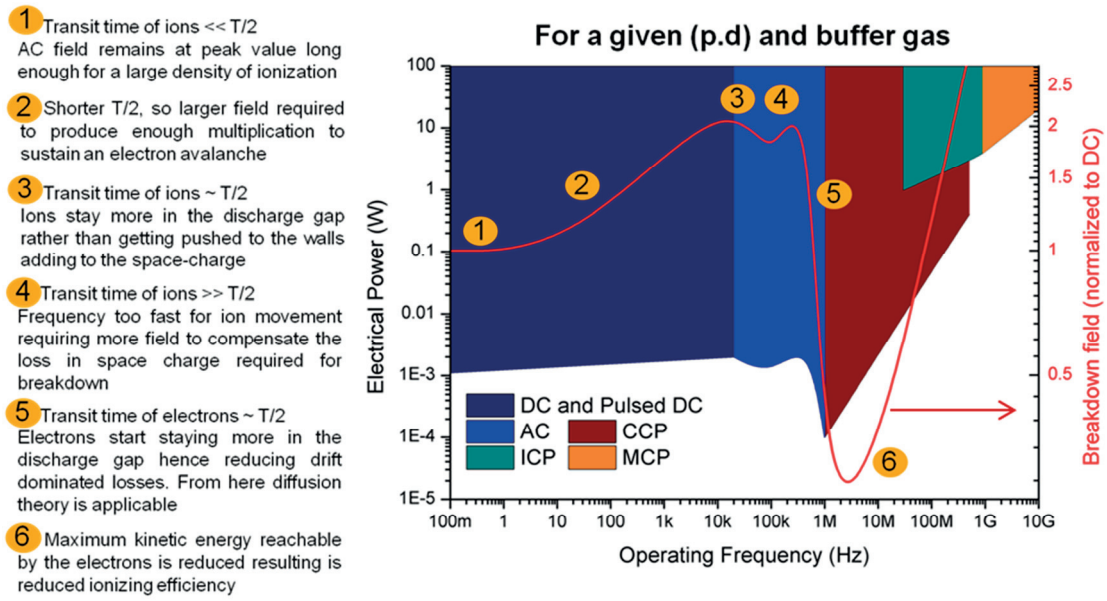

Figure 2.9: General behaviour of the breakdown field required versus the operating drive frequency normalized to the DC value (for a constant p.d and buffer gas) for mm-scale discharge lengths. The different discharge drive techniques and their typical drive power requirements for igniting and sustaining discharges are also illustrated. This graph is only for understanding the overall trend of the breakdown field versus drive frequency and the exact values vary with the gas type, (p.d) and other conditions.

Figure 2.9 gives a picture of how the breakdown field (red plot) varies with change in drive frequency (given all the other conditions are constant) for mm-scale discharge lengths. It can be seen that at the breakdown field can reach a minimum at ~>1 MHz as the electrons start to stay more in the discharge gap rather than being driven to the walls. Hence, it is an interesting frequency range for the rubidium light source.

It is possible to energy couple the field to the electrons through several methods (Figure 2.9), for example, by applying a time-varying magnetic flux density using a coil carrying a high-frequency high-intensity current, which would induce a solenoidal high-frequency electric field that can

accelerate the electrons and sustain a discharge. This coupling technique is widely called the inductively coupled plasmas (ICP) [47] and is currently the predominant principle used for developing glass-blown rubidium discharge lamps for atomic clock applications [48]. The other popular technique, primarily used in plasma processing applications, is the capacitively-coupled plasma (CCP) which applies an AC electric field across two parallel plates, following the same fundamental physics described so far in this chapter. If there is at least one insulating layer or a dielectric between the two parallel metal electrodes of a discharge emitting light source, it can be called a dielectric barrier discharge or DBD light source, and such light sources are discussed in the next section (2.7).

The ICP technique has been reported to have some advantages, the primary advantage being the ability to achieve relatively higher plasma densities ($10^{12}>n_0>10^{11}$ cm^{-3}) than capacitively coupled plasmas (CCP) where the plasma density is typically around 10^{10} cm^{-3} for the same pressure conditions [34]. It has been widely used in materials processing [49], mass spectrometric detection [50], [51] atmospheric-pressure torches (Figure 2.10c) [52], light sources [53], [54] and many other applications [55]. It has two broad types of electrode configurations: **(1)** cylindrical helix and **(2)** flat helix. In the first configuration, a coil is wound around the discharge chamber or lamp (depending on the application) while a flat helix or spiral is wound from near the axis to near the outer radius of the discharge chamber/lamp, separated from the discharge region by a dielectric [56]. The advantage of the flat structure is reduced plasma power loss and better ion generation efficiency but better heating control, deposition control (for sputter applications) is possible only with the cylindrical structure. A microfabricated ICP generator (Figure 2.10c) has also been demonstrated for ionizing applications [57], but the coils were placed inside the chamber of plasma activity for low power consumption. This would be unsuitable for lamp applications as the electrodes would be eroded from the plasma discharges over time. The biggest limitation of the ICP technique is that it requires high power for lamp operation (at least several Watts) when the electrodes are placed external to the discharge gap, also due to plasma skin effects [58] and hence is unsuitable for a miniature portable lamp application. The efficiency of field coupling is also high only for cylindrical helix configurations and spherical discharge volumes, which requires an external coil for the drive that is unsuitable for a compact integrated atomic clock solution. However, a CCP is very suitable for planar discharge cells (and hence for stack-integration solutions) as a high field coupling efficiency can be achieved with a parallel electrode configuration.

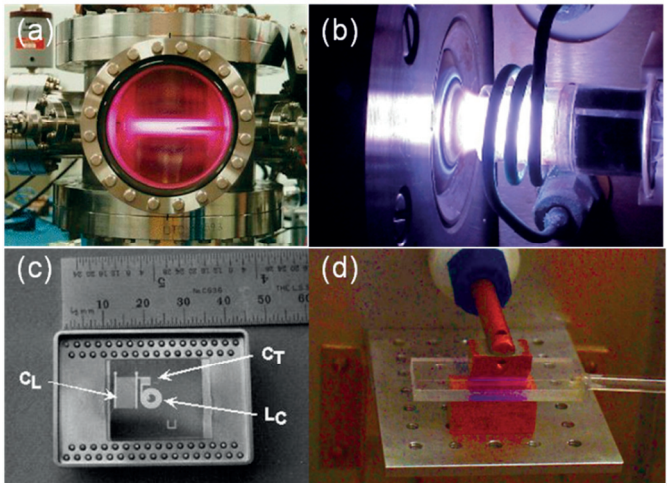

Figure 2.10: (a) A 13.56 MHz capacitive coupled plasma reactor, Source: PAL, University of Texas, Dallas (b) An inductively-coupled plasma torch, Source: Elemental analysis, Inc. (c) a micro-coil inductively-coupled plasma generator for ionizing applications [57], (d) a capacitively coupled micro-plasma generator for gas chromatography applications [64].

The CCP technique is widely used in plasma reactors Figure 2.10a [59], [60], especially at 13.56 MHz (an ISM radio-frequency allotted by international communications authorities at which one can radiate a certain amount of energy without interfering with radio communications), sputtering and thin film deposition [61], [59] and other plasma processing applications [62]. There has also been a lot of research on developing capacitively coupled micro-plasmas, for light sources [63] and especially for gas chromatography applications (Figure 2.10d) [64], [65]. It allows the use of an AC-RF field and insulated electrodes, which would avoid the problem of electrode erosion. It is very suitable for the preferred planar light source configuration, as it enables low power operation and low drive frequency operation (lower transmission losses) due to the high efficiency of energy that could be coupled to the electrons by the applied electric field with a parallel electrode configuration and hence is chosen for designing the first Rb light source prototype.

The other possible techniques for discharge lamps include microwave coupled plasmas (MCP) [66], surface-wave discharges [67], travelling-wave discharges [68] but the power required for these discharges are typically very high (at least tens of Watts in most cases). Hence, they are not discussed any further in this report.

2.7 Dielectric barrier discharge light source design

A dielectric barrier discharge light source design would include all the requirements identified so far - insulated electrodes, capacitively coupled plasma and an RF drive frequency range (1-500 MHz). The fundamentals of DBDs, its applications and its design suitability for the miniature light source are discussed in this section.

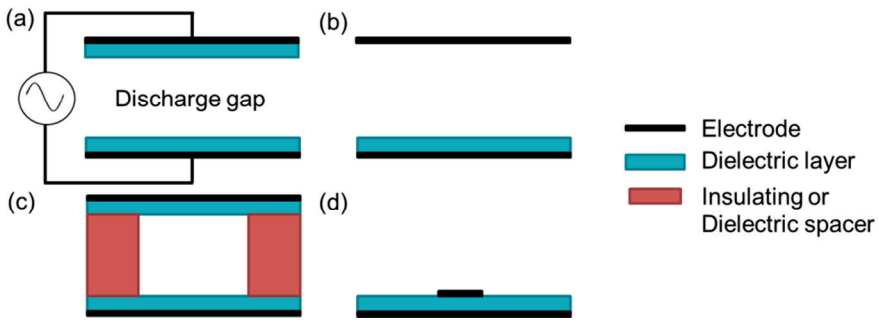

Figure 2.11: Typical DBD configurations where design type (c) is a useful sealed cell solution for the rubidium discharge light source.

2.7.1 Dielectric barrier discharges

Dielectric barrier discharges (DBD) or just barrier discharges are the electrical discharges between two electrodes separated by an insulating dielectric barrier (typical configurations shown in Figure 2.11) [69]. They are based on the same physics as capacitively coupled plasmas (CCP), where an AC field is used to drive a discharge between metal electrodes but are characterized by the presence of one or more insulating layers in the current path or the discharge gap between the electrodes [70]. While these discharges have many general advantages including non-equilibrium plasma operation over a wide pressure range, they offer two specific advantages for light source applications: **(1)** the current through the discharge gap is limited because of the

dielectrics, and **(2)** no electrodes are in contact with the plasma. These aspects enable low-power operation of a light source by allowing a low sustaining AC voltage, and also eliminate the problem of electrode erosion, which is otherwise a major lifetime limiting process.

DBDs have been used in several applications originating from industrial ozone generation applications in the early 20th century [71] (Figure 2.12a and b), excimer UV lamps for medical applications [72] to plasma display panels where arrays of sub-mm DBD cells (pixels) are ignited for light and display (Figure 2.12c and d) [73], [74], [75]. The main DBD lamp applications to date generally required high light output in the UV. This light is either irradiated on phosphors to reemit the desired visible wavelengths [76], [77] or directly irradiated on substrates for chemical processing applications [78], [79], [80]. High-power (several Watts) large-sized lamps have been used for chemical treatments and other purposes [81], [82] while low-power (<tens of mW) miniature plasma discharge cells are now widely commercially used in plasma displays. In either case, typically a high gas pressure (> few hundred mbar) is always used as it favors excimer formation and helps achieve a high luminous efficiency [69], [83]. Hence an active focus in recent years has been in the high p.d (product of pressure and discharge gap length) range with an operating frequency at the kHz range.

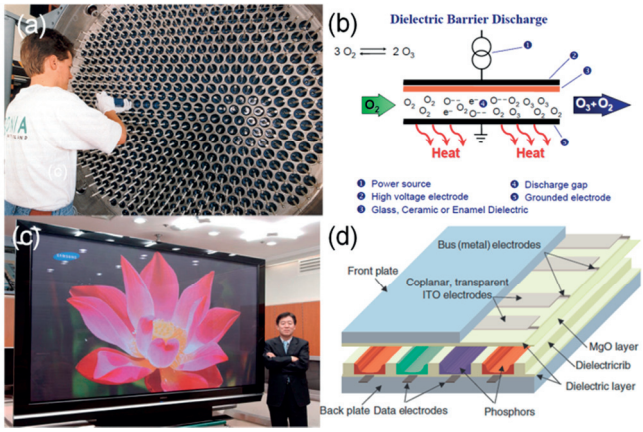

Figure 2.12: Typical DBD applications: (a) Ozone generation using DBD reactors, (b) schematic of the ozone generation in each DBD tube, (c) a plasma TV display containing DBD micro-light sources, (d) a schematic of the plasma display panel showing the DBD cells [73]. Image source for (a), (b), (c): Jose Lopez, Dielectric barrier discharge, ozone generation and their applications, 2008.

2.7.2 Types of DBDs

DBDs are composed of two primary groups: **(1)** volume discharges – microdischarges that take place in thin channels between parallel electrodes and **(2)** surface discharges which are usually independent of discharge gap and homogenous over short distances take place in thin layers off dielectric surface [69] (Figure 2.13). Siliprandi [84] reports that, depending on the buffer gas and pressure in the discharge gap, DBDs operate in two regimes: at low pressure (generally less than 50 hPa), they operate in the Townsend breakdown regime generating a diffuse glow discharge, while at higher pressures (approximately more than 50 hPa), the discharge generally splits up into a large number of randomly distributed microdischarges or

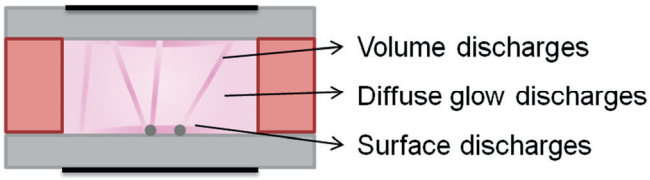

Figure 2.13: The plasma discharge in a DBD cell can be divided into two primary groups of DBDs - volume and surface microdischarges, along with diffuse glow discharges which are better described by diffusion theory. Volume discharges also include the filamentary discharges and streamers which occur at certain input conditions (usually low frequency and/or high electric field conditions).

current filaments of nanosecond duration also called the streamer regime [84], [85]. In both regimes, the dielectric barrier serves two functions: **(1)** it distributes the microdischarges evenly over the entire electrode area and **(2)** it limits the amount of charge and energy that can be fed into an individual microdischarge. After typically a few nanoseconds, the microdischarge is choked due to charge build up on the dielectric which results in a local reduction of the electric field within the filament [84]. Typically an electric field of few hundred V/cm is required to sustain a visible glow discharge in these conditions, however the breakdown voltage required to ignite the discharge is around several hundred Volts depending on gas pressure and discharge gap conditions.

For the light source design, it is not possible to theoretically determine any further the ideal values of discharge cell parameters for a stable and low-power light source operation. As now there is a solid understanding of the fundamental physics involved and a mature set of starting point conditions for the light source design, the next step is to identify the appropriate fabrication techniques to develop the desired miniature Rb DBD cell.

Chapter conclusions

In order to develop a miniature Rb plasma discharge light source, the fundamental physics behind discharges were discussed. Insulated electrodes were identified as necessary to avoid electrode erosion from ion and electron bombardment. Several discharge drive techniques exist but rubidium excitation by an alternating electric field condition was identified as most suitable and power-efficient. Capacitively-coupling the electric field to accelerate the electrons in the discharge volume using a parallel-electrode configuration would allow for a compact cell design and low-frequency operation hence reducing transmission losses. A dielectric barrier discharge light source design would allow for all the requirements identified so far - insulated electrodes, capacitively coupled plasma and an RF drive frequency range (1-100 MHz) and hence is the chosen design approach in this research.

Chapter 3 Miniature DBD cell development

Following the discussion on the preliminary miniature Rb DBD vapor cell design specifications in chapter 2, this chapter details the cell design considerations and the fabrication techniques used to develop this miniature discharge cell. First in section 3.1, the size and performance requirements of the Rb light source are briefly discussed, to identify the cell filling conditions for low-power and stable operation. A brief review of different cell filling and fabrication techniques used by peer researchers and the state-of-the-arts is presented in section 3.2, followed by a detailed explanation of the two types of Rb vapor cell fabrication methods: **(1)** solder-sealing and **(2)** anodic bonding, used in this research. All the lamp-cells used for the characterization studies in this thesis were anodically bonded Rb vapor cells. The list of cells fabricated for discharge experiments and the different cell-electrode deposition methods and materials used are discussed.

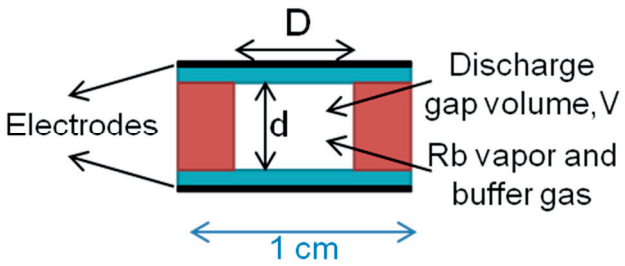

Figure 3.1: Cross-sectional schematic view of the miniature DBD cell where d=2mm and D=5mm for most of the anodic bonded cells used in this research.

Some of the results reported in this chapter have been published in the Sensors and Actuators A: Physical journal [86] and presented at the 2010 Eurosensors conference [87].

3.1 Rb light source – size and performance requirements

The target application of the miniature rubidium discharge light source here is its integration into a miniature portable atomic clock, being developed by our partners in the MACQS project (more details in section 1.3), with a physics package volume in the order of few cm^3. The double-resonance (DR) clock physics package can be built with four main components, as discussed earlier: **(1)** ^{87}Rb discharge light source, **(2)** ^{87}Rb resonance cell, **(3)** microwave cavity and **(4)** a photodetector as a simple stacked configuration (as shown in Figure 3.2). Alternative solutions can also work, for instance, the type of rubidium isotope could be changed to ^{85}Rb or natural Rb (usually around 72% ^{85}Rb and 28% ^{87}Rb) in the case of the discharge light source and the resonance cell [88], [89], [90]. Also, an additional Rb cell consisting of an isotope other than the dominant one used in the discharge lamp can be inserted between the lamp and the resonance cell for isotopic filtering of Rb D line for performance improvements (shown in Figure 3.1) [91], [92]. However, these solutions are possible and more relevant for performance improvements and optimizations after a chip-scale DR clock has been fully developed. In this research, where the objective is to

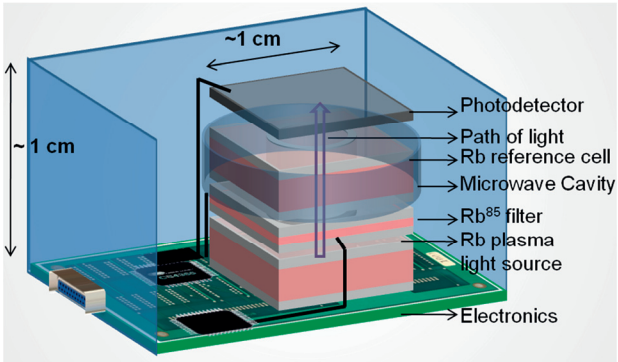

Figure 3.2: Envisioned integration of our light source in a miniature double-resonance clock with the optional Rb isotope filter.

develop the proof-of-concept few cm^3 DR clock physics package, the discharge light source cell volume has to be less than 1 cm^3, preferably being as small as possible.

The minimum optical power needed from the discharge light source for stable optical pumping in an atomic magnetometer is a few μW on the Rb D line wavelength (D1: 795 nm or D2: 780 nm). This value was determined through optical pumping experiments using a laser in an atomic magnetometer test setup with Dr. Christoph Affolderbach at LTF, University of Neuchâtel and the typical interrogation frequency was in hundreds of kHz. However, for an atomic clock, the expected minimum optical power for optical pumping will be slightly more for a detectable signal (one reason being the high-frequency interrogation frequency in GHz) and the desired optical pumping power in miniature scale clocks has been reported to be 10 μW (using a laser and attenuating optics) [4]. Also a highly stable optical output with optical power fluctuations <0.2% is required (for example, more than 0.2% variations from the Rb discharge lamp have caused clear changes in satellite clock frequencies [15]). In summary, Table 3.1 gives the list of the desired performance and geometry requirements of the light source.

Table 3.1: List of the desired performance and geometry requirements of the light source for portable optical pumping applications.

Performance parameter	**Requirement for optical pumping applications**
Size	< 1 cm^3
Optical output	10 μW of Rb D1/D2 line
Optical stability	< 0.2% sub-second fluctuations
Power consumption	< tens of mW
Lifetime	> several years

3.1.1 Physical properties of Rb

Rb is an alkali metal with an atomic number of 37 and an atomic mass of 85.4678 amu (nat. Rb). It is a silvery-white metallic element with a melting point of 39.3 °C. It has only one stable isotope – ^{85}Rb and another isotope ^{87}Rb with a half-life of more than 48 billion years. 72% of all naturally available Rb is ^{85}Rb and almost all the remaining 28% is ^{87}Rb with a very negligible percentage shared by other unstable isotopes. It is the 23rd most abundant element on Earth (also more than cesium) and hence not too scarce for such low-volume consuming applications.

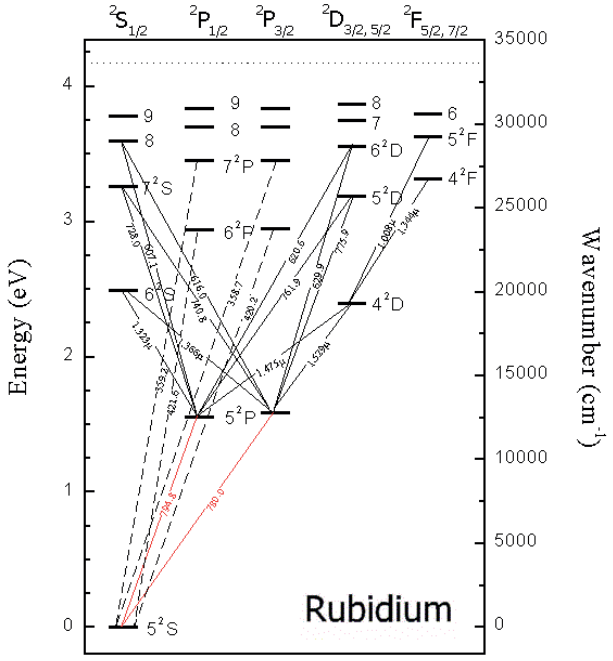

Figure 3.3: Energy level diagram of the Rb atom showing all probable excitation and decay transitions and the corresponding discharge emission wavelengths. The D lines are shown in red. Source: www.chem.purdue.edu

What is needed for the light source is Rb vapor. Few μL of liquid Rb would be enough to create the vapor pressure needed by heating the cell to the necessary temperature. However, more volume is

usually added to compensate the Rb vapor atoms diffusing into cell walls with time [16]. However, dispensing Rb in cells is not straight-forward as Rb is explosive with air and water, undergoing rapid oxidation when oxygen is present [93]. Hence, both dispensing and sealing Rb (or Cs) in cells have to be done in oxygen-free (and H_2O free) environments, for example in pressure-controlled vacuum chambers or N_2 glove boxes. There are also other techniques, for example, where an alkali compound, which does not react to oxygen or decompose while cell-bonding, is sealed in a cell and then UV light is irradiated on the compound to release the alkali vapor [94], [95]. All these techniques are discussed in more detail with references in section 3.2.2.

The vapor pressure of Rb increases with temperature – this allows control of the number of Rb vapor atoms by heating and controlling the temperature of a Rb sealed cell. The vapor pressure of Rb can be given as (where T is temperature in Kelvin and p is pressure in mbar) [96]:

$$\log_{10} P_{v\_Rb} = -125.08 - \frac{2608.47}{T} - 0.051T + 56.63\log_{10} T \quad \text{(solid phase)} \tag{3.1}$$

$$\log_{10} P_{v\_Rb} = 21.12 - \frac{6024.42}{T} + 0.000078T - 3.98\log_{10} T \quad \text{(liquid phase)} \tag{3.2}$$

The energy structure of the Rb atom can be seen in Figure 3.3. It shows the different atomic energy levels of Rb and all probable excitation and decay transitions and the corresponding discharge emission wavelengths.

3.1.2 Buffer gas and pressure conditions

Adding a buffer gas to the Rb vapor cell (Figure 3.1) significantly reduces the breakdown field requirements, essential for the desired low-power lamp operation, and the suitable gas conditions are discussed in this section. The Rb D line, D1 for example, corresponds to the emission of energy when an excited Rb atom decays back from the $5^2P_{1/2}$ to the 5S state, while D2 corresponds to the $5^2P_{3/2}$ to 5S transition (shown in Figure 3.3). This corresponds to wavelengths of 795 nm or energy of 1.56 eV in the case of D1, 780 nm or energy of 1.58 eV in the case of D2. The lifetime of the $5^2P_{1/2}$ and $5^2P_{3/2}$ states have been reported to be around 27.7 ns and 26.2 ns respectively [96]. The inverse of this lifetime also gives the spontaneous decay rate (Einstein A coefficient), which is the natural line width of the emitted radiation. If N is the average number of Rb decay transitions per second needed for a steady-state emission of 10 μW Rb D line power, then, in the simple case, there needs to be at least N number of neutral Rb atoms being collided per second by electrons with kinetic energy >1.56 eV. For the case of D2, 10 μW => 10 μJ/s = $N.h.c/\lambda.\tau = (N.E_{photon})/\tau = N.(1.6*10^{-19}).(1.56)/(26.2*10^{-9})$ => N = $1.1x10^6$ photons/s or number of excited Rb atoms/s.

The theoretical minimum number of Rb vapor atoms required in a purely Rb vapor cell, according to elementary kinetic theory, would be $2*N = 2.2x10^6$ Rb atoms to achieve the desired output (irrespective of applied field strength). This is because, N number of neutral Rb atoms need to be ionized to produce enough electrons to excite the remaining N Rb atoms under an applied electric field. However, this is not true due to many reasons, mainly: **(1)** the electron density and energy is dependent on all input conditions and cannot be monitored, distributed or controlled to a theoretical minimum value, **(2)** neutral Rb atoms can absorb the emitted D lines

from the neighboring excited Rb atoms decaying to its ground state. This **(2)** means that the total optical power output is reduced and the number of neutral Rb atoms available for impact ionization is also reduced. Hence, these factors have to be included in calculating the required Rb vapor pressure in a cell for successful optical pumping.

Assuming the worst case for **(1)** when all ionizations are caused only by single electron impacts, the ionization efficiency of an electron, η_{ei}, (η_{ei} is the number of ionizations produced by one electron moving by 1 mm) can be given as [24]:

$$\eta_{ei} = \frac{dN}{dx} = a.p.(V - V_i) \qquad for \qquad V \leq 2V_i \tag{3.3}$$

$$\eta_{ei} = p.\eta_{\max}.\left(1 - e^{-b(V-V_i)}\right) \qquad for \qquad V \leq V_{max} \tag{3.4}$$

where p is the vapor or gas pressure in mbar, V is the electron energy in eV and V_i is the ionization energy of the gas atom in eV. The constants a, b and η_{max} (ionizations/mm.mbar) have been experimentally determined using DC discharge tube conditions [24] and is mentioned here for some inert gases and Rb vapor in Table 3.2 for preliminary calculations (p in mbar and η_{ei} in ionizations/mm). η_{max} for alkali vapors usually corresponds to around 20 eV and V_{max} corresponds to the energy at η_{max}.

Table 3.2: Values of a, b and η_{max} of some inert gases and Rb for ionization efficiency calculations.

	He	**Ne**	**Ar**	**N_2**	**Rb**
a (x 10^{-3})	3.5	4.2	53	19.5	143
b (x 10^{-3})	2.6	1.4	41	1.9	*
η_{max}	0.097	0.22	0.97	0.76	0.48

As a low-power operation is desired, the average electron energy in this desired operation mode would be $<2V_i$ and hence the equation (3.3) can be used for the η computations. For Rb vapor atoms at room temperature (p ~ 10^{-6} mbar) and substituting $V = 2V_i$, [V_i of Rb = 4.17 eV], η_{ei} = $6x10^{-7}$ ionizations/mm. This would correspond to too few ionizations for cells with discharge lengths in the mm-scale or lesser for an electrical breakdown and eventual discharge emission. In order to have η_{ei} to be at least 1 for a purely Rb 1 mm gap cell, the temperature of the cell needs to be increased to more than 300 °C to increase the Rb vapor pressure, or the input power and the discharge length has to be increased drastically. All these correspond to either high power or size requirements and are hence a purely Rb cell is not a viable solution for the light source design. However, by adding a buffer gas, that is inert with Rb, the pressure can be increased leading to higher ionization efficiency without increase in input power or cell size. For example, adding 10 mbar of Argon to the Rb vapor pressure and substituting $V = 2V_i$ [V_i of Ar = 15.75 eV], the ionization efficiency, η_{ei}, is now 8.34 ionizations/mm. The two cases are not fully comparable yet as now the average electron energy is $2V_i$ = 31.5 eV which is about 3.7 times the previous case ($2V_i$ = 8.34 eV). If the electron temperature can be considered as a linear function of input power, the ionization efficiency in the 10 mbar Ar case, after factoring the 3.7 times, is still 2.25 ionizations/mm, which is magnitudes higher than the purely Rb cell case. Hence,

adding a low-pressure buffer gas would drastically reduce the power needed for breakdown but the exact gas type and parameter values that would be suitable for the desired performance requirements have to be experimentally determined. It is known that plasma displays using DBDs usually work in the pressure-discharge gap (pd) product of 1-25 mbar.cm range [97] with a preference for higher pressure (p) by adjusting distance (d) for better photon yield (for example NEC uses 670 mbar Xe-Ne and a gap of 100-300 μm [98]).

The idea is to have the lowest addition of other gases to the Rb cell to have the highest probability of Rb excitations rather than buffer gas excitations. Or in other words, moving electrons with energy higher than the Rb 5P state but less than the first ionization energy will encounter more collisions with gas atoms and lesser collisions with Rb atoms with increase in buffer gas pressure. This will lead to a lower percentage of Rb optical power output for the same input power conditions when compared to a Rb cell with a lower buffer gas pressure. Adding such a optimum buffer gas and pressure has been the commonly used solution for Rb discharge lamps [48], [99]. The ideal buffer gas would **(1)** be inert to Rb, **(2)** have a low first ionization energy (IE1) for low-power ignition and **(3)** have a low atomic diameter for a higher mean free path and electron acceleration. The IE1 of the gas atom needs to be higher than Rb's IE1 so that Rb is always preferentially ionized at low electron temperature conditions. Also, a low atomic diameter usually means a higher IE1 and hence a suitable trade-off between these conditions needs to be experimentally determined. Gases such as Ar, Xe, Ne, Kr, He, N_2 and mixtures of these gases are suitable choices. Experimental results obtained from Ar, He and N_2 are reported in section 6.1.3.

3.2 Rb cell fabrication techniques

A Rb vapor cell has been the essential component of all Rb DR clocks for several decades now, being mainly used as the atomic resonance cell for interrogation. Hence, there has been quite a bit of research in developing different fabrication techniques for Rb vapor cell development, with more focus towards miniaturized cells development since the advent of microtechnology and the rising demand for portable applications. Importantly, these Rb vapor cells can be used as a discharge lamp if a field sufficient enough to induce an electrical breakdown can be applied using suitable electrodes and drive circuitry. Although almost all Rb vapor cells other than glass-blown cells were fabricated for use as resonance cells, their fabrication processes are highly relevant for this research and are discussed in the following sections.

3.2.1 Glass-blown Rb discharge lamps

The most popular, and in fact, the only type of Rb vapor cell reported before this research, to be used as a Rb discharge lamp, is fabricated using the conventional glass-blowing technique. These ICP lamps are commercially manufactured with a typically spherical geometry of diameter 1-3 cm and are inductively-coupled using a high-frequency (typically 30-150 MHz, several Watts) single-turn current coil around the cell. Figure 3.4 shows a compact rubidium frequency standard (manufactured by Spectratime) using a glass-blown Rb vapor cells (shown in the same figure) for the discharge lamp and the resonance cell. A low-pressure (typically less than few mbar) buffer gas is added to allow for a lower breakdown voltage [100] and also avoid Rb self-absorption at room temperature or operating temperatures [101].

Rb self-absorption refers to the neutral Rb atoms absorbing the emitted discharge lines from neighboring Rb atoms fluorescing to their ground state from an excited state. By adding a low-pressure gas, the dominance of this phenomenon is shifted to higher temperatures and is negligible at temperatures lower than what is called the Rb self-absorption temperature. This is generally understood to be the temperature when the number of Rb atoms to the number of buffer gas atoms is roughly 1:1000 [102]. A plot of this trend: Rb self-absorption temperature versus Argon pressure is shown as an example in Figure 3.5.

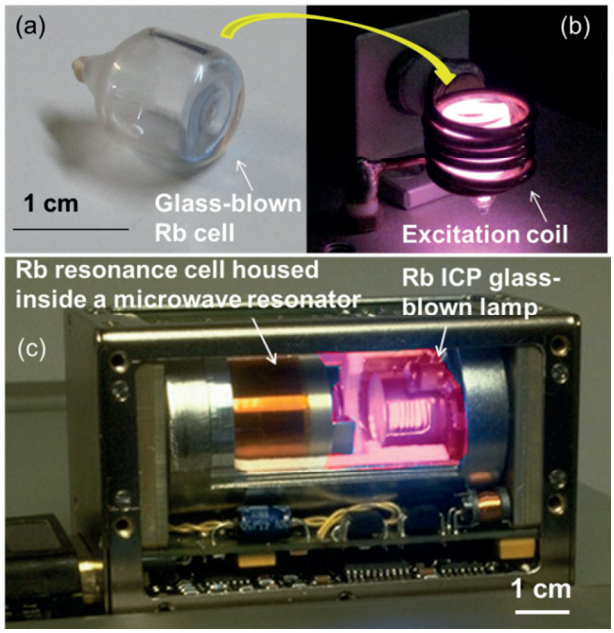

Figure 3.4: (a), (b) Photographs of a glass-blown Rb cell developed at LTF, Neuchâtel and the Rb ICP lamp with the cell placed inside an excitation coil. (c) A compact Rb DR clock (Spectratime), showing a conventional glass-blown lamp emitting light to a resonance cell.

The standard spherical lamps are unsuitable for miniature atomic clocks, as discussed already, because of component integration issues. A cylindrical but miniature Rb glass-cell was fabricated (not by conventional glass-blowing) for performance evaluation as resonance cells by Yves Pétremand et al. (Figure 3.6) [103]. While a miniature-scale (<1 cm^3) volume was possible to fabricate using glass-blowing, the cell was highly non-planar with high surface variations which would severely reduce the transmission intensity. This approach also leaves a few mm long seal-off tube attached to the tube which makes is difficult to integrate with other components. Also, due to the high surface tension of glass, as well as the possibility of the alkali atoms reacting with glass at elevated temperatures, scaling down to mm scale is very challenging [4].

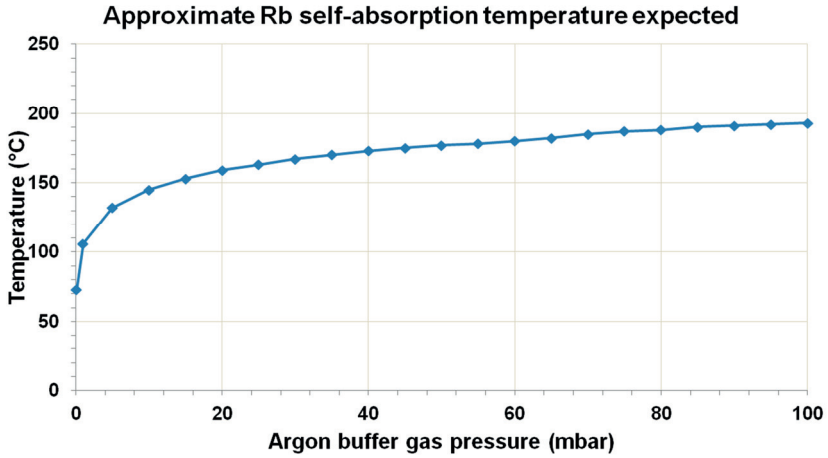

Figure 3.5: The expected Rb self-absorption temperature calculated based on 1:1000 ratio of Rb vapor to Ar atoms in the discharge volume.

3.2.2 Miniature Rb vapor cell fabrication methods – state-of-the-art

This section reports on the different methods and the current state-of-the-art techniques for fabricating miniature Rb vapor cells. These miniature cells have always been developed for resonance cell applications in atomic clocks and other quantum devices. However, a similar

miniature cell is required for the lamp-cell, which with addition of appropriate electrodes (section 3.5) can be developed into a plasma light source.

There are only a very few cell bonding and fabrication techniques that can be compatible with alkali (Rb and Cs specifically) sealing. This is broadly due to the incompatibility (or non-negligible reactivity) of the alkali metals with many metals and materials used for bonding and also due to the significant challenges posed by Rb and Cs for any high-temperature bonding because of its high vapor pressure and conductivity. First of all, at least one of the cell walls needs to be transparent to the D lines (which are almost in the visible range) for a high optical output and this already limits the possible hermetic sealing techniques to glass-compatible cell bonding processes only.

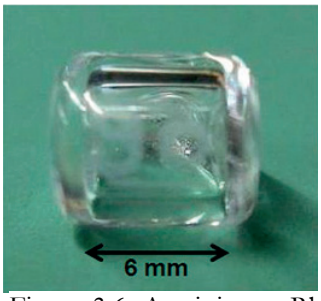

Figure 3.6: A miniature Rb cell fabricated by the glass-blowing technique [103].

The miniature alkali cell fabrication can be divided into two distinct steps: **(1)** dispensing alkali atoms in a miniature cell and **(2)** cell bonding and hermetically sealing the alkali atoms. There are many different approaches used for alkali dispensing in miniature volumes but all approaches using microfabrication technologies share an overall common process flow for hermetically sealing the cell. Both Cs and Rb have very similar properties when it comes to cell-sealing and hence the overall sealing schemes for both elements can be used interchangeably. The exact sealing process parameter values for the respective element can then be changed appropriately.

Rb cell fabrication by anodic bonding

Currently, the most successful hermetic sealing technique developed for fabricating miniature planar Rb vapor cells is the anodic bonding technique. Some reasons being: (1) this technique is highly efficient for bonding glass (typically Pyrex) with Si (typical bond strengths between 10 to 20 MPa from pulling tests [104]), which can hence be used to fabricate a glass-Si-glass Rb vapor cell that can both be used as Rb discharge cell or as a clock resonance cell. (2) It can create tight hermetic seals (no measurable gas leakage rates in many cases; sometimes as low as 10^{-15} mbar/s) that are important for clock applications [105]. (3) It can allow relatively low-temperature sealing (<400 °C) which reduces the complexities of Rb vapor sealing at elevated temperatures.

The fabrication method implemented at NIST [94] is given as an example (Figure 3.7). Figure 3.7 shows the schematic of a miniature Cs cell

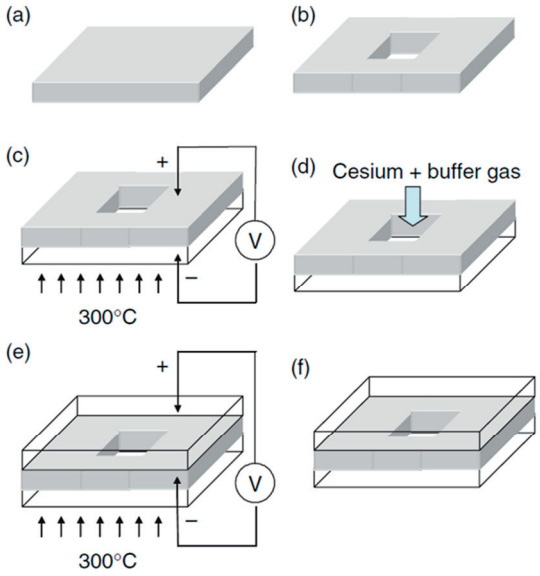

Figure 3.7: A schematic illustration of cell fabrication based on silicon etching and anodic bonding. A Si wafer (a) with holes etched through it (b) is anodically bonded to a piece of glass (c). It is then filled with alkali atoms and buffer gas (d), and a second piece of glass is bonded on top (e) to form a robust, hermetically sealed vapor cell (f) [94].

fabrication based on silicon etching and anodic bonding. A Si wafer is DRIE etched to create through hole using the desired lateral dimensions of the discharge volume. Using the anodic bonding technique by applying around 1 kV across the Si and a Pyrex layer (heated to 300 °C and placed on the bottom), the Pyrex layer is bonded to the Si layer. Then elemental Cs was injected into the cavity/preform with a micropipette in an anaerobic chamber, followed by back-filling with the desired buffer gas pressure. Now within the same pressure-controlled environment, the second Pyrex layer is anodically bonded (using similar conditions to the first step) to the top Si layer to create a hermetically sealed cell. Some other leading research groups and atomic clock manufacturers like Symmetricom and Sarnoff also use a similar technique [106], [13]. However, the dispensing technique used in Sarnoff is slightly different, where a thin Tungsten-carbide drill is used to transfer a Cs droplet into the preform.

All Rb discharge cells studied in this research were fabricated using the anodic bonding principle by Yves Pétremand, at the Rb-cell bonding setup developed by EPFL-SAMLAB and UniNE-LTF. A brief concept of this technique and the fabrication process flow are discussed below.

Concept of anodic bonding

Anodic bonding is an irreversible bonding process performed by heating a glass and a semiconductor (or metal) sandwich and applying a DC voltage across the layers (AC voltage also possible). Here, a Pyrex wafer and a p-type Si wafer are used for the bonding. [Pyrex has been used extensively to develop Rb vapor cells and has been reported to have lower Rb diffusion rates in the increasing presence of buffer gas atoms [107]].

The cathode (negative terminal) is connected to the Pyrex layer and the anode to the Si layer using metal contacts and the whole setup is placed on a heating stage (dual-side heating stages are also used). Figure 3.8 shows the schematic view of the bonding process [108].

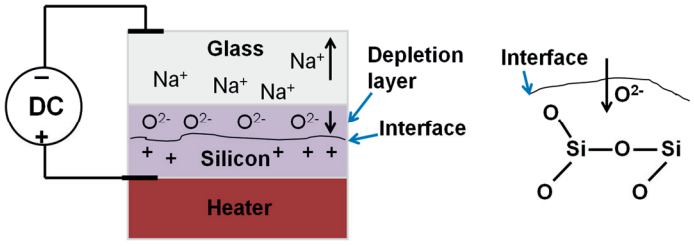

Figure 3.8: The anodic bonding process showing the formation of the depletion layer and the interfacial electrostatic field. The oxygen anions migrate to the positively charged Si to form a permanent bond.

With the application of heat and voltage, two types of reactions occur in forming an intermediate SiO_2 bond interface layer: ion dissociation/association reactions and interfacial bonding reactions [109]. The elevated temperature permits ionic conduction within the glass, while the imposed potential drives the migrating ions of opposite charge towards the interface (as it moves towards the cathode). Cations (mainly Na) move through the glass toward the cathode, hence leaving a depletion layer behind and allowing glass reconstruction. This reconstruction allows for the excess oxygen anions to move towards the interface due to the applied field. This space charging of the depletion layer generates an interfacial electrostatic field and a force pulling the glass and Si surfaces together and holding them during the formation of a permanent bond. The contact usually starts at a single point between the interfaces and allows the diffusion of the oxygen anions into the positively charged Si. Hence, bond formation can occur only when surfaces are

very clean and have low surface roughness (typically <1 μm surface variations reported for glass-metal bonding [110]).

Fabrication process flow of the vapor-cells used in this research

This sub-section gives the details of the process flow and parameter values used to fabricate the Rb vapor cells for experimental studies. Figure 3.9 illustrates the process flow for developing the micro-fabricated Rb cell (height: 0.3 cm) – bonded stack of three layers: Pyrex (500 μm thick), silicon (2 mm thick), Pyrex (500 μm thick) enclosing a 5-mm-diameter, 2-mm-thick cylindrical cavity in which a few micrograms of rubidium and the desired pressure of argon are hermetically sealed by a two-step anodic bonding process.

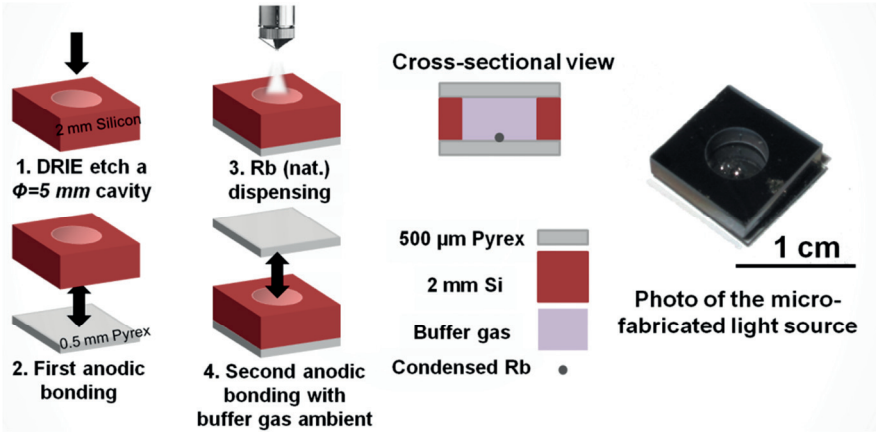

Figure 3.9: Microfabrication process flow of the Rb light source showing Rb dispensing and hermetic sealing of the buffer gas+Rb vapor cell. Steps 1 and 2 are performed at wafer level and steps 3 and 4 are completed at chip level.

First, the cavity is created by deep reactive-ion etching (DRIE) a 5 mm diameter through-hole in a silicon wafer. Then, the etched silicon wafer is anodically bonded to the bottom Pyrex layer at 300°C while applying 1000 V between the two layers. The wafer is then diced to 1 cm x 1 cm chips for continuing the next steps in chip-scale level. After this first bonding step, natural Rb/^{87}Rb is dispensed into the cavity under vacuum from a commercial Rb source (SAES Getters). A stable rubidium chromate compound is heated ex-situ using a high current coil to produce Rb vapor that is sprayed on to the cavity through a nozzle. The desired pressure of buffer gas (2 to 70 mbar Ar in most cases) is is then back-filled in the chamber, and the top Pyrex layer is anodically bonded to the bottom layers at 300 °C and 400 V (for approximately one hour) to create the hermetically sealed Rb vapor cell.

Other Rb dispensing and sealing methods

Few other alkali dispensing and sealing approaches have been reported [111], [112], [113], [114], [115], [116]. For example, Radhakrishnan and Lal (2005) encapsulated rubidium in wax micropackets, as shown in Figure 3.10 [117]. The cell preforms were made by anodic bonding of bulk micromachined silicon wafers to Pyrex under a xenon atmosphere. One side of the cavity array has a silicon nitride membrane that gets thermally bonded to the wax micropackets, as shown in Figure 3.10. The rubidium is released into the cavity by laser ablation of the silicon

nitride membrane. Rubidium absorption was measured in these cells successfully, but the effect of the wax on the ground-state hyperfine coherence has not been studied yet.

Liew et al. (2007) [94] developed a wafer-level process to make arrays of nitrogen buffer gas cells with cesium. Here, cesium azide (CsN_3) is evaporated through an aluminum shadow mask into cell preforms made from silicon with borosilicate glass windows. The cavities were closed under vacuum by anodically bonding a wafer of borosilicate glass onto the top. The cesium azide is then decomposed into cesium and nitrogen by exposing the cells to ultraviolet light (the decomposition is stopped when the nitrogen pressure reaches the desired value). Another interesting technique, demonstrated by Gong et al. [113], uses cesium-enriched glass as a source for alkali atoms in microfabricated cells. The glass pieces are melted into a well on the bottom of an anodically bonded cell preform and the cell is sealed by anodic bonding under the desired buffer gas atmosphere. Finally, the cesium atoms are released from the glass by passing an electrolytic current through the glass at 500 °C and 1 kV between a $NaNO_3$ anode and the silicon (cathode).

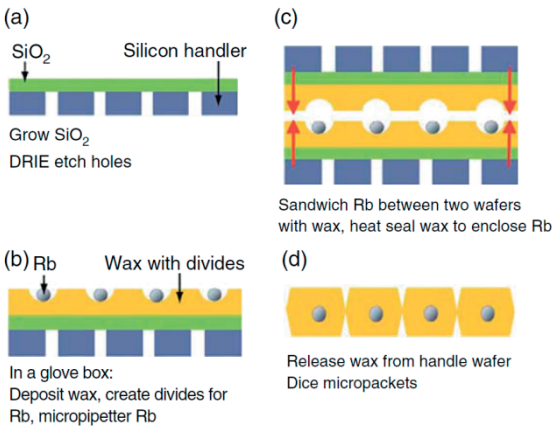

Figure 3.10: Process to enclose Rb in wax micropackets. By Radhakrishnan et al.

Researchers at NIST also presented another dispensing method where liquid solution of a stable cesium compound (CsCl) and barium-azide (BaN_6) is placed in the preform outside the vacuum chamber [118]. During the second bonding step, cesium is released according to the scheme: $CsCl+BaN_6 \rightarrow Cs+3N_2+BaCl$ by placing the setup inside a UHV (ultra high vacuum) chamber and heating the preform to 200 °C [119]. The biggest advantage of this technique is that it allows the alkali (RbCl in the case of Rb) dispensing in normal room conditions. While this technique worked well for big centimeter-sized cells, it had three main problems for miniature cells: **(1)** it was not possible to remove all the residual N_2 gas before sealing, **(2)** the free barium still present in the cavity after sealing reacted with N_2 to form compounds like BaN_6 and **(3)** the released compounds, especially in the case of Rb, are highly toxic and explosive – undesirable for laboratory level research. Due to these conditions, there are cell impurities and high variations in cell pressure with time hence deeming this process unsuitable for lamp cells without further optimizations in the sealing process.

Discussion on Rb dispensing and sealing

Alkali dispensing using micropipettes in a glove-box might seem straight-forward but even the presence of tiny amounts of residual oxygen oxidizes/partially oxidizes the tiny alkali volumes used for dispensing. Hence, it is highly practical for commercial level fabrications where a systematic control of all process parameters can be rigorously implemented with possibly automated dispensing to produce hundreds of cells. The reduction method, on the other hand is a relatively easy and cheap way to produce cells if the reduction is made to happen somewhere outside the cavity and only the alkali vapor product is evaporated into the cavity through a small

nozzle (Chloride reduction is only an example, there are many other compounds that are suitable for this technique, like rubidium azides and chromates – the central point is reducing a stable alkali compound ex-situ by initiating a chemical reaction with reducing agents and heat to produce pure alkali vapor for targeted dispensing). This was explored by other research groups, including here in EPFL-SAMLAB, Switzerland, which led to further improvements in this type of sealing process to develop pollutant-free alkali sealed cells. One variant of such an optimized reduction and dispensing technique is what was used in this research to develop anodically-bonded Rb vapor cells which was reported in the fabrication process flow sub-section.

A low-temperature (<250 °C) bonding technique would be convenient for fabrication of Rb vapor cells. This would drastically reduce the complexities encountered in other high-temperature bonding processes where the main problem is the complete escape of alkali vapor atoms from the cavity at elevated temperatures and/or the presence of alkali vapor between bonding interfaces creating hermeticity problems. In order to avoid these problems, low-temperature bonding techniques like solder-sealing [120] and glass-frit bonding [121], suitable for Rb discharge cell development were explored in this MACQS project - by EPFL-LMTS and EPFL-LPM [86] and low-temperature indium bonding [122] and anodic bonding [103] by EPFL-SAMLAB. A low-temperature solder-sealing process developed in collaboration with EPFL-LPM to fabricate hermetically-sealed Rb cells for this research is discussed in the next section.

3.3 Novel Rb cell fabrication technique by solder-sealing

In this section, a fast and low-temperature solder-sealing technique developed (in collaboration with Fabrizio Vecchio and Dr. Thomas Maeder at EPFL-LPM) for fabricating a hermetic 1.4 x 1 x 0.3 cm^3 Rb cell is presented and discussed. This is a novel Rb dispensing and hermetic sealing technique for convenient Rb handling and batch fabrication of miniature Rb cells and has been published in the Sensors and Actuators A: Physical journal [86]. Several solder and metallic combinations were studied and sealing temperatures down to 138 °C were possible using a Sn-Bi eutectic (58Bi-42Sn) solder. A novel Rb storage and dispensing technique using high order alkanes was also researched. Some advantages of these developments:

1. Low-temperature sealing avoids the complexities experienced in Rb sealing at elevated temperatures which include **(1)** the complete escape of alkali vapor atoms from the cavity and/or **(2)** the presence of alkali vapor between bonding interfaces creating hermeticity problems;

2. The sealing process is accomplished within few minutes, with the peak temperature (solder melting time) of 150 °C in the order of 10 seconds. This fast process minimizes Rb evaporation and the reactions with the bonding interface. Despite the low melting point of both Rb and traditional solder metals, intermediate compounds are formed especially during bonding [123], but they have very high melting points and hence exhibit very limited solubility and very low levels of mixing with the alkali liquids. This essentially means that some impurities are indeed formed on the bonding interface and also would be present in small concentrations inside the sealed cell as a result of solder-Rb interactions, but they are practically inert and have not been observed to affect the reliability of the cell;

3. It is a batch fabrication compatible process and highly cost-efficient;

4. A novel Rb dispensing and storage technique using high order liquid alkanes that would allow the alkali dispensing in normal room conditions without the need of a glove box.

3.3.1 Rb solder-cell design and development

The primary objective here is to develop a reliable low-temperature cell sealing technique using solders and materials that would be compatible with Rb to create miniature Rb vapor cells. For this, first a Rb-compatible transparent (at 780 and/or 795 nm) solid substrate needs to be identified. Glass, in general, is the only option as no other material seems to meet the cell wall requirements. It is also cheap, easily available and well established in terms of physical and chemical properties. However, not all glasses are equally good for Rb due to the presence of some oxides groups with low dissociation energies and importantly some metal groups which can be reactive with Rb. While SCHOTT glass 8436 is understood as the best Rb resistant glass manufactured yet due to the lowest Rb consumption rates [124], borosilicate glass or Pyrex and soda-lime glass, which are relatively easily available and are used in this study, also have similar compositions to the tested glasses [125] with acceptable Rb diffusion rates.

The idea is to pattern a closed-shape solder layer on two glass substrates, which can then be placed one on top of the other with the solder layers aligned and in contact with each other (Figure 3.11). By applying a compressive force on the two substrates while they are heated to a temperature more than the melting point of the solder, the solder layers mix homogeneously and create a hermetic enclosure. Figure 3.11 shows the cell bonding setup which includes the alignment and heater arrangement designed for this purpose. An intermediate metallization layer is required to bind/adhere the solder layer to the glass substrate. This is because solder layers form very weak bonds (bad wetting) when directly deposited on glass substrates and hence a suitable intermediate layer is deposited to ensure good wetting and firm adhesion.

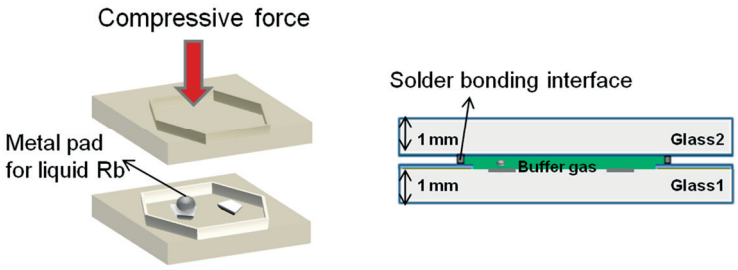

Figure 3.11: Schematic of the bonding procedure of two solder-layer deposited glass substrates and the cross-sectional view of a bonded cell.

The solder and metal layer pastes are patterned on the glass substrates using the mesh screen-printing technique. This work was done in collaboration with Fabrizio Vecchio while the photo masks were (except for one time) made by the LPM technicians. First, the inverse of the shape/solder layer design is printed on a transparent sheet to act as a shadow mask. This sheet mask is placed on top of a photo-sensitive flexible sheet and exposed to UV light. After exposure, this sheet is then manually pressed on to a mesh plate (after typical cleaning procedures) of appropriate mesh size (typical mesh diameter: tens of microns) to create the mesh mask. This mesh mask now acts as a stencil and can be used to screen-print the necessary solder/metal paste using appropriate squeegees in the EKRA E1 screen-printing machine. The metallization layer is screen-printed first and is then heated to a high temperature (typically 500-700 °C) by placing it in a firing oven to form a permanent bond with the glass substrate. The solder layer is then screen-printed exactly on top of the metallization layer using the same mask

design (but larger mesh diameter) using typical alignment procedures and dehydrated by heating it for few minutes at a temperature less than the solder melting temperature (say 100 °C).

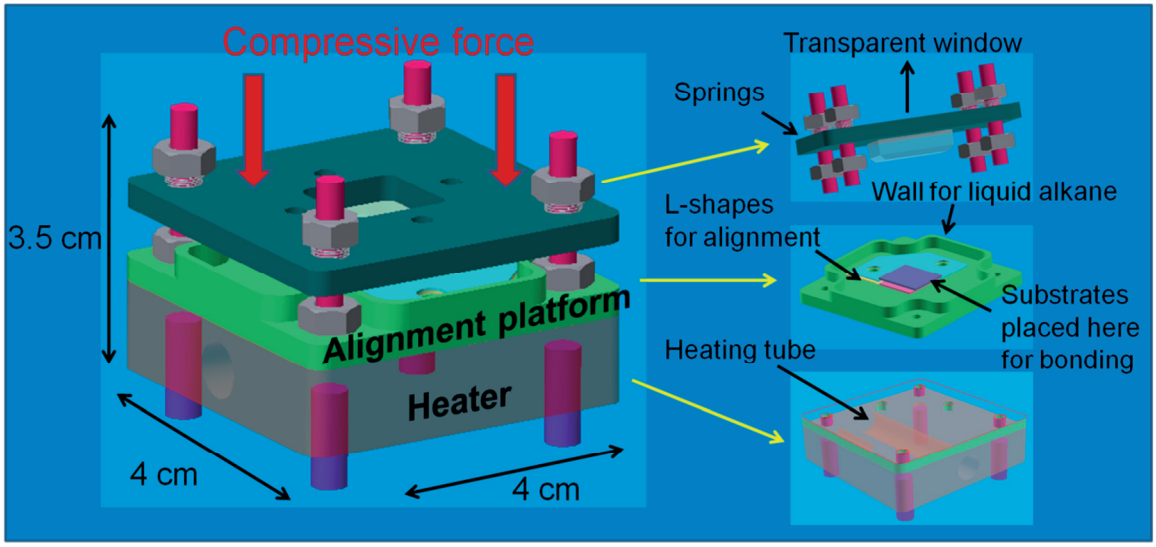

Figure 3.12: The illustration of the solder-bonding setup using four springs for a balanced compressive force, L-shaped pieces for alignment of the rectangular substrates, walls to submerge the dispensed Rb in liquid alkane and a 300 °C capacity heater with temperature control.

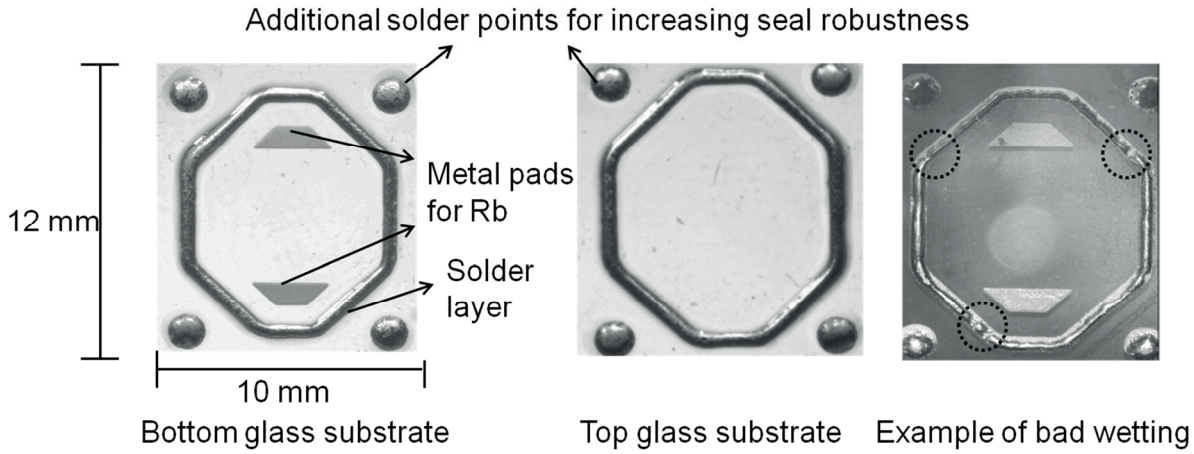

Figure 3.13: Photographic illustration of some screen-printed glass substrates for bonding. An example of a substrate with a bad wetting solder/metallization layer combination is also shown.

Table 3.3: Visual observations and comparisons of the different metallization–solder combinations on 1 mm thick glass substrates.

Solder↓\Metallization→	**Sn-Bi**	**Sn-Pb-Ag**	**Sn-Ag**
ESL 590G (Ag, 525 °C)	Bad wetting	60% yield	Bad wetting
ESL 9912A (Ag, 625 °C)	50% yield	Good wetting	Good wetting
ESL 9695 (AgPd, 625 °C)	30% yield	Good wetting	Good wetting

Different solder/metallization combinations were tried, in order to arrive at the best solution and also provide a selection of promising alternatives. For the metallization layer, ESL 590G (Ag, 525 °C firing temperature; ElectroScience Laboratories (ESL), USA), ESL 9912A (Ag,

625 °C firing temperature) and ESL 9695 (AgPd, 625 °C firing temperature) thick-film pastes were tested. Besides the metals, these pastes contained LPM-proprietary glass frits and oxides designed to allow bonding to nonmetallic substrates [126].

For the solder, standard eutectic 58Bi42Sn, 62.5Sn36.5Pb1Ag and Bi–Sn–Ag solder pastes were used (all proportions given in weight). The resulting cells were first visually compared using an optical microscope, with the aim to find combinations exhibiting reliable and complete wetting of the metallization by the solder (results in Table 3.3 and illustrated in Figure 3.13). ESL 9912A together with Bi–Sn/Bi–Sn–Ag was found to be the best combination, featuring good wetting and a low melting point that reduces both the Rb evaporation and leaching of the metallization by molten solder [127].

3.3.2 Rb dispensing in liquid alkane and sealing method

The developed Rb (or any other alkali metal) dispensing and storage method is illustrated in Figure 3.14. The vapor cell is comparatively large with a dedicated metal pads where a few µL of Rb is dispensed using a glass micropipette. One of the novelties of this method is that all manipulations are carried out inside a large pool of dodecane, which protects the alkali metal from oxidation during handling and, being hydrophobic, does not readily take up water.

First, the Rb is slightly heated up to its melting point, and dispensed into the solder-enclosure when staying under the dodecane. Then, the other substrate is placed on top and this assembly is rapidly transferred into a vacuum chamber where the solder-sealing would be done (Figure 3.12). During the transfer, short-term protection of the Rb from air is still ensured by the small volume of dodecane that is maintained by the solder walls. In the chamber after flushing out the ambient air, the cell is first progressively heated up to 80 °C in the presence of a buffer gas (20 mbar N_2 here) to gently evaporate the dodecane inside the reservoir while avoiding outright boiling. Boiling, i.e. a greater solvent vapor pressure than the ambient total pressure (the 20 mbar partial vacuum used here), is avoided because it may disturb the position of the Rb drop or even the position of the top substrate. After this evaporation step, the cell is further heated up to the soldering temperature for typically 20 s in the final desired buffer gas and pressure, ensuring hermetic closure.

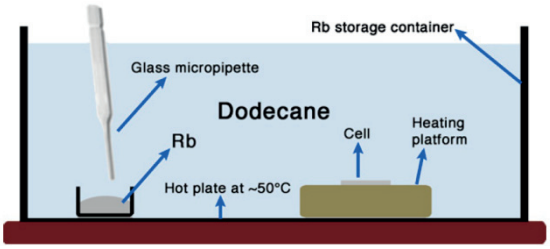

Figure 3.14: Rb dispensing and storage in a pool of dodecane (liquid alkane). The Rb is dispensed using a micropipette on the cell inside a walled platform to keep the Rb submerged even after removal from the dodecane pool.

3.3.3 Hermeticity tests

The hermeticity of the cell can be tested by monitoring the encapsulated pressure inside the cell after sealing. The first type of test that was performed was integrating a miniature pressure sensor to the cell and monitoring the pressure inside the cell with time (Figure 3.15). Figure 3.15d shows an example cell that has been integrated with an Intersema MS5540 pressure sensor module. Before the sealing procedure, a tiny hole (0.8 mm) is drilled through one of the glass

substrates (inside the solder enclosure, Figure 3.15c) and a miniature pressure sensor (Figure 3.15b) is fixed on the flat side of the substrate using a strong vacuum epoxy (Varian Torr Seal). The sealing procedure is then followed as mentioned in the previous section, after which the pressure inside the cell can be monitored through this sensor which is connected to a computer via a dedicated USB module. Figure 3.16 shows the results attained for one of the cells. It can be seen that the cell pressure remained very close to the initial sealing pressure value for several days but reached atmospheric pressure over time (within weeks). In some cases, it was observed that the cell pressure increased to values slightly higher than the ambient pressure indicating that there might be non-negligible outgassing from the Torr Seal. Hence, using this test, it was difficult to confirm the hermeticity of the cell and hence another technique using FTIR spectroscopy was also investigated.

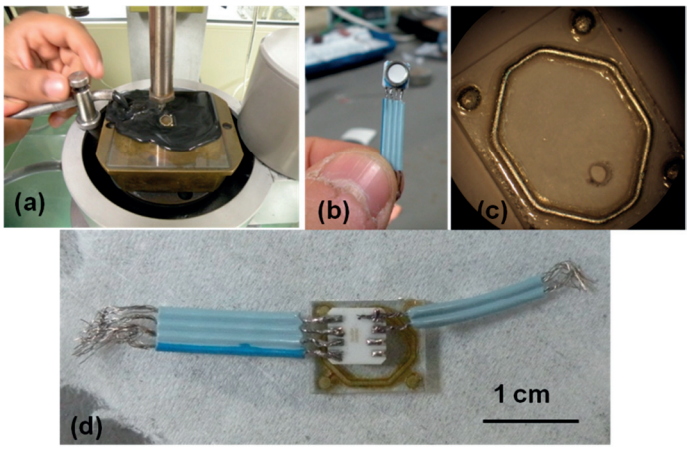

Figure 3.15: (a) Drilling a hole through the glass substrate using an ultrasonic drill, (b) a miniature pressure sensor, (c) a drilled glass substrate, (d) an integrated sensor and substrate.

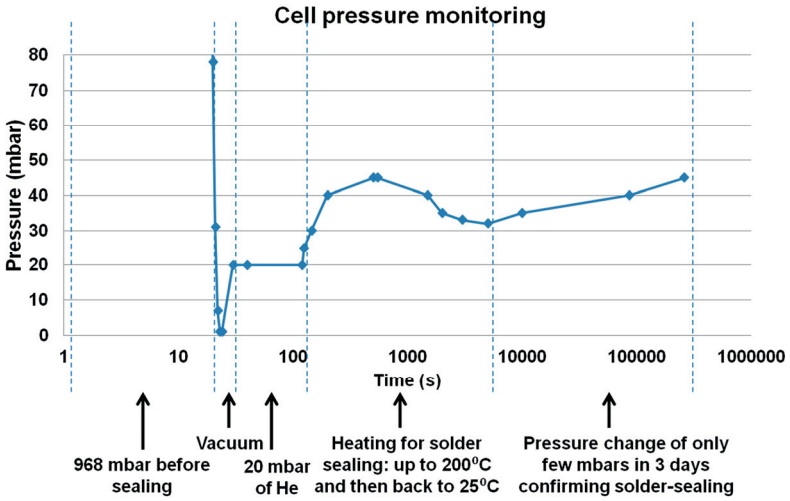

Figure 3.16: The pressure of the cell plotted during and after the cell is sealed. While the cell was found to be sealed, there was a slight increase in cell pressure with time which could be leak or because of outgassing.

If the cell is sealed with N_2O gas (other gases also possible), it is possible to use an FTIR spectrometer at CSEM, Neuchâtel, to detect the presence of N_2O and its concentration by monitoring the absorption spectrum of the cell. N_2O has its strongest absorption peak at 2250 cm^{-1} and the absorption intensity at this wavenumber is proportional to the N_2O pressure inside the cell. Figure 3.17 shows the transmission curves

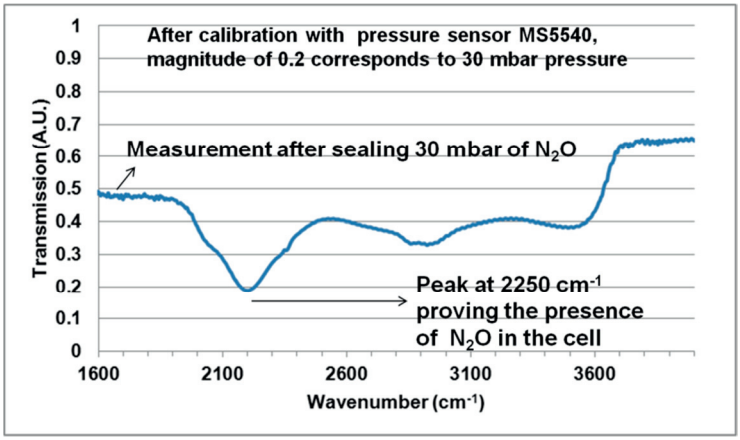

Figure 3.17: An absorption spectrum of a sealed cell obtained from FTIR spectroscopy showing the presence the N_2O and confirming hermeticity.

of the background and in the presence of an N_2O (30 mbar) sealed cell. The N_2O absorption can be clearly seen and this value corresponds to a 30 mbar pressure – proving the hermeticity of the cell (a calibration test was done by soldering a pressure sensor on top of the cell and comparing the FTIR peak intensity with the pressure read by the pressure sensor). The change in the absorption intensity was measured over time, and the cell was observed to stay sealed with around the same initial pressure for 2 weeks. After, the pressure started to slowly increase until reaching atmospheric value, indicating that further developmental work was necessary to improve the durability of the sealing.

These results were encouraging as it showed a high potential for establishing a new and easy fabrication technique for Rb vapor cell production. However, more efforts necessary to optimize this process towards long-term hermetically-sealed cell solutions were not possible due to time and resource constraints. Several steps can be taken towards process optimization, starting with a further investigation into the metallization and soldering materials for **(1)** minimum leaching and enhanced wetting of the metallization by solder and **(2)** elimination of contamination by solder flux residues.

Following these results, the solder-sealed cells were not used for lamp characterization experiments. Hermetic Rb cells, with geometries suitable for lamp development, could be fabricated using the anodic bonding technique. Hence, these anodically bonded Rb cells were used for lamp characterizations and the list of fabricated cells are reported in the following section.

3.4 List of fabricated cells used as light sources

Table 3.4: The list of microfabricated cells used in this research and their properties.

Cell reference number	Rubidium content	Buffer gas type	Buffer gas pressure (mbar)	Discharge gap length (mm)
CN0	No Rb	Argon	70	2
CN1, CN2	Nat. Rb	Argon	70	2
CN3	Nat. Rb	Argon	30	2
CN4	^{87}Rb	Argon	30	2
CN5	Nat. Rb	N_2	100	2
CN6	Nat. Rb (several μL)	Argon	70	2
CN7	^{87}Rb	Argon	15	0.5
CN8	^{87}Rb	Argon	15	2
CN9	Nat. Rb	N_2	150	2
CN10	Nat. Rb (several μL)	Argon	30	2
CN11	Nat. Rb	Argon	2	2

In order to develop a Rb DBD lamp-cell, first a hermetically sealed Rb vapor cell is fabricated after which the electrodes are deposited on the external cell walls for drive and plasma ignition. The list of Rb vapor cells that have been developed using the anodic bonding process described in 3.4.2 and used in this research are mentioned here in Table 3.4. All cells have the same lateral dimensions of 1 cm x 1 cm with a discharge volume diameter of 5 mm.

Following the discussion in section 3.1.2, the ideal buffer gas would **(1)** be inert to Rb, **(2)** have a low first ionization energy (IE1) and **(3)** have a low atomic diameter for a higher mean free path and electron acceleration. A low atomic diameter usually means a higher IE1 and hence a suitable trade-off between these conditions needs to be experimentally determined. And the ideal buffer gas pressure needs to be as low as possible to allow for higher ratio of Rb excitations for a given input voltage and temperature. 70 mbar of Argon has an acceptable trade-off between the above conditions, whose pressure is also suitable for a low-power breakdown and high Rb line output operation and hence a good test gas for the first prototype (CN1). Based on experimental observations, reported in chapter 5, the pressure values for the other cells were chosen later for further optimization of the lamp's power consumption and the output light stability.

3.5 Electrode deposition for Rb DBD cells

For the planar cell, external and parallel layers of electrodes are most efficient in coupling the energy to the electrons in the cavity by maximizing electric field lines through the discharge volume. The electrodes are to be deposited on both the top and bottom Pyrex layers outside the cell after it is sealed with Rb and buffer gas. However, the exact geometry and type of electrode material that would be best for the Rb light source needs to be experimentally determined (reported in section 5.3) for which three different electrode materials were tested in this study with each material having its own respective deposition technique. If a specific cell was deposited with a certain electrode material, it was reused again for testing with other electrode materials only after the complete removal of the original electrode layer.

1) Indium solder: Indium solder circular pre-forms, with a thickness of hundreds of microns, were used as electrodes by depositing it on the Pyrex layers manually using heat and solder guns (illustrated in Figure 3.18). The main reason for choosing this material is because of its excellent wetting properties with glass. The second reason being the geometry of the electrodes can be easily modified using a solder iron. The main disadvantage of this material though is that the melting point of this solder is 156.6 °C which could cause problems when the discharge lamp temperature reaches near this value. Even if the cell is not heated thoroughly to this temperature, there could be some local heating phenomena which could possibly rupture the electrodes locally and cause changes in the energy coupled to the discharge volume. This melting point however allows the easy removal of the electrode when a heat above 160 °C is applied. The limitation of this deposition technique is that the geometry is not very accurate with high surface variations as it is manually done, increasing the

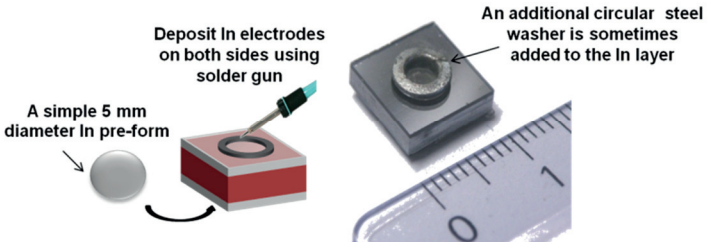

Figure 3.18: Illustration of In solder deposition.

probability of field inhomogeneities. So this electrode material is more useful for basic tests and development but not for long-term commercial solutions.

2) Aluminium thin film: 200 nm thick Al thin films were tested as electrodes by depositing a thin layer of Al atoms on the Pyrex using the evaporation technique (Figure 3.19). A source of Al is heated and evaporated to produce Al vapor inside a vacuum chamber which then is allowed to condense on the unheated Pyrex layer of the cell. Using custom-built shadow masks, any electrode pattern with a resolution of few hundreds of microns was possible. The advantage of this technique is that the deposition is more reliable and the geometry is highly accurate with very low surface variations as compared to the Indium solder. This reduces field inhomogeneities and hence possible performance variations within different sets of cells. When a high-melting solder alloy like Sn-Ag or Sn-Pb-Ag (with a small amount of Indium mixed for better wetting) is used for connecting the deposited electrodes to external power, the melting point of the solder interface is more than 200 °C and hence does not limit the lamp operation for a wider temperature range. However, its main limitation is that it is opaque and hence cannot be patterned directly on top of one side of the discharge gap for optical output. Although, due to its smooth surface, a blanket bottom Al electrode would act as a mirror during lamp operation, increasing the photon yield output through the top. The Al deposition on Rb cells was performed by technicians of the CSEM cleanroom in Neuchâtel.

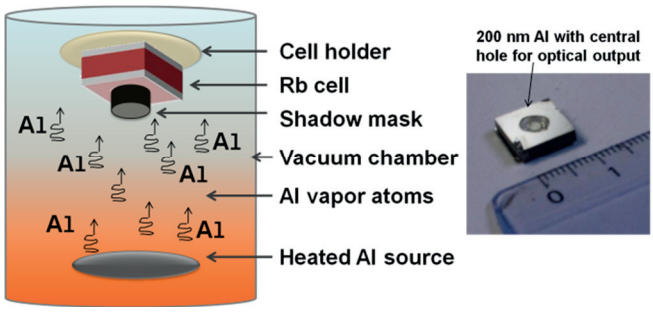

Figure 3.19: 200 nm Al thin film electrode deposited using the evaporation technique (concept schematic).

3) ITO thin film: ITO thin films were tested as electrodes by coating a 100 nm thin film top electrode through sputtering or physical vapor deposition (basic concept shown in Figure 3.20). By igniting a plasma discharge near an ITO target, high energy particles are made to bombard the target to release the molecules as vapor that then condense on the top Pyrex layer of the cell. This electrode material is very interesting as it is conducting and has high transmission of more than 90% at 100 nm thickness. This allows for the electrode to the directly deposited over the discharge gap, hence maximizing the efficiency of field coupling. However, it has a non-negligible resistance (surface resistivity R_{sq} ~ 20 Ω/sq), increasing with the area and thickness of deposition. This additional resistance increases the power consumption of the light source but also helps in heating the cell. Hence, it is a good but not an obvious choice for the lamp design and has to be experimentally tested in terms of power consumption for different geometries to understand its performance metrics. The ITO deposition was performed at EPFL-PVLAB.

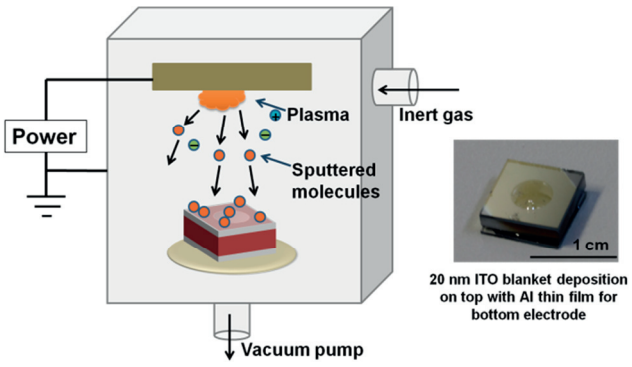

Figure 3.20: 100 nm ITO thin film electrode deposition by physical vapor deposition (concept schematic).

The details of the size and geometry of the electrode configurations used in this research are given in section 5.3.

Chapter conclusions

This chapter explained the design and fabrication of the miniature Rb discharge cell used in this research and the reasons for the choice of geometry: 1 cm x 1 cm x 0.3 cm to be compact and to integrate with the other components of the miniature DR clock. A buffer gas is needed for a low-power ignition and 70 mbar of Argon was chosen as the test gas as it had an acceptable trade-off between the atomic diameter and ionization energy properties and was in the suitable pressure range for a high Rb line output and low-power breakdown operation.

A low-temperature Rb hermetic sealing and dispensing technique was developed, in collaboration with LPM, EPFL, based on solder-sealing for fast and easy fabrication of Rb discharge cells. While this technique showed promising potential, due to time and resource constraints and due to the establishment of a successful Rb cell fabrication technique using anodic bonding at IMT, Neuchâtel, further efforts towards optimizing the solder-sealing technique were abandoned.

The concept of anodic bonding and the state-of-the-art fabrication process flow used for fabricating discharge cells were described. The full list of cells used in this research and the different electrode deposition methods used in this study were described. The next chapter will focus on developing the electrical drive circuitry to optimally power the lamp and achieve high power efficiency.

Chapter 4 Electrical drive circuitry for the miniature Rb DBD lamp

The design approach taken towards developing an electrical drive circuitry to achieve a desired output of 10 μW on a Rb D wavelength from the miniature micro-fabricated Rb DBD cell (cell list in section 3.4) at minimum power consumption is discussed in this chapter. To achieve the above-stated goal, external electrical power has to be first efficiently transferred to the miniature Rb DBD cell, which is later optimized for best results. An electric field changing polarity in the RF range (> 1 MHz and < hundreds of MHz), if applied across the chosen parallel-electrode configuration, would accelerate the scattered electrons resulting from random collisions, eventually leading to electron avalanches, breakdown and a sustained capacitively-coupled plasma (CCP) discharge (refer section 2.5). The gain in acceleration of the electrons is directly proportional to the strength of the applied field and for a given (p.d) and cell condition, a minimum value of breakdown field is required for a specific applied frequency. The idea here is to achieve this field strength with the lowest power consumption.

The necessary concepts involved in the rf drive circuit development for the DBD CCP cell is first discussed (in section 4.1) including the considered boundary conditions. The LC resonant drive circuit developed and optimized in this research is reported in section 4.2 where the appropriate LC components selection using a vector network analyzer, load impedance modeling in MATLAB and electrical circuit modeling and voltage calculations using PSPICE are discussed. The electrical equivalent model of the Rb cell is described in section 4.3, to understand the distribution of the cell impedance, the different power loss mechanisms and the magnitude of power that is coupled to the discharge gap. The modeling and results reported in sections 4.2 and 4.3 have also been published in the IEEE Transactions on Ultrasonics, Ferroelectrics and Frequency Control journal [128] and the Journal of Physics D: Applied Physics journal [129].

4.1 RF drive design concepts for a CCP discharge cell

In order to build a drive circuit to produce a high-intensity rf (>1 MHz and <500 MHz here) field across the discharge volume, the relevant concepts and the rf drive design requirements need to be understood first. The following sub-sections explain **(1)** the electrical power propagation model for the rf range considered in this research, **(2)** the description of the rf field applied across the discharge volume using the electrostatic approximation applicable in the low-rf (<tens of MHz) range and **(2)** the rf design elements and the structure of the full drive circuit developed towards achieving highly power-efficient operation.

4.1.1 Electromagnetic wave propagation model

For a simple DC or a low frequency AC (<1 kHz) field across two parallel plates, the conventional Kirchoff's voltage and current laws can be applied for analysis. However, they fail at higher frequencies where the electromagnetic wave propagation model, as explained by Maxwell's equations [130], describes the electrical behavior in a highly convincing manner. In order to understand this more clearly, an electrical field propagating in a direction (positive z-direction in a Cartesian co-ordinate system for example as shown in Figure 4.1) in free space is considered and can be written in a sinusoidal form as:

$$E_x = E_{0x}\cos(\omega t - \beta z)$$
$$H_y = H_{0y}\cos(\omega t - \beta z) \quad (4.1)$$

where E_x and H_y are the x-directed electric and y-directed magnetic field vector components and E_{0x} and H_{0y} are the constant amplitude factors in V/m and A/m in the respective x and y directions. These waves possess an angular frequency ω and a propagation constant β that defines the spatial extent in terms of the wavelength, λ, such that $\beta = 2.\pi/\lambda$. Classical field theory based on Maxwell's equations shows that the ratio between the electric and magnetic field components is defined as the so-called intrinsic impedance, Z_0, (or the characteristic impedance of free space) and is given by [131]:

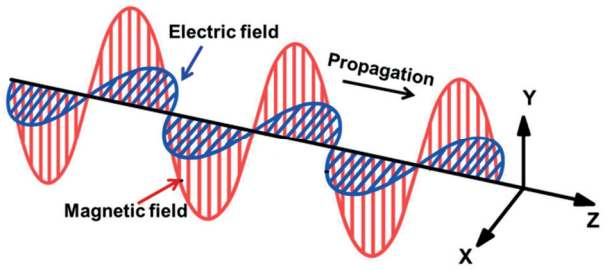

Figure 4.1: The schematic of the electromagnetic wave propagation model with the orthogonal electric and magnetic field components.

$$\frac{E_x}{H_y} = Z_0 = \sqrt{\frac{\mu}{\varepsilon}} = \sqrt{\frac{\mu_0.\mu_r}{\varepsilon_0.\varepsilon_r}} = 377.\sqrt{\frac{\mu_r}{\varepsilon_r}}\ \Omega \quad (4.2)$$

where μ and ε are the magnetic permeability and electrical permittivity of the material (through which the EM field is propagation) and are defined as $\mu = \mu_0.\mu_r$ and $\varepsilon = \varepsilon_0.\varepsilon_r$ with μ_0 and ε_0 being the absolute permeability and permittivity of free space [$\mu_0 \approx 1.26\text{x}10^{-6}$ H/m and $\varepsilon_0 \approx 8.85\text{x}10^{-12}$ F/m] and μ_r and ε_r are the relative values of the material. The field components, as observed are orthogonal to each other with both of them orthogonal to the direction of propagation. This is called the transverse electromagnetic mode or TEM and it is the dominant wave propagation mode in the RF range. There are other modes, such as, transverse electric and magnetic wave modes, which are of more relevance only at much higher frequencies - in the microwave and optical range, as the field vectors tend to no longer be orthogonal to the direction of propagation. The phase velocity, v_p, of this TEM wave can be given as [132]:

$$v_p = \frac{\omega}{\beta} = \frac{1}{\sqrt{\varepsilon.\mu}} \quad (4.3)$$

Substituting free space values in equation (4.3) gives the speed of light, c. Equation (4.3) is mentioned here only for understanding the fundamental property of the TEM waves used in this research and not necessary for any further calculations. Although, the electromagnetic model is described very briefly here, it can be noted that the electric field, with units V/m, can be understood as a normalized voltage wave while the magnetic field, with units A/m, can be understood as a normalized current wave. The power per unit area, P_{EM}, and the average power per unit area, $\overline{P_{EM}}$, transported by an EM wave at any instant of time is given by [132]:

$$P_{EM} = \frac{E.B}{\mu_0} \text{ and } \overline{P_{EM}} = \frac{1}{c.\mu_0}.E_{0x}^2.\overline{\cos^2(\omega t - \beta z)} = \frac{E_{0x}^2.c.\varepsilon_0}{2} \quad (4.4)$$

4.1.2 The electrostatic approximation

A simple model of the microfabricated Rb discharge cell (figure 3.15) as a parallel electrode, with dielectrics in between (Figure 4.2), is considered – the distance between the electrodes being 3 mm (2 mm gap + 2x0.5 mm dielectric layers). Now when an electromagnetic wave, changing polarity in the radio-frequency range, for example 10 MHz, is applied on one of the electrodes while the other is grounded, the wavelength of the applied rf is around 30 m. To accelerate the electrons and influence the breakdown efficiently, a high electric field/voltage is required and not a high current/magnetic field (refer section 2.5). Hence, in this case when the applied rf wave has a high characteristic impedance (high voltage to current ratio) and the rf wavelength is much higher than the discharge length, it can be approximated that the electric field is homogeneous across the discharge volume and dominant enough to neglect the effect of the magnetic field component. This is the electrostatic approximation and is sometimes referred to as the E-mode (electrostatic mode) operation in plasma reactors [133]. When the rf wavelength gets closer to the order of the discharge length, the effect of the magnetic field becomes non-negligible resulting in the transition to what is called the H-mode (electromagnetic mode) operation [133], [134]. Even higher frequencies (>several GHz) leads to the W-mode (wave mode) operation but is not discussed further here.

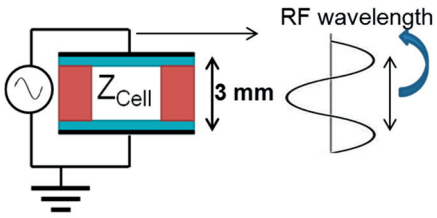

Figure 4.2: Simplified DBD cell model as a capacitive load with parallel-electrodes. The RF wavelength diagram is only for understanding and is not to scale.

As the first target frequency range is in tens of MHz, the electrostatic approximation is initially considered for developing the rf drive design.

4.1.3 RF input power options for driving the Rb lamp

A steady source of rf excitation with precise (±0.01 dBm) control over the power level and frequency is required for the Rb light source. A low-voltage, negligible-power (less than a mW) and accurate frequency 'signal' can be generated from, for example, an appropriate quartz oscillator which when supplied a DC voltage can produce an AC voltage signal of similar amplitude in the radio-frequency range. This generated signal has its own characteristic impedance defined by the ratio of the output voltage to the output current. Figure 4.3a shows the electrical equivalent circuit of a generic quartz oscillator operating in the fundamental mode and Figure 4.3b shows the two resonance modes of such an oscillator where the parallel resonance is preferred for its higher voltage output. Many driver concepts for DBDs exist [135], [136], [137] but almost all of them have been designed for high-power lamp emission purposes. The most power-efficient drive circuit is needed for the miniature lamp.

Using the simplified model shown in Figure 4.2, the rf drive design approach is explained starting from the ideal case for clear understanding. The cell, which is the load, is assumed to have an overall impedance, Z_{Cell}, and can be defined as, $Z_{Cell} = Z_R + j.Z_I$ where Z_R is the total real/resistive part of the impedance or the proportion of incident real power that will be absorbed and Z_I is the reactive part or the proportion of incident real power that would be

reflected. The equivalent model of the cell is explained in more detail in section 4.3. The typical voltage values for an rf electrical breakdown in mm-scale discharge gaps have been reported to be in the range of several tens of Volts to hundreds of Volts [138], [139], [140], [141]. Assuming V_{BR} is the breakdown voltage across the cell-electrodes for a given frequency, the power required for breakdown can be given as, $P_{BR} = V_{BR}^2/Z_{Cell}$. P_{BR} here represents the theoretical minimum power required for breakdown and would equal P_{abs} in equation (2.16) for an ideal capacitive load. That is, if the cell is considered an ideal capacitor (all cell dielectrics being ideal with no losses), the only power that is absorbed is by the electrons in the discharge volume (or Z_R = free electrons energy absorption factor). However, obviously an ideal capacitive load does not exist and Z_R here represents all the losses in the cell (including dielectric resistive losses). Z_{Cell} can be thought of as a few pF capacitive load or a 50-100 kΩ impedance load until it is redefined more precisely in section 4.2.

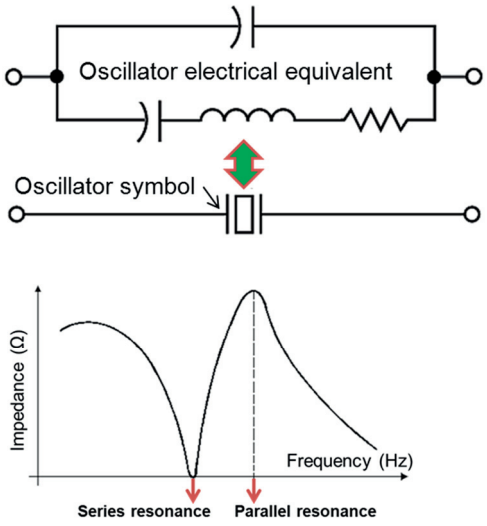

Figure 4.3: (a) Electrical equivalent model of a crystal oscillator with the (b) typical impedance spectrum versus frequency.

So, in the most ideal case, an external input in the order of 100s of Volts from a crystal or such oscillator with a characteristic impedance of Z_{Cell} would only require one DC supply and a minimal transmission line (with the impedance of the transmission line, $Z_{Tr} = Z_{Cell}$) leading to lowest total power consumption (Figure 4.4). If P_{tot} is the total power supplied, it would be, $P_{tot} = P_{BR} + P_{Tr\_loss} + P_{Osc\_loss}$. P_{Tr_loss} represents the amount of real power lost in the transmission line and P_{Osc_loss} includes the damping and conversion losses of the oscillator. However, such a direct application is not possible yet due to the various issues with oscillators such as lowering of the output quality factor and increasing frequency instabilities [142] which severely limits the maximum output voltage (usually less than 5 V). Also, it is almost impossible to find an oscillator or a transmission line/cable with the exact characteristic impedance of the cell. Such a transmission line can be custom-developed but requires a major effort and is outside the scope of this research. Hence, a voltage amplification stage along with appropriate transmission lines and impedance matching circuits are required between the oscillator and the cell-load (Figure 4.5).

Figure 4.5 illustrates the rf drive design schematic showing the required modules for achieving the desired V_{BR} across the cell-electrodes. The total circuit can be split into two stages: the input stage and the LC stage [143], as shown in the figure, for easier understanding. The input stage consists of an oscillator with an impedance of Z_{Osc}, whose output rf voltage signal is connected to an amplifier [144] through a transmission line (with impedance Z_{Tr1}) and an impedance matching

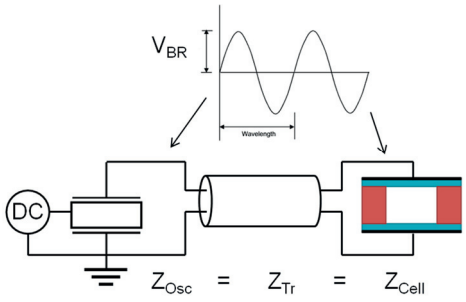

Figure 4.4: Schematic of the ideal rf input power supply to the Rb cell-load.

circuit. This impedance matching circuit is a combination of L, C and R components to match or convert the source impedance to the load impedance for maximum power transfer (discussed in section 4.1.4). The amplifier output also has similar transmission lines and matching circuits to have a 10s of Watts capacity output with characteristic impedance, Z_{in}. The LC stage consists of the Rb cell-load and the appropriate LC-impedance matching circuit to maximize voltage transfer from Z_{in} to Z_{Cell}.

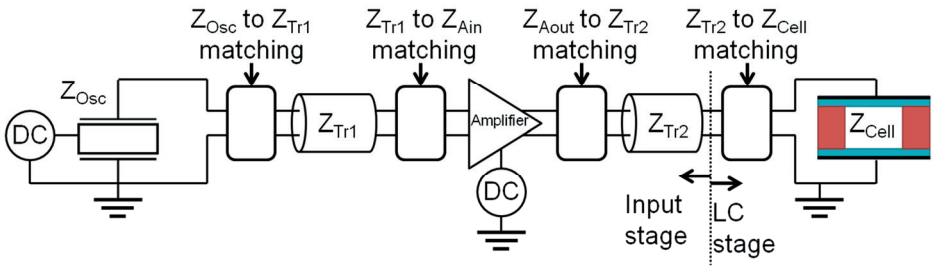

Figure 4.5: The rf drive design schematic showing the input and LC stage of the drive circuit.

In this research, only commercially available rf components and instruments that are suitable for the drive circuit design were used for the input stage design, which practically limits the choice to only 50 Ω impedance instruments, connectors and transmission lines (coaxial cables). This is mainly because of two reasons: **(1)** The main focus here is to characterize the Rb discharge cell performance and identify the optimum operating parameters of the LC stage (Figure 4.5) of the rf drive circuit for a given input stage - as the input stage can later be custom-redesigned independently based on the identified ideal operating frequency, cell-impedance and power conditions for stable optical pumping applications. **(2)** Building a complete custom rf circuitry which includes a low-noise low-loss rf amplifier with an output capacity of several Watts, and characterized transmission lines with an optimized cell-specific characteristic impedance requires a huge effort (probably several years of study and development) and is outside the scope of this research. Hence, the drive circuit developed in this research is optimized for a 50 Ω input impedance system and is discussed further from section 4.2. However, as much higher power efficiencies can be achieved by custom-designing the complete rf circuitry, some discussions in this regard are included in the next sub-section which describes the rf drive elements.

4.1.4 Elements of RF drive design

The relevant elements and their respective definitions used for building and modeling the rf drive circuit for the Rb DBD lamp are discussed in this section. The electrical behavior of conductors and LC components when operating at the rf range are described including their equivalent electrical circuits that are used for voltage and power computations reported in section 4.2 and 5.4. The impedance matching technique, based on which the LC drive components are selected and the LC stage drive circuit is developed in this research, is described in the last sub-section.

Transmission lines

A transmission line is simply an electromagnetic wave carrier. As it can be seen from equation 4.2, the intrinsic impedance of an electromagnetic wave is inversely related to the electrical permittivity of the material through which it is propagating. In air, the impedance is

almost 377 Ω. However, metals have a very high, almost infinite, relative electrical permittivity (value of the real part is one but very high value of the complex part). Hence, typically metals are used as transmission lines to easily transfer high power. The equivalent circuit model of a transmission line is shown in Figure 4.6. The characteristic impedance of a transmission line can be defined as:

$$Z_{Tr} = \frac{V(x)}{I(x)} = \sqrt{\frac{R + j.\omega.L}{G + j.\omega.C}} \tag{4.5}$$

While the L and C are reactive components that do not absorb any power, the transmission power losses are due to the R and G resistive components of the transmission line impedance. R is the resistance and G is the conductance, both dependent on the resistivity of the transmission line material and the increasing skin depth effects when carrying a high-frequency field. The typical resistance and loss functions of different materials, geometries and lengths can be found here [131]. Using this model, it is possible to develop transmission lines with the specific Z_{Tr} required for the application by choosing the right materials and geometry to achieve lowest R and G values for minimum losses. Here, in this research, all transmission lines and connectors (except the wires connecting the cell to the matching circuit in the LC stage) are standard 50 Ω BNC-type cables and connectors.

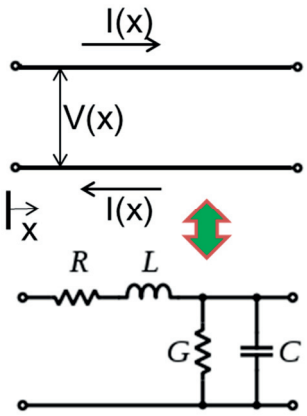

Figure 4.6: The transmission line and its characteristic impedance model.

High-frequency capacitor

A parallel-electrode capacitor configuration with surface area of the electrodes, A, and distance of separation, d, (given that the shortest lateral dimension of the electrode is always greater than d) filled with a material with relative electrical permittivity, ε_r, will have a capacitance C, given by [119]:

$$C = \frac{A.\varepsilon_0.\varepsilon_r}{d} = \frac{A.\varepsilon_0.(\varepsilon_r^{'} - j.\varepsilon_r^{''})}{d} \tag{4.6}$$

Ideally there is no current flow between the electrodes. However at high frequencies, the dielectric materials become lossy mainly due to the frictional losses of oscillating dipoles. The relative permittivity is thus defined by the complex function: $\varepsilon_r = \varepsilon_r^{'} - j.\varepsilon_r^{''}$ where ε_r'' denotes and contributes to real or resistive losses in the dielectric material and ε_r' contributes to the reactive power stored in the dielectric. The ε_r'' and ε_r' values for different materials can be obtained from the loss tangent value, δ, of the material which has the relation: $\tan\delta = (\omega\varepsilon_r^{''} + \sigma)/\omega\varepsilon_r^{'}$.

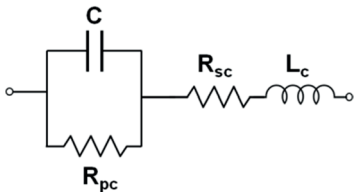

Figure 4.7: Electrical model of a high-frequency capacitor with parasitics.

A real capacitor operating at the rf range has many non-negligible parasitic components which need to be modeled to accurately establish the voltage and power losses of the capacitive

components. Figure 4.7 shows the electrical model of a real high-frequency capacitor with the non-negligible parasitic resistances, R_{sc} and R_{pc} (representing the current leakage and dielectric frictional losses) and a series parasitic inductance, L_c (representing the increasing reactive power storage loss with higher frequency and the component self-resonance effects). The impedance of the capacitor, Z_c, can be derived and given as:

$$Z_c = \frac{R_{pc}}{1 - j.\omega.C.R_{pc}} + R_{sc} + j.\omega.L_c \tag{4.7}$$

Regarding the selection of rf capacitors for the drive circuit, it is important to identify the ones with the lowest DC series resistance for lower power losses. Higher the value of the capacitance, lower its self-resonance frequency and hence the upper frequency limit within which it can be used for becomes lower. However, its reactance becomes lower, making R_{pc} power losses more insignificant with increase in the value of capacitance.

High-frequency inductor

A coiled wire when supplied a current in the RF range, exhibits **(1)** an inductance due to the resistive force created by the time-varying magnetic field lines in proximity, **(2)** a frequency-dependent wire resistance primarily due to the skin and proximity effects, **(3)** a DC series resistance representing the DC wire resistance and **(3)** a parasitic capacitance arising due to the conductive wires in proximity with each other. These components constitute the electrical equivalent circuit model of a high-frequency inductor which is shown in Figure 4.8.

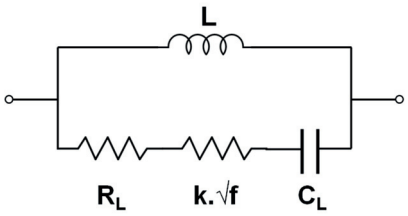

Figure 4.8: Electrical model of a high-frequency inductor with parasitics.

The skin effect is the tendency of the applied rf current in a wire to become unevenly distributed within the wire volume such that the current density is largest near the surface and decreases towards the centre [131]. This happens due to the opposing eddy currents induced by the changing magnetic field resulting from the rf current. This causes the effective resistance of the conductor to increase at higher frequencies with the decreasing effective wire cross-section available for conduction or skin depth (the depth from the surface effectively used for current flow). For thin-wire single-turn RF coils and axial inductors (used in this research), the proximity effect can almost be considered negligible and the frequency dependent resistance can be considered to be directly proportional to √f due to the dominant skin effect [Skin depth is inversely proportional to √f for a given material]. The impedance of the high-frequency inductor, Z_L, can be given as:

$$Z_L = \frac{R_{sL} + k.\sqrt{f} + j.\omega.L}{1 + \omega.C_L - j.\omega.C_L(k.\sqrt{f} + R_{sL})} \tag{4.8}$$

Selecting the appropriate rf inductors for the drive circuit is based on some considerations: **(1)** High power (several Watts) lamp operation requires inductors with high power/current rating. Higher the current rating, higher is the resistivity of the conductor leading to higher resistive losses. **(2)** The component has to be as small as possible as the target is a portable application.

(3) Higher inductance value means higher intensity of the time-changing magnetic field effects from the rf current through the conductor in proximity leading to higher skin effect (and proximity effect) resistive losses. Hence, lower inductance values are always preferred. For example, if a high inductance value is needed, using several lower value inductors in series (adding up to the desired value) is usually more power-efficient than one inductor of the desired value.

Impedance matching circuits

High power transfer efficiency from the rf power supply to the Rb-cell load is required for a low power operating lamp. In the following paragraphs, the principles behind identifying this maximum power transfer and efficiency operation for a given input radio-frequency power are discussed. When power needs to be transferred from one stage (source) to another (load), the maximum possible power, for a given input voltage, can be transferred when the impedance of one stage is the complex conjugate of the other. It is not the same as maximum power transfer efficiency, which, for stages with purely real/resistive impedances, increases with the ratio of load to source impedance. Figure 4.9 shows the general trend of these two behaviors for a given input voltage [145].

As voltage transfer is the primary interest, it can be seen from the figure that the maximum real voltage transfer is possible with a higher load to source resistance ratio with the maximum power transferrable getting significantly reduced. This result is useful only for situations where the real part of the load impedance is dominant and is representative of the total load impedance (for possible matching circuits in the rf input stage design). However, for a largely reactive load, such as the Rb cell, the load impedance is dependent on the applied frequency and hence the maximum voltage transfer condition also becomes frequency dependent and is described below.

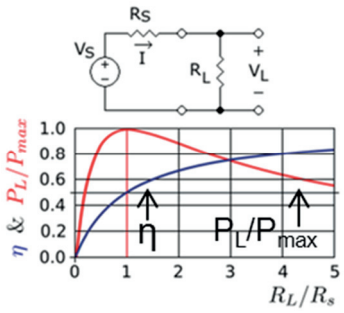

Figure 4.9: Maximum power transfer and maximum power efficiency versus impedance for a purely real load [145].

Considering a simplified circuit (Figure 4.10), where the parallel electrode-Rb cell model shown in Figure 4.2 is considered as an ideal capacitive load, the impedance/reactance of this cell can be given as: $X_{Cell} = -1/j.\omega.C_{Cell}$ (C_{Cell} is the capacitance of the cell in pF and ω is the applied angular drive frequency in radians/s). It is connected to a 1V RF-AC voltage source with fully-inductive impedance $X_L = j.\omega.L$ (L is the inductance in Henries). The voltage across the cell can be given by $V_{Cell} = I.X_{Cell}$. Now it can be seen that, when the values of L, C and ω have been chosen such that $\omega.L = 1/\omega.C_{Cell}$, the total impedance of the circuit becomes zero resulting in infinite current (in the ideal condition). And, X_{Cell} is still finite resulting in an infinite increase in V_{Cell}. But all real circuit components/cells have a non-zero resistive component which limits it to a large finite value. This frequency is the series LC resonant frequency, f_r, given by $f_r = \frac{1}{2\pi\sqrt{LC}}$ [$\omega = 2.\pi.f_r$] and the voltage across the cell can be given by:

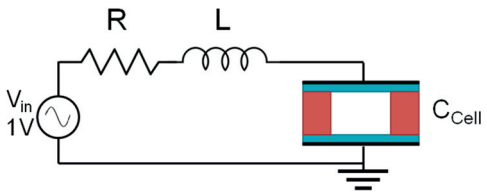

Figure 4.10: A simplified LC series resonant circuit with the capacitive cell load.

$$V_{Cell} = Q.V_{in} \quad (4.9)$$

where Q is termed the quality factor of the LC circuit. The quality factor is defined as the ratio of power stored to the power dissipated at the resonance frequency. This equals the ratio of one of the reactive impedances to the parasitic resistance of the LC-R circuit, R, and can be derived as:

$$Q = \frac{\omega L}{R} = \frac{1}{R}\sqrt{\frac{L}{C}} \quad (4.10)$$

Hence, for a largely reactive load, it can be seen that the maximum voltage transfer (equation 4.9) happens at the series LC resonance condition and is governed by the Q value for the chosen f_r (it must be noted that V_{Cell} in such circuits will almost be fully reactive). For the output rf drive stage development in this research, this reactive load impedance matching/voltage amplification concept is used. Equation (4.10) is a simplified definition of the Q factor for an ideal LCR circuit and the real circuit quality factor, Q_{rp}, calculation requires the modeling of all the circuit parasitic components, shown in the next section 4.2.

4.2 LC resonant drive circuit for the Rb DBD lamp

Following the discussion in the last section, a series LC resonant circuit design approach was chosen for driving the Rb DBD lamp. The rf input power is supplied by a 50 Ω rf amplifier (discussed in 4.2.1) and the LC stage consists of the Rb-cell load connected to LC components to equal a 50 Ω impedance load at the series resonant frequency of operation. The following sub-sections explain the rf input drive stage used and the LC-stage circuit developed for driving the Rb lamp-cell at different frequencies over a wide range (2-500 MHz).

4.2.1 Drive circuit - input stage

The input stage of the drive circuit (as mentioned in Figure 4.5) refers to the rf power source and amplification circuitry used for driving the LC stage: the impedance-matched Rb cell-load. As explained earlier, all the chosen components in the input stage have a 50 Ω input/output real impedance. The rf sinusoidal voltage signal was generated using an HP 8642A (0.1-1050 MHz range) signal generator with a 50 Ω output impedance. This was connected to the 50 Ω input of an rf amplifier (two amplifier modules used: (A1) 1059-BBM1C3KFL model, 30 W minimum CW power, (A2) 1028-BBM1C3KAJ 10 W minimum CW power, both models: 1-500 MHz, Class AB, Empower RF Systems) through a 50 Ω coaxial cable with appropriate BNC connectors on both ends. The amplifier has its own internal impedance matching circuit to give out a 50 Ω output terminal which is connected to the forward terminal (50 Ω BNC coax) of an rf power meter with a dual-directional coupler (Rohde & Schwarz NRT power reflection meter with NAP-Z7 power head). The LC stage can then be connected to the rf power

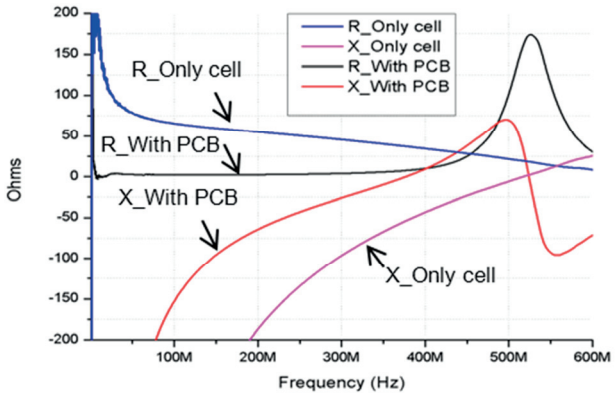

Figure 4.11: The measured impedance spectrum of the cell with and without PCB (Figure 4.12) calibration showing its high capacitive reactance at frequencies <200 MHz.

meter's output terminal for driving the Rb cell-load after appropriate impedance matching. The photographs describing the complete drive circuitry and measurement setup can be found in section 5.1.

4.2.2 Drive circuit - LC stage

The LC stage, as illustrated in Figure 4.5, refers to the load stage that constitutes the series LC resonant circuit and the Rb DBD cell, as schematically shown in Figure 4.12. The LC components are represented as ideal components for easier understanding, however they have non-negligible parasitics as explained later in this section. The Rb DBD cell, after electrode deposition, is a capacitive load whose precise impedance needs to be determined for developing the electrical drive circuit for igniting rf discharges. The impedance spectrum (Figure 4.11) of a 70 mbar Argon filled Rb vapor DBD cell (CN1), with 5 mm diameter circular In bottom electrode and a 5.5 mm outer diameter and 4.5 mm inner diameter In ring top electrode, was accurately measured using a vector network analyzer (Agilent ENA 5071C) after necessary instrument calibration steps. The values measured by directly connecting the Rb cell electrodes to the BNC input of the vector network analyzer and the values measured through a BNC connection of the PCB when the chip was placed on its designated place (as shown in Figure 4.12) are shown in Figure 4.11. The cell-load was found to be almost fully capacitive at the tens of MHz frequency range with a capacitance value of around 1.2 pF and a total impedance of around 80 kΩ. Hundreds of LC drive circuits have been built for characterizing the Rb cell in a wide range of frequencies between 2 and 500 MHz, out of which 10 optimized drive circuits at relevant drive frequencies and the resulting data have been reported in this section.

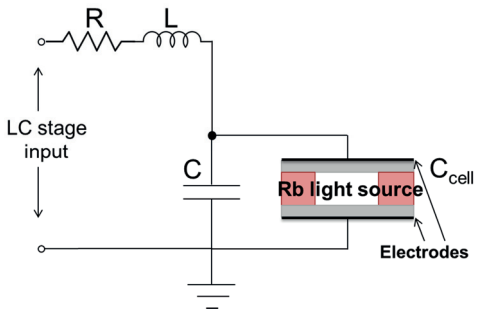

Figure 4.12: A schematic representation of the LC-stage and the series LC resonant circuit configuration.

LC components selection

The first test drive frequency was chosen to be 13.56 MHz since it is an ISM band and in the frequency range chosen for the first plasma ignition test (refer section 2.5). Now for maximum voltage transfer across the cell, a tunable inductor in series with the cell needs to be added as the source such that the inductive reactance is the complex conjugate of the cell impedance exactly at the resonant frequency, that is, 13.56 MHz. Also, as the output terminal of the input stage has a real 50 Ω impedance, an appropriate resistor needs to be added in the LC stage to equal the total impedance to a purely real 50 Ω load. For a 1.2 pF cell and 13.56 MHz drive frequency, the appropriate inductance value can be calculated to be around 950 μH. Such a high inductance typically has a self-resonance frequency at less than 10 MHz and hence cannot be used in this circuit (Some high-performance rf inductors in this inductance range could have their self-resonance beyond 15-20 MHz but will usually have a bad quality factor at the

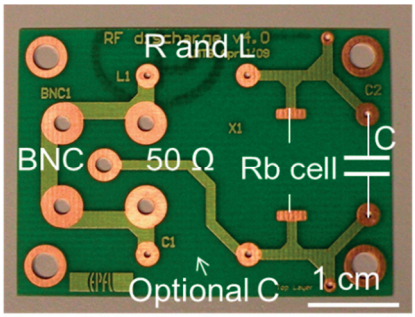

Figure 4.13: A photograph of the PCB for the Rb-cell and the LC stage components for impedance matching.

desired frequency). Higher inductance values also entail higher skin and proximity effects leading to higher resistive losses. In order to bring the required inductance value to an acceptable range, a tunable capacitor, with a higher capacitance than the cell-load, is added in parallel with the cell-load (can be seen in Figure 4.16 and Figure 4.18) to reduce the overall cell load reactance. For example, adding a 10 pF capacitor brings the cell+capacitor reactance from >80 kΩ to ~ 1 kΩ. This would now necessitate an inductance of around 12 μH for the desired reactance matching at 13.56 MHz, which is now in the acceptable range as it will not be limited by the component's self-resonance and it will also have a lower real impedance at this frequency due to relatively lower skin effects. This is the first step used for selecting the appropriate inductor and capacitor components for the LC stage. Now the exact values can be optimized for maximum voltage transfer for which the impedance of these components and the resulting circuit need to be measured first using the vector network analyzer (VNA) (high-precision LCR meters and impedance analyzers can also be used but additional calculation steps might be necessary depending on the instrument).

Single port load-matching using network analyzer

First, the Rb cell is placed and fixed on a PCB designed at LMTS for the LC stage circuit and cell (Figure 4.13). The PCB has circular copper pads on the top layer (and bottom layer) for soldering the component connections and thin copper interconnects in the insulated middle layer. Few mm long lengths of metals are used to solder-connect the top and bottom electrode, using In solder, to the PCB metal pad (Figure 4.15). A variable capacitor with a tuning range around the desired value (example tuning range: 1-45 pF) is selected and soldered on to the PCB to be in shunt with the cell electrodes. A variable inductor with a suitable tuning range is then soldered in series to the cell (a fixed inductor can also be used as only a minimum of one tunable LC component is necessary to accurately match the reactive impedance). The PCB has two input terminals: for the high-voltage rf and ground connections, designed for a 50 Ω BNC connector, although other high-frequency connectors can also be used.

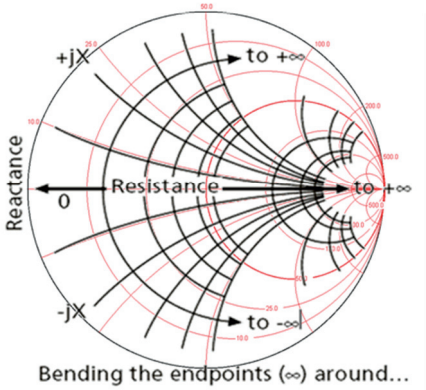

Figure 4.14: Concept of a Smith chart with the infinities of both resistance and reactance meeting at the centre-right of the circular plot. The 50 Ω load point is at the centre.

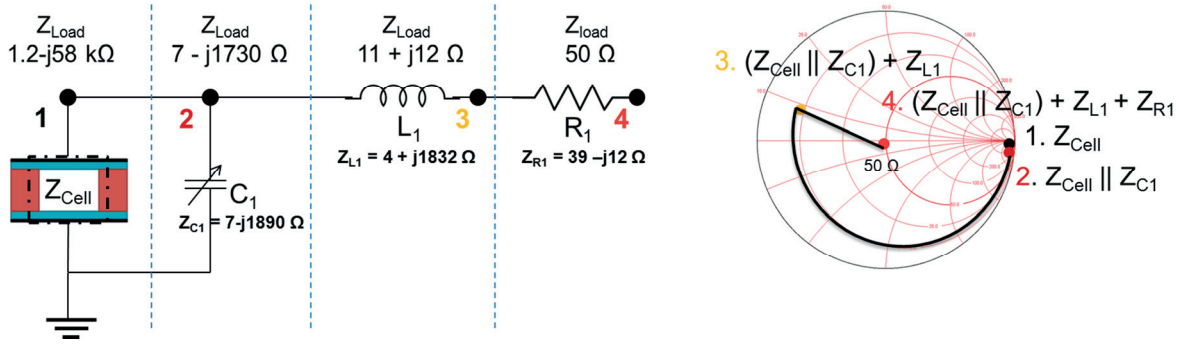

Figure 4.15: Impedance matching example showing the addition of components to match the cell-load to 50 Ω at 13.56 MHz and the corresponding change in the Smith chart (refer Figure 4.14)

Now this LC stage PCB with the BNC terminal is connected to one port of the network analyzer (after it is calibrated to a 50 Ω real impedance) to plot the impedance spectrum (scatter parameter s_{11}) of the circuit on a Smith chart. The concept of the Smith chart is illustrated in Figure 4.14. Figure 4.15 showcases the steps taken towards achieving a fully-matched LC load with an example components used for the drive operation at the desired radio-frequency. The impedance measured across the load with the addition of each component and the corresponding transition in the Smith chart, are shown to finally reach the target real 50 Ω load. Figure 4.16 shows the final LC stage PCB with all the components for 13.56 MHz drive operation.

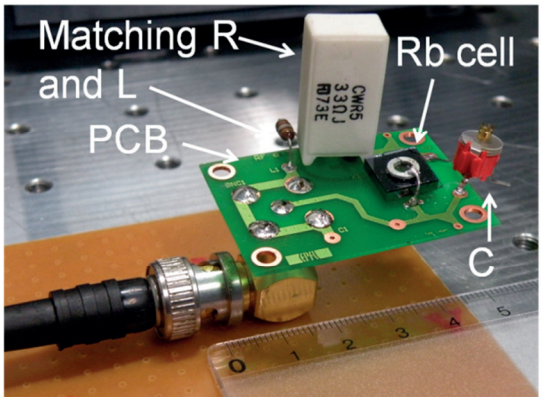

Figure 4.16: A photograph of the LC stage PCB with a Rb discharge cell (with In electrodes) fixed on to a PCB along with the soldered matching LCR components. It is impedance matched to 50 Ω at 13.56 MHz with an output BNC connection.

A log plot of the scatter parameter, s_{11}, versus frequency, obtainable from the network analyzer, would also give the measured reflection coefficient or an estimate of the LC circuit quality factor at the resonant frequency and it has the following relation with the circuit impedance, Z_{11}:

$$s_{11} = \frac{Z_{11} - Z_0}{Z_{11} + Z_0} \text{ or } Z_{11} = Z_0 . \frac{(1 + s_{11})}{(1 - s_{11})} \quad (4.11)$$

where Z_0 is the reference characteristic impedance (50 Ω here).

Optimizing LC component values

As seen from the previous sub-section, all components have non-negligible real and complex parasitic values at the rf range in the real world, as opposed to the 'ideal' component behavior. In more words, with increase in frequency, inductors and capacitors can have a high real impedance due to the DC resistance, inductive skin effects and the increasing significance of parallel parasitic resistances, and resistors can have a non-negligible capacitive or inductive reactance depending on the proximity effects of the conductor. When the cell impedance has a high capacitive reactance (which is the case for the microfabricated Rb cells at approximately <200 MHz), a series inductor is needed to compensate the high reactance of the cell. However, a separate resistor is not always needed to equate the LC stage to a real 50 Ω load, as the parasitic resistances of the LC components can be administered for this purpose. This is important because, resistors are obviously lossy, having many unwanted and

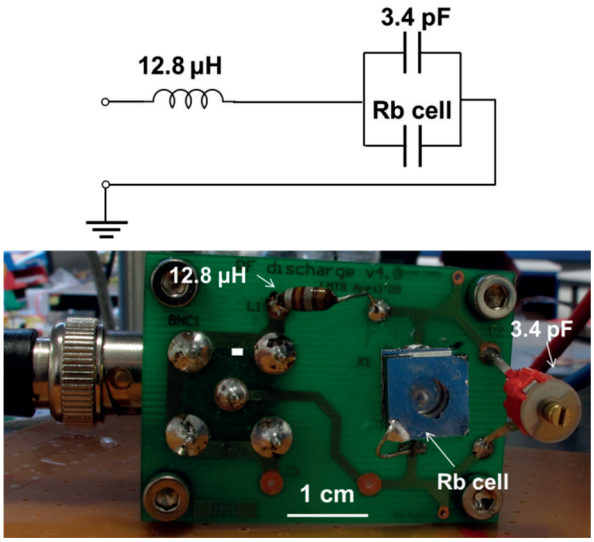

Figure 4.17: A 50 Ω matched LC stage with a Al electrode Rb cell and using only an series inductor and a parallel capacitor. A schematic of this circuit is also shown for reference.

uncontrolled parasitic reactances that lead to voltage losses and reduction of the maximum voltage transferrable across the cell-load. Hence, an LC stage circuit impedance-matchable to 50 Ω without the use of a separate resistor will be much more power-efficient. An example LC stage built on this idea using an Al electrode Rb cell (with 30 mbar Ar), is shown in Figure 4.17 which is 50 Ω matched for drive operation at 20.7 MHz. The only reason a resistor should be used is for achieving a very precise drive frequency of operation for testing. That is, if a very-specific lamp operating frequency is desired (better than 1 MHz precision), it is difficult or impossible to find the exact selection of LC components with the desired parasitics to achieve the 50 Ω matched load at the desired frequency. In such cases, an appropriate resistor needs to be added. The parasitics of the resistors were observed to add significant losses to the system and has a very weak dependence on the actual resistance value. Hence, if such a drive circuit is to be batch-produced in the future, it is better to custom-develop the LC components for a purely LC-based load operation at the desired frequency rather than use high-frequency resistors.

The one disadvantage of this design approach is that: when a separate resistor is used, most of the 50 Ω resistance in the LC-load is contributed by the resistor and hence most of the real power that is dissipated as heat is handled by the resistor. When a separate resistor is not used, the full 50 Ω resistance is distributed across the parasitic resistances of the LC components, which lead to higher heating of those components. The component that is primarily affected by this is the inductor due to its significant skin effect resistance. Hence, this approach would be useful only if the lamp operating power level is within the power-rating of the components and the higher component temperature does not induce unacceptable levels of shifts in the components' quality factor. Appropriate mini-cooling fans can also be improvised on these components to mitigate these effects.

At frequencies above 200-300 MHz, the cell-load is no longer dominantly capacitive that a capacitor component is needed in parallel with the cell to reduce the capacitive reactance. In such cases, only one appropriate inductor (with desired parasitics) in series with the cell is necessary to cancel the reactance and achieve the 50 Ω condition. Results obtained from these different drive circuits at different frequencies and their performance analysis are reported in section 5.4.

LC-load circuit modeling using MATLAB

In this sub-section, the impedance modeling of the LC-load circuit using MATLAB is described, which is used to extract all the parasitic of the LC components used. This is necessary for calculating the voltage across the Rb-cell using PSPICE (discussed in the next sub-section).

The forward terminal of an rf power meter (refer 4.2.1) is connected to the output terminal of the rf amplifier and the load terminal connected to the 50 Ω matched LC stage. This would allow the direct measurement of the power delivered to the LC-load, P_{in}, (measured forward power minus the measured reflected power) and hence the voltage, V_{in}, incident on the LC-load BNC input [$V_{in} = \sqrt{P_{in}.50}$]. However, the exact voltage across the cell is needed for optimizing the drive circuitry, and it can be determined by modeling the complete LC-load electrical circuit in the PSPICE simulation tool [146] and running an AC frequency analysis. To obtain good accuracy of the voltage values using PSPICE, exact values of all the parasitic elements associated

with the circuit components need to be known and modeled along with the component models in PSPICE as the simulation tool solves lumped-parameter models [The voltage across the cell cannot be measured accurately with a high-frequency high-voltage probe as any probe would strongly alter the circuit – the cell capacitance is only in the order of 0.5–5 pF, which is lower than the minimum input capacitance of high frequency probes (typically at least several pF)]. Some DBD breakdown potential determining techniques are listed here as references [147], [148].

In order to accurately model the components, the impedance versus frequency plots of the complete LC-load circuit and of each component is measured separately using the VNA (frequency range: 1-500 MHz, 1600 data points). When measuring separate components, the components were solder-connected to a 50 Ω BNC connector with a minimal transmission line and measured after calibrating the VNA for the BNC connector and the transmission line impedance compensation. The electrical impedance function (Z_{load}) of the LC-load circuit and the respective LC components are coded in MATLAB [149], where the high-frequency electrical equivalent models of LC components, as described in section 4.1.4, are considered to represent the respective drive components of the circuit. Considering an example LC circuit shown in Figure 4.18 developed for drive operation at 20.7 MHz, the impedance function of this circuit coded in MATLAB is:

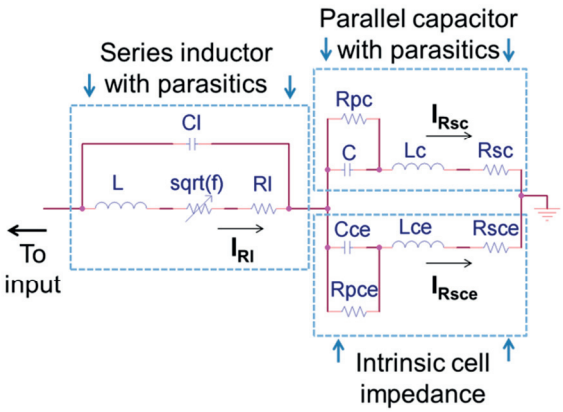

Figure 4.18: The electrical circuit model of the LC stage load based on which the impedance equation (4.12) is calculated. This load is connected to a transmission line with an inductance L_t in series and capacitance C_t in parallel.

Z_{load} = sqrt(real((i.*ω.*(Lt*1e-6)) + (((-i./(ω.*(Ct*1e-12))).*(((Rl + k.√ω + i.*ω.*(L*1e-6))./(1 + i.*ω.*(Cl*1e-12).*(Rl + k.√ω) - (Cl*1e-12).*(L*1e-6).*(ω.^2))) + ((i.*ω.*(1.242*1e-6) + (Rpc./((i.*ω.*(5*1e-12).*Rpc) + 1))).*(i.*ω.*(Lce*1e-9) + (Rpe./((i.*(ω.^2).*(Cce*1e-12).*Rpe) + 1))./((i.*ω.*(1.242*1e-6) + (Rpc./((i.*ω.*(5*1e-12).*Rpc) + 1))) + (i.*ω.*(Lce*1e-9) + (Rpe./((i.*ω.*(Cce*1e-12).*Rpe) + 1)))))))./((-i./(ω.*(Ct*1e-12))) + (((Rl + k.√ω + i.*ω.*(L*1e-6))./(1 + i.*ω.*(Cl*1e-12).*Rl - (Cl*1e-12).*(L*1e-6).*(ω.^2))) + ((i.*ω.*(1.242*1e-6) + (Rpc./((i.*ω.*(5*1e-12).*Rpc) + 1))).*(i.*ω.*(Lce*1e-9) + (Rpe./((i.*ω.*(Cce*1e-12).*Rpe) + 1))).*((i.*ω.*(1.242*1e-6) + (Rpc./((i.*ω.*(5*1e-12).*Rpc) + 1))) + (i.*ω.*(Lce*1e-9) + (Rpe./((i.*ω.*(Cce*1e-12).*Rpe) + 1))))))))).^2 + imag((i.*ω.*(Lt*1e-6)) + (((-i./(ω.*(Ct*1e-12))).*(((Rl + k.√ω + i.*ω.*(L*1e-6))./(1 + i.*ω.*(Cl*1e-12).*(Rl + k.√ω) - (Cl*1e-12).*(L*1e-6).*(ω.^2))) + ((i.*ω.*(1.242*1e-6) + (Rpc./((i.*ω.*(5*1e-12).*Rpc) + 1))).*(i.*ω.*(Lce*1e-9) + (Rpe./((i.*ω.*(Cce*1e-12).*Rpe) + 1))).*((i.*ω.*(1.242*1e-6) + (Rpc./((i.*ω.*(5*1e-12).*Rpc) + 1))) + (i.*ω.*(Lce*1e-9) + (Rpe./((i.*ω.*(Cce*1e-12).*Rpe) + 1)))))))./((-i./(ω.*(Ct*1e-12))) + (((Rl + k.√ω + i.*ω.*(L*1e-6))./(1 + i.*ω.*(Cl*1e-12).*(Rl + k.√ω) - (Cl*1e-12).*(L*1e-6).*(ω.^2))) + ((i.*ω.*(1.242*1e-6) + (Rpc./((i.*ω.*(5*1e-12).*Rpc) + 1))).*(i.*ω.*(Lce*1e-9) + (Rpe./((i.*ω.*(Cce*1e-12).*Rpe) + 1))).*((i.*ω.*(1.242*1e-6) + (Rpc./((i.*ω.*(5*1e-12).*Rpc) + 1))) + (i.*ω.*(Lce*1e-9) + (Rpe./((i.*ω.*(Cce*1e-12).*Rpe) + 1))))))))).^2) [ω=2.π.f_r] (4.12)

By curve-fitting the measured impedance plot versus frequency of the complete LC-load with the impedance equation of the circuit, such as equation (4.12), all the parasitic values of the elements can be extracted for voltage calculations in PSPICE. As it can be seen, the impedance functions, such as equation (4.12), are complex functions with many variables and hence the curve-fitting toolbox in MATLAB was used for extracting the fitting variables.

The steps taken towards reliably extracting the parasitic values of the circuit through curve-fitting are described here. For curve-fitting in MATLAB, the curve-fit equation (impedance function), the list of variables (component and parasitic values), their initial values and the expected minimum and maximum value of these variables are needed as input.

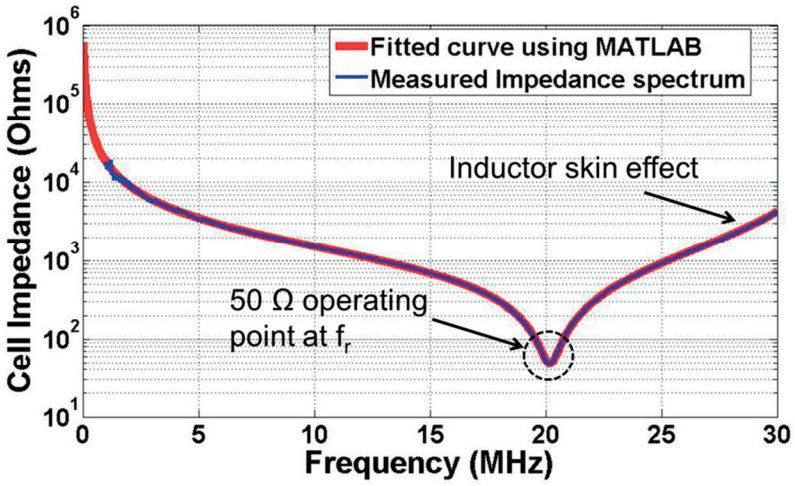

Figure 4.19: An example curve fit (red) using the equivalent circuit model for the recorded impedance spectrum data (blue) for a drive circuit operation at 20.7 MHz.

Seeing equation (4.12), from a general mathematical perspective, there are many more variables than defining equations; hence many possible sets of solutions would yield good fits. The set of parameters which yields the closest fit with the minimum R^2 value (coefficient of determination) is sought but does not automatically mean that it is the best solution and additional steps are needed to identify the correct solution set of variables. For this, the initial input range of all the component values needs to be as accurate as possible and this can be obtained from the impedance spectrum of the individual components measured using the VNA. Also, as the variables have values ranging between 25 orders of magnitude (10^{10} to 10^{-15}), the fitting function needs to be redefined such that the initial values of the variables are within few orders of magnitude, so that the fitting analysis is made error-free by not allowing the solver to reach the out-of-bounds conditions often, and to produce faster and accurate set of output variables within few orders of magnitude (the variables can be later appended with the relevant order of magnitude). The values of the LC components (not the parasitics) can also be extracted from curve-fitting the impedance spectrum of the individual components, and this would reduce the number of variables in the circuit impedance equation as the component values are known and can be inserted. In this case, it is important to include the compensation of the PCB parasitics in the VNA calibration.

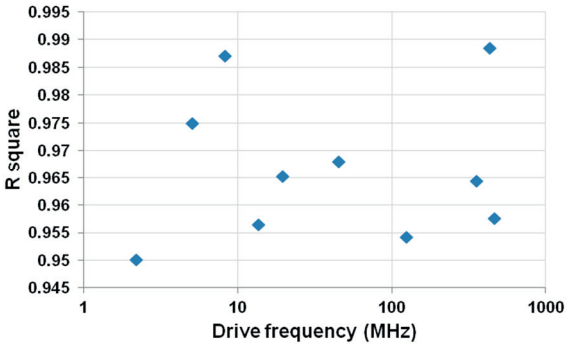

Figure 4.20: The R^2 values recorded from the respective curves fitted for various drive circuits with impedance matched LC resonant frequencies between 2-500 MHz.

The curve-fit using the circuit impedance equation on the measured impedance spectrum of an LC-stage circuit for impedance matching and drive operation at 20.7 MHz is shown in Figure 4.19 as an example. All fits were made sure to yield an R^2>0.95. Figure 4.20 shows the R^2 values obtained for the different fitting curves for some drive circuits developed over a wide frequency range.

The parameter values from the best fit were substituted in the PSPICE model (explained in the next page) of the same equivalent circuit to attain the modified quality factor: Q_{rp}, the voltage across the electrodes and the power transferred to the cell. It should be noted that these values can also be calculated algebraically but would be tedious and inefficient. This procedure is repeated for all other impedance matched LC drive circuits resonant at different frequencies and is used to calculate the breakdown voltage, V_{BR}, across the electrodes for the measured input breakdown power, P_{in}. Depending on the drive frequency and fit values, some parasitic components were sometimes ignored to make it easier to solve as they make a negligible difference to the output. For example, L_{ce} (typically ~30 nH), shown in Figure 4.18, can be ignored for low drive frequency circuits (<5 MHz) as it has a non-negligible effect on the impedance or Q_{rp} only at very high frequencies (>~100 MHz).

Cell voltage calculations using PSPICE

The complete set of parasitic and component values of the LC-stage circuit under analysis can be obtained as output from the MATLAB impedance curve-fit described earlier. Now the same electrical circuit used for impedance curve-fitting is used to design an electrical circuit model in PSPICE (OrCAD Capture) for calculating the voltage across the Rb-cell. Figure 4.21 shows the PSPICE model created to simulate the 20.7 MHz drive circuit and also output the s_{11} or impedance plot versus frequency. Standard parts were used for modeling the LCR components and the skin effect of the inductor was modeled as a GLaplace transform with Xform value: (1/k.(sqrt(S/2.π)). Using an AC analysis simulation and choosing the appropriate frequency range and the number of points per decade, the model is first verified by reproducing the impedance spectrum of the LC-stage in PSPICE (s_{11} circuit) and comparing it to the measured impedance (the voltage values marked numerator and denominator in Figure 4.21 correspond to the impedance). After verification, the voltage difference markers are placed across the modeled cell (C_{ce}) for an AC analysis versus frequency. Figure 4.22 shows the plot of this voltage (V_{Cce}) versus frequency. V_{Cce} here directly reflects the Q_{rp} value. This is because a 1 V AC input supply is used and Q_{rp} is the voltage gain/amplification from the input voltage to the load – or the ratio of the voltage across the cell to the input voltage ($Q_{rp} = V_{Cce}/V_{in} = V_{Cce}/1 = V_{Cce}$). Hence, the Q_{rp} values can be obtained similarly for all the other drive circuits in the 2-500 MHz frequency range and the voltage across the cell, V_{Cell}, can thus be calculated by substituting $Q=Q_{rp}$ in equation (4.9). Figure 4.23 shows the Q_{rp} values observed for

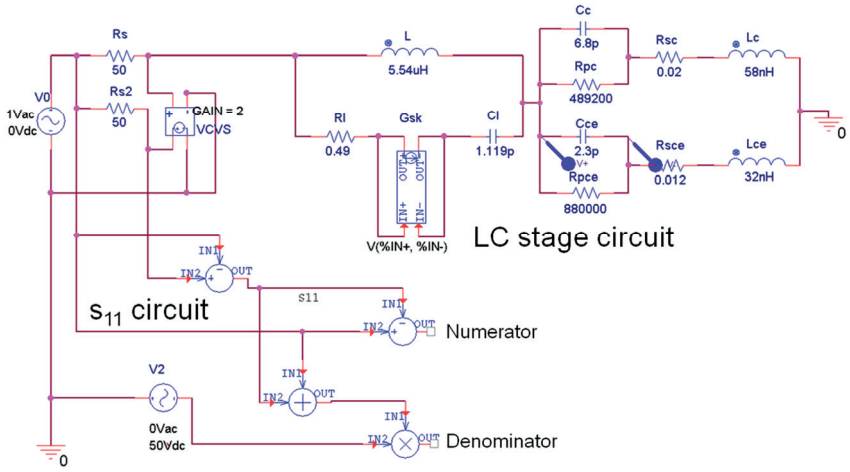

Figure 4.21: An example PSPICE circuit for the 20.7 MHz drive circuit showing the s_{11} plot and LC stage circuit parts and the voltage markers.

different drive circuits using cell CN3 with Al electrodes. It is also compared with the theoretical Q values obtained using equation (4.10).

The observed reduction in the quality factor (voltage amplification factor) with frequency is mainly due to the reducing cell impedance with frequency. The voltage across the cell roughly scales according to equation (4.12), which can be derived from equations (4.9) and (4.10).

$$V_{Cell} = \sqrt{\frac{P_{in}.L}{R.C}} \qquad (4.12)$$

For a given input power and load resistance, V_{Cell} reduces with a decreasing series inductance or an increasing total capacitance and vice versa. As the cell capacitive reactance reduces with increase in frequency, the series inductance value used also reduces to maintain zero-reactance matching. This trend contributes to the decrease in the Q_{rp} at higher frequencies. For drive frequencies approximately less than 50 MHz, a capacitor is connected in parallel (in most cases) to the cell to reduce its capacitive reactance to accommodate an inductor with an acceptable value (<few hundred μH for lower resistive losses and heating effects). This capacitance value, however, decreases with higher frequency with the parallel capacitor no longer needed for frequencies >70 MHz. This trend contributes to the increase in the Q_{rp} with increase in frequency. However, the decrease in inductance (950 μH at 2 MHz to 15 nH at 464 MHz) is orders more than the decrease in capacitance (55 pF at 2 MHz to 1.2 pF at 464 MHz) with frequency and hence the overall behavior is as observed in Figure 4.23.

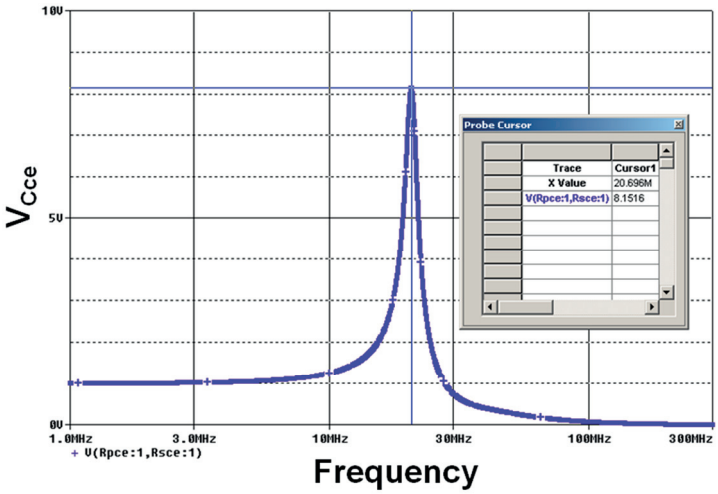

Figure 4.22: The plot of the voltage across the cell versus frequency and $V_{Cce} = Q_{rp}$.

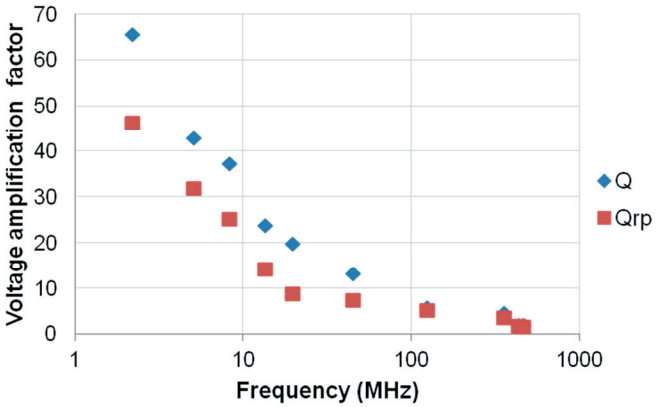

Figure 4.23: The plot of Qrp versus frequency for impedance matched Rb-cell CN3 with Al electrodes.

Alternative drive design - high-voltage RF transformers

An alternative solution to impedance-matching circuits for the LC stage design is an RF transformer [150]. The transformer works on the standard voltage transformer principle: $V_s.N_p = V_p.N_s$ where V_p is the input voltage on the primary winding which has N_p number of turns and V_s is the induced voltage on the secondary winding which has N_s number of turns. For a loss-less transformer, if an impedance Z_s is connected to the secondary winding, it appears to the primary circuit to have an impedance of $(N_p/N_s)^2.Z_s$. For a Rb cell load $Z_s = Z_{Cell}$ and the

ratio of N_p/N_s can be chosen to get Z_p value closest to Z_s for high power transfer to the cell. Z_p is the impedance of the primary winding which is the primary DC resistance and input capacitance. High-voltage high-frequency (up to 50 MHz) RF transformers (Communication concepts, RF400 model, figure) with different turns' ratios were tested for the Rb lamp drive but were found to be unsuitable and highly power inefficient when compared to the LC-matched circuits. This is because **(1)** the transformers were found to have high resistive losses at >8 MHz range of operation, **(2)** the transformers could only achieve near-impedance matching conditions which lead to a lot of reflected power and losses due to heating and (3) adding LC components to the secondary load for more accurate $Z_s=Z_p$ matching was still highly power inefficient compared to the LC-matching circuits. Hence, RF transformers were considered unsuitable and are not discussed in more detail in this report.

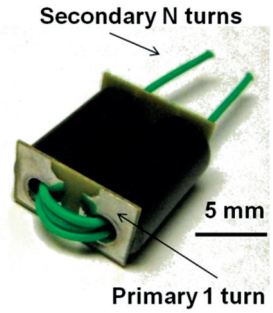

Figure 4.24: A high-frequency RF transformer for driving cell voltage.

4.3 Electrical modeling of the Rb DBD lamp

Power consumption must be minimized for the Rb DBD lamp to be used in a portable application. The previous section discussed about how the voltage across the cell and hence the power incident on the cell can be calculated from externally measurable parameters. Now, the main goal of this section is to electrically model the microfabricated DBD light source to understand where the power is dissipated, and hence ultimately predict light output for a given lamp cell, and circuit within an rf range of 2–500 MHz. Table 4.1 shows the list of different power and voltage parameters along with their electrical notations used in this report.

Table 4.1: List of electrical notations of the different powers and voltages used in this report.

Parameters	Total input power	Power coupled to the electrodes	Power coupled to the gap	Power absorbed by the gap	Total power consumed by pyrex layer	Power lost in pyrex layer	Power lost in Si layer	Power lost in the drive circuit
Notations	P_{in}	P_e	P_g	P_{abs}	P_{py}	P_{pyloss}	P_{siloss}	P_{LCloss}

Parameters	Optical power of the discharges	Optical power on the Rb D line	Voltage across the gap	Voltage across the dielectric	Voltage across the pyrex layer	Voltage across the silicon layer
Notations	P_{op}	P_{op_RbD}	V_g	V_d	V_{py}	V_{si}

The externally measurable parameters are power delivered by the amplifier, the drive frequency and the impedance of the cell. We seek to determine the power that is coupled to the discharge gap (P_g), to determine the actual electrical to optical power efficiency of the cells, and understand what fraction of power is dissipated in the discharge gap, the dielectric layers and the matching circuit. The model described below has as output P_g and P_{op_RbD} as a function of externally measurable parameters.

The drive frequency and the discharge gap conditions primarily control the discharge behavior. Under conditions when the electron oscillation amplitude, A_e, given by:

$$A_e = \frac{e.E}{m.\nu_m.\omega} \tag{4.13}$$

(where E is the electric field across the gap, m is the electron mass, ν_m is the collisional frequency with momentum transfer and ω is the drive frequency) is well below half the discharge gap length, d/2, the breakdown is diffusion controlled occurring mainly due to the oscillation of electrons with the applied electric field inducing momentum transfer collisions with other entities at a frequency, ν_m [30]. While there can be many possible electron energy distribution functions resulting in breakdown, a simplifying assumption is considered: after a diffusion-controlled electrical breakdown and at a relatively low mean electron temperature range (less than the first ionization energy of the gas atoms), the total optical discharge power is directly proportional to the mean electron temperature in the discharge gap. As the applied rf power is too fast in switching polarities to be considerably absorbed as kinetic energy by the heavy ions in an rf cycle, it is almost fully absorbed by the electrons in the simplified case and hence the mean electron temperature of the gap will be directly proportional to the rf power coupled to the gap [As the ionization and excitation processes depend more on the number of electrons in the high energy tail of the electron energy distribution (electrons with energies higher than the respective ionization and excitation potentials), the proportionality constant is in turn directly proportional to this local population density (refer section 2.2.3)]. Therefore, the real power absorbed in the discharge gap, P_{abs}, can be given by equation (2.16) and is equal to the total kinetic energy (KE) gained by the electrons over time.

Assuming the optical power is proportional to the mean electron temperature implies a constant ratio between the total optical power, P_{op}, and the calculated discharge gap power, P_g, for different input conditions (drive frequency considered here) with the same optical output power (at the A << d/2 regime and for the same gas type). However, when the amplitude A >> d/2, many electrons are lost to the walls and hence, some energy in the gap is distributed or lost to the dielectric walls adding to drift losses. For this case, we expect a lower ratio of P_{op}/P_g since the effective P_g available for conversion to P_{op} is $P_g – P_{Driftloss}$. Thus, using these conditions, we have developed functions which can estimate the efficiency of power coupled to the discharge gap, $\eta = P_g/P_{in}$ (P_{in} - total power to load), total optical power, P_{op}, and the Rb D line optical power P_{op_RbD} for a given set of input parameters: **(1)** gas type, **(2)** pressure, **(3)** discharge gap length, **(4)** cell materials – relative permittivity, **(5)** drive frequency and **(6)** drive and cell parasitics. These functions are limited to cell temperatures lesser than the Rb red mode transition temperature or the Rb self-absorption temperature (section 3.2.1).

For realizing these functions, an equivalent electrical model of the cell was developed (shown in Figure 4.25) to calculate P_g, the power lost from P_{in} to P_g and the mechanisms responsible for the losses. The first step was to calculate the voltage across the electrodes, V_e, for a given input rf power, where $V_e = Q_{rp}.V_{in}$ with $V_{in} = \sqrt{(P_f - P_r).50}$ for a 50 Ω load where $P_{in} = P_f – P_r$ and P_f and P_r are the electrical forward and reflected powers to the load.

The input power value, P_{in}, is fully real with a zero reactive component as the input current and voltage are fully in phase due to the (50 + j.0) Ω resistive load at f_r. However, the cell is a capacitive load (with the current leading the voltage by 90◦ in an ideal capacitor) which hence

absorbs almost only reactive power but some of this power is lost as real power losses due to the polarization of the dielectric layers. This can be calculated using equation (4.6) where the complex relative permittivity of the dielectric couples with the complex reactive power incident on the cell to yield real resistive losses (equation 4.14). Most of the real power is still dissipated in the matching circuit (P_{LCloss} in equation 4.15 where ESR is the equivalent series resistance) because of the low $R_{cell}/R_{circuit}$ ratio (at f_r) and with V_e and P_e values known, the power lost in the dielectrics and the Si walls can be calculated. The total power lost in a dielectric (for Pyrex and Si) can be given by:

$$P_d = \frac{\omega.V_d^2.A.\varepsilon_0.\varepsilon_r^{"}}{d} + j.\frac{\omega.V_d^2.A.\varepsilon_0.\varepsilon_r^{'}}{d} \tag{4.14}$$

$$P_{LCloss} = \Sigma((\text{ESR of component}) \times (\text{I through component})^2)$$
$$= I_{Rl}^2.(R_l + k.\sqrt{f_r}) + I_{Rsc}^2.R_{sc} + I_{Rsce}^2.R_{sce} \tag{4.15}$$

The intrinsic cell impedance is modeled as a lumped parameter model for the hermetically sealed Rb cell (with silicon walls and Pyrex thickness: 0.5 mm), the schematic of which is shown in Figure 4.25. The capacitances, C_{Py} and C_{Si}, of the respective Pyrex and Si layers an be derived from the equation (4.6). The respective relative permittivity values (ε'_r and ε''_r) of Pyrex and silicon can be substituted to get the respective power loss functions, P_{Py} and P_{Si} whose real part is the power lost on polarizing the dielectrics and the imaginary part is the power stored. Typical loss tangent values for Pyrex and silicon at room temperature and low frequencies (<100 MHz) are 0.003 and 0.005 [151]. The gap capacitance, C_g is defined using (4.6) where ε''_r of the gap (ε''_{rg}) can be derived from the power dissipated in the gap equation (2.16) as:

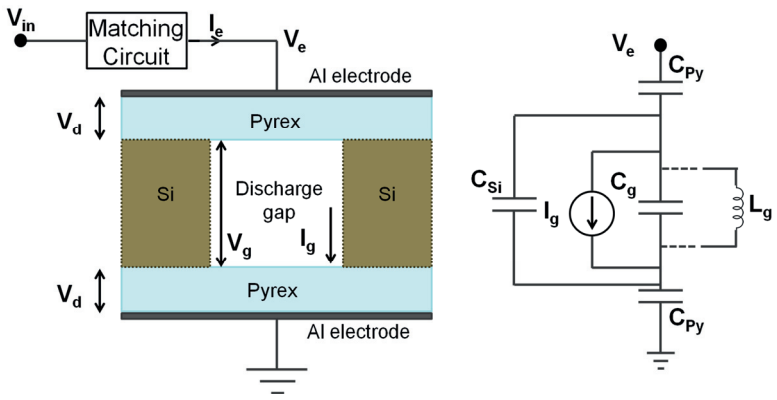

Figure 4.25: Cross-sectional view of the microfabricated Rb light source with circuit notations. On the right, equivalent circuit of the Rb light source (without matching circuit) with the discharge current modeled as a voltage-controlled current source, I_g. L_g is the parasitic inductance induced in the gap after electrical breakdown.

$$\varepsilon_{rg}^{"} = \frac{n_0.V.e^2}{2.\nu_m^2.A_g.m.d.\varepsilon_0} \tag{4.16}$$

where A_g is the surface area of the gap walls and $\varepsilon'_{rg} \approx 1$. The power coupled to the discharge gap can be given by:

$$P_g = P_e - 2.P_{Py} - P_{Si} \quad \text{where} \quad \text{Re}(P_g) = P_{abs} \tag{4.17}$$

The optical power (400-1000 nm range), P_{op}, is defined as:

$$P_{op} = k_g(P_g - P_{Driftloss}), \; [P_{Driftloss} = 0 \text{ for } A<d/2 \text{ and } P_{Driftloss} > 0 \text{ for } A \geq d/2] \tag{4.18}$$

where k_g is the electrical to optical power (400-1000 nm range) conversion factor in the gap for a specific gas type. For a given k_g, it would be possible to calculate P_{op} using equation (4.18) and the experimentally observed k_g values for Argon is reported in section 5.4.3.

To calculate P_g at and after breakdown, the plasma discharge was modeled as a voltage controlled current source (VCCS), current: I_g, which is a function of the voltage across the electrodes, V_e, following the approach of Liu et al, and of Fang et al. [152], [153], shown in Figure 4.25. Several other models have been reported in the literature [154], [155], [148] including a dynamically varying resistance or capacitance but this VCCS model was chosen as it has some advantages including having a constant discharge gap capacitance (for a given discharge gap condition) and avoiding time variation definition conditions of the dynamic resistance or capacitance. $P_{Driftloss}$ is not quantified in this report but only conceptually acknowledged to analyze observed results in section 5.4.3.

Considering C_{Py} is the capacitance of the Pyrex substrates (Figure 4.25) and C_g is the discharge gap capacitance in the Rb cell, I_g – the discharge current in the gap, I_e – the external current to the electrodes, V_e – the voltage across the electrodes, C_{Si} – capacitance of the Si wall and neglecting L_g, it can be derived that:

$$I_g(t) = (1 + (2.(C_g + C_{Si})/C_{Py})).I_e(t) - (C_g + C_{Si}).dV_e/dt \tag{4.19}$$

The value of L_g (Figure 4.25) can be calculated by experimentally observing the difference or shift in the resonant drive frequency upon plasma ignition and using the circuit impedance equation (model in Figure 4.18) to match the corresponding value of L_g to the measured shift.

To calculate the voltage across the discharge gap, V_g, the memory effect has to be taken into consideration. Memory effect or memory charges are the additional charges present on the dielectric surface from previous drive half-cycles, apart from the free charges reaching the dielectric during the rf drive half-cycle [155]. If $V_d(0)$ is the voltage difference at time t=0 of an rf cycle, created due to the memory charges for the first and second cases respectively, and T is the time period of one rf cycle, then it can be derived that [152], [156],

$$V_d(0) = \frac{-1}{2.C_{Py}} \int_0^{T/2} I_e(t).dt \tag{4.20}$$

Equation (4.20) is applicable only after the charge accumulation reaches a steady state after the first several breakdown cycles as $V_d(0) = 0$ for the first breakdown cycle. The voltage across the discharge gap, including dielectric losses and charge accumulation on the dielectric surface now is:

$$V_g(t) = V_e(t) - 2.V_{py}(t) = V_e(t) - \frac{2}{C_{py}} \int_0^t I_e(t).dt - 2.V_d(0) \tag{4.21}$$

Using (4.21), (4.19) and (4.6), the power coupled to the discharge gap, P_g, can be derived as a function of the input power P_{in} to attain the power coupling efficiency:

$$P_g / P_{in} = (P_{in} - P_{LCloss} + P_e - 2.P_{Py} - P_{Si}) / P_{in} = (V_g.I_g) / P_{in}$$

$$= \frac{C_g}{50}.\left(\frac{Z_{ce}}{Z_c + Z_{ce}}\right)^2.\left(Z_{ce} - 2.X_{Py} - \frac{V_e.Z_{ce}}{4.C_{Py}.\omega}\right).\left(\frac{C_{Py} + 2.(C_g + C_{Si})}{2.C_{Py}.(C_{Si} + C_g)} - \omega.Z_{ce}\right) \quad (4.22)$$

where Z_{ce} is the impedance of the lamp-cell (Figure 4.25), X_{Py} is the reactance of the Pyrex layer and the impedance of L_{ce} is considered negligible. The real part of P_g is the power available for absorption in the discharge gap and it can be seen from equation (4.22) that the drive frequency and the cell material/impedance primarily decide the efficiency of total power coupled to the gap. Using the Rb vapor partial pressure function (function of T – cell temperature in K and p_{bg} is the buffer gas pressure in mbar [157]), the emitted power on the Rb D line from the discharge gap can be given by:

$$P_{op\_RbD} = 10^{\left(7.2 - \frac{4040}{T}\right)}.P_{op} / (0.75 * \rho_{bg}) = 10^{\left(7.2 - \frac{4040}{T}\right)}.k_g.(P_g - P_{driftloss}) / (0.75 * \rho_{bg}) \quad (4.23)$$

Hence, for a given set of input conditions, the power loss functions (equations 4.14, 4.15, 4.18, 4.22) would help identifying and modifying the appropriate parameters to reduce losses (results discussed in section 5.4.3). Also, using equation (4.23), it would be possible to calculate the expected output Rb D light from a low-pressure dielectric barrier discharge light source. The experimentally observed values of k_g for three buffer gases are reported later in section 5.4.3, which can be used in equation (4.18) to calculate P_{op}. This model can also be generalized and applied to any other such DBD lamps and drive circuits to calculate the efficiency of power coupled to the discharge gap.

Chapter conclusions

The relevant and necessary rf design concepts for developing a compact and power-efficient Rb DBD lamp drive circuit were identified. This is the first reported capacitively-coupled miniature Rb light source and series LC resonant drive circuits were developed for driving the lamp at various frequencies between 2-500 MHz. High voltage amplification could be achieved across the lamp-cells using these developed rf circuits, which were impedance matched to 50 Ω at the desired frequencies for maximum power transfer to the lamp-cells.

The electrical model of the DBD lamp was developed to calculate the voltage and power coupled to the discharge gap for characterizing the lamp-cells in terms of power consumption for various p.d and electrical input conditions. As these parameters cannot be measured directly using high-voltage probes, an impedance model of the lamp-cell and drive circuit was modeled in MATLAB followed by PSPICE circuit simulations to calculate the voltage and power coupled to the lamp-cell. These electrical models help understand the different power loss mechanisms and the voltage distributions across the cell, which are useful for power optimization purposes. The next chapter reports on the various results obtained from the plasma ignition and operation experiments starting with the explanation of the drive and measurement setup.

Chapter 5 Electrical and optical characterization of the Rb DBD lamp

The observed performance of the developed miniature Rb DBD lamp, by varying different input variables (electrical power and frequency, electrode material and geometry, cell pressure and temperature) within an identified range of interest, and using different electrical and optical experimental characterization techniques, is reported in this chapter. The main purpose of these characterization experiments is to observe the primary parameters: electrical power consumption and optical power stability of the Rb lamp, as a function of these input variables, and identify the minimum operating power conditions for the lamp when its output optical power characteristics can meet the double-resonance optical pumping application requirements.

First, the experimental test and measurement setup, including the input lamp drive and the various electrical and optical measuring instruments, used for the characterization analysis reported in this chapter, is described in section 5.1. Preliminary data showing an ignited and functioning Rb lamp at 13.56 MHz, including the recorded output optical spectrum of the lamp, is reported in section 5.2. Design optimization of the electrodes to achieve a high lamp-power efficiency by experimentally observing the lamp's performance for different geometries using In, Al and ITO materials (for a Rb cell with a given p.d), and the electrode geometries used in this research are reported in section 5.3. The observed electrical power consumption of Rb lamp-cells having different p.d conditions, for a specific electrode design, as a function of the input frequency (using different LC circuits with resonant frequencies varied between 2-500 MHz), is reported in section 5.4. The optical power and stability characteristics of the emitted Rb D lines for different input frequencies and cell conditions, and the observed DBD and rf-discharge dominant regimes (important for identifying the best lamp operating frequency and cell p.d value), are reported in section 5.5. The effect of temperature, rf input power on the light source performance and the observed red-mode transition and Rb self-absorption characteristics are reported in section 5.6. The lifetime and reliability characteristics of the Rb lamp, which are important for evaluating the feasibility of the lamp to be used in a potential atomic clock application, are experimentally analyzed and reported in section 5.7. An integrated Rb mini-lamp module with an LTCC cell heater and platform for the drive circuit developed for optical pumping applications in collaboration with LPM, EPFL is reported in section 5.8

Some of the results reported in this chapter have been published in the IEEE Transactions on Ultrasonics, Ferroelectrics and Frequency Control journal [128] and have been presented in the European Time and Frequency Forum 2011 & 2012, Transducers 2011 and the 2012 IEEE SIITME conferences and published as proceedings [158], [159], [129], [160].

5.1 Experimental test setup for Rb DBD lamp characterization

The experimental test setup and the apparatus used for electrical and optical characterization studies of the microfabricated Rb DBD lamp is described in this section. The test setup is illustrated schematically in Figure 5.1 and can be split into four sections for easier understanding: (**1**) rf drive – the input and the LC stage of the drive circuit (section 4.2) after impedance matching the LC-stage to 50 Ω using the VNA (Vector network analyzer) as discussed in

section 4.2.2, (**2**) temperature control – a cell heater with a temperature sensor and an external temperature control, (**3**) optical measurement – the devices and optics used for obtaining the necessary optical spectral data and (**4**) the read-out and feedback control interface – a PC (personal computer) with a control interface, which is connected to all measuring instruments for data recording and feedback control when necessary. The LabVIEW [149] program was used as the control interface in most cases where the necessary graphical VIs (Virtual Instruments) were coded for receiving, saving and sending data from/to the various instruments. In the next few pages, the specific instruments used and the important notes in each section are mentioned. There was an additional test setup realized in this research for continuous long-term (several months) monitoring of the Rb-lamp operation for understanding the lifetime and reliability aspects of the Rb-lamp (for the clock application) and the details of this setup is discussed in section 5.7.

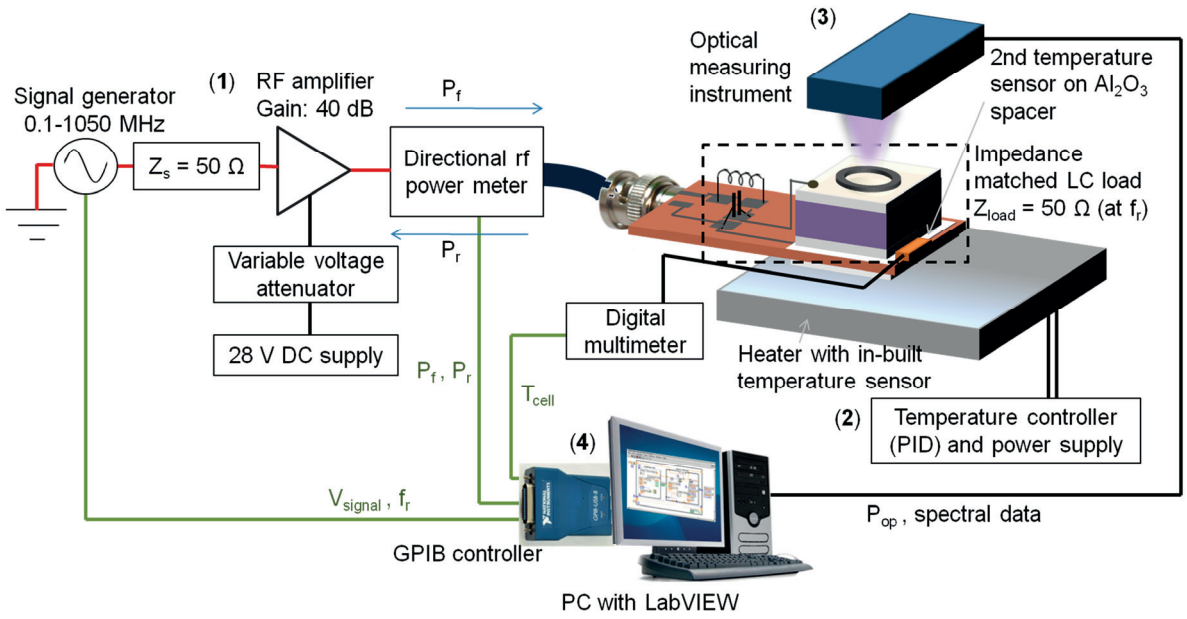

Figure 5.1: A schematic illustration of the test and measurement setup showing the four sections used for device characterization. The red lines are 50 Ω BNC coaxial cables, green lines are GPIB cables and black lines are standard laboratory cables/wires. The LC-stage was placed inside a electromagnetically shielded enclosure (Pomona box) or a Faraday cage whenever necessary.

(**1**) The rf drive setup, as shown schematically in Figure 5.1, consists of a 0.1-1050 MHz HP 8642A **signal generator** (set to 0 dBm/1 mW output at 50 Ω) connected to the input of an rf amplifier through a 50 Ω coaxial cable with BNC connectors on both ends (Agilent 33521A and 33220A signal generators were also used in some experiments when the required drive frequency was less than 30 MHz). A sinusoidal waveform was always chosen and appropriate BNC-SMA and BNC-N type 50 Ω adapters were used wherever required.

Two **rf amplifier** modules were used in this research, where one of them had to be selected for every experiment: (A1) 1059-BBM1C3KFL model, 30 W minimum CW power, (A2) 1028-BBM1C3KAJ 10 W minimum CW power, both models: 1-500 MHz, Class AB, Empower RF Systems. The amplifier was selected for an experiment based on availability and amount of power required. Both rf amplifiers require a 28 V DC and a minimum of 3 A supply for operation and appropriate laboratory bench-top DC power supplies were used for this purpose.

A good heat sink was attached to the amplifier and an additional cooling fan was placed on top of the heat sink to avoid the highly likely event of the amplifier shutting down due to over-heating. The output power of the amplifier was controlled by connecting a 0-5 V variable voltage attenuator (VVA) circuit module (a voltage stabilized manually tunable potentiometer) developed for conveniently adjusting the output power as desired.

The 50 Ω output terminal of the amplifier is connected to the forward terminal (50 Ω BNC coax) of a power sensor connected to an **rf power meter** with a dual-directional coupler (Rohde & Schwarz NRT power reflection meter with NAP-Z7 power head). The rf power meter (model NRT) is a high-precision instrument capable of measuring rf power between 0.3 mW – 2000 W within the frequency range: 200 kHz – 4 GHz. The NAP-Z7 power sensor/power head, which can detect rf power in the range of 0.05 to 200 W in the frequency range: 0.4 to 80 MHz, is connected to the NRT and used to measure the forward rf power, P_f, propagating from the amplifier (connected to input terminal: 1) to the LC-stage load (connected to output terminal: 2) and the power reflected back, P_r, from terminal 2 to 1. These measurements are used to calculate the total power delivered to the LC-stage which is $P_{in} = P_f - P_r$. The voltage incident on the LC-stage input can also be calculated from P_{in}, as $V_{in} = \sqrt{P_{in}.50}$. Another rf power meter DAIWA CN801H, which can measure the same parameters [0.1-2000 W detection range at 1-200 MHz], was also available but was only used when the NRT model was unavailable for an experiment. This is because of DAIWA's lower accuracy in read-out (analog needle meter) and the rf power data cannot be automatically recorded in a PC as it does not have any analog or GPIB output [GPIB = IEEE 488 standard bus].

The prepared impedance-matched LC stage is then connected to the rf power meter's output terminal: 2, for driving the Rb lamp. When the drive power level was more than few Watts and/or the drive frequency in the tens-hundreds of MHz range, the LC-stage load was either placed inside an **electromagnetically shielded** enclosure, a Pomona box (10.5x6.5x4cm^3 with a 2 cm x 2 cm rectangular drilled hole on the top cover- optical window) or inside a large custom-built Faraday cage along with the necessary measuring apparatus, to avoid any escape of radiation that could possibly jam with some radio-communication signals. The Faraday cage (40x30x30cm^3) has the grounded conducting top surface of the optical table as the base, copper mesh for walls (mesh hole size: 0.11 mm diameter) held by tall (40 cm) stainless steel rods (Thorlabs) fixed to the optical table and aluminum foil covering the top, and all spacing in-between the entities were covered with conductive tapes leaving a maximum gap spacing that is less than 1/20th of the drive wavelength.

(**2**) The purpose of the temperature control setup is to heat, control and monitor the temperature of the cell. With increase in the Rb cell temperature, Rb partial pressure in the cell rises leading to an increased Rb D line power during lamp operation (at temperatures below Rb self-absorption, section 3.2.1). And to maintain a stable output Rb D line power, the cell temperature needs to be kept constant or controlled and hence this setup (2) is needed for this purpose. The Rb-cell can technically be heated by simply placing it on a **temperature-controlled heater**. However, as a power-efficient and compact heater is typically driven by electrical currents, there needs to be an electrically insulating and yet highly thermally conductive layer, with a certain minimum thickness, between the lamp-cell and the heater surface. This is because the top and

bottom layers of the lamp-cell are conductive electrode layers which would electrically short with a conducting heater surface when placed on it. Even in the case of an electrically insulated heater surface, the bottom cell-electrode can capacitively-couple with the conductive heating elements present inside the insulated heater surface and hence a certain minimum thickness of this intermediate layer is required to reduce these effects (heating the lamp-cell by placing its side-wall on the heater would be highly power-inefficient and inconvenient for testing).

A 500 μm thick Al_2O_3 layer was chosen for this purpose as it was a suitable choice - an easily available material that meets the above requirements. Additional Al_2O_3 layers were added (stacked) whenever the capacitive interference from the heater was observed to be non-negligible and had to be reduced. A modified LC-stage PCB was developed by milling out a square hole in the PCB layer with a size slightly more than the lamp-cell lateral dimensions (1.2 cm x 1.2 cm) and attaching a custom-cut 1.3 cm x 1.3 cm Al_2O_3 layer (500 μm thickness) on the bottom of the PCB to seat the lamp-cell (as shown in Figure 5.2).

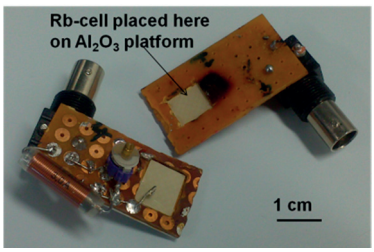

Figure 5.2: Test PCBs for powering and heating Rb-cells placed on a 500 μm Al_2O_3 layer.

Different sets of components have been used for the setup (2) and they are discussed here. Three different types of heaters have been used in this research, as shown in Figure 5.3. The heater H1 (machined by Idonus Sarl, a company based in Neuchâtel after the design was sent) is a 4 cm x 4 cm x 0.5 cm metallic hot-plate (resistive heater) that has a **Pt1000 temperature sensor** glued (using high thermal conductivity adhesive tape, 3M 8943, thermal conductivity: 0.9 W/m.K) to it. [Pt1000 is a temperature sensor, with a temperature coefficient of 3.85×10^{-3} $^0C^{-1}$ at 0-100^{0}C]. The heater is connected to an **external control box** (manufactured by Idonus Sarl) which uses PID feedback for temperature control and also powers the heater at 15 V DC (heating with a 230 V AC supply is also possible) with a heating capacity up to 250 ^{0}C. This heater was used for lamp heating and temperature control but was found to highly couple/interfere with the cell-electrodes leading to high power losses when the Al_2O_3 thickness was less than 3 mm in many cases. H1 was used as the cell heater for the long-term testing of the Rb lamp (reported in section 5.7) after placing a 3 mm thick Al_2O_3 spacer between the cell and heater surface. However, more compact and less interference ceramic heaters H2, and later H3, were explored and used for cell-heating during experiments in this research.

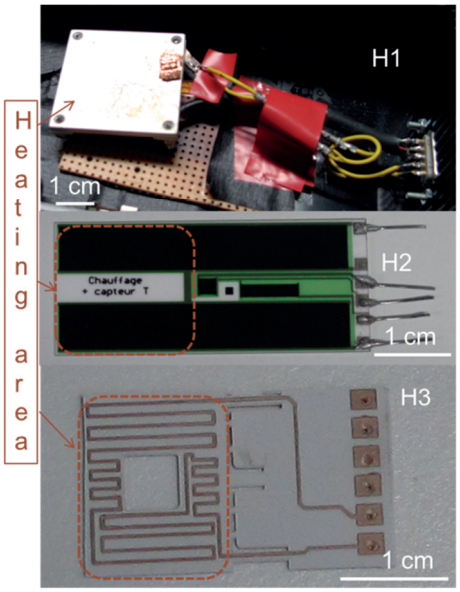

Figure 5.3: The heaters H1, H2 and H3 used in this research showing the active heating area on top of which the Rb cell with the Al_2O_3 spacer is placed.

Heaters H2 and H3 were developed at LPM, EPFL. H2 is a ceramic heater with a high resistance (~5 kΩ) DP 5092D paste patterned and deposited on top of an Al_2O_3 platform using screen-printing. The top metal layer is then over-glazed with a glass-ceramic for electrical insulation. High-temperature solders and SIL pins were always used for soldering connections to

the heater (Sn96Ag4 with melting point of 229 ^{0}C was used in this research). This heater when used with a separate Pt1000 temperature sensor placed on it, can be powered and temperature controlled using the same Idonus box used for H1. However, it would first require a re-calibration of the PID loop parameters in the control box for this specific heater for precise temperature control (up to 0.1^o C variations from the set temperature over time).

H3 is an LTCC (Low temperature co-fired ceramic) heater, developed by Fabrizio Vecchio, fabricated using the traditional steps of LTCC technology: laser cutting of green tapes, screen-printing, stacking and lamination, and firing. It has a serpentine design heater patterned as the top layer of a 4-layer LTCC stacked platform and a PTC sensor (DP 5092D paste, TCR = 4x10^{-3} ^{0}C^{-1}) patterned on the bottom. A 2 mm thick thermal foam (k = 0.044 W/mK at 25 ^{0}C) was attached to the bottom layer for thermal insulation and mechanical support. H3, like H2, can be powered and temperature controlled using the Idonus box when used with a separate **Pt1000 sensor** placed on the heater surface. If the PTC sensor must be used, the heater is powered by a DC power supply that is connected to a PC through a RS-232 or a GPIB port. The change in temperature corresponds to a change in resistance in the PTC that can be measured by a digital multimeter (Keithley 2000 used here) that is in turn connected to the PC (through GPIB here). By continuously running a PID feedback loop programmed in LabVIEW, it is possible to control the DC power to the heater (and hence control the temperature), as the PID loop can acquire the measured temperature and send the desired control voltage signal to the DC power supply indefinitely during every read/write cycle. Also, a temperature calibration (with the resistance) of the PTC sensor is required before it can be used as mentioned. In this research, the Pt1000 was used in almost all occasions except for the experiments shown in Appendix 2. A second Pt1000 sensor was also always placed on the bottom cell surface during experiments for recording the cell temperature by connecting it to a multimeter (in turn connected to the PC through the GPIB port) and measuring the change in resistance before multiplying it by the calibrated temperature function.

(**3**) The optical measurement setup includes the components and apparatus used to measure the optical spectral data from the Rb lamp for its performance characterization. Two main instruments: **(1)** an optical spectrometer, **(2)** an optical power meter, along with several optical components were used for the experiments. An Ocean Optics USB4000 **spectrometer** with a detection range of 390 nm -1090 nm, suitable for measuring the intensities of Rb D and the strong buffer gas discharge wavelengths was chosen for recording the optical spectra of the lamp. It has a wavelength resolution of around 1.5 nm which is sufficient for detecting the total Rb D line intensities but a much higher resolution (for example, a Fabry-perot interferometer) is required if the relative intensities of the 5^2P->5^2S(F=2) and 5^2P->5^2S(F=1) transitions need to be distinguished. The spectrometer has a 2 m fiber optic cable with a 600 μm aperture (SMA-905 connector) for optical detection – which is too small for collecting all the light from the 5 mm diameter optical window of the

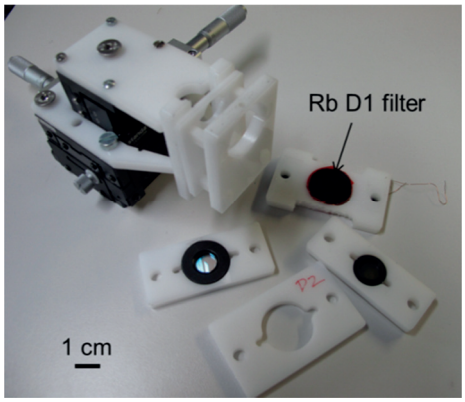

Figure 5.4: Some mounts and stages developed using milling POM and PTFE for the lamp experiments.

lamp. Hence, an additional collimating lens (COL-UV-30, Mikropack) with diameter 30 mm, focal length 30 mm, 200-2000 nm wavelength range with the SMA-905 connector was always connected to the end of the fiber optic cable for spectrum measurements from the lamp.

As the interesting optical power range from the lamp is within the hundreds of nW to few mW range and the Rb D lines are at 780 nm and 795 nm, an **optical power meter** (Ophir Nova II with an RS-232 port) with an optical power sensor (PD-300-BB), which has (a) a suitable aperture of 10 mm x 10 mm, (b) a flat spectral response from 400 to 1000 nm and (c) a detectable power range of 50 pW-8 mW, was chosen for measuring all optical power in this research. When the sensor/photodiode is placed directly above the optical window of the light source, the total optical power of the discharges (including Rb and buffer gas lines) within the 400-1000 nm can be measured. An optical narrow **bandpass filter** is placed between the power sensor and the light source to measure the optical power of specific wavelengths (Filters with narrow bandwidths (<12 nm) are required for effectively filtering out all other discharge lines occurring adjacent to the line of interest). Three such bandpass filters (all manufactured by Edmund Optics) with a 10±2 nm narrow bandwidth and 84% peak transmission (manufacturer specified information) were used in this research:

(i) to measure Rb D1 line power – a 795 nm filter with a measured transmission of 52% (calculated by measuring and comparing the intensities of the D1 line from an ignited Rb-lamp 1. with and 2. without the D1 filter between the spectrometer input). Additional data on measured transmissions of 60%, 50% and 10% transmission at 0°, 10° and 20° angles of incidence respectively (measured by Christoph Affolderbach at LTF, Neuchâtel using a 795 nm laser)

(ii) to measure Rb D2 line power – a 780 nm filter with a measured transmission of 55% (same technique used for (i) but with D2 filter). Additional data on measured transmissions of 64%, 46% and 3% transmission at 0°, 10° and 20° angles of incidence respectively (measured by Christoph Affolderbach at LTF, Neuchâtel using a 780 nm laser)

(iii) to measure the strongest Ar line (764 nm) power – a 766 nm filter with a measured transmission of 58% (using technique similar to (i))

Whenever required, the test setup is covered by a black cloth held by the stainless steel rods (used for the Faraday cage walls described in (**1**)) and this acts as an **optical cage** to remove all background light noise. A cardboard box with fully black walls was also used sometimes when such a shape was more convenient for the tests.

All optical components were positioned or clamped as needed using various **optical post assemblies** (made of anodized Aluminum or stainless steel and manufactured by Thorlabs) fixed on an optical table. Suitable XY and Z optical stages, and custom-built cage systems were used when position adjustments were required for measurements. As the presence of a metal too close (<5 mm) to the lamp electrodes was observed to highly interfere with the lamp operation, several **mounts** were custom-built by milling commercially-available POM (polyoxymethylene) or PTFE (Teflon or polytetrafluoroethylene) sheets (choosing the necessary thickness) with a CNC router machine available at LMTS. Some examples are shown in Figure 5.4, which includes mounts to hold the Rb D1/D2 filter milled out of a 6 mm thick POM sheet using the CNC

router. Many general parts were created by CNC milling, whenever it was necessary to realize desired optical assemblies in this research. POM is usually more sturdy and robust especially for long parts but had a reasonably low melting temperature (175 °C) while PTFE parts can withstand much higher temperatures (melting point: 327 °C) but not very stiff. Hence, PTFE was usually chosen for parts that need to be near the lamp-cell or heaters while POM was chosen for any other part.

(**4**) The signal generator, rf power meter and the multimeter measuring the cell temperature were connected using Agilent GPIB cables to a National Instruments GPIB controller that was in turn connected to a USB port of a PC. Necessary VIs with the appropriate VISA (Virtual Instrument Software Architecture) configurations were coded in **LabVIEW** to communicate with the instruments – read, write and save data in the PC. All data were made to save directly as spreadsheets. The number of points saved per instant of time depended on the number and type of tasks performed. The optical power meter and the spectrometer came with their own specific software, which were used to record their respective data.

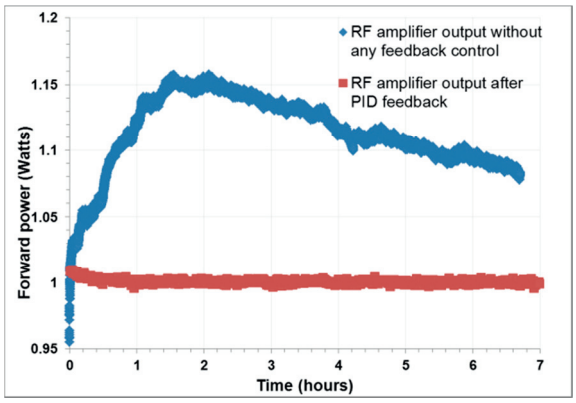

Figure 5.5: The output of the RF amplifier when set initially to 1 W output. It was controlled using a PID feedback loop through LabVIEW to avoid the observed drifts in forward power.

Whenever long-term (>hours) experiments were performed with the light source, the output rf power from the rf amplifier had to be feedback controlled to a constant value using a PID VI programmed and run in LabVIEW. This is because, the amplifier output was found to drift with time (Figure 5.5) irrespective of the load impedance and hence this **PID feedback** (with P_f as the input and set value) was needed to continuously control the voltage amplitude of the rf signal from the signal generator, to keep the input rf power to the LC-stage constant. Figure 5.5 shows an example of the long-term constant power set to 1 W achieved from the amplifier.

5.2 A functional miniature Rb DBD lamp

The test setup, as described in the previous section, was realized and made ready to drive an LC-stage load that has been impedance matched to 50 Ω at 13.56 MHz (section 4.2.2). After switching on the rf power supply and increasing the rf power, the Rb lamp (cell CN1 and Indium ring electrodes EL4, refer section 5.3) was ignited at 1.1 W of forward power and observed to emit 100 μW of total optical power when forward power was reduced to 650 mW. This research had the unique opportunity to report the first ever Rb discharge to be ignited in a miniature or microfabricated Rb cell (Figure 5.6) [128]. The output spectra of the lamp recorded

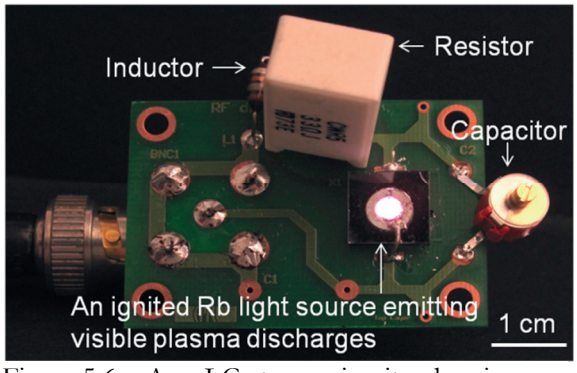

Figure 5.6: An LC-stage circuit showing an ignited microfabricated Rb light source, with Indium ring electrodes, emitting a visible glow discharge.

at different cell temperatures are shown in Figure 5.7 for cells CN1 and CN3. The Rb D line intensities increase with increase in cell temperature due to the rise in Rb vapor pressure in the cell, as expected. The corresponding optical power of the Rb D2 line with increase in temperature, when the initial total optical power was set at 100 μW for CN1, is shown in Figure 5.8. The measured intensities of the Rb D2 and Ar 764 nm lines versus temperature for both cells are shown in Figure 5.9.

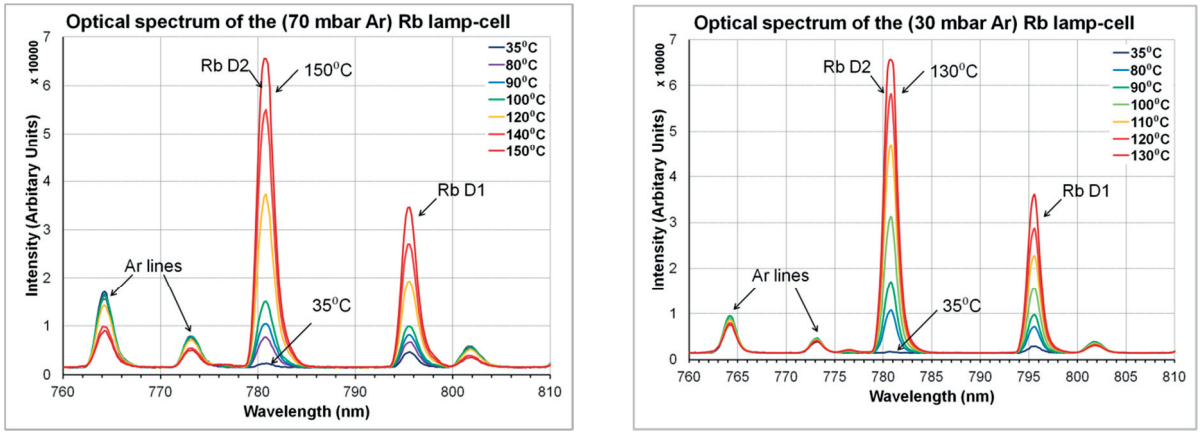

Figure 5.7: Optical spectrum showing the Rb D lines measured from cells: CN1 (a) and CN3 (b) at different cell temperatures.

Two observations can be made from the Figure 5.7: **(1)** for a given temperature, the Rb line intensity is stronger for the lower buffer gas pressure cell CN3 and **(2)** with increase in temperature, a reduction in the Ar line intensities is observed.

Observation **(1)** is mainly because of the higher Rb vapor atom to Ar atom ratio in the cell (for CN2 than CN1) which leads to higher proportion of Rb excitations and hence Rb discharges. However, as it is important to achieve the ideal gas pressure for low-power operation, effect of cell pressure has been investigated in more detail and reported in section 6.1.

Observation **(2)** has also been reported by other researchers [161], [162], where the main factor responsible for this phenomenon has been understood to be due to the increasing proportion of high energy electrons losing its momentum through exciting collisions with the increasing number of Rb vapor atoms at higher temperatures. Hence, this overall reduction in the electron temperature leads to lower Ar

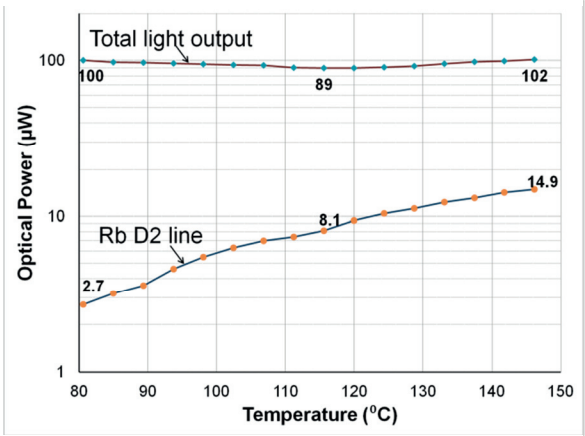

Figure 5.8: The total optical power and Rb D2 line power emitted by CN1 at different cell temperatures.

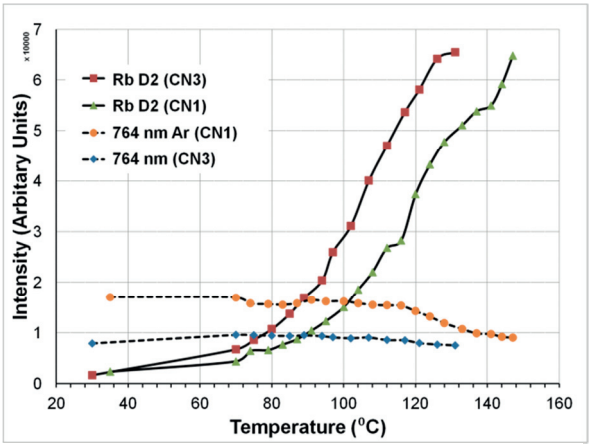

Figure 5.9: Comparison of Rb and Ar line intensity variations with temperature.

excitations and eventual Ar discharge emission. Another factor contributing to this behavior is the increased lifetime of the Ar metastable states at higher temperatures which results in a lower Ar decay rate to its ground state and hence a lower emission of the Ar line power. In the following sections, the different power, lifetime and other performance characteristics of the Rb DBD lamp are reported (sections 5.3-5.7).

5.3 Electrode geometry optimization

Different electrode geometries have been used for the experiments in this research and the relevant details of the various electrode properties are mentioned here in this section. To efficiently couple the applied rf electric field across the discharge gap, the electrode geometry and its material properties need to be optimized for best results. In order to identify the best electrode configuration, the power required for breakdown and the stability of the output discharges for different electrode geometries were recorded and analyzed. Figure 5.10 shows the various electrode patterns (top and bottom electrodes) tested using Indium solder, where EL4 was used for the initial lamp characterization experiments. Figure 5.11 shows the measured capacitance of the cell (CN2) for the electrode configurations [EL1-EL6] with Indium and the breakdown power measured at around 5 MHz (all tested drive frequencies within ±0.5 MHz). Higher the surface area of interaction of the electrodes, higher was the observed capacitance and lower was the electrical breakdown power. The inner ring diameter of all electrodes were 4.5 mm (0.5 mm encroaching over the optical window) to increase the electric field lines through the gap without significantly reducing the optical output.

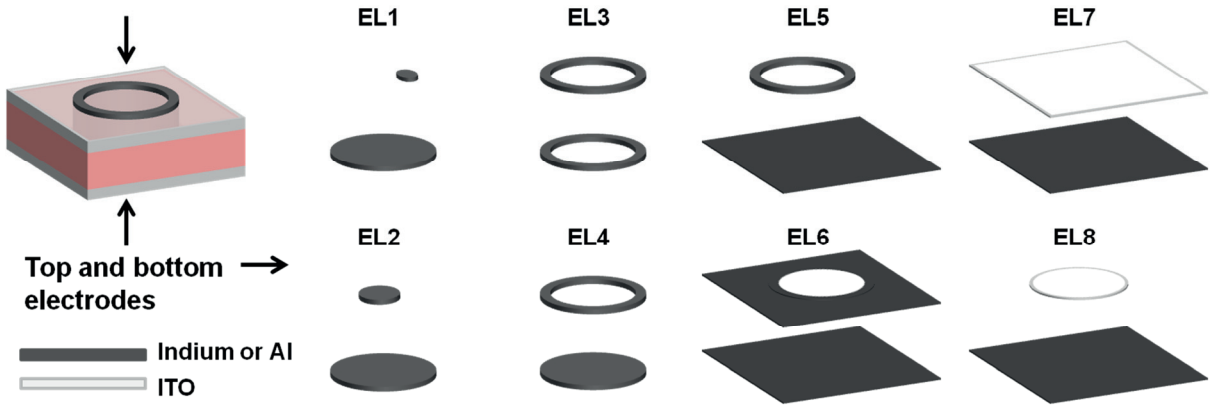

Figure 5.10: The various electrode configurations used in this research where the electrodes are drawn to the cell scale on the left. The ring inner diameter is 4.5 mm and outer diameter is 6 mm.

The configuration EL6 was identified, from the electrical breakdown experiments, to be the most power-efficient and was chosen for all Al electrode configurations. EL7 configuration was used only for cell CN8 and EL8 was used for cell CN7 only. Figure 5.12 shows the comparison of the power consumption of the CN2 cell with Indium and Al electrodes (EL6) at different drive frequencies in the 2-500 MHz range, to produce 10 μW of Rb D2 output power. [EL7 and EL8 configurations could not be compared as they were not deposited on CN8 and CN7 cells which had different buffer gas pressures and discharge lengths]. The Al electrodes were found to yield a more than 50% improvement in power consumption at the >tens of MHz drive range when compared to the initial Indium ring electrodes. This was mainly due to the drastically reduced surface roughness of the Al electrode layer when compared to In (manually deposited

using a solder gun or a hot plate) and the good adhesion properties of the Al on the Pyrex surface.

As Al and In are opaque, they cannot be deposited right above the discharge gap, which is the most efficient field coupling configuration. A 100 nm thick ITO (90% transmission measured) was deposited as the top electrode on CN8 and a 200 nm thick Al blanket electrode for the bottom (EL7). This electrode configuration has three important advantages: **(1)** high transmission or transparent electrode - ITO allows for the electrode to be directly deposited over the optical window enabling high electric field lines coupling into the discharge gap while being almost transparent (>90% transmittance at the D line wavelengths). **(2)** It helps reduce the thermal gradients across the discharge gap - as the ITO layer has a non-negligible surface resistance (with surface resistivity: 40 Ω/sq), some of the input rf power is converted to heat due to resistive losses which helps in top-side heating of the cell and significantly reducing the temperature gradient across the cell. This in turn reduces rubidium vapor condensation on the inner top wall of the light source that decreases rubidium self-absorption and Doppler broadening of the Rb D lines and increases the overall transmission intensity and stability of the D lines. **(3)** The Al layer bottom electrode acts as a light mirror increasing the photon yield through the optical window of the Rb cell. A direct comparison of the Al and ITO electrodes on the electrical breakdown properties was not possible as they could not be tested on the same cell or similar cells with the same buffer gas pressure.

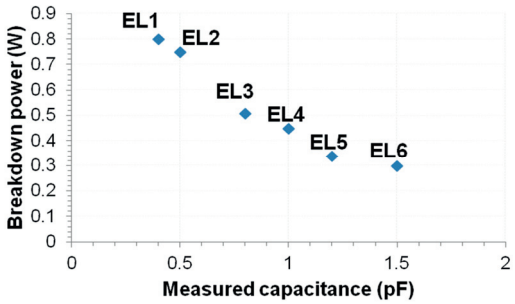

Figure 5.11: The measured breakdown power and capacitance values of CN2 for different electrode configurations at ~5 MHz.

5.4 RF input characterization of the Rb DBD lamp

In this section, the effect of the input rf power and frequency on the Rb-lamp operation for different cell p.d conditions are reported. There were two broad operation regions identified to have their own characteristic discharge behaviors: drift-dominated and the diffusion-controlled regions and the effects of different rf input powers in these regions are discussed in section 5.4.1. The change in the discharge breakdown characteristics at different drive frequencies are discussed in section 5.4.2 and the effects of impedance mismatch conditions are reported in section 5.4.3.

5.4.1 Effects of input RF power on discharge emission

When the input rf power to a 50 Ω matched LC-stage load is switched on and increased, the voltage across the cell increases (as described in section 4.2.2). At some specific value of the input power (P_f–P_r measured by the rf power meter), the voltage across the cell equals the breakdown voltage, V_{BR}, of the specific cell in test and this ignites a visible discharge in the cell discharge gap. The input power corresponding to this breakdown is the breakdown power and is directly measured using the rf power meter. However, this value is not the minimum power required for sustaining the discharge and the input power can be drastically lowered to still maintain a visible discharge emission from the Rb lamp. The optical power would reduce but a

discharge emission is sustained until a certain minimum value, termed minimum sustaining power, is reached (below which no visible discharge emission is observed). This is because of the presence of a significant density of electrons, even at lower voltages after breakdown, with a mean electron temperature that is sufficient to produce enough ionizing collisions with gas atoms/molecules for sustained discharge emission.

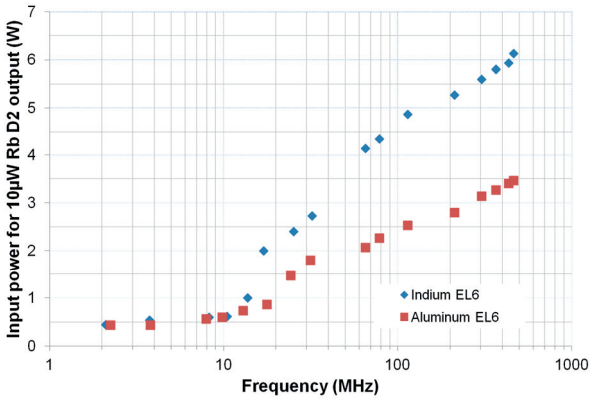

Figure 5.12: The comparison of the power consumption of the CN2 cell with Al and In electrodes (EL6) to produce 10 µW of Rb D2 output. More than 50% improvement in the power consumption is achieved with Al electrodes over In at the >10 MHz drive range.

In the following sub-sections, the observed discharge emission powers for different input power levels are reported. At low power levels (P_{in}<few Watts), the discharge behavior depended on the chosen drive frequency. Two distinct discharge behavior regions, classified primarily by the drive frequency, were identified: the diffusion-controlled and drift-dominated breakdown regions. The rf drive frequency range, when the electron oscillation amplitude, A_e, is much higher than the discharge gap length, d, is conceptually the diffusion-controlled region and the frequency range when $A_e \approx d$ is the drift-dominated region [A_e is calculated using equation 4.13]. The two regions, whose theories were explained in section 2.3 and whose boundary conditions have not been defined accurately, are mainly distinguished based on two experimental observations: **(1)** the emitted optical power varies differently with changing input drive power in the two regions (reported in the next paragraph) and **(2)** the optical stability of the discharges changes drastically with a significant formation of DBDs on the inner dielectric surfaces in the drift-dominated region (reported in section 5.5). For the Rb cells, with their respective p.d values considered in this research: 3 mbar.cm to 14 mbar.cm, the corresponding drift-dominated breakdown region was observed to be approximately between 2.7 MHz to 8.2 MHz respectively and the diffusion-controlled region at higher drive frequencies. These values also correspond well with the expected drift-dominated frequency range from A_e calculations. At very high input power levels (more than several Watts) however, the distinct discharge characteristics of the two regions become lower, as the density of plasma discharges formed in between the discharge gap becomes significantly more than the surface DBDs.

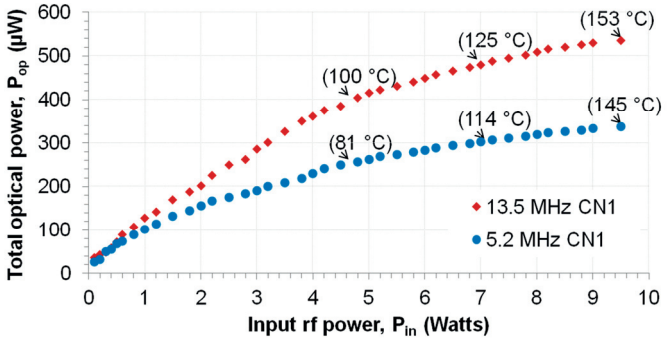

Figure 5.13: The measured optical power from CN1 at two regions of operation: 13.5 MHz diffusion controlled breakdown (red) and 4.2 MHz drift-dominated breakdown (blue). Measured cell temperatures at some relevant data points are mentioned for reference.

The red plot in Figure 5.13 shows the total optical power measured from cell CN1 (with In EL6 electrodes) when driven at 13.5 MHz for different values of input power, P_{in}. A linear relation

between P_{op} and P_{in} was observed for this power range, where the maximum cell temperature reached in these experiments was 153 °C (corresponding to 9.5 W; it is much lesser than the cell's expected Rb self-absorption temperature: 192 °C). A further increase in the input rf power led to heating the cell temperature to more than the melting point of the In electrodes (156.6 °C) which induced an erratic discharge behavior (most probably due to the highly inhomogeneous fields created across the gap due to the liquid electrodes) and an eventual discharge emission shut-off. [Increasing the input rf voltage increases the cell temperature due to several factors, namely: (1) frictional and collisional power losses in the discharge gap leading to heating effects, (2) ohmic heating of electrodes, (3) power dissipated as heat by all the cell dielectrics. The effect of increasing the rf voltage to heat the cell beyond its Rb self-absorption temperature is reported in section 5.6 where Al electrodes and high-melting temperature solders were used for the test.]

The P_{op} became a slower varying function of P_{in} at higher input power values (typically more than 5 W for most circuits when sustained for more than few minutes), and this is thought to be due to three main reasons: **(1)** higher input power leads to an observed undesired heating of the inductor coils used in the LC-stage due to the high current flowing though the inductors' DC and skin effect resistances. This reduces the circuit Q_{rp} and hence the effective V_e across the cell **(2)** Higher V_e leads to an increase in the electron oscillation amplitude (equation 4.13) making more electrons reaching the walls and increasing drift-dominated losses. Hence, due to this increasing loss mechanism, the electron density in the discharge gap would reduce and lead to a lower increase in P_{op} with increase in P_{in}. **(3)** Also, as observed in and Figure 5.8, the Argon line intensities reduce with higher temperature and the overall power reduces in the 90-140 °C temperature range (Figure 5.8) despite the increase in the Rb D line emissions. The respective cell temperatures recorded for some data points have been marked to understand this relation.

Table 5.1: The slope values (linear regression and keeping intercept zero) of the Pop function of Pin, when Pin is less than 5 W, for different cells at the diffusion and drift dominated regions.

Lamp-cells	**Argon pressure (mbar)**	**Slope value at $f_r \approx 13.5$ MHz and $P_{in}<5W$ (µW/W)**	**Slope value at $f_r \approx 4.2$ MHz and $P_{in}<5W$ (µW/W)**
CN0	70 (no Rb)	80	55
CN1	70	91	60
CN2	70	89	58
CN3	30	105	75
CN4	30 (^{87}Rb)	102	73
CN6	70 (high liquid Rb)	92	67
CN10	30 (high liquid Rb)	104	81

In the drift dominated region (below approximately 8 MHz), a significant number of electrons start hitting the Pyrex walls and hence the secondary electron effects of the DBDs start to play a significant role in the discharge process. The blue plot in Figure 5.13, using CN1 cell and 5.2 MHz drive frequency, shows a typical example of the P_{op} to P_{in} relation when the electron drift-dominated losses are non-negligible. P_{op} here is observed to be a slower varying function of P_{in} in this range as an increase in the cell voltage, V_e, manipulates two primary mechanisms: **(i)** increases the electron temperature and **(ii)** increases the electron oscillation amplitude which leads to higher drift-losses. Mechanism **(i)** is similar in both regions but **(ii)** is a loss mechanism that is significant only in the drift-dominated region. Hence, the overall increase in P_{op} with a given increase in P_{in} (and hence V_e) is much lower than the diffusion-controlled breakdown case

(red plot) where mechanism **(ii)** has a negligible dependence on the cell voltage in the chosen power and p.d range in this research.

Similar linear relations as shown by the red and blue plots in Figure 5.13, but with slightly different slopes, were found for the other cells: CN0, CN2-4, CN6 and CN10 and the slope values (from best fit using linear regression and setting the intercept as zero) at drive frequencies around 13.5 MHz and 5.2 MHz for the different cells are given in Table 5.1. [To drive all the LC-stage circuits with different Rb cells at the exact same drive frequency value, was not considered as it is very time-consuming, unnecessary for the study and sometimes unachievable without an exhaustive number of LC component options. It is only important to compare the different Rb cells within an acceptable drive frequency range (within 0.5 MHz here) as the discharge physics does not vary drastically within such a small range]. It can be seen from Table 5.1 that the slope was observed to be higher when the buffer gas pressure was lower in the diffusion-controlled region, indicating the possibility that there are higher inelastic collisional power losses at higher gas pressure leading to lesser effective gain in electron acceleration. This lowers the density of electrons with energy above the gas excited levels and hence leads to a lower discharge emission (in the case of CN2 for example). Considering two similar cells with the same buffer gas and pressure (CN1 and CN6 for example with 70 mbar Ar), the presence of more liquid Rb does not make a significant difference to the optical power characteristics in the diffusion controlled region but however at the drift-dominated region, the optical power to the input rf power is much higher due to the surface discharges formed on the Rb droplet (more details in section 5.6). It can also be seen that a purely Ar filled cell (CN0) has a lower slope value than the cells CN1 which has the same Ar pressure as CN0 but with Rb vapor atoms. This is due to the lower ionization energy of Rb (IE1: 4.17 eV) compared to that of Argon (IE1: 15.75 eV) which leads to the overall reduction in the electron temperature required for ionizing collisions in the discharge gap for a sustained discharge formation in the increasing presence of Rb atoms.

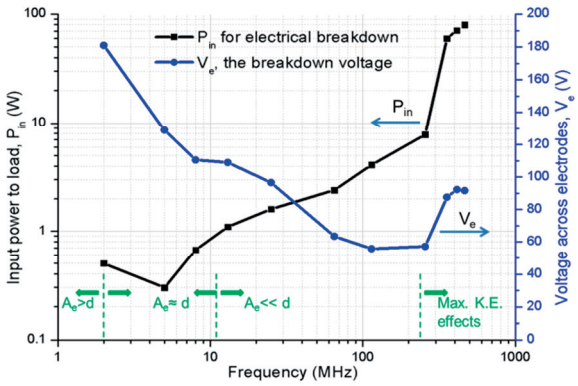

Figure 5.14: The measured input power (black) at breakdown and the calculated breakdown voltage (blue) of CN3 (with EL6 electrodes) at different drive frequencies between 2-500 MHz. A_e is the electron oscillation amplitude.

5.4.2 Effects of drive frequency on the light source performance

For the atomic clock application, any drive frequency value is suitable for the lamp except the clock interrogation frequencies and its multiple harmonic frequencies as it may possibly cause undesirable coupling effects and higher timing errors (both in GHz range). As discussed in sections 2.5 and 2.6, for the chosen test discharge length of 2 mm, at least 1 MHz would be required to increase the density of electrons and hence the space charge in the discharge gap (rather than being pushed to the walls at lower frequencies) for low power operation. To identify an ideal drive frequency value or range for the lowest power lamp operation, a set of experiments were performed whose main results are reported.

For a given Rb lamp-cell, the LC-stage was developed after choosing the component values to accurately impedance match the cell to 50 Ω at the chosen f_r and the P_{in} value at breakdown (P_{BR}) was noted. The breakdown voltage was then calculated using the procedure mentioned in section 4.2.2. This was repeated for different drive frequencies in the range of 2-500 MHz and the obtained results for CN3 (with EL6 electrodes) are shown in Figure 5.14. In order to avoid a considerable difference in parasitic values, the inductors in the LC-stage were chosen from the same manufacturer and the parallel capacitor (whenever used) was the same tunable capacitor with a wide tuning range (2-45 pF). The overall behavior observed in Figure 5.14 is indicative for other Rb lamp-cells (CN1 with EL6 electrodes and CN8 with EL7 electrodes) as well and the relevant critical frequencies of these cells are summarized in Table 5.2.

The electron oscillation amplitude (A_e) decreases with increase in the drive frequency value. Referring to the blue plot in Figure 5.14, at values where the discharge gap length (d) is much lower than A_e, a plasma was not ignitable. This is most probably due to the very high breakdown voltage (unachievable with the available rf amplifiers) required in this region due to the significant loss of electrons into the walls which are not compensated by the secondary electron emission from the Pyrex walls [163]. At values when $A_e \approx d$, there was a non-negligible amount of secondary electron emission from the Pyrex, evident from the significant number of surface DBDs observed, to allow a breakdown and the calculated breakdown voltage was observed to decrease with higher frequency as there would be more electrons adding to the space charge (hence higher electron temperature and ionizing collisions) in the discharge gap.

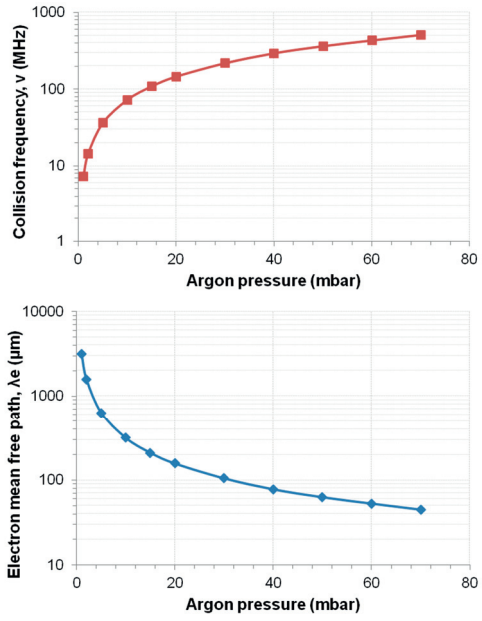

Figure 5.15: The calculated collision frequency and the electron mean free path for different pressures of Argon at 300 K and 12 eV electron temperature.

According to the kinetic theory of gases, the breakdown voltage would be lowest when the drive frequency equaled the electron collision frequency in the discharge gap (refer to section 2.5). A trend on these lines can be seen here where the breakdown voltage was observed to reduce as the drive frequency got closer to the collision frequency, ν (calculated to be 219 MHz for CN3 at 300 K). The estimated ν and λ_e values for Argon, calculated from the kinetic theory equations for different pressures at room temperature (300 K), are shown in Figure 5.15 and the value calculated for CN3 is mentioned here as a reference. The electron mean free path in CN3 (30 mbar Ar) at 300 K can be given by: $\lambda_e \approx 4.\sqrt{2}.\lambda_{Ar} = 105$ μm [using equation 2.1, Argon atomic diameter = 142 pm and $\lambda_e \approx 4.\sqrt{2}.\lambda_{Ar}$ when the velocity of the electron is assumed to be much more than the velocity of the Argon molecules, derived in classical kinetic theory]. Assuming a Maxwellian distribution and the mean electron temperature to be 12 eV (above Ar metastable excited states), using equation 2.4, the random velocity of an electron, v_r, can be calculated to be 2.3×10^4 m/s. The collision frequency can then be given by: $\nu = v_r/\lambda_e = 219$ MHz (the random velocity is higher than the electron drift velocity and hence

used here). The lowest breakdown voltage was recorded at f_r=114 MHz for CN3 after which the breakdown voltage was observed to rise slightly with increase in the drive frequency. This difference in the estimated minimum voltage condition (at $\nu=f_r$) and the observed minimum is due to two main reasons: **(1)** the collision frequency calculations are simplified and not very accurate as Rb atoms were not included in the calculations and the electron temperature is assumed to be 12 eV (which is not accurate) and **(2)** the maximum kinetic energy that can be gained by the electrons can be limited at these high drive frequencies (electron kinetic effects) and this has not been considered in kinetic theory. Table 5.2 gives the drive frequency, f_r, values for some Rb lamp-cells obtained from similar experiments where the breakdown voltage was observed to be minimum, the lowest and highest recorded frequencies when a breakdown could be initiated with the available resources, and the estimated ν value for each cell.

At high drive frequencies (>100 MHz here), the breakdown voltage was observed to increase before the estimated ν value and this behavior is possibly due to the electron maximum kinetic energy effects, similar to the behavior observed by Walsh et al. [164]. At such high excitation frequencies, the time available for electron acceleration before the polarity change in the applied voltage becomes increasingly limited. This may compromise effective electron heating and subsequent gas ionization by such inadequately accelerated electrons. Walsh et al. reported on PIC (particle-in-cell) simulations for an atmospheric pressure rf discharge, where the maximum kinetic energy achievable by an electron started to reduce by 3% from 20 MHz for a 2 mm gap to about 15% at 500 MHz (at 1 atm pressure and 75 V/m). While these exact values do not apply here due to the different pressure, power and electrode conditions, the reported trend is relevant to the observed results. It is also possible that the experimentally observed f_{BRmin} was almost equal to the actual collisional frequency, above which the electrons started to have lower ionizing collisions (than at f_{BRmin}) due to the rf field changing polarities too quickly and changing the direction of electron motion before it can make sufficient ionizing collisions. This would lower the mean electron temperature, leading to a higher breakdown voltage needed to increase the electron oscillation amplitude and compensate this effect.

Table 5.2: The experimentally observed fr values for different cells where the breakdown voltage was minimum. The estimated ν values for Ar, assuming 300 K and 12 eV electron temperature, are also mentioned for reference.

Rb lamp-cells	**Lowest plasma ignitable frequency, f_{min} (MHz)**	**Highest plasma ignitable frequency, f_{max} (MHz)**	**Lowest recorded breakdown voltage, V_{BRmin} (V)**	**P_{INmin} - Input power corresponding to V_{BRmin} (W)**	**f_{BRmin} - frequency corresponding to V_{BRmin} (MHz)**	**Estimated ν (MHz)**
CN1	2.1	465	86	6.7	265	511
CN3	1.7	484	65	4.1	114	219
CN8	4.6	434	98	2.1	76	110
CN11	11.5	31	338	8.9	11.5	14.6

As observed from Table 5.2, the f_{BRmin} reduced with lower Ar pressure. The f_{max} values for CN1 and CN3 were most probably limited because of the available rf amplifier whose upper limit specification was 500 MHz. It is to be noted that CN11 could only be ignited at two drive frequencies: 11.5 MHz and 31 MHz (range more important than exact frequency value) and the plasma extinguished within seconds of ignition. These observations point towards the fact that the mean free path in CN11 is almost equal to the discharge gap length (Figure 5.15) and hence

only at the ignited frequency range there might have been enough ionizing collisions to instigate a brief breakdown. After breakdown however, most of the electrons could have possibly been lost into the walls, due to the high electron oscillation amplitude, leading to a reduction in the discharge gap electron temperature and eventual shut-off.

Even though the breakdown voltage can decrease with increasing frequency, the power required to achieve a said cell voltage increases with increasing frequency for the capacitive Rb-cell ($V_e^2 = P_e/C_{cell}.f_r$) (Figure 5.14). Also, the inductive parasitic components and the skin effect resistance of inductors become significant resulting in higher power coupling losses, low Q_{rp} and hence lower lamp-operating power efficiency. For CN3, 114 MHz drive operation can be seen to be the most power-efficient with the lowest breakdown voltage and with the highest emission of optical power for a given input power (more than 25 μW of Rb D2 at 700 mW of input power, reported in Figure 5.20). Almost 4 W of power is required for breakdown at 114 MHz after which the power can be reduced (700 mW here) to emit the desired output power. As power consumption is the primary concern for the Rb light source, this breakdown power magnitude would be unsuitable for a portable application and hence a lower drive frequency might be required for the chosen cell. The buffer gas pressure can also be reduced to shift this V_{BRmin} minimum point to a lower frequency, CN8 (15 mbar Ar) for example where the f_{BRmin} changed to 76 MHz. However, the V_{BRmin} value increased to 98 V (as compared to 65 V for CN3). This still corresponds to a lower breakdown power value (2.1 W compared to 4.1 W for CN3) and hence would be a better solution from a power consumption perspective. However, there are also other light source performance parameters like optical stability (section 5.5) and lifetime (section 5.7), which also vary with the rf inputs and cell conditions and hence they need to be understood before the ideal lamp operating conditions can be evaluated.

5.4.3 Power coupled to the discharge gap

The Rb DBD lamp was electrically modeled in section 4.3, to: **(1)** understand the distribution of the applied rf power, P_{in}, within the cell and circuit, **(2)** calculate the proportion of input power that is incident on the cell, P_e, and **(3)** calculate the power coupled to the discharge gap, P_g, that is dissipated as optical discharges, P_{op}, and heat due to collisional losses. This section reports on the various calculated power and voltage distributions and losses in the CN3 cell using the model described in section 4.3.

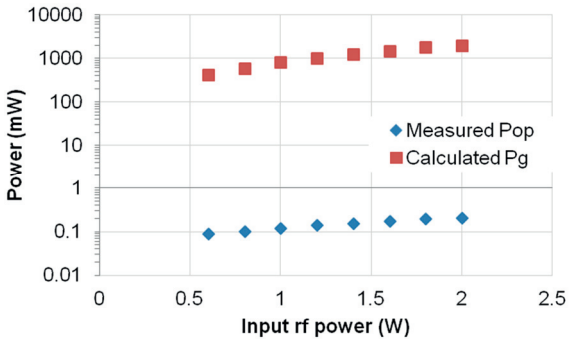

Figure 5.16: Plots of measured P_{op} and calculated P_g for CN3 when driven at 25 MHz at different input power values.

First, the frequency and power range where this model would be valid need to be understood. Figure 5.16 shows the plot of P_{op} and P_g (using equation 4.19) for CN3 at a drive frequency of 25 MHz but for different total rf input power values. An almost linear increase in optical power with the increase in P_g is observed at lower input powers, although it becomes a slower varying function of P_g at higher input power values, similar to what was observed in a Rb–Xe lamp experiment in [165]. The ratio of the optical power (400–1000 nm), P_{op}, measured from microfabricated Rb cells and P_g is plotted for different circuits with different drive frequencies.

The total rf electrical power required to produce 100 μW of total optical power (P_{op}) was measured at different drive frequency points for CN3, shown in figure 9(b). It can be observed in Figure 5.17 that there is almost a constant ratio of around 0.00025 between ~10 and 100 MHz while the ratio is much lower at <5 MHz and >100 MHz drive frequencies. At <5 MHz, a lower ratio might be because there are many electrons lost in the dielectric walls due to the high drive wavelength leading to a lower mean electron temperature and lower output optical power. And at >100 MHz, it is possible that the maximum kinetic energy reachable by an electron becomes lower and hence the overall mean electron temperature reduces along with the optical power. Hence, it might be valid to use this model under conditions when the drive wavelength is much lower than the discharge gap and the drive frequency is lesser than the maximum K.E. critical limit condition. Outside of this frequency range, this model can be used if appended with appropriate adjustment factors: $P_{Driftloss}$ and $P_{KEeffects}$ which are not discussed further here. The experimentally observed k_g value in this case is 0.0067 or 0.67%. For a comparative analysis, around 1.5% of visible light was estimated for sub-mm gap ac plasma display pixels for a given amount of power dissipated in the discharge gap [73], but the power efficiency in such cells is much higher because of the **(1)** phosphors utilizing the UV discharges, and **(2)** dielectric wall coatings with high secondary electron emission coefficient.

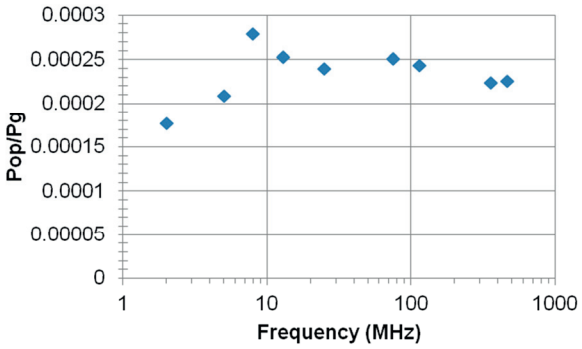

Figure 5.17: Ratio of the measured optical power, P_{op} and the calculated P_g for the same cell when emitting a total optical power of 100 μW (400-1000 nm range).

The measured breakdown power, P_{in} and the calculated breakdown voltage across the cell, V_e, at the 2-500 MHz drive frequency range was shown in Figure 5.14. V_e here was calculated based on the MATLAB model described in section 4.2.2. For this set of data points, Figure 5.18 shows the calculated P_g, P_e and voltage across the discharge gap, V_g, values at breakdown. As the discharge gap is modeled as a capacitance, C_g, the incident power is reactive. This reactive power couples with the reactive part of the discharge gap impedance (equation 4.16) to yield real power dissipation in the discharge gap or the power absorbed by the electrons (equation 2.16). As observed from Figure 5.18 and Figure 5.14, V_g and P_g are much lesser than V_e and this difference in this voltage is primarily lost in the Pyrex layers with additional losses due to the surface charge build-up on the inner Pyrex walls.

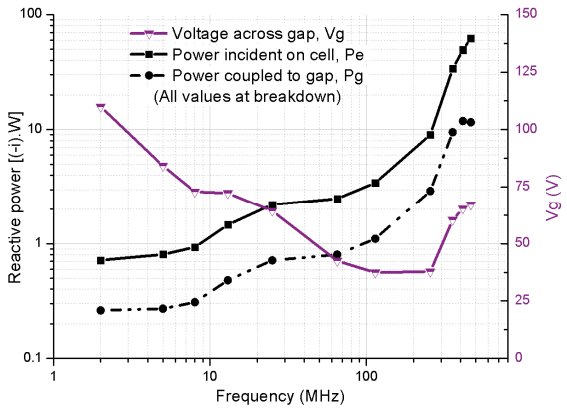

Figure 5.18: The calculated values of the power incident on the cell, P_e and the voltage and power coupled to the gap, V_g and P_g respectively for CN3 at breakdown in the 2-500 MHz range.

Using the power loss functions described in section 4.3, we can calculate the respective reactive powers and power losses of the cell layers and the circuit at different resonant drive frequencies.

Table 5.3 shows the Q_{rp} of different matching circuits and the different power distributions (where P_e, P_{py} and P_g are total magnitude values and P_{pyloss} and P_{siloss} are the power dissipated in the Pyrex and silicon layers) for CN3. For most of the cases, it can be seen that more than 50% of the input power is dissipated as P_{LCloss} in the drive circuit with the remaining dissipated as polarization losses in the Pyrex and silicon layers. Even though the power stored ($P_{py} - P_{pyloss}$) and power lost (P_{pyloss}) in the dielectric increase with increasing frequency (where $P_{siloss} > P_{pyloss}$ due to the higher relative permittivity of Si), the power efficiency of P_g/P_e becomes 10.4% at 465 MHz from 1.58 % at 2 MHz. However, the input power required for electrical breakdown increases significantly with increasing drive frequency (due to decreasing Q_{rp}) making a lower drive frequency preferable for a low-power lamp operation where the lower limit is primarily decided by the quality factor of the LC components.

Table 5.3: The different calculated power losses for CN3 along with the measured input power, Pin and power coupled to the gap, Pg, at electrical breakdown condition for different resonant drive circuits.

f (MHz)	P_{in} (W)	Q_{rp}	P_e (W)	P_{LCloss} (W)	P_{py} (W)	P_{pyloss} (W)	P_{si} (W)	P_{siloss} (W)	P_g (W)
2	0.5	36.2	0.695	0.289	0.132	0.033	0.421	0.173	0.011
5	0.3	33.3	0.883	0.011	0.167	0.041	0.525	0.253	0.014
8	0.67	19.1	1.038	0.319	0.195	0.049	0.629	0.304	0.018
13	1.1	14.7	1.640	0.529	0.306	0.078	0.997	0.485	0.031
25	1.6	10.8	2.476	0.738	0.454	0.117	1.513	0.739	0.054
75	2.4	5.8	2.785	1.166	0.496	0.132	1.717	1.098	0.076
114	4.1	3.9	3.773	2.772	0.646	0.179	2.352	1.136	0.128
256	7.8	2.9	8.911	4.735	1.312	0.422	5.786	2.618	0.501
356	60	1.6	29.017	49.342	3.037	1.375	20.332	9.273	2.611
414	71	1.6	37.475	56.579	3.326	1.776	27.078	12.639	3.745
465	80	1.5	41.505	63.053	3.297	1.967	30.559	14.973	4.351

Only a small fraction of the applied input power is observed to be actually coupled to the discharge gap. This result is good for a Rb DBD lamp to be potentially used in a portable clock application as it suggests that the actual useful power needed to achieve a desired Rb D line output is only within few tens of mW. However, it also means that the current cell impedance and circuit does not allow the desired breakdown voltage to be achieved in a highly power efficient way with low losses in other components. Most of the power losses are observed to be in the circuit (P_{LCloss}), where the primary loss component is the parasitic resistance of the inductor. Hence, using a technique as suggested in section 4.1.3, these losses can be drastically reduced to make it very low power consuming and suitable for optical pumping in chip-scale atomic clocks.

5.4.4 Impedance mismatch conditions

In this research, LC-stage loads were matched to 50 Ω for drive and testing where the reflected power is usually negligible to the forward power. This is important for two primary reasons: **(1)** maximum power transfer to the load, as mentioned before in section 4.1.3 and **(2)** for the accurate calculation of the voltage across the cell and components. However, the consequences on the Rb lamp and LC-stage performance when there is an impedance-mismatched condition or a shift in the input frequency (in the case of L_g for example, mentioned in section 4.3) has not

been discussed yet and are reported here. Figure 5.19 shows the observed total optical power output from the Rb lamp which is driven (and impedance matched) at 15.7 MHz as an example, after which the rf drive frequency is varied to plot the P_{op} vs. P_r, P_f and $P_{f\text{-}r}$.

With increase in the rf drive frequency from the impedance-matched value, the P_{op} and P_f always decreases while P_r increases. With decrease in the drive frequency, the P_{op} and P_f initially increase, reaching a maximum value and then decrease consistently. The maximum P_{op} value typically corresponded to the point of the P_f-P_r value maximum and this maximum was observed to occur not at the exact impedance-matched frequency but always few % below the matched frequency. This is most probably due to the fact that decreasing the frequency makes the load have a non-negligible capacitive reactance and hence a negative phase difference between the reflected voltage and current. This when re-reflected back (explained in the next paragraph) to the load, can be absorbed easier by the capacitive Rb lamp-cell than a voltage signal with a positive phase difference (when drive frequency was increased above the initially matched value).

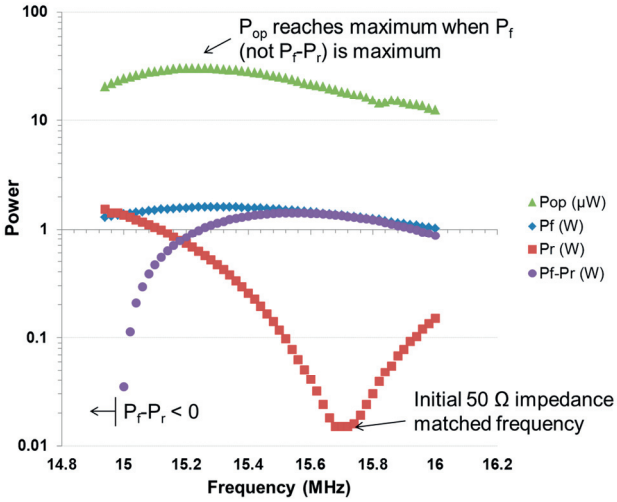

Figure 5.19: The measured optical power and electrical powers at different input frequency values starting from the initial impedance matched value at 15.7 MHz.

For cell voltage calculations, as described in section 4.2.2, accurate LC-stage impedance matching is necessary, as the actual forward and reflected power measured during highly mismatched conditions are not reliable and is explained here. RF power is propagated to the LC-stage load where it gets completely absorbed if the load impedance is the same as the characteristic impedance of propagation. The load here can be viewed as, for easier understanding, a transmission line of infinite length with the same characteristic impedance, and hence the propagated rf power never returns. However, more the difference between the load impedance and the transmission line impedance, more of the propagated power in the forward direction travels back as reflected waves in the same conducting path, where some of which is lost as resistive losses in the transmission line and most of which reaches the source. [The reflection coefficient is defined as the ratio of these waves and is given by the ratio of reflected voltage amplitude to the forward wave voltage amplitude.] Most of the power that is reflected back to the source is dissipated as heat but the remaining power is re-reflected to travel back in the direction of forward propagation (for the same characteristic impedance). This re-reflected wave voltage adds to the forward voltage but the resultant peak amplitude is not a simple addition of their voltage amplitudes as their phase difference need to be considered. Hence, a two-port network with the LC-stage load connected between two rf power meters are needed if the cell voltage needs to be calculated under impedance mismatch conditions.

In summary, the measured P_f-P_r using a one-port rf power meter gives the actual power delivered to the load but this is accurate only at and near impedance matched conditions. At

highly mismatched conditions, this value would be highly inaccurate and a two-port network of rf power meters would be necessary. The observed increase in P_{op} at different mismatch conditions is only due to the unaccounted re-reflected power to the load. The shift in the resonant drive frequency induced by plasma ignition can be used to calculate L_g but the drive frequency has to be re-adjusted to the impedance matched condition for accurate evaluation of the input powers and cell voltages.

5.5 Optical power and stability of the Rb DBD lamp

The optical power measured from the Rb DBD lamp-cells CN1 and CN3 at different drive frequencies have been reported here. The effects of the electrode design, input rf power and frequency on the optical power and stability of the Rb DBD lamp-cells have been discussed in the previous sections of this chapter and these effects are briefly explained and summarized in this section. The optical characteristics for different cell p.d conditions and buffer gases are discussed in section 6.1.3.

The maximum stable Rb D2 output power achieved in this research was 380 μW and the Rb D1 output was 172 μW (measured using the D1 and D2 filters mentioned in section 5.1) from CN3 at 114 MHz and an input rf power of 7.5 W. Any further increase in the rf input power lead to the red-mode transition (section 5.6) and lowering of the output Rb D line power.

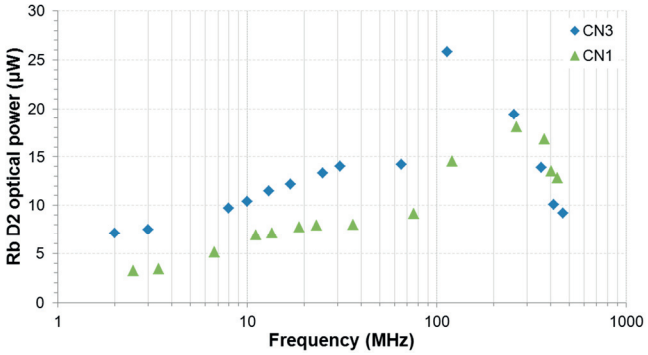

Figure 5.20: The measured Rb D2 optical power from CN3 and CN1 at different drive frequencies for an input power of 700 mW.

The Rb DBD lamp needs to emit at least 10 μW of Rb D line (D1 or D2) output with less than 0.2% sub-second fluctuations to meet the optical pumping requirements of the atomic clock. Figure 5.20 shows the variation of the Rb D2 optical power from CN3 and CN1 (both with Al EL6 electrodes) for a chosen input power of 700 mW. These values were measured after the optical power reached a steady-state, approximately within five minutes, and the measured cell temperatures were no longer at room temperature at this point, as expected. No external heater was used for this experiment. Lower the breakdown voltage, higher was the observed optical power emitted for a given input power/voltage at a given f_r (can be seen from Figure 5.14). At low drive frequencies (<10 MHz) the increase in the output Rb D2 power (slope) with frequency was low but it increased beyond this range as most of the electron motions would have been reversed before they could reach the Pyrex walls (leading to higher electron density and temperature in the gap). The reason for the decrease in the Rb D2 optical power after 114 MHz (for CN3) and 265 MHz (for CN1), is attributed to the electron kinetic effects explained in section 5.4.2. The measured cell temperatures induced by the constant applied rf power at the respective drive frequencies have been mentioned at some relevant data points for reference.

The stability of the optical power can vary between tens of percent fluctuations to less than 0.1% percent fluctuations depending on the cell and rf drive conditions. There are three types of discharges that are formed in the discharge gap: **(1)** volume discharges (VD), **(2)** diffuse glow

discharges (DGD) and **(3)** surface discharges (SD). The volume and surface discharges are the dielectric barrier discharges (DBDs) and they are usually homogenous over short distances (<few cm), that take place in thin layers off the dielectric surface [69], [34]. The main source of fluctuations in optical power is these DBDs as they are localized groups of discharges that can occur randomly over the dielectric surface. From the optical stability perspective, a fully diffuse glow discharge would be preferable as highly stable (<0.1% fluctuations) optical power is emitted but it is more power consuming than the DBD regime. Siliprandi [84] reports that, depending on the buffer gas and pressure in the discharge gap, DBDs operate in two regimes: at low pressure (generally less than 50 mbar), they operate in the Townsend breakdown regime, generating a diffuse glow discharge, whereas at higher pressures (approximately more than 50 mbar), the discharge generally splits up into a large number of randomly distributed volume discharges or streamers of nanosecond duration, also called the streamer regime, as discussed in section 2.7.2. In both regimes, the dielectric barrier serves two functions: 1) it distributes the microdischarges evenly over the entire electrode area and 2) it limits the amount of charge and energy that can be fed into an individual microdischarge. After typically a few nanoseconds, the microdischarge is choked because of charge build up on the dielectric, which results in a local reduction of the electric field within the filament [166]. Also, the mean energy of the electrons and the short duration of the microdischarges strongly limit any heating of the gas atoms, allowing the major fraction of the energy gained by the electrons in the electric field to be deposited in excited atomic states.

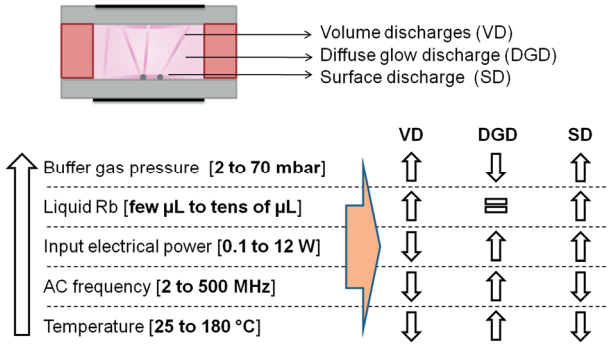

Figure 5.21: The change in the number of the volume, diffuse and surface discharges with increase in the magnitude of different input conditions. The test range for each condition within which these observations are valid is mentioned. Lower VDs and SDs lead to higher optical stability but higher breakdown power.

The effects of changing various input parameters on the different discharges are shown in Figure 5.21. The optical stability depends on all the mentioned parameters and hence a quantized characterization of the optical stability versus all these parameters is complicated. Hence, for a given set of initial input conditions, the optical stability can be manipulated by changing these parameters as mentioned in Figure 5.21. In summary, a lower buffer gas pressure, higher frequency, lower amount of liquid Rb, higher temperature and higher input power lead to more optical power stability in the mentioned DBD lamp operating ranges.

5.6 Temperature tests and Rb self-absorption

The Rb D line intensity increases with increase in the cell temperature. This was shown in section 5.2 with the output spectrum of the lamp at different temperatures along with the recorded optical power values. Here, some relevant performance characteristics of the lamp that is affected by the cell temperature are discussed: **(1)** the red-mode transition at high cell temperatures induced by high input power and its characteristics (section 5.6.1) and **(2)** the effect of Rb vapor pressure on the cell breakdown power (section 5.6.2).

5.6.1 Rb red-mode transition at high cell temperatures

As mentioned before in this chapter, the applied rf power leads to cell heating. When the applied power heated the cell to above its Rb self-absorption temperature, the output discharge was observed to undergo a distinct transition and started to appear fully 'red'. Also, all the spectral lines corresponding to the buffer gas completely vanished and the full output spectrum of the lamp consisted only lines corresponding to Rb transitions (Figure 5.22). Camparo, in his paper [102], explained this phenomenon is a result of significant radiation trapping of the emitted Rb D lines at these temperatures leading to lower Rb atoms available for ionizing collisions. This changes the dynamics of the alkali atoms multi-step ionization process and leads to a lowering of the electron temperature. Since inelastic electron/noble gas collisions are the dominant mechanism for populating noble gas excited states, the lower electron temperature leads to a drastic reduction in the intensity of buffer gas emission in this 'red mode'.

Table 5.4 shows the different power levels at certain drive frequencies (within 1 MHz of the specified frequency) where the cells CN1, CN3 and CN10 (all with Al electrodes) were found to enter the red mode. As CN3 and CN10 (30 mbar Ar) have a lower buffer gas pressure than CN1 (70 mbar Ar), the Rb self-absorption temperature for these cells was expected to be reached at a lower rf input power level (section 3.2.1) as observed. The average cell temperature measured within tens of seconds of the Rb red-mode transition for the CN1, CN3 and CN10 cells were found to be 185 °C, 165 °C and 162 °C respectively. These results were found to be in reasonable agreement with the expected Rb-self-absorption temperature of the tested cells: 192 °C, 168 °C and 168 °C respectively (Figure 3.4). The cell temperature was measured about 1 mm away from the cell surface (to avoid capacitive interferences) during these red mode transitions. From previous studies, a difference of about 15% in temperature was noticed between this position and at the center of the bottom cell surface at temperatures above 140 °C. Hence, this factor was added for a closer reference to the actual temperature inside the discharge gap.

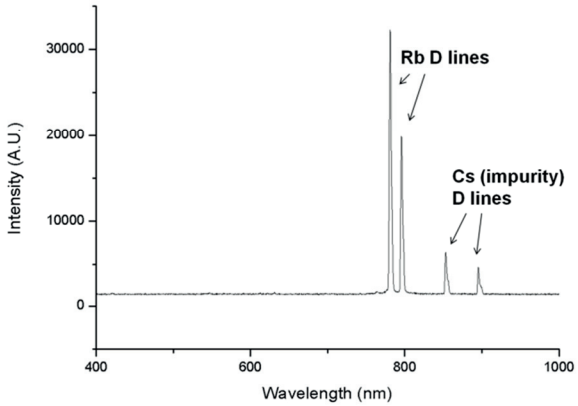

Figure 5.22: The spectrum of the emitted light from the Rb lamp-cell during the red-mode operation.

There was also another method for achieving high intensity Rb D lines, which sometimes transcends to the red mode, with significantly lower rf power (<~1 W to the LC-stage). In the case of CN10, there was at least 10 μL of Rb more than CN3 which forms a large (roughly 3 mm diameter and 0.5 mm height) spherical droplet on the bottom Pyrex surface in the discharge gap. Using the electrode design EL1 with Indium deposition, and a low drive frequency such that a significant number of electrons get drifted to the walls (3.7 MHz used here), the electrons are made to highly bombard the liquid Rb surface. If a low rf power (<few hundred mW) is applied, this locally heats the liquid Rb to emit a high intensity of Rb D lines (whose intensity at room temperature corresponds to the intensity achievable from externally heating a Rb cell with the same conditions but with no significant liquid Rb to 110 °C). However, at higher rf power levels (more than a Watt), this local heating creates a very high Rb vapor pressure locally near the liquid

Rb surface leading to high radiation trapping and transition to the red mode. Hence, a very high intensity of Rb D lines can be achieved by this method for very low input power but the main disadvantage of this operation is that it can uncontrollably transcend into the red mode. Even though, it is possible to achieve optical pumping in an atomic clock using a Rb lamp in the red mode, some of its features were found to be undesirable that could lead to a lower device performance when compared to the standard operating mode (at temperatures lower than Rb self-absorption): **(1)** the Rb line intensities were found to be unstable with time (few % fluctuations at temperatures well above the red mode transition temperature, up to 50% fluctuations near the transition temperature) and **(2)** the Rb D lines have been reported by other researchers to be Doppler broadened [167] in this mode that would lead to higher clock frequency instabilities.

Table 5.4: The measured input power values at different drive frequencies for the three cells when they were observed to transcend to the red mode. The accuracy of the drive frequency values is ±1 MHz.

Cells	5 MHz	20 MHz	434 MHz
CN1	No red mode observed	8.8 W	9.7 W
CN3	No red mode observed	7.3 W	8.4 W
CN10	4.7 W	7.1 W	8.5 W

There were many tests performed to identify the Rb self-absorption temperature of cells by heating the cell using an external heater (H1) up to 190 °C but however no obvious red-mode transition was observed during these experiments (The only important observation from these experiments, especially with CN6 and CN1 was that: a reduction in the Rb D2 optical power was consistently noticed at temperatures around 120-130 °C). The results of these experiments are not presented here as they are inconsequential. But as a red-mode has been observed at much lower temperatures but with the addition of rf power, it suggests that the red-mode transition is not simply dependent on the cell temperature but also on the discharge physics of the cell. However, more analysis to understand the exact phenomenon is beyond the scope of this research and hence is not discussed further here.

5.6.2 Breakdown power versus cell temperature

The first ionization energy of Rb (4.17 eV) is significantly smaller than that of Ar (15.75 eV). Hence, if a significant amount of Rb vapor is mixed with the Ar atoms, the breakdown power is expected to reduce by a certain percentage. CN1 and CN0 cells were experimentally investigated in order to understand if a significant reduction in the breakdown power can be achieved by igniting the discharge at higher temperatures. Figure 5.23 reports on the electrical breakdown power measured for CN0 and CN1 cells at 76.8 and 76.6 MHz and also for the CN1 cell at 8.5 MHz at different cell temperatures (using external heater H2). CN0 and CN1 have the same Argon pressure with the only difference being no Rb atoms in CN0. The first observation is that the breakdown power of CN1 at room temperature was found to be

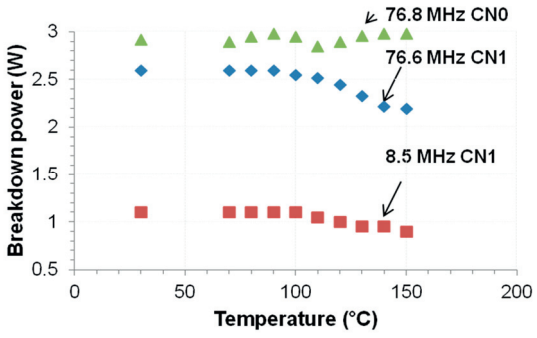

Figure 5.23: The measured breakdown power values for CN0 and CN1 at different cell temperatures.

around 11% less than that of CN0. With increase in temperature, the CN0 breakdown power did not consistently reduce but the breakdown power of CN1 reduced by 15% at 150 °C (when compared to room temperature breakdown). At 8.5 MHz, the breakdown power at 150 °C was found to be 18% lower than that at room temperature. However, at a practical lamp temperature of 100 °C, the breakdown power was usually almost the same as that at room temperature with a difference of less than a few percent.

From these observations, it can be seen that the presence of liquid Rb and Rb vapor atoms does reduce the breakdown potential for the cell (when compared to CN0). However, there are no significant advantages observed by igniting the discharge after heating the cell to practical lamp operating temperatures (around 100 °C), when compared to standard room temperature ignition.

5.7 Lifetime and reliability studies

The microfabricated Rb light source, with all its good performance and compact integration properties, is of no use for atomic clocks or magnetometers if it cannot function reliably for at least several years. This section reports on the experiments performed and data analyzed towards determining the device lifetime and the long-term reliability of its output and performance. The results in this section have been presented at the 2013 SPIE MOEMS-MEMS conference.

First, the hermeticity of the anodic bonded cells has been tested by Yves Pétremand, where the concentration of Rb atoms in an anodic bonded Rb cell (only cell, no plasma ignition) were monitored using laser absorption spectroscopy measurements. The cells produced by this sealing technique have been found to be highly hermetic for more than 2 years now [168] and has also been tested at 180 °C for several months to yield similar results.

The first set of observations from the various Rb lamp-cell discharge tests over the last 2.5 years is that the Rb lamp-cells were very robust with no significant change in performance after: **(1)** being ignited thousands of times, **(2)** heated to more than 150 °C hundreds of times and **(3)** being accidentally dropped on the floor several times.

Rb light source lifetime test

An experiment was set to allow an ignited Rb light source (CN2 cell and EL4 electrodes) to continuously emit discharges for an indefinite period of time, for monitoring the long-term stability of the output optical power (P_{op}), all other parameters of interest (Γ_{cell}, P_f, P_r) and the long-term reliability aspects of the device in general. The experimental setup is the same as illustrated in the schematic (Figure 5.1), where the optical power meter was a SM05PD1A Si broadband photodiode (Thorlabs Inc., 350-1100 nm range, active area: 13 mm^2) connected to a photodiode amplifier (Thorlabs Inc., PDA200C, 100 nA to 100 mA measurement range), the analog output of which is connected to a NI DAQ to allow the data to be recorded using LabVIEW. The entire setup, with all the necessary instruments, were kept inside a closed steel cabinet and isolated in a room corner, fully covering the cell setup with black sheets to remove any background light noise. The LC-stage was impedance matched to 50 Ω at 17.1 MHz and the forward power from the rf amplifier (A2) was PID feedback controlled using LabVIEW, to give out a steady and constant output power (Figure 5.5). As explained in section 5.1, this was

because the output power amplitude of the rf amplifier was found to drift with time, hence an external control was needed to ensure steady input conditions for the Rb lamp under test.

The lamp was ignited and the initial conditions were chosen to emit an optimal P_{op} of 100 μW when heated (using heater H1) to 100 °C. As 90-120 °C is the relevant operation temperature range for the Rb light source, 100 °C was chosen for this experiment which corresponded to a Rb D2 output of 6 μW. A 4 mm thick Al_2O_3 spacer was placed between the Rb cell and the heater surface (to remove the observed capacitive interference at closer separations) and the photodiode was positioned around 1 cm away from the top electrode for the same reason. The exact position was set in such a way that the optical power reading from there was 25 μW when it was 100 μW if measured right above the electrode surface. A high-power rating inductor (3 A current rating) with a high temperature tolerance was used in the LC-stage for this experiment to avoid the inductor failing due to over-heating effects during the long-term operation. Figure 5.24 shows the optical power recorded (one data point every 20 seconds) for the long-term experiment, with the initial conditions set as mentioned above and this corresponded to a PID-controlled input forward power of 1.25 W to the LC-stage. The Rb light source was ignited on 10th November 2011 to indefinitely emit discharges and this operation ended on 5th June 2012 only because the bottom cell electrode interconnect was found to be unsoldered and disconnected most probably due to the continuous heating effects (100 °C) from the nearby heater. The interconnect was then re-soldered and the lamp was re-ignited to confirm that the Rb lamp was still indeed functional, with an observed performance that matched the last recorded data point and hence the test was confirmed to be hindered only due to an external mechanical soldering defect and not anything because of the Rb-lamp.

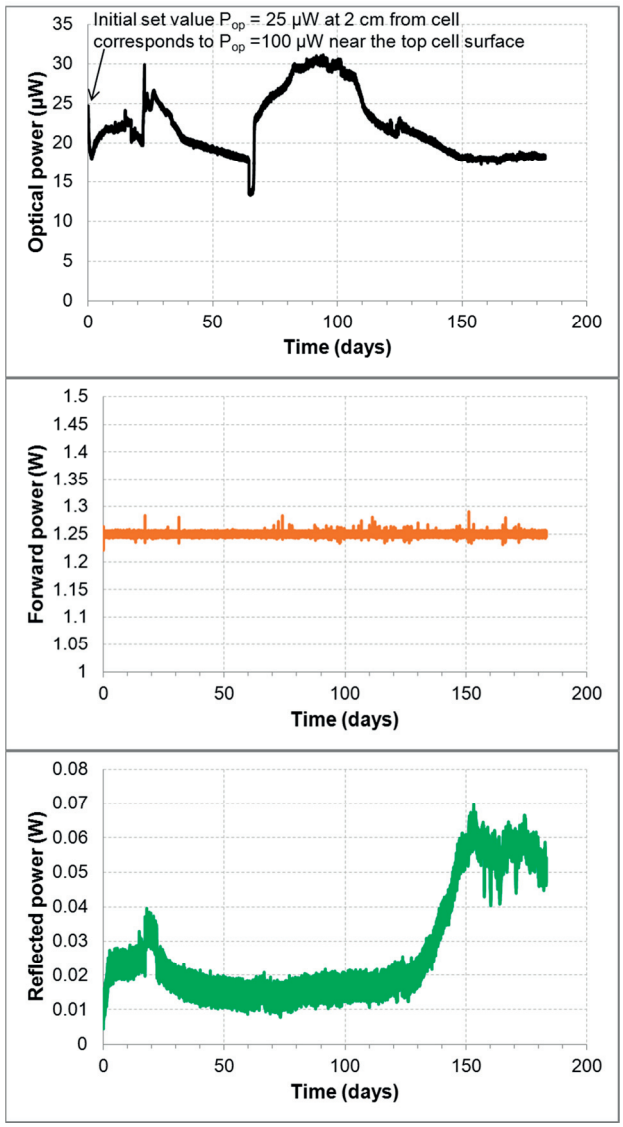

Figure 5.24: The measured optical power and forward and reflected electrical powers to the LC-stage of the Rb DBD lamp lifetime test. The lamp was initially set to emit 100 μW of optical power (corresponding to 25 μW from the position of measurement. The lamp was still fully functional after the test.

The first observation from this lifetime test was that the Rb lamp was found to operate without any functional problems for at least six months to emit a stable 100 μW of total optical power at 100 °C (corresponds to 6 μW of Rb D2 line power). The short-term (sub-second) fluctuations in

the optical power was found to be less than 0.2% (which is in the acceptable range for the atomic clock applications [15]). As seen from the figure, there were drifts in the optical power over time and it has not been possible to prove the exact causes for the observed behavior. There are some possible reasons identified, based on the observations made from various lamp experiments, which are thought of as the main causes for the observed fluctuations: **(1)** the resistance change of the inductor with time due to long-term heating effects, **(2)** solder interconnects losing their full integrity which leads to changes in the power coupled to the lamp and **(3)** Rb diffusion into the inner glass walls leading to a lower transmission of light from the Rb-lamp. **(1)** and **(3)** can possibly explain gradual and consistent changes in the optical power but **(2)** can result in erratic and random changes. This is because such behaviors were observed many times before in other lamp tests when the interconnects were not 'perfectly' soldered to the electrodes. The measured reflected power, shown in Figure 5.24, shows a steady drift after 100 days possibly indicating the failing solder interconnect. The solder used was 100% Indium, which is a good choice as it wets the Pyrex surface well but an additional non-metallic mechanical support should probably make the interconnect more stable and avoid any unpredictable power coupling losses and optical power fluctuations.

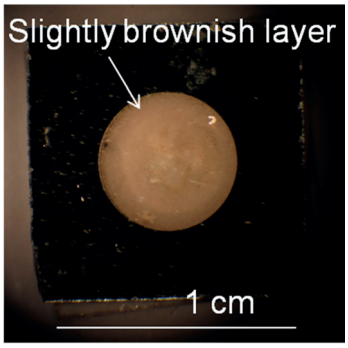

Figure 5.25: CN2 after the lifetime test showing a slightly brownish thin layer of Rb on the inner dielectric wall indicating possible Rb diffusion in the Pyrex walls.

Rb diffusion into Pyrex wall

Figure 5.25 shows a picture of the CN2 cell after the 6-month lifetime test showing the mildly brownish layer formed on the inner Pyrex wall. This is most probably due to the Rb atoms diffused into the wall over time (similar to the observations reported by other researchers [125], [169]). This layer causes problems like increased Rb self-absorption leading to Doppler broadening of the emitted Rb D lines and also overall reduced transmission of the D line power [161], [102]. However, as the Rb lamp is intended to be operated at low power (10 μW Rb D output), this would not be a limiting factor for its use in an atomic clock application - as seen from Figure 5.24, the optical power emitted after 6 months is still in the same range as the initially set value.

Plasma erosion of inner dielectric walls

Placing electrodes external to the discharge gap (electrodeless) avoids a major lifetime-limiting problem of electrode erosion from plasma discharges. However, the inner dielectric walls are in contact with the discharges and hence get slightly eroded with time. The erosion rate should primarily depend on the input rf power, the drive frequency and the cell temperature. When the electron oscillation amplitude is significantly smaller than the discharge gap length (f_r>10 MHz for most Rb cells here), most of the discharges are contained within the discharge gap with minimal DBDs occurring on the dielectric surface. For lower drive

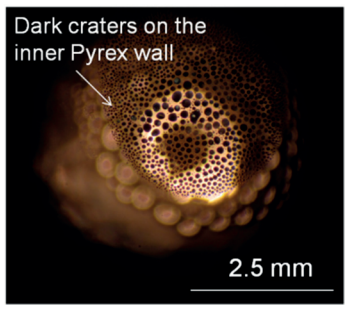

Figure 5.26: Dark craters observed on the inner Pyrex wall after several months of plasma operation in CN6. The surface discharges formed on liquid Rb droplets are the most likely cause.

frequencies or high input power, the wall erosion will be much higher due to the significant amount of surface discharges leading to wall erosion. Separate set of experiments were not performed to study this phenomenon as all Rb cells were tested at various frequencies and power levels. However, some fundamental visual observations have been made and are reported here. Figure 5.26 shows the picture of CN6 photographed using an optical microscope with focus on the inner dielectric wall after several months of operation. From visual observations, almost no etching of the dielectric layers was observed but dark shallow spots that would reduce the output transmission are seen The dark spots are most probably high concentrations of diffused Rb originating into the glass wall. Similar spots also occurred when there was a significant presence of liquid Rb in the cells (in CN6 and CN10), especially when the light source was operated for hundreds of hours (not necessarily continuously) at the drive frequency less than ~8 MHz. When the light source was predominantly operated at a higher frequency (such as in the lifetime test), a Rb thin film was formed rather than dark spots with no visually observable Pyrex erosion.

5.8 LTCC integrated Rb DBD lamp module

By heating and temperature controlling a Rb light source at a high enough temperature (typically 100-130 °C), stable and high intensity of Rb D lines can be emitted with reduced drifts in optical power, meeting the optical pumping requirements of many applications. For this purpose, a Rb DBD lamp module with an LTCC (Low Temperature Co-fired Ceramic) integrated heater, temperature control and the drive circuit was developed (in collaboration with Fabrizio Vecchio and Dr. Thomas Maeder, LPM, EPFL) for optical pumping applications and is presented here in this section. The results in this section have been presented at the 2012 IEEE SIITME conference [160].

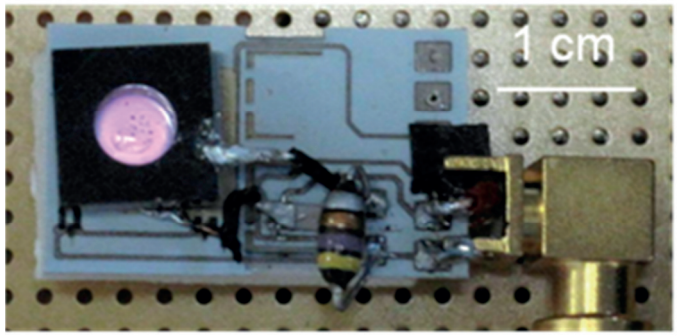

Figure 5.27: The LTCC integrated Rb mini-lamp module at operation (lamp powered at 25 MHz).

The Rb mini-lamp module (15x26x4 mm^3) (Figure 5.27) consists of the CN8 cell, positioned on top of a 0.6 mm thick (thickness adjustable) 4-layer LTCC (Low Temperature Co-fired Ceramic) stacked platform, containing a serpentine heating resistor design with high heating capacity (up to several hundred °C) for lamp heating, a fast response DP 5092D PTC temperature sensor [170] for temperature stabilization using PID feedback and a patterned pad layout for the drive circuit components and interconnects. The LTCC heater and drive circuit platform was fabricated by Fabrizio Vecchio and the thermal loss optimizations can be found in [171], . The reason for choosing LTCC technology [172] is because it allows for high-level integration, easy batch fabrication and compact multi-functional modules, offering many advantages with respect to traditional techniques (thick films on alumina substrates and hybrids) including: **(1)** excellent 3D structuration, **(2)** low firing temperatures, **(3)** possibility to integrate many functions in one same module, and **(4)** resistance to harsh environments.

The ITO layer has two distinct advantages for this application. The first advantage being high transmission or transparent electrode: ITO allows for the electrode to be directly deposited over

The ITO layer has two distinct advantages for this application. The first advantage being high transmission or transparent electrode: ITO allows for the electrode to be directly deposited over the optical window enabling high electric field lines coupling into the discharge gap while being almost transparent (>90% transmittance at the D line wavelengths). The second advantage is that it helps reduce the thermal gradients across the discharge gap. As the ITO layer has a non-negligible surface resistance (with surface resistivity: 40 Ω/sq), some of the input rf power is converted to heat due to resistive losses which helps in top-side heating of the cell and significantly reducing the temperature gradient across the cell. This reduces rubidium vapor condensation on the inner top wall of the light source and hence **(1)** decreases rubidium self-absorption and Doppler broadening of the Rb D lines and **(2)** increases the overall transmission intensity and stability of the D lines. The Al layer bottom electrode acts as a light mirror increasing the photon yield through the optical window of the Rb cell.

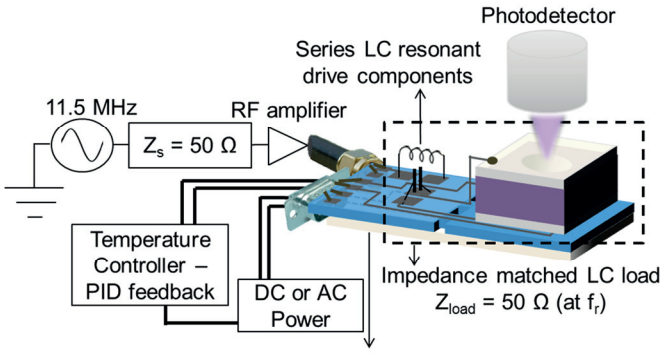

Figure 5.28: The schematic of the LTCC module operation and test setup.

The fast-response PTC temperature sensor (DP 5092D paste) [10], with a resistance value of 7.1 kΩ, was calibrated before use. Conducting pads (AgPd) for LC drive components are screen-printed on the top layer where the heater and the pads are thermally isolated with 0.4 mm thick bridges connecting the two sections. A 2 mm thick thermal foam (nominal k = 0.044 W/(m.K) at 25 ^{0}C) (Evonik Industries, Germany) was attached to the bottom layer for thermal insulation and mechanical support. A thin thermally conductive and electrically insulating adhesive layer (3M, 8805 tape) is used to fix the light source on to the LTCC platform. A thin alumina substrate can also be added as a spacer between the heater and the light source to further reduce capacitive interferences and for homogeneous cell heating.

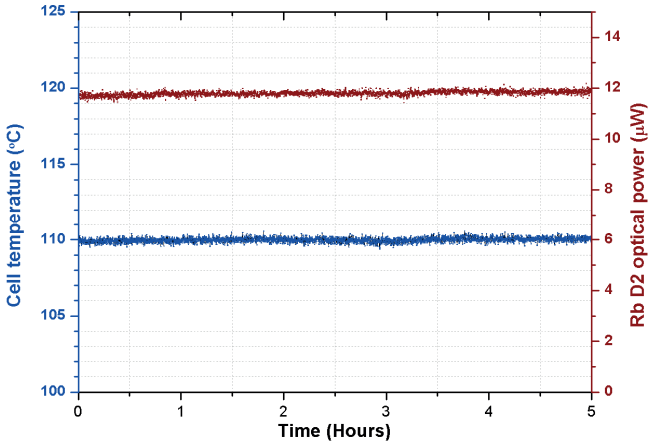

Figure 5.29: Cell temperature and Rb D2 optical power measured during a continuous run of 5 hours. Lamp drive frequency: 25 MHz, forward power: 1.1 Watts.

Module operation and results

The module is operated through two connectors: **(1)** SMA for the rf input power and **(2)** D-pin connector for heating and temperature sensing (Figure 5.28). The light source is powered at 11.5 MHz (hence requiring a high-frequency connector), which was found to be optimal for the test cell used here (Rb and 15 mbar Ar). The heater was powered by a DC power source whose input voltage is calibrated to the cell temperature readout. The heater can be powered by a DC

or an AC power source depending on the target application. For example, in a magnetometer pumping application, a DC powered heater will create magnetic field inhomogeneities when detecting a DC magnetic field while an AC powered heater should conceptually avoid this problem. However, for general applications, DC heating is used as it is uncomplicated and more power efficient than AC heating. The corresponding change in resistance of the PTC sensor with change in temperature is monitored and is fed to the heating power source via a PID (Proportional-Integral- Derivative) feedback controller loop to set and control the temperature and achieve up to less than 0.2 degree Celsius fluctuations with time.

The emitted Rb D2 (780 nm) line optical power and the temperature stability of the Rb lamp-cell recorded over time are shown in Figure 5.29. The heater was powered by a DC source (Input conditions: 7.1 V, 0.2 A for 110 ^{0}C) where the temperature was set and controlled using a PID feedback loop. The optical power was detected using a standard broadband silicon photodiode and a photodiode amplifier. The observed result in Figure 5.29 shows the capacity of the LTCC module to enable highly stable optical pumping in miniature atomic clocks and other applications.

Chapter conclusions

This chapter reported on the characteristics of the first ever Rb discharge ignited from a miniature microfabricated light source. The electrical and optical characterization experiments of different Rb lamp-cells and the relevant results obtained were reported in this chapter for performance evaluation of microfabricated Rb DBD lamps for miniature atomic clocks. The lowest breakdown power was observed to occur when the calculated collision frequency, ν was around the same range as the drive frequency, f_r (drive frequency) - this confirmed that the kinetic theory assumptions are reasonable and a lower pressure buffer gas is preferable for a lower drive frequency (hence lower breakdown power) adding to the advantage of a higher Rb D output efficiency (with lower buffer gas pressure) for a given power and temperature. Two distinct operation modes, dependent on the electron oscillation amplitude (A_e), were identified and were named the DBD (drift-dominated breakdown, $A_e>d/2$) and the rf-discharge (diffusion controlled breakdown, $A_e<d/2$) regions. The main characteristics of these regions were observed to be: DBD – lower breakdown power, higher optical instability and rf-discharge – higher breakdown power, lower optical instability. The suitable region for the light source operation was found to be when $A_e \approx d/2$, where a power-efficient emission of Rb D line power was possible with an acceptable amount of optical fluctuations. This corresponded to the 8-15 MHz frequency range and an Argon pressure of 15-30 mbar.

The power coupled to the discharge gap was calculated using the developed MATLAB and PSPICE models and it was observed to be less than tens of mW in the preferred drive frequency range (8-15 MHz) for a 30 mbar Ar buffer gas cell. Lifetime and long-term reliability tests, a 6-month continuous monitoring experiment performed on the microfabricated Rb light source, were reported and the light source was found to be robust without any significant degradation in its performance. The effect of cell temperature on the Rb DBD lamp performance was reported and the breakdown power reduced by 15% only when the lamp was heated up to 150 °C. 'Red-mode' transitions could be observed at the expected Rb self-absorption temperatures only when supplying rf power but not when externally heated to much higher temperatures. The

observations suggest that the red-mode transition is not simply dependent on the cell temperature but also on the discharge physics of the cell. A miniature LTCC integrated Rb lamp module was developed in collaboration with LPM, EPFL, where a temperature-controlled and long-term stable output light of 12 μW RB D2 was demonstrated.

While this chapter gives an indication of the suitable drive and cell conditions for a Rb DBD lamp, there are several other parameters like buffer gas type, discharge gap length and the secondary electron coefficient of the material that can be modified to further engineer the device towards the desired clock application. The experiments and simulations carried out to investigate these effects are reported in the next chapter.

Chapter 6 Experiments and simulations for optimizing discharge gap parameters

Very high power efficiency and output optical stability is required from the Rb DBD lamp and this requires a rigorous optimization of both the drive circuit and the lamp-cell parameters to meet the optical pumping performance requirements. As seen from chapters 4 and 5, the range of cell parameters tested using the microfabricated cells were limited – only one buffer gas: Argon with a limited number of gas pressure values and a constant discharge gap length of 2 mm (with the exception of CN8 with 0.5 mm gap length) were tested. The effect of different buffer gases, pressures, discharge lengths, surface area and cell wall conditions on the DBD lamp performance could not be tested using microfabricated Rb cells as such a large number of cells could not be microfabricated with the available resources in the short time-frame of this research. Hence, a set of experiments and plasma simulations were performed to study the effect of varying these cell parameters that can potentially further optimize the DBD lamp power efficiency and the results from these analyses are reported in this chapter. There is also very limited literature on low-pressure DBDs [173], [174] and thus these experimental results are very useful towards realizing the desired low-power miniature Rb lamp.

Two sets of data are reported in this chapter: **(1)** results from igniting plasma discharges between dielectrics for different p.d, buffer gas and surface area values in a pressure controlled chamber in section 6.1, **(2)** results from DBD simulations using a two-term Boltzmann equation solver in COMSOL in section 6.2. Some of these results were also published as a peer-reviewed article in the Journal of Physics D: Applied Physics [129] and also presented at the 2012 European Frequency and Time Forum conference [129].

6.1 Plasma characterization at different discharge gap conditions

This section reports on the experiments performed for identifying the ideal buffer gas and p.d values for a low-power consuming and optically stable plasma light source. The discharge gap test setup, explained in the following sub-section, was built to simulate the effect of different buffer gas types and pressures without having to microfabricate a Rb cell. Also, as discussed in

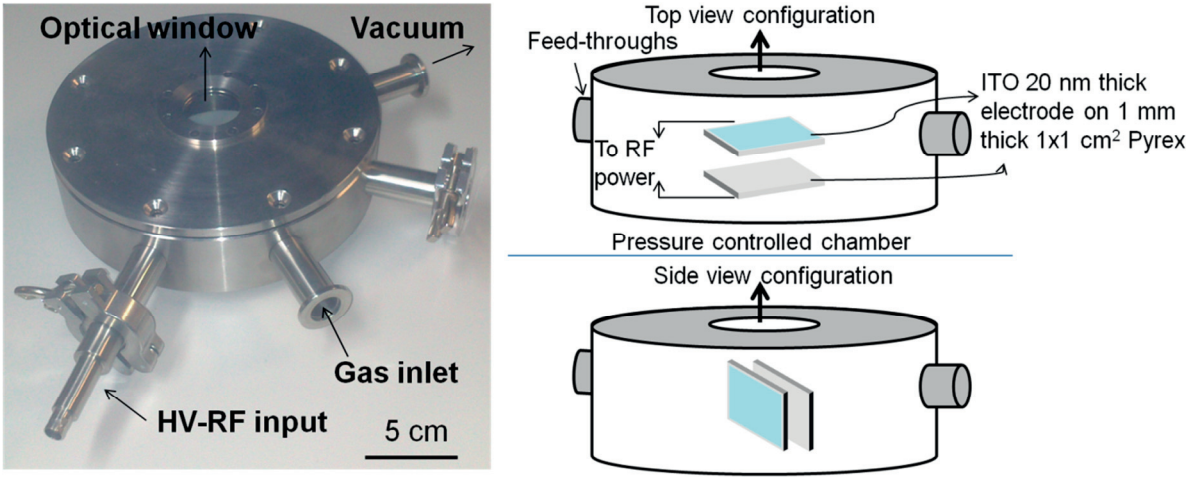

Figure 6.1: The photograph of the pressure chamber and the schematic of the discharge gap experiment setup inside which the ITO coated Pyrex substrates were aligned in parallel inside a pressure-controlled chamber to ignite DBDs by connected the ITO electrodes to rf power.

section 3.1, the size of the light source needs to be preferably as small as possible with a maximum cell volume of 1 cm^3. A discharge gap length of 2 mm is acceptable with a maximum lateral cell surface area of 1 cm^2. Reducing these dimensions can be beneficial as it can enable highly compact clocks or possibly chip-scale clocks but this is of interest only if the lamp's power consumption and optical stability performance properties can remain the same or made to improve on size down-scaling. Any buffer gas that is inert to Rb and any pressure up to an atmospheric pressure are suitable for the light source microfabricated by anodic bonding and hence different p.d values within these ranges with some suitable buffer gases were tested for identifying the optimal cell conditions.

6.1.1 Discharge gap experiments – test setup

The test setup built for performing the discharge gap experiments are described here. Figure 6.1 shows a schematic of the test setup where two Pyrex substrates (of 1 mm thickness and varying surface area) with 20 nm thick ITO thin film electrodes (on one side of the substrates) are positioned using mechanical alignments inside a pressure-controlled chamber. Figure 6.2 shows a photograph of one of the milled POM alignment parts which were used to define the discharge gap length needed for an experiment (six different discharge gap lengths were tested 0.2, 0.5, 0.8, 1, 1.5 and 2 mm). The discharges were ignited between the substrate gaps for different gap lengths, buffer gas and pressure conditions where the electrode side of the substrate is external to the gap. The ITO electrodes were connected to an LC matching circuit to form a 50 Ω load that is powered by an rf power supply, similar to the one used for the Rb cells. The parallel ITO electrodes acted as a capacitive load and different matching LC components were used depending on the desired testing frequency. The optical power meter was placed right above the optical window of the chamber. No external heater was used and all measurements correspond to room temperature.

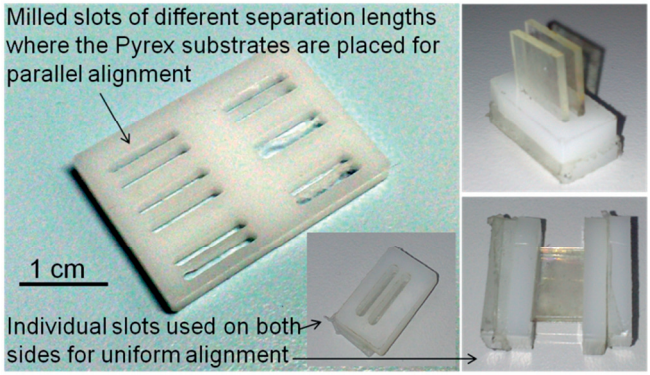

Figure 6.2: Photographs of an example bases with the milled slots, with different separation lengths, where the Pyrex substrates are placed.

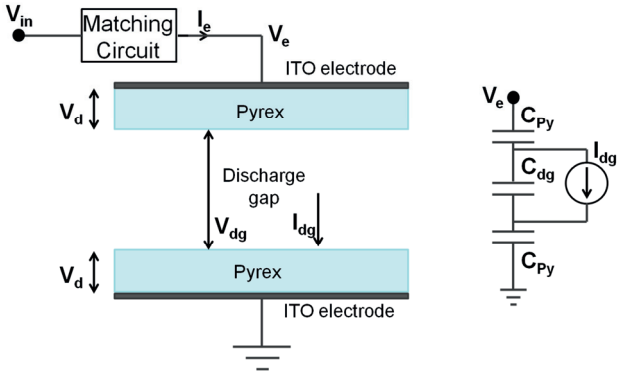

Figure 6.3: Cross-sectional view of the discharge gap ITO coated substrates. On the right, equivalent circuit of these substrates (without matching circuit) with the discharge current modelled as a voltage-controlled current source, I_{dg}.

The main advantage of this test setup is its ability to quickly vary the gap length, gas type, gas pressure, electrodes and materials and measure optical and electrical characteristics without the presence of Rb. Rb is highly reactive in air and hence is not possible to test it unless it is in a continuously

hermetically sealed condition. But the presence or absence of Rb for the discharge gap experiments almost makes no difference to the measurements as the amount of Rb vapor atoms to the number of buffer gas atoms in the gap at room temperature would be <0.001% for the range under study. Hence, the observed results are relevant and are indicative of the breakdown behavior in DBD Rb light sources.

Three different buffer gases were used in this study: He, Ar, and N_2 with their respective atomic/molecular diameters of 62 pm, 142 pm and 280 pm and their respective first ionization energies of 24.5 eV, 15.7 eV and 14.53 eV. The choice of test gases was based on several factors, first of which is that the gas has to be inert with Rb. While it seems preferable to have gas atoms with low ionization energy for a larger electron density and a lower breakdown field, a high atomic diameter means a lower mean free path for electron acceleration, resulting in a lower electron temperature (for a given p.d, P_{in} and f_r). Hence, an ideal combination of both these characteristics would be best for the Rb light source low-power operation.

6.1.2 Electrical equivalent model

Similar to the electrical model discussed in section 4.3 for the Rb DBD cell, the electrical equivalent model of the discharge gap is shown in Figure 6.3. The V_{dg}, $V_{dg}(0)$ and V_{dg} values can be defined by the equations (4.19), (4.20) and (4.21) and I_{dg} here can be defined as:

$$I_{dg}(t) = (1 + (2.C_{dg} / C_{Py})).I_e(t) - C_{dg}.dV_e / dt \qquad (6.1)$$

Using equations (4.21), (6.1) and (4.6), we can derive the power coupled to the discharge gap, P_{dg}, here as a function of the input power P_{in} to attain the power coupling efficiency:

$$P_{dg} / P_{in} = (P_{in} - P_{LCloss} + P_e - 2.P_{Py}) / P_{in} = (V_{dg}.I_{dg}) / P_{in}$$

$$= \frac{C_{dg}}{50}.\left(\frac{Z_{dg}}{Z_c + Z_{dg}}\right)^2.\left(Z_{dg} - 2.X_{Py} - \frac{V_e.Z_{dg}}{4.C_{Py}.\omega}\right).\left(\frac{C_{Py} + 2.C_{dg})}{2.C_{Py}.C_{dg})} - \omega.Z_{dg}\right) \qquad (6.2)$$

where Z_{dg} is the impedance of the discharge gap, X_{Py} is the reactance of the Pyrex layer and ω is the angular drive frequency.

6.1.3 Plasma discharge characterization results

The discharge gap tests were performed for the three different buffer gases at varying pressures (within 1-200 mbar depending on other input conditions), drive frequencies (2-500 MHz) and discharge gap lengths (0.2-2 mm). Plasma discharges were successfully ignited inside the discharge gap for most of the input conditions, however, for the remaining set of conditions, either a plasma discharge could not be ignited with the available rf power supply or the plasma ignited outside the discharge gap. These observations are explained in more detail in the following sub-sections. An example view of an ignited discharge seen through the optical window is shown in Figure 6.4.

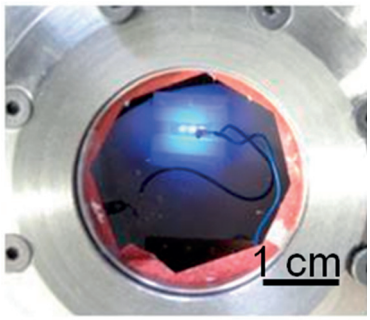

Figure 6.4: An ignited discharge between the ITO coated Pyrex substrates viewed through the optical window

The following sub-sections report: **(1)** the electrical breakdown power required and **(2)** the optical power and stability of the discharges, for different p.d values at drive frequencies: 4.4 MHz, 75.7 MHz and 465 MHz.

Electrical breakdown characteristics versus p.d and frequency

Figure 6.5a shows the measured power delivered to the load (matching circuit and the electrodes), P_{in}, plotted against p.d (d = 0.2, 0.5, 1, 1.5 and 2 mm) for the three buffer gases at a drive frequency of 4.42 MHz (where the electron oscillation amplitude is in the discharge gap

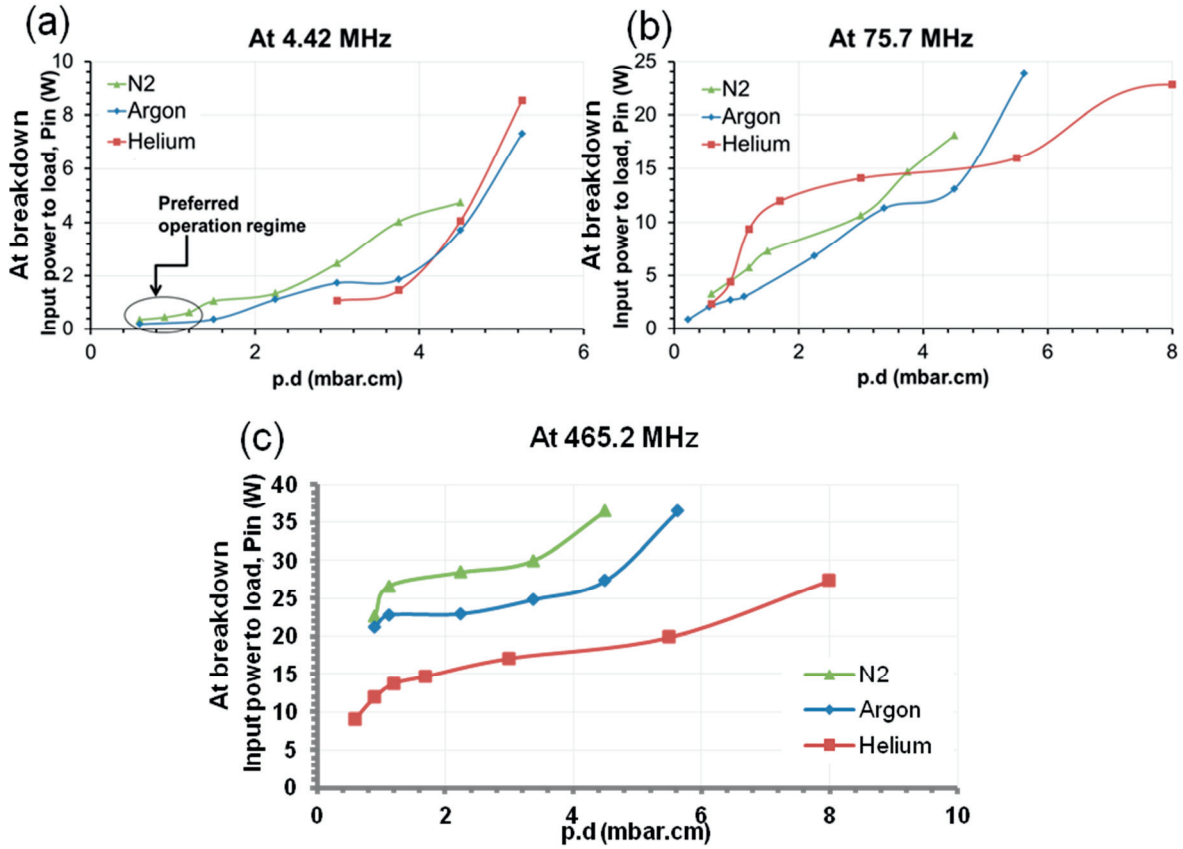

Figure 6.5: Input electrical breakdown power, P_{in}, of three different buffer gases for different pd conditions at (a) 4.42 MHz, (b) 75.7 MHz and at 465.2 MHz. Measured data points are marked but line plots were chosen only for convenient understanding.

length range (0.5-2 mm)). Figure 6.5 (b) and (c) show the corresponding data at 75.7 MHz and 465.2 MHz drive frequencies respectively. Only discharges ignited between the substrates are recorded and shown here; electrical breakdown at p.d values lower than those shown in these figures took place outside the discharge gap, which can be explained by the increase in required breakdown power across the discharge gap as the electron oscillation amplitude exceeds d/2. During these input conditions, the p.d values around the discharge gap are more suitable for breakdown than the p.d value inside the discharge gap (due to the electron mean free path explained in sections 2.4) and hence the plasma discharge slowly progresses outside of the discharge gap with decrease in the buffer gas pressure (below the last recorded p.d data point). At the other end of the data plots, when the p.d was very high, no plasma could be ignited as most probably the power required for such an ignition was not possible with the available rf

power amplifiers. These higher p.d ranges are anyway not of interest for this research as even higher input powers are required for breakdown.

It can be seen from Figure 6.5 (a) that under low pressure conditions, Ar has a lower breakdown power than N_2 or He. At a higher pressure (p.d > 3 mbar.cm), He has lower breakdown power than the other two gases. From these data it can be understood that He, in spite of its low atomic diameter, has a high breakdown field at low pressures due to its high ionization energy. Argon, even though it has higher atomic diameter, has much lower ionization energy than He and hence the reached electron temperature is sufficient for ignition. N_2 has its first ionization energy value very similar to Ar but a much higher atomic diameter. Hence, it requires a higher breakdown field than Ar but lower than He at low pressures. At higher gas pressures, the mean free path is reduced for all gases and hence a gas atom with a higher mean free path can reach a higher electron temperature for a given input power, He in this case. The observed operating regime that would be preferable for the Rb light source is shown in the figure as it corresponds

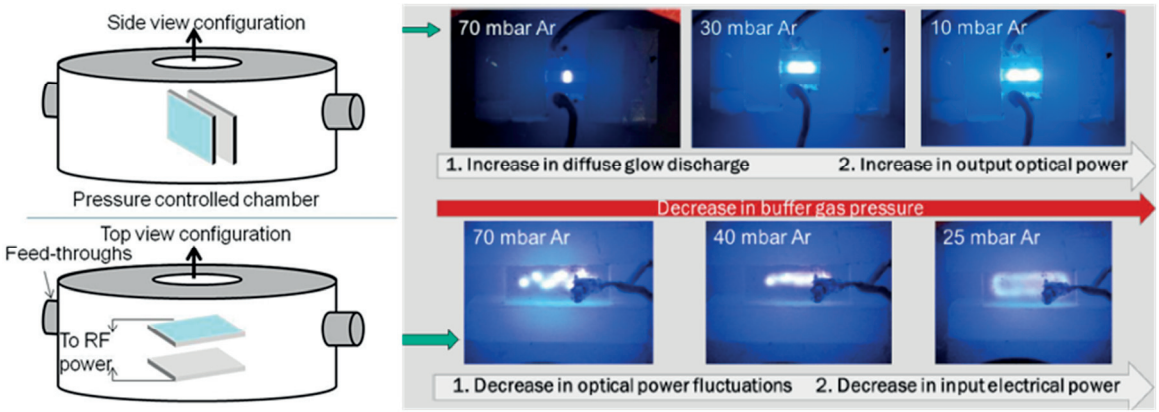

Figure 6.6: Top and side view photographs of observed discharge behavior at different pressures of Ar.

to the lowest recorded breakdown power and a low buffer gas pressure. A low buffer gas pressure is preferred for a Rb light source as a higher Rb D line intensity can be achieved at a given temperature when compared to higher buffer gas pressures.

At higher drive frequencies (at 75.7 and 465.2 MHz as shown) where the electron oscillation amplitude is much smaller than d/2, the breakdown voltage decreases but the required breakdown power is higher than at 4.4 MHz. This is primarily due to the capacitive load where the power required to produce a certain voltage across the load increases with frequency. **Hence, from a power consumption perspective, a lower drive frequency would be preferable for the Rb light source operation.**

Optical characterization of discharges

Alkali light sources for optical pumping in atomic frequency standards must provide high short-term (sub-second) stability of output optical power (<0.2 % fluctuations) with a long lifetime of several years. Depending on the cell gap conditions, drive frequency and electrode geometry, the lamp can operate in different plasma regimes and it is preferable to operate the lamp in the homogeneous diffuse glow discharge regime where the emitted optical power is highly stable. Figure 6.6 shows the observed discharges at different pressures of Argon where both the top and side views are included. It was observed that the plasma discharge enters the diffuse discharge regime only at lower pressures (values depending on the buffer gas), emitting higher optical

power per input electrical power. The stability of the emitted optical power was found to be higher at lower pressures or higher drive frequency where the electron oscillation amplitude becomes smaller than the discharge gap length.

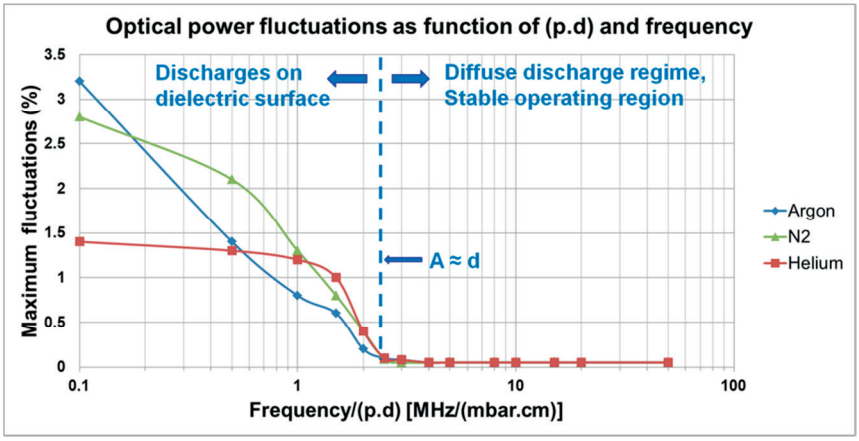

Figure 6.7: Optical power fluctuations (sub-second) observed in the discharge gap setup, as a function of drive frequency/(*pd*) ratio.

Figure 6.7 shows the sub-second optical power stability for the three test gases as a function of frequency and p.d ($f_r/(p.d)$) (measured wavelength range 400–1000 nm). It was observed that for input conditions where the calculated electron oscillation amplitude was greater than half the gap length due to a low drive frequency, the lamp was no longer operating in the homogeneous diffuse glow discharge regime, but several locally homogeneous volume discharges and surface discharges were formed on the Pyrex inner walls and they primarily contribute to the more than 0.5% fluctuations in optical power. The volume discharges occurring on the Pyrex surface were observed to be fairly large (few mm^3 on visible inspection) and homogeneous at frequencies between 4.5 and 9 MHz. At lower frequencies (2–4 MHz), the size of the discharges reduced, becoming more random in occurrence on the Pyrex surface. Due to the presence of trace quantities of liquid Rb on the inner dielectric surface, a number of surface discharges (increases with decreasing drive frequency) are formed on the Rb microdroplets and the Pyrex inner surface which have been observed to be highly fluctuating in magnitude possibly due to local field inhomogeneities and Rb droplet heating. The overall optical power from both these discharges, for a given input power, was observed to be lower than that of the diffuse glow discharge because the volume discharges have a much lower overall plasma density in a discharge gap than a diffuse discharge. The lower optical power is also because volume discharges are quickly quenched by the surface charge accumulation on the dielectric surface and hence the discharge time and power are much lesser than that of the diffuse discharge. **As seen in Figure 6.7, for mm-scale discharge gap lengths, a minimum drive frequency of around 4 MHz and a buffer gas pressure less than ~40 mbar are required to ensure lamp operation in the diffuse discharge regime.**

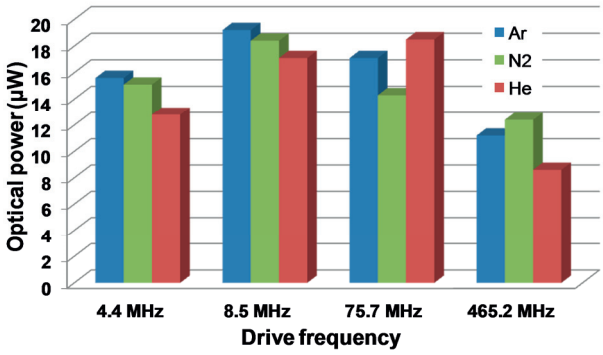

Figure 6.8: The optical power measured above the optical window for the different buffer gases at various drive frequencies for P_{in}=1W.

The optical power measured at different frequency values for the three buffer gases are shown in Figure 6.8 for a given input power (P_{in}) of 1 W. As seen from this figure, a drastic difference in optical power between buffer gases is not observed. Some interesting trends can be observed such as: **(1)** He has a higher optical power output at higher

frequencies, corresponding to the higher collision frequency of He expected at higher frequencies due to its smaller atomic diameter, **(2)** Ar and N_2 have similar power values throughout the frequency range but the value of N_2 is usually lower than Ar and this corresponds to the higher first ionization energy and molecular diameter of N_2 when compared to that of Ar, **(3)** the overall increase in the values from 4.4 MHz to 8.5 MHz is due to the decrease in the drift-dominated electron losses owing to the decrease in the electron oscillation amplitude with increasing drive frequency. At even higher frequencies, the input power coupled to the discharge gap reduces (as discussed in section 5.4.2) and hence an overall decrease in optical power is observed. **Hence, from the experimental observations, Argon is a better choice as a buffer gas for the Rb light source, with a 2 mm discharge gap length, as it offers the lowest breakdown power and highest optical power efficiency at the preferred operation range of the light source.**

Discharge behavior at different drive frequencies

For a given buffer gas, pressure and input power (hence the V_e), the drive frequency affects the electron oscillation amplitude and hence the breakdown and discharge powers. The effect of the drive frequency on the Rb light source operation was reported in section 5.4.2 and here some visual observations of the discharges, sustained in the discharge gap experiment at different frequencies, are reported in Figure 6.9 for a better understanding. The frequency and pressure values were appropriately chosen to clearly show the different discharge behaviors observed in the relevant operating range for the light source. Images corresponding to **(1)** 15 mbar here represent the 'low pressure' range (8-35 mbar) within which the discharge behaviors were similar and 70 mbar represents the 'high pressure' range (35-80 mbar). Regarding frequency, as discussed earlier, there are three interesting breakdown regions: **(1)** $A_e < d/2$ represented by 5.3 MHz, **(2)** $A_e \approx d/2$, corresponding to 10.2 MHz and **(3)** $A_e >> d/2$, represented by 36.7 MHz.

Many interesting observations can be made from Figure 6.9: **(1)** at 5.3 MHz, and for both

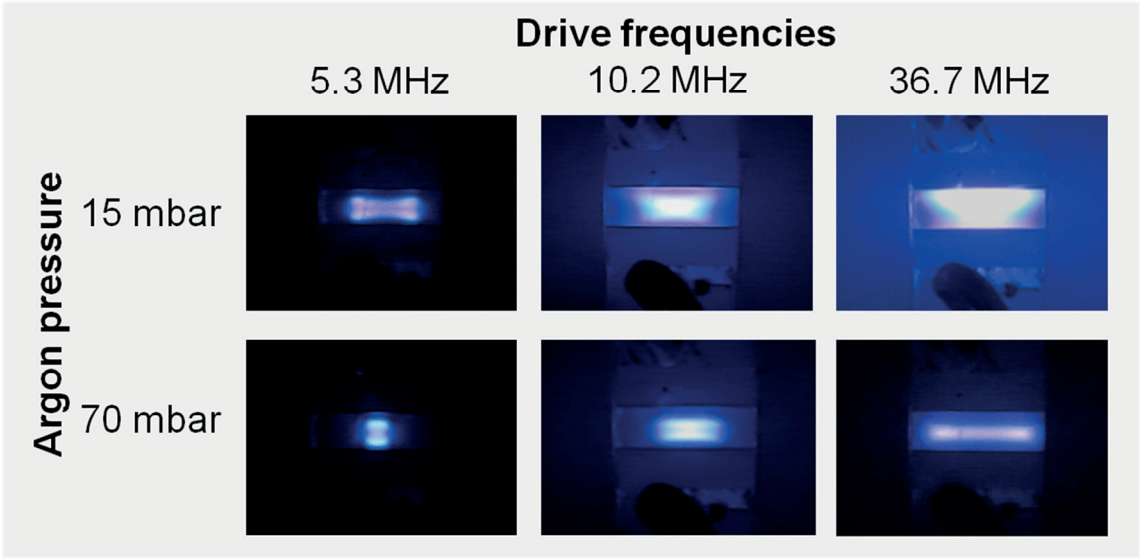

Figure 6.9: Side-view photographs of the observed plasma in the discharge gap at different frequencies and Argon pressures for a 2 mm discharge gap length and P_{in}=1 W. The increase in the diffuse glow discharge is observed at lower pressures while a decrease in the number of dielectric barrier discharges can be seen at higher drive frequencies.

pressures, it can be seen that the concentration of the discharges are higher near the dielectric surfaces with a clear dark area in the middle (when compared to the images taken at higher drive frequencies). This is most probably due to the higher electron oscillation amplitude leading to high electron bombardment on the dielectric surface leading to significant secondary electron emission and higher concentration of discharges near the Pyrex walls. Hence, in this frequency range (~<8 MHz), there is a high concentration of volume discharges that lead to high optical power instabilities. **(2)** With increase in the drive frequency, at 10.2 MHz, at both pressures, it was observed that the discharges started to concentrate more towards the centre of the discharge gap - more diffuse, less optical fluctuations and higher optical intensity. While DBDs were observed on the surface at lower pressures, they were found to be highly homogeneous with less than 0.2% short-term fluctuations. **(3)** At a much higher frequency, 36.7 MHz, the discharges are much more concentrated in the centre of the discharge gap, as expected and was much more homogeneous and diffuse compared to the lower frequencies. **(4)** At a lower pressure, the discharges were observed to be more wide spread across the discharge gap. This is probably due to the higher electron mean free path leading to higher electron movement and dispersion across the discharge gap.

6.2 COMSOL plasma discharge simulations

A plasma physics model was built in COMSOL, a finite element analysis software with a partial differential equation solver; using which it was possible to simulate the electron density, the electron temperature and estimate the output Rb D line power from a defined discharge gap for a given set of input conditions. A plasma simulation model helps estimate the Rb D output from a defined discharge gap geometry for an unlimited range of cell, electrode and electrical input conditions. In particular, it helps to understand the effect of adding a layer with a higher secondary electron coefficient on the inner dielectric walls (which was not possible to be determined experimentally) and also to estimate the light source performance at smaller discharge gap geometries if further miniaturization of the device is considered. Using the drift-diffusion equation solver pre-defined in the plasma module of COMSOL, it was possible to simulate the complete collision kinetics leading to an rf discharge, and hence the study the effects of the above parameters by keying in: **(1)** all the gaseous species in the discharge gap and their atomic/molecular properties, **(2)** all possible electron impact collisions and their corresponding collision cross-section data and **(3)** all important ionic and neutral species collisions and their corresponding reaction rate constants. The details of all the considered collisions, collisions cross-section data, reaction rate constants and their references can be found in Appendix 2.

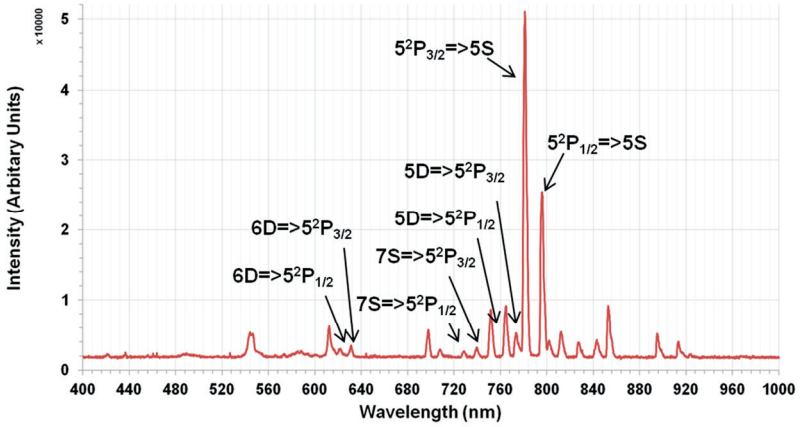

Figure 6.10: Experimentally measured optical spectrum of the CN10 cell at 100 °C showing the observed Rb lines and their corresponding transitions. All other spectral lines correspond to Ar or Cs impurities.

6.2.1 COMSOL plasma model

The discharge gap geometry was defined as a one-dimensional (1D) model in the COMSOL plasma module. [A 2D model was first built in COMSOL, however, due to several problems including memory allocation problems and very high computation times (up to few days for detailed simulations), the 1D model was chosen instead as it allowed to do the desired computations with acceptable accuracy and run-times.] Argon was considered as the buffer gas and the temperature was always 373 K for all reported data (unless otherwise stated). The collision cross-section data of both Ar and Rb were defined along with all the electron impact collisions resulting in atomic excitations and ionizations. Only the strong Rb transitions in the 400-1000 nm range were considered and the many Argon metastable excited states were defined as one single metastable state for easier computation purposes. The strong Rb lines were identified by recording the optical spectrum emitted by microfabricated light sources (the spectrum measured from CN10 is shown in Figure 6.10 as an example where the dominant Rb lines and the corresponding atomic transitions are marked). All other peak intensities correspond to Argon or Cs impurities. Further details on all the included reaction species, transitions and kinetics are reported in Appendix 2.

The dielectric constant of the Pyrex layers and the discharge gap were assumed to be 4.5 and 1 respectively and a fine plasma-specific mesh was used for the discharge gap. The secondary electron coefficient of Pyrex was fixed to be 1.5 and the initial electron density of the discharge gap was assumed to be 10^6 per m^3 with a temperature of 2 eV. One external side of the Pyrex was defined as a high-voltage RF-AC source (sinusoidal waveform) while the other external side was defined as the ground. All simulations were run for at least 40 rf cycles to allow the discharges to reach a steady-state condition.

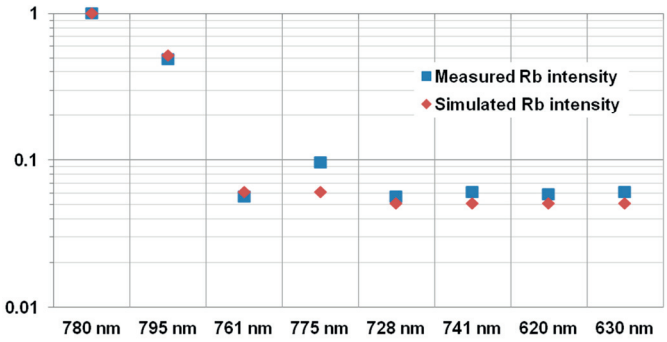

Figure 6.11: The normalized Rb line intensities in the 400-1000 nm range from both measured and simulated data corresponding to CN10 at 100 °C. The values were found to be closely matched.

Model validation

In order to use this plasma model to understand the effect of changing/optimizing cell materials and geometry conditions, it needs to first be validated by comparing it to known experimental results. The optical spectrum emitted by CN10 (shown in Figure 6.10) was obtained when the cell temperature was 100 °C. For the same cell conditions including temperature, Argon pressure and the input voltage (130 V at 8 MHz here – voltage calculated from the measured breakdown power), the plasma discharges were simulated and the density of the corresponding Rb decay transitions were recorded. The values were normalized to the strongest Rb line wavelength – the D2 line 780 nm in both cases and plotted in Figure 6.11. As it can be seen, the simulated values reasonably match with the experimentally recorded values and hence this model can be used for the intended further studies.

6.2.2 Simulation results

Several sets of simulation data were recorded for different input conditions with particular focus on understanding the electron density, electron temperature values (which could not be experimentally determined), the number density of the Rb D2 emissions and some interesting results attained from these simulations are reported here. Surface plots of the electron density and electron temperature for one of the simulations: (2 MHz, 150 V, 373 K and 30 mbar Argon) are shown in Figure 6.12. The x-axis is the space dimension denoting the Pyrex layers and the discharge gap in between them; the y-axis is time and hence the surface plot shows the discharge characteristics evolving with time. The simulation was run for 40 rf cycles (and not more due to time constraints) and a near-steady-state values could be achieved. Using these types of simulations, it is also possible to understand the spatial distribution of the electrons which can in turn indicate the suitable cell and input frequency values for the Rb light source operation where there are minimal surface discharges and hence a higher estimated optical stability. It can be seen from the figures that while there is a higher electron density near the inner dielectric surfaces, especially near the high-voltage side, the mean electron temperature is higher in the center of the discharge gap.

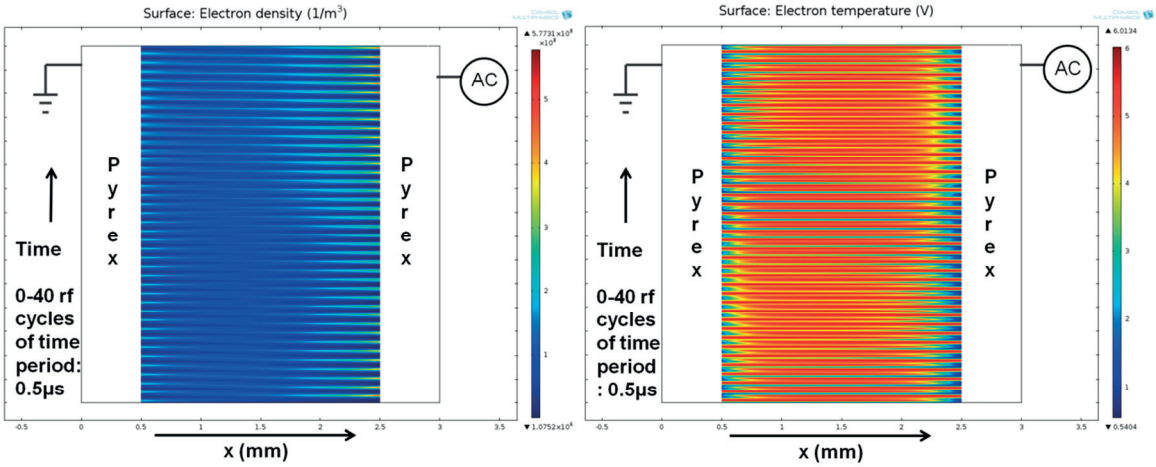

Figure 6.12: A surface plot of the electron density and the electron temperature from a 1-D discharge gap simulation with the input parameters: 2 MHz, 150 V, 373 K and 30 mbar Argon.

Five different sets of data tables are reported below to compare the electron energies at **(1)** different drive frequencies, **(2)** buffer gas pressures, **(3)** secondary electron emission coefficients, **(4)** input voltages and **(5)** at shorter discharge gap lengths while keeping all other conditions constant. The electron temperature and the electron density values reported here in all the tables are the observed maximum values in the discharge gap after 40 rf cycles. The observed density of the Rb D2 transitions for each simulation are also given which directly gives an estimate of how the output power changes with change in the respective input parameter. Table 6.1 reports on the results attained from simulating a 30 mbar Ar buffer gas pressure with an input voltage of 150 V. An optimal value of 150 V was chosen for most simulations for data comparisons as it was in the relevant range for light source operation and certainly above the breakdown voltage at the tens of MHz, as observed from the Rb light source experiments.

Table 6.1: The electron properties in the discharge gap recorded for a 30 mbar Ar and 2 mm discharge gap length with an input voltage of 150 V at different drive frequencies.

Drive frequency (Hz)	Electron temperature (eV)	Electron density (1/m³)	Density of Rb D2 transitions (1/m³)
100k	6.1	2.2E+11	3.6E+15
2M	6.0	5.7E+08	8.1E+12
13M	6.7	1.1E+09	6.9E+12
125M	6.8	4.6E+10	6.0E+12
460M	16.8	2.1E+13	2.8E+14

As observed from Table 6.1, the electron temperature was found to not vary too much between a wide frequency range (100 kHz to 125 MHz) but steadily increase after 2 MHz. The electron density however, is observed to be at least two magnitudes higher at 100 kHz when compared to the 2-125 MHz range. This should be mainly due to the significant contribution of secondary electrons emitted from the Pyrex walls leading to high electron densities near the Pyrex surface. While drive frequencies near 100 kHz have been widely tested by many researchers [175], [176], [177], especially for plasma display panels, it has never been tested on the Rb lamp-cell due to the unavailability of a suitable amplifier. However, while the data suggests that driving a Rb-lamp near 100 kHz might allow for a low-power operation, there is a high chance that there might be significant number of surface discharges due to the electron bombardment on the liquid Rb droplets inevitably present on the dielectric surface, leading to high optical instabilities and higher Rb diffusion with time. Hence, such a lower frequency might be preferable compared to the MHz operating frequency range only if Rb is not made to condense on the inner dielectric walls. Further studies will be required on that aspect before such a design can be implemented.

The electron temperature remained almost the same, possibly reducing slightly from 6.1 eV at 100 kHz to 6.0 eV at 2 MHz. A reduction is expected due to the uncompensated loss of secondary electrons from impact ionizations due to the lower drive wavelength at 2 MHz. However, the electron energy increases at higher frequencies as expected due to the higher impact collisions which also leads to a higher electron density. At 460 MHz, the electron density is significantly higher than at lower frequencies, most probably because 150 V at this frequency would correspond to a much higher power incident on the discharge gap resulting in these elevated electron energies. As the collision frequency of 30 mbar Ar was calculated to be 219 MHz for a 2 mm discharge gap, a reduction in the electron temperature was expected and hence this result was contrary to expectations.

Table 6.2: The electron properties in the discharge gap recorded for an input voltage of 150 V at 13 MHz for different Argon pressures at a 2 mm discharge gap length.

Argon pressure (mbar)	Electron temperature (eV)	Electron density (1/m³)	Density of Rb D2 transitions (1/m³)
0.01	68.1	2.1E+06	2.6E+09
2	28.3	2.4E+07	6.5E+11
30	6.7	1.1E+09	6.9E+12
70	5.1	4.0E+08	1.4E+13

Table 6.2 shows the observed electron properties for different Argon pressures for an input of 150 V at 13 MHz. The electron temperature significantly reduced with increasing gas pressure and these elevated electron energies at the low pressures (≤2 mbar) must be because of the very

low number of momentum transfer collisions with neutral species leading to high momentum gain and kinetic energy by the electrons. The cell CN11 had 2 mbar Ar and it could be ignited to emit discharges only few times at two drive frequencies: 11.5 MHz and 31 MHz and the plasma extinguished within seconds of ignition. Hence, this simulated value might suggest that while the electrons might have had high energies, there might have not been enough number of electrons to sustain the rf discharge. As observed, the electron density increases significantly at 30 mbar which is probably why the breakdown power is lower around this pressure range, as observed for CN3. A higher breakdown power recorded for CN1 and CN2 correspond to the decrease in both the electron density and temperature at 70 mbar. Hence, the suitable pressure range for a 2 mm discharge gap seems to be between few mbar-tens of mbar, which corresponds well with the experimentally measured values.

Table 6.3: The electron properties in the discharge gap recorded for an input voltage of 150 V with 30 mbar Ar and 2 mm discharge gap length for different secondary electron emission coefficients of the inner dielectric walls.

Drive frequency (Hz)	**γ = 1.5**			**γ = 3**		
	Electron temperature (eV)	**Electron density (1/m³)**	**Density of Rb D2 transitions (1/m³)**	**Electron temperature (eV)**	**Electron density (1/m³)**	**Density of Rb D2 transitions (1/m³)**
2M	6.0	5.7E+08	8.1E+12	6.0	1.5E+09	1.2E+13
13M	6.7	1.1E+09	6.9E+12	6.8	1.9E+09	7.5E+12

One of the useful studies using COMSOL was to understand the improvement in the light source performance achievable by adding a secondary electron emissive (SEE) material on the inner dielectric surface. At higher drive frequencies (approximately more than 10 MHz for a 2 mm discharge gap and tens of mbar buffer gas pressure), the effect of this additional layer would have a minimal effect on the light source's performance because of the low electron oscillation amplitude. However, as a low drive frequency is preferred for low-power operation, such an addition could potentially reduce the power required for breakdown significantly and hence could possibly offer a better solution in the future. Table 6.3 reports on the data simulated to understand these effects discussed above. For a drive frequency of 2 MHz, the electron density almost triples with the addition of a layer with a SEE coefficient, γ=3, showing a promising potential for breakdown at a lower voltage. The increase is less pronounced at a higher frequency, 13 MHz, as expected but still improves the number of electrons available for impact ionizations. The electron temperature however does not increase significantly, as expected.

Table 6.4: The electron properties in the discharge gap with 30 mbar Ar and a 2 mm discharge gap length with different input voltages when the drive frequency is 13 MHz.

Input voltage (V)	**Electron temperature (eV)**	**Electron density (1/m³)**	**Density of Rb D2 transitions (1/m³)**
30	4.3	1.0E+08	4.6E+10
150	6.7	1.1E+09	6.9E+12
500	29.0	6.2E+17	5.7E+18

There already exist many such materials with a high γ value [178], [179], such as MgO, MgF_2 and other compounds and they are used in discharge light sources and also in plasma display panels. The main obstacle here is that most of these materials might not be compatible with Rb and

hence unsuitable for the Rb light source. Thus, further studies on the reaction rates of Rb with these materials are required to identify a suitable material with a high γ value for the Rb lamp.

Table 6.4 reports on the change in both the electron temperature and density with increase in the applied rf voltage. A relevant frequency of 13 MHz was chosen and both the electron properties were observed to not increase significantly at 150 V when compared to the data at 30 V. However, a drastic increase was found at 500 V, which however is only for reference and will most probably never be needed for the light source operation.

Table 6.5: The simulated electron properties on reducing the discharge gap length when the drive frequency is 13 MHz, 150 V input voltage and 30 mbar Ar buffer gas pressure.

Discharge gap (mm)	**Electron temperature (eV)**	**Electron density ($1/m^3$)**	**Density of Rb D2 transitions ($1/m^3$)**
2	6.7	1.1E+09	6.9E+12
1.5	7.9	1.8E+09	7.4E+12
0.8	10.0	4.1E+09	1.1E+13

As size, along with power, is of prime importance for the light source design, a further miniaturization of the light source, while not mandatory for miniature-scale clocks, will be welcome for chip-scale clocks. However, power is the first concern for the light source and hence a further down-scaling of the discharge gap length would be considered only if the same performance of the light source could be achieved with a lower or same power requirement. Table 6.5 reports on the electron properties for a given set of conditions (30 mbar Ar, 150 V at 13 MHz) for different discharge gap lengths. It can be seen that both the electron temperature and the electron density increases with decrease in the discharge gap length possibly due to the higher electric fields incident on the gap and the higher contribution of the secondary electrons than electrons losses into the walls. The disadvantage of this further miniaturization would again be the condensed Rb droplets interfering with the electrons near the walls. A much higher drive frequency would reduce this effect but would require a higher input power to achieve the same said voltage. Hence, overall, a lower breakdown power can be expected at lower discharge gap lengths for a 30 mbar Ar pressure at 13 MHz condition but also necessary steps need to be taken to avoid optical fluctuations due to the expected Rb surface discharges on the dielectric walls.

Chapter conclusions

This chapter reported on the discharge gap experimental setup and its results for studying the effects of varying the buffer gases, pressures, discharge lengths, surface area and cell wall conditions on the DBD lamp performance, which couldn't be extensively tested using microfabricated Rb cells as such a large number of cells could not be microfabricated with the available resources in the time-frame of this research.

The discharge gap experiments helped identify all the cell parameters that can be changed to further optimize the DBD lamp power efficiency and optical stability for efficient optical pumping in atomic clocks:

- For mm-scale discharge gap lengths, a minimum drive frequency of 4 MHz and a buffer gas pressure less than 40 mbar are required to ensure a stable and diffuse optical output

- Among the tested gases, Argon is a better choice as a buffer gas for the Rb light source, with a 2 mm discharge gap length, as it offers the lowest breakdown power and highest optical power efficiency at the preferred low-pressure operation range of the light source.
- The gas pressure, discharge gap length and drive frequency values need to be chosen such that $A_e \approx d/2$, for an optimum light source operation as a suitable trade-off between power consumption, optical stability and optical power efficiency occurs in this range.

A plasma model of the Rb and Argon discharge in a Rb DBD light source was simulated using COMSOL to understand the electron properties and the expected Rb output at different cell and frequency conditions. The light source performances after wall-coating the inner dielectric layers with a higher secondary electron coefficient and after further miniaturization were estimated. The model was validated by comparing it to the measured Rb spectral data from a light source with the same input conditions. These results help identifying the next steps that could to be taken to further optimize the light source performance in terms of size and power consumption and potentially engineer it for even smaller chip-scale atomic clock applications.

Chapter 7 Optical pumping experiments

The final goal of the Rb light source is to integrate as an optical 'pump' into a miniature atomic clock or in other miniature quantum sensors such as the atomic magnetometer. Experiments performed and the test setups built for demonstrating the optical pumping ability of Rb light sources with a microfabricated Rb resonance cell, are reported in this chapter. A magnetometer pumping experiment setup was built for this purpose and is described in section 7.2. A Rb D1 laser and glass-blown ICP Rb lamps were used as reference light sources to record the optical pumping signals at different input conditions and confirm a functional built test-setup. A successful optical pumping signal with the microfabricated Rb light source could not be achieved within the research time-frame, however the experiments performed and the steps that could be taken towards achieving this goal are presented here in this chapter.

7.1 Magnetometer optical pumping

This section reports on the magnetometer optical pumping test setup built for demonstrating the optical pumping ability of the Rb light source. First, the background experiments performed using an atomic clock pumping test setup are described. The reasons for choosing this test setup, the principles behind atomic double-resonance magnetometers and the details of the test setup built are described in this section.

7.1.1 Background: atomic clock DR experiment

As the primary target application of the microfabricated Rb light source is the atomic clock, it is ideal if the lamp could be tested in an atomic clock test setup for demonstrating its optical pumping abilities. A double-resonance atomic clock test setup, for testing the optical pumping characteristics of lasers, already existed at the Laboratoire Temps-Fréquence, University of Neuchâtel. The setup has already been confirmed to be functional from the pumping results

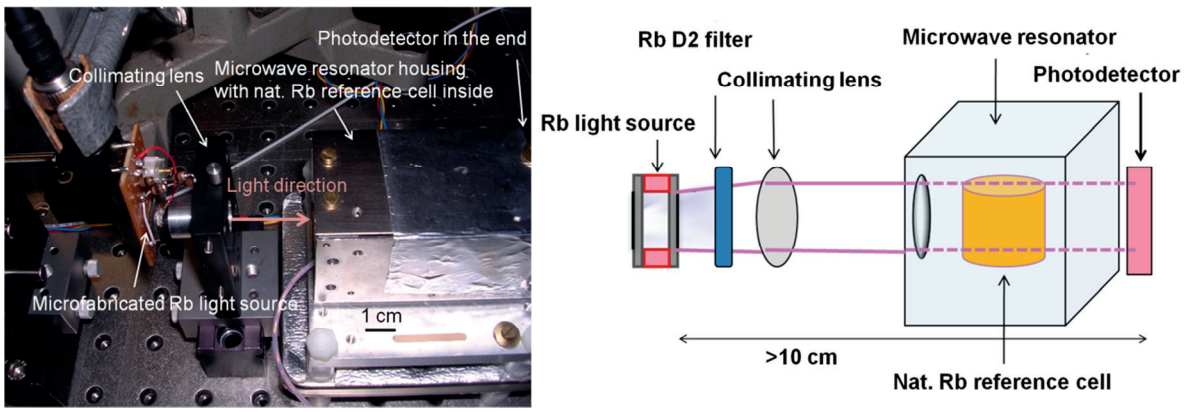

Figure 7.1: The DR atomic clock test setup (photograph and schematic) to test the optical pumping characteristics of the microfabricated Rb light source at LTF, University of Neuchâtel.

achieved with the Rb D1 lasers. Here, the laser was replaced with the microfabricated Rb light source to test the lamp's optical pumping characteristics. Several trials of this experiment were performed between 2010 and 2011 with constant improvements in the lamp output power characteristics after learning from each trial's result. However, a successful pumping signal could not be achieved using this light source and the DR test setup, but the reasons were identified. The test setup and the results are discussed below, mentioning the lessons learnt from the trials.

The setup, shown in Figure 7.1, constituted of a microwave resonator housing, placed on an optical table, with a nat. Rb resonance cell placed inside and a photodetector at the rear end of it. The microwave interrogation field was frequency-modulated and the photodiode input was connected as input to a lock-in-amplifier, whose output was in-turn connected to an oscilloscope for monitoring the pumping signal. The resonance cell was heated to temperatures between 80-100 °C. The microwave housing had a hole on the front end for light input, before which the light source was placed and carefully aligned using optical mounts. A suitable collimating lens (focal length: 3 cm) was inserted between the light source aperture and the microwave housing to maximize the light coupled to the resonance cell. The cell CN1 was used and was driven at 3.7 MHz to emit more than 10 µW of optical power on the Rb D2 line (measured within few mm from the light source surface). The main problems encountered in the first trials were: **(1)** the high instability of the output optical power from the light source and **(2)** the low Rb D line optical power incident on the resonance cell (<few µW). The first problem was identified to be because of the low drive frequency that led to the significant formation of surface DBDs resulting in high fluctuations in optical power. It was solved by choosing a drive frequency more than 8 MHz and a 30 mbar Ar filled Rb cell. To solve the second problem, inductors with a high-current rating (11 A rating) was used for the LC-load matching to allow for high power lamp-operation in the next trial. The cells CN2 and CN3 were used as the lamp-cells with EL4 electrodes for the tests, driven at 5.6 MHz and 17.5 MHz respectively to emit more than 30 µW of stable (<0.2% sub-second fluctuations) optical power on the Rb D2 line (measured within few mm from the light source surface). An aspheric collimating lens (details mentioned below) was also used to improve the light output on the resonance cell. However, the light incident on the resonance cell was still probably not good enough for a detectable signal (< few µW) and no successful optical pumping signal was observed.

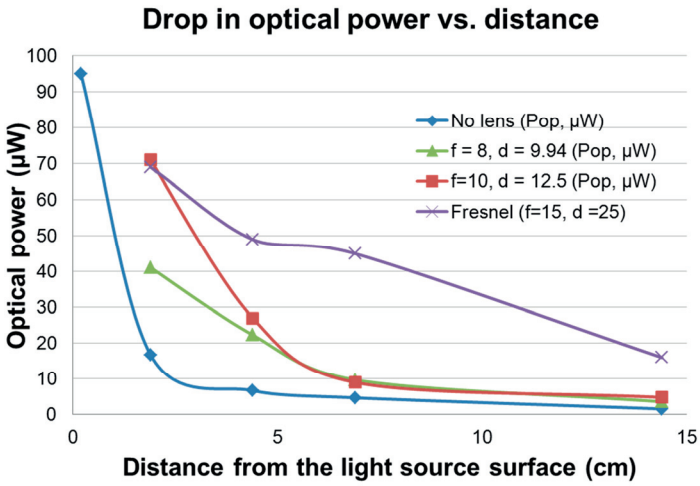

Figure 7.2: The drop in optical power versus distance from the light source surface. The focal length and diameter are in millimetres. The measured data points are marked and line plots were chosen for easier understanding.

One of the main problems encountered in this test setup was the distance between the light source and the resonance cell (and the photodetector). It was more than 10 cm and as the lamp-cell was a diffuse light source, the efficiency of light coupled to the resonance cell was negligible without the use of an appropriate collimating lens. As seen from Figure 7.2, only a few % of light is actually coupled to the resonance cell if the distance is more than few cm and no optics are used. The ideal lens here would have the lowest focal length and the highest diameter, with the ability to withstand a high temperature (at least up to 125 °C). It also needs to be an imaging system to increase the amount of Rb atoms in the resonance cell interacting with the emitted Rb light. Two different aspheric collimating lenses (Thorlabs Inc.) were shortlisted and studied – **(1)**

with focal length 10 mm and a diameter of 12.5 mm, **(2)** with focal length 8 mm and a diameter of 9.94 mm. While they showed a significant improvement in the optical power at low distances (<4 cm), at distances of 8-10 cm the improvement was insignificant. Also due to the inflexible nature of the atomic clock test setup, it was also not possible to reduce the distance to any lesser than 8 cm. Hence, a DR test setup with a shorter working distance was needed for demonstrating the optical pumping ability of the lamp and thus the atomic magnetometer test setup was conceived for this purpose.

In the envisioned chip-scale DR clock (Figure 1.3), the light source will be within millimeters from the resonance cell and hence ample light will be available for optical pumping in that situation. However, such a miniature microwave cavity is still under research and hence such a chip-scale atomic clock test setup was not available for testing the lamp's optical pumping characteristics. The atomic clock requires interrogation in the GHz range and only a large microwave resonator was available for testing, however an atomic magnetometer requires interrogation typically in the kHz range and a much more compact setup using Helmholtz coils is possible. The principles of this concept and the setup built are discussed in the following section.

A Fresnel lens, with focal length of 15 mm and diameter of 25 mm, was tested later as it offers the advantage of a collimating lens with a higher diameter to focal length ratio when compared to aspheric lens. It can be observed from Figure 7.2 that for longer distances (8-10 cm), more than 35% of optical power can be coupled to the resonance cell when using the Fresnel lens and hence it is a better choice for future atomic clock DR pumping experiments.

7.1.2 Atomic double-resonance magnetometry

The microfabricated Rb light source, is not only useful for realizing chip-scale DR atomic clocks, but also many other applications, especially chip-scale Rb magnetometers [180]. Miniature or chip-scale magnetometers are of high interest for several portable applications including navigation, geophysical mapping [181], magnetic mapping of the human heart beat [182] and magnetoencephalography [183] due to their small volume (<few cm^3), easy handling abilities and low power consumption (<tens of mW). A magnetometer here can be used for measuring the strength of the magnetic field in a given direction. The basic principles for testing and developing a chip-scale Rb DR magnetometer using the M_z technique are discussed below.

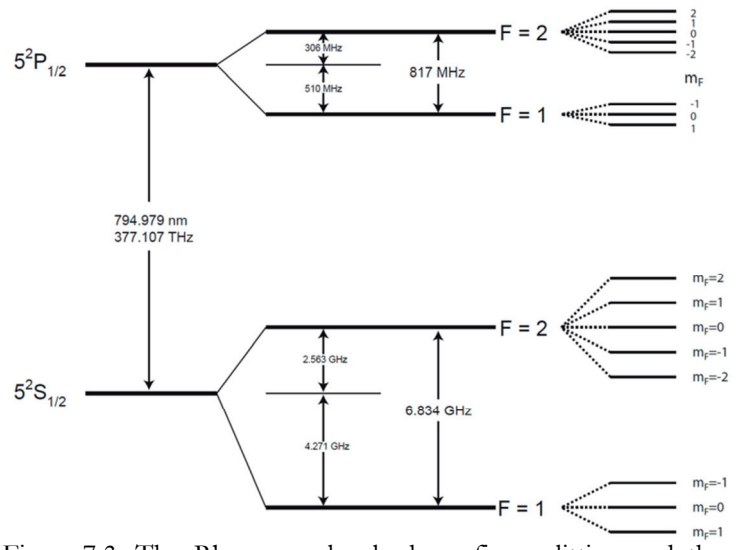

Figure 7.3: The Rb energy levels, hyperfine splitting and the Zeeman splitting in the presence of a magnetic field [185].

In a Rb atom, the ground and excited states split into hyperfine levels as the two states have different angular momentum or spin [184]. These hyperfine levels further split to Zeeman levels

in the presence of a magnetic field as the magnetic field changes the angular momentum of the hyperfine states, as shown in Figure 7.3 [185].

Fig represents the ground ($|g\rangle = |F, M\rangle$) and excited states ($|e\rangle = |f, m\rangle$) of Rb atoms [186] placed in a static magnetic field, B. The atoms precess about the B field axis with a frequency called the Larmor frequency, ω_L and the energy separations/differences of Zeeman levels are directly proportional to the B field strength, such that:

$$B = \omega_L/\gamma \tag{7.1}$$

where γ is termed the gyromagnetic ratio. γ is approximately equal to 7 kHz/μT for ^{87}Rb and 4.66 kHz/μT for ^{85}Rb from reported literature [187]. If σ+ (or σ-) circularly polarized Rb D1 (or D2) light is irradiated on these Rb atoms, they are excited from various Zeeman levels from $nS_{1/2}$ ($|g\rangle$) mF to $nP_{1/2}$ ($|e\rangle$) mF+1 levels because the circular polarization adds angular momentum to the excitations (as shown in Fig). Excited atoms decaying back to their ground states |F, M≠F (M≠-F for σ-) can be excited again but the atoms in the M=F (M=-F for σ-) 'dark state' remain trapped there as these atoms cannot excite to higher states. The Rb atoms now become transparent to the irradiating light from the light source. If the atoms are exposed to an oscillating magnetic field B_{rf} with a frequency $\omega_{rf}=\omega_L$, then the atoms in the $|F, M=F\rangle$ state jump to M=F-1 and lower states and hence an absorption in the incident Rb D light will resume [186]. The exact determination of ω_{rf} corresponding to the light absorption would yield ω_L and hence the strength of the B field using equation (7.1). This is the Rb magnetometry principle and the test setup used to realize this and demonstrate the Rb lamp's optical pumping ability is described in the following section.

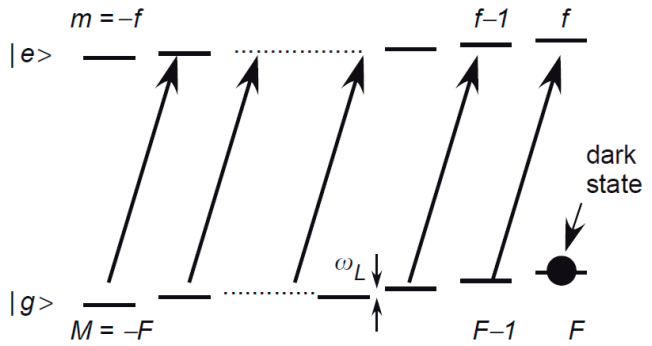

Figure 7.4: Representation of the ground and excited states of Rb atoms in the presence of a static magnetic field and the transitions induced by pumping these atoms with circularly polarized light [186].

7.1.3 Magnetometer test setup

A magnetometer test setup, following the atomic magnetometry principles discussed in the previous section, was built for demonstrating the optical pumping abilities of Rb light sources and the schematic of this test setup is shown in Figure 7.5. There are two ways to realize the test setup: **(1)** sweeping the electromagnetic field frequency while keeping a constant magnetic field and **(2)** sweeping the magnetic field strength and keeping a constant electromagnetic field frequency. The method **(1)** is used here in this research as it is a more direct approach in determining the magnetic field strength.

The test setup was a vertical stack alignment where all the components were held and aligned using a custom-milled POM parts-cage system, as shown in Figure 7.6. The distance between the light source and the final photodetector was reduced to less than 4 cm and hence a high light coupling efficiency could be achieved with this test setup (refer section 7.1.1).

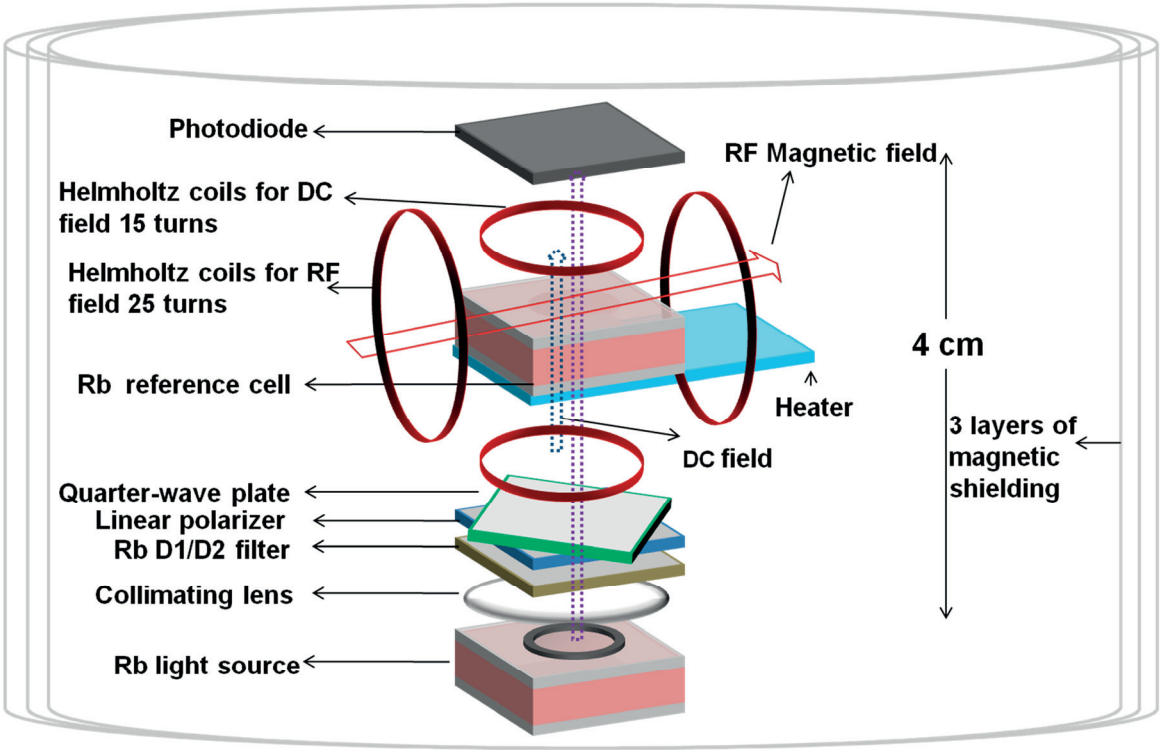

Figure 7.5: The magnetometer test setup schematic showing the vertical stack configuration of the various components.

The setup constituted of (from bottom to top): **(1)** the microfabricated Rb light source placed on a heater whenever necessary, **(2)** a collimating lens (the aspheric and Fresnel lens discussed in section 7.1.1 were used), **(3)** a Rb D1 or D2 filter, depending on the wavelength needed, **(4)** a linear polarizer, **(5)** a quarter wave plate placed 45° to the linear polarizer plane for circularly polarized light, **(6)** the resonance cell arrangement and **(7)** a Si broadband photodiode. The resonance cell arrangement includes the Rb resonance cell, cell heater placed on a POM platform and the Helmholtz coils for both the DC and RF interrogation fields. The Rb resonance cell was CN5 – a microfabricated nat. Rb cell with 100 mbar of N_2 as buffer gas, placed on a heater with a hole in the centre for allowing the light to pass through. A resonance cell with a high buffer gas pressure was preferred to reduce the number of depolarizing Rb atomic collisions with the cell walls and an increased pumping efficiency [188]. The heater was an LTCC serpentine heater (H3) shown in Figure 5.3. A DC field was established

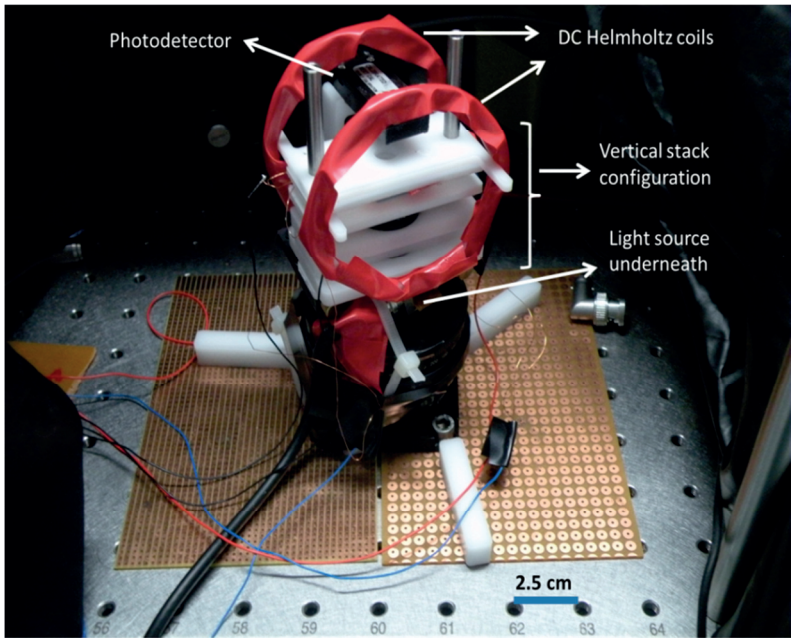

Figure 7.6: A photograph of the realized magnetometer test setup with the vertically aligned cage system using milled POM parts.

by placing two custom-made 15 turns Helmholtz coils of diameter 2 cm (frame material: PTFE), above and below the Rb resonance cell (and heater in such a way that the distance of separation between the coils equaled the radius of the coils for a highly homogeneous field. The coils were connected to a low-noise current supply to produce steady DC fields up to several hundred μT at the centre. The RF interrogation field was established by two similar Helmholtz coils but of diameter 10 cm and 25 turns and placed at 90° to the DC field and the light propagation direction. A 45° angle was also used in many experiments, because of the higher signal-to-noise in detection [188] but all the results reported here in this thesis correspond to the 90° placement.

The whole setup was magnetically-shielded by three cylindrical layers of mu-metal. The height of all the shielding layers were 38 cm (15 inches) and the diameter of the layers were 15 cm, 18 cm and 20 cm. The ambient DC magnetic field without any shielding was around 78 μT. After shielding, the DC field was reduced to less than 1.5 μT where the Rb resonance cell was placed. The whole setup including the magnetic shielding layers was covered by a Faraday cage (described in section 5.1) when necessary and a black cloth-optical cage to remove all background light noise.

7.1.4 Signal noise reduction using FM

The FM field modulation technique, widely used by other researchers [188], [189], is used to frequency modulate the applied radio-frequency EM field for a high SNR detection of the pumping signal.

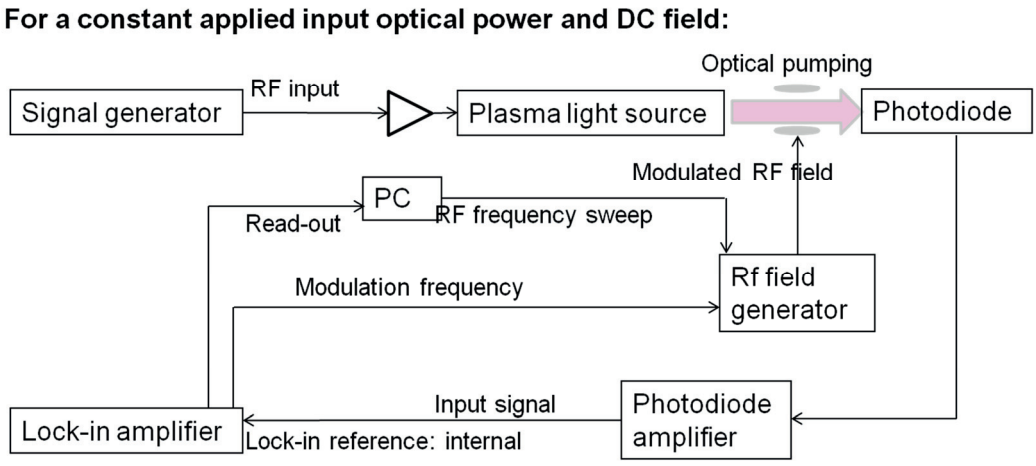

Figure 7.7: The FM of the rf field technique to produce a high SNR pumping signal and avoid the influence of optical power fluctuations on the signal detection.

An LIA was used to generate the modulation frequency to the rf signal generator that was connected to the Helmholtz coil producing the rf field (Figure 7.7). The modulation frequency was chosen to be 188 Hz to avoid any ambient harmonic interferences and also to have an acceptable time constant (100-300 ms or $>20/f_m$) in the LIA [f_m = modulation frequency]. The frequency deviation was chosen to be less than half the expected line width for best results and hence values between 10-20 kHz were chosen typically. The photodiode output (analog voltage output from the photodiode amplifier) was connected as the input to the LIA and the output of the LIA was monitored through an oscilloscope and also recorded in a PC using a National

Instruments A/D converter and LabVIEW. The results obtained from this technique are discussed in section 7.2.2.

7.2 Optical pumping results

This section reports on the pumping results obtained using the magnetometer test setup described in the previous section. The magnetometer pumping signals obtained from using: **(1)** a Rb D1 wavelength laser without any FM or LIA and **(2)** conventional Rb ICP lamps with the FM technique are reported here. The preliminary tests and observations from optical pumping tests using the microfabricated light source are also discussed.

7.2.1 Rb D1 laser pumping test

In order to first verify the functionality of the realized magnetometer setup, a Rb D1 laser was used instead of the microfabricated light source in the schematic shown in Figure 7.5. The pumping experiment was performed with Dr. Christoph Affolderbach at LTF, University of Neuchâtel, where the modified test setup, shown in Figure 7.8, was placed inside a triaxial Helmholtz coil cage to cancel out all background/external DC fields. Circularly polarized light from the Rb D1 laser was made incident on the heated microfabricated nat. Rb resonance cell (CN5) and the light was measured by a photodetector positioned behind the cage setup.

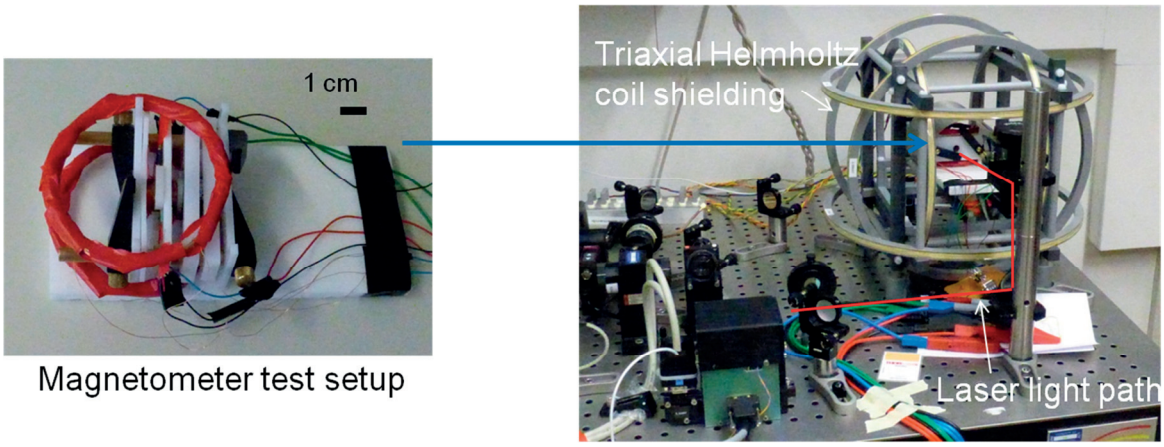

Figure 7.8: The modified magnetometer test setup placed inside a triaxial Helmholtz coil shield stage for the Rb D1 laser pumping test.

The pumping results from the laser-magnetometer experiment for different applied DC fields of 85 μT, 65 μT and 48 μT are shown in Figure 7.9. The CN5 resonance cell was heated with DC power to 110 °C (to allow for ~25% absorption of the Rb D light for efficient pumping), the optical power emitted from the D1 laser was 600 μW and the voltage across the RF Helmholtz coils was 70 mVpp (resistance of the coils: ~1 Ω). The corresponding RF field was measured be in the few μT range when measured at the frequency range less than 75 kHz (the maximum detection range of the 3-axis AC gaussmeter was up to 75 kHz). The applied radio-frequency field was swept from 1-800 kHz as a linear sweep with a sweep time of 8 seconds. Clear Rb absorption signals could be observed with the peaks occurring at different radio-frequencies, as expected for the different applied DC field conditions. Many other parameters were also varied for better understanding of the reference values: **(1)** the strength of the applied RF field, **(2)** the minimum Rb D1 optical power needed for a detectable pumping signal and **(3)** the effect of the

DC powered cell heater on the pumping signal. The linewidths of the absorption lines, as observed in Figure 7.9, was more than 80 kHz at the half-height point. This could be significantly reduced to less than 10 kHz by reducing the strength of the rf field and removing the inhomogeneous DC magnetic field created by the DC-powered serpentine design reference-cell heater. The minimum optical power needed to observe a pumping signal was observed to be around 10 μW of Rb D1 as shown in Figure 7.10. While it is possible to produce 10 μW of Rb D1 from the microfabricated light source, a lower power requirement would allow for a lower power operation of the light source. The rf field FM technique using a LIA would allow for a high SNR at much lower optical powers and hence this was first investigated using a conventional Rb ICP whose results are reported in the next sub-section.

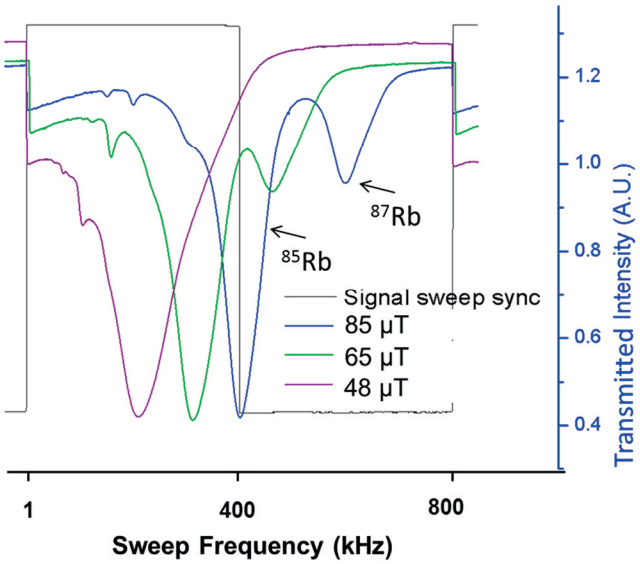

Figure 7.9: The pumping test results using a Rb D1 laser showing the Rb absorption signals. The DC current through the DC field coils shown correspond to 85 μT, 65 μT and 48 μT DC fields respectively. The intensity (Y-axis) values correspond to the voltage measured across a 100 kΩ resistor connected to the photodetector.

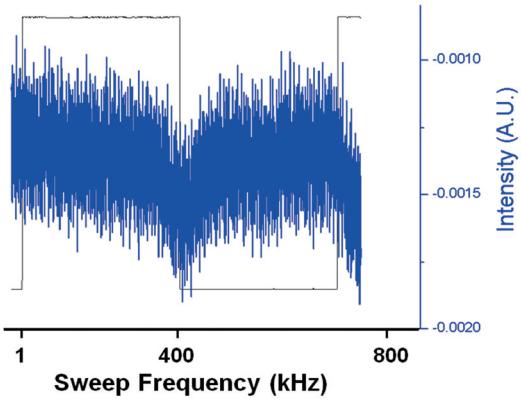

Figure 7.10: The pumping signal when the optical power of the Rb D1 laser was 10 μW. A detectable magnetometer signal without the rf field FM technique can be understood to be around 10 μW.

7.2.2 Optical pumping tests with Rb discharge lamps

The pumping results obtained using a conventional 1 cm diameter glass-blown Rb discharge lamp. The lamp was inductively coupled with an external spiral excitation coil around it and being driven at 125 MHz. The pumping tests and observations from using a microfabricated Rb DBD lamp are also discussed in this sub-section. The test setup, shown in Figure 7.5, was used by replacing the light source with a nat. Rb ICP lamp (shown in Figure 1.5). Two lamp-cells (nat. Rb and ^{87}Rb with a few mbar of an unknown buffer gas) and the excited circuit were borrowed from LTF, University of Neuchâtel for the pumping experiments. The rf field FM technique, as shown in Figure 7.7, was used where the following settings were used after optimization: Modulation frequency: 188.5 Hz, frequency deviation: 10 kHz, lock-in time constant: 100 ms, lock-in sensitivity: 500 μV, rf sweep step size: 1 kHz, rf sweep wait time for each frequency step: 600 ms. Main results: **(1)** successful pumping results could be achieved with both Rb D1 and D2

lines, where the signal contrast was found to be marginally better in the case of D1 **(2)** Only few μW (3.5 μW for D1 and 5 μW for D2) was observed as needed for a detectable pumping signal using the FM technique for both D1 and D2 lines.

The pumping signal, the magnitude (R) of the signal vector obtained from the LIA for a DC magnetic field of 25 μT is shown in Figure 7.11. The resonance cell here was heated by an AC power supply at 1.07 kHz to a temperature of 70 °C and switched off just before the radio-frequency field was swept from 10 kHz to 250 kHz. Hence, the actual temperature of the heater was around 52 °C when the ^{85}Rb absorption was recorded and around 46 °C when the ^{87}Rb was recorded.

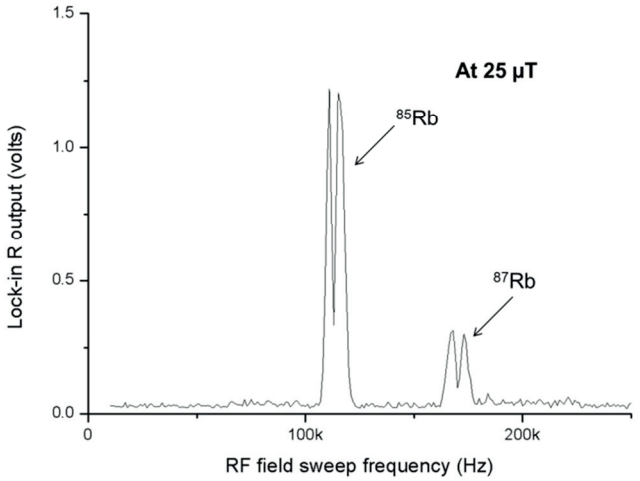

Figure 7.11: The pumping signal recorded using the LIA (R output) and the rf field FM technique from a nat. Rb ICP lamp at a DC magnetic field of 25 μT.

An AC heater was first used instead of a DC heater because a DC-powered heater would produce magnetic field inhomogeneities in the DC range, hence disrupting the homogeneity of the applied DC field (using the Helmholtz coils) at the interrogation area of the Rb resonance cell. However, it was noticed that an AC-powered heater completely suppressed the absorption signal when powered at any frequency between 50 Hz to 10 kHz. This is shown in Figure 7.12 where the absorption signal at different temperatures and when the AC-heater is switched ON are shown. It is not very clear why exactly this should happen, other than the expected random inhomogeneities caused by the AC supply frequency (and its multiple harmonics). A similar effect was also observed when applying DC power for heating. Hence, to avoid this signal suppression, the heater had to be switched off before measuring the signals.

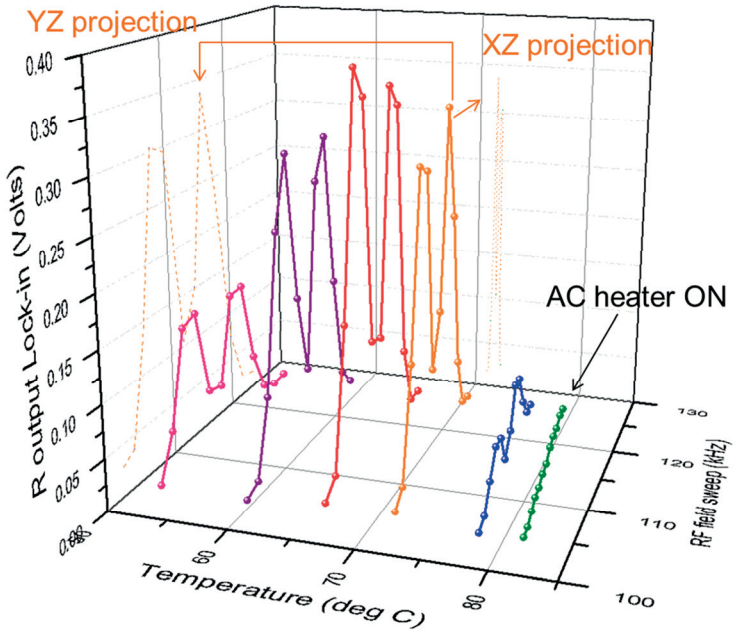

Figure 7.12: The measured ^{85}Rb pumping signals at 110 kHz at different cell temperatures. When the AC heater was switched on, the signal was highly attenuated or almost vanished possibly due to the field inhomogeneities introduced by the heater.

Discussion on the pumping experiments with Rb DBD lamps

The magnetometer test setup built was verified to be functional, as confirmed by the pumping results attained from the laser and conventional Rb lamp tests. The expected linewidth, the input

rf field conditions, the lock-in settings and all other parameters were understood from the previous experiments, which play as important starting points for the DBD lamp pumping tests. Several pumping experiments with the microfabricated Rb lamps were conducted with the FM technique, using both nat. Rb and ^{87}Rb lamp-cells, with an optical power up to 20 μW on the Rb D2 and 16 μW on the Rb D1 line and a stabilized power output with less than 0.2% sub-second fluctuations but a successful optical pumping signal could not be achieved.

There were many reasons suspected over time for these unexpected pumping results but most of them were eliminated: **(1)** the optical power fluctuations of the light source – [it was stabilized to the same order as the Rb ICP lamp and hence was not the limiting factor]; **(2)** the optical power was not enough – [an optical power of more than 10 μW on the Rb D lines could be produced from the DBD lamp and even a few μW from the Rb ICP could produce a pumping signal]; **(3)** for a detectable signal contrast, only D1 could be used – [the D1 line has been reported to be highly efficient for optical pumping compared to the D2 line in alkali vapor magnetometers [188]. As the Rb DBD lamps have Argon as buffer gas, one of the Argon spectral lines coincides with the Rb D1 line (794.8 nm for Rb D1 and 794.82 nm for Argon) which could probably make it less efficient for pumping due to self-absorption and Doppler broadening of the D1 line. However, the D2 line has no such interferences and a pumping signal could be achieved with D2 line pumping using the Rb ICP lamp.].

Two possible reasons have been narrowed down after all trouble-shooting experiments: **(1)** the cell electrodes interfering with the light field and/or the magnetic field and **(2)** inadequate optimization of the frequency modulation parameters. The modulation frequency used was 188.5 Hz while the frequency deviation was at least more than 5 kHz during tests. Hence, it is possible that the modulation parameter, ΔR, was not optimum to detect the absorption [190]. More steps are necessary in this direction to improve the signal contrast and possibly record a pumping signal with the DBD lamp. Also, the M_x technique has been shown to yield a higher signal contrast when compared to the M_z technique [186], [185] and hence might be a better solution to demonstrate the optical pumping ability of the DBD lamp.

Chapter conclusions

This chapter reported on the efforts taken towards establishing the optical pumping abilities of the microfabricated Rb DBD light source. The DBD lamp-cells were tested in a double-resonance atomic clock test setup for microwave interrogation but a successful pumping signal could not be observed after several trials. Many improvements in the drive circuitry and the necessary optics were implemented but due to the high working distance of ~10 cm between the light source and the resonance cell, enough light could not be coupled for a detectable signal. A double-resonance test setup following the principles of atomic Rb magnetometry was developed to avoid this problem and a Rb D1 laser and conventional Rb ICP discharge lamps were tested for a reference pumping signal. The optical pumping was successfully demonstrated using both these light sources and valuable information regarding the optical power, field strengths and expected signal contrasts for different input conditions were learnt from these experiments. It was observed that only few μW of the Rb D1 or D2 line was required for a detectable signal, which highly encourages the potential of the microfabricated Rb light source in low-power chip-scale applications. Optical pumping tests were conducted using the Rb DBD lamp but a

successful pumping signal could not be demonstrated possibly because of the cell electrodes interfering with the light field and/or the magnetic field and/or inadequate optimization of the frequency modulation parameters. It is necessary to resolve these problems to achieve a successful pumping signal with the Rb DBD lamp. Also, the M_x technique has been shown to yield a higher signal contrast when compared to the M_z technique and hence might be a better solution to demonstrate the optical pumping ability of the DBD lamp

Chapter 8 Conclusions

The motivation behind this research was to extend the advantages of the double-resonance interrogation technique to miniature atomic clocks to improve the performance of a broad range of portable applications. One of the main factors preventing this extension, other than the difficulty of creating a high-Q miniature microwave cavity, was the Rb ICP discharge lamps' difficult-to-integrate non-planar geometry and power consumption of several Watts. A low-power consuming planar mm-scale Rb discharge light source, even though previously deemed a challenge, would help enabling a chip-scale DR atomic clock. Developing and studying such a miniature Rb light source was the primary objective of this research.

The design, development and characterization of a novel microfabricated low-power consuming mm-scale Rb dielectric barrier discharge (DBD) light source, for optical pumping in miniature atomic clocks and magnetometers, was presented in this thesis. The goal of this thesis was to create a functional mm-scale Rb discharge light source, where the light source needs to consume less than tens of mWs of power. A minimum of few μW of optical power on one of the Rb D lines with less than 0.2% short-term fluctuations was required for stable optical pumping and an acceptable clock performance. A stable output of 10 μW of Rb D2 with less than 0.2% sub-second fluctuations could be emitted from the Rb DBD light source for a discharge gap power consumption of less than 20 mW (but ~700 mW total power consumption by the 50 Ω impedance-matching LC circuit). This was achieved after various optimization experiments involving the cell, electrode and electrical input parameters and the 15-30 mbar Argon buffer gas range, a discharge gap length of 2 mm, a drive frequency in the 8-15 MHz range and the Al EL6 (blanket Al electrodes with 4.5 mm centre-hole on top electrode) electrode geometry was identified to be the most suitable for a low-power and stable operation of the anodically bonded Pyrex-Si-Pyrex Rb lamp-cell. The microfabricated Rb light source also functioned continuously for 6 months without any significant degradation in its performance, showing its high potential for a new class of portable DR clocks and quantum sensors.

This work was published in peer-reviewed journals:

(1) V. Venkatraman et al., "Microfabricated chip-scale rubidium plasma light source for miniature atomic clocks", *IEEE Transactions on Ultrasonics, Ferroelectrics and Frequency Control*, vol. 59, pp. 448-456, 2012.

(2) V. Venkatraman et al., "Characterization and modelling of low-pressure rf discharges at 2-500 MHz for miniature alkali vapour dielectric barrier discharge lamps", *Journal of Physics D: Applied Physics*, vol. 45(50), 505205, 2012.

(3) F. Vecchio, V. Venkatraman, et al., "Dispensing and hermetic sealing Rb in a miniature resonance cell for integrated atomic clocks", *Sensors and Actuators A: Physical*, vol. 172(1), pp. 330-335, 2011.

and also presented at 7 international conferences, published proceedings articles [158], [159], [129], [160], [87], and won the best poster award for 'LTCC integrated miniature Rb discharge lamp module for stable optical pumping in miniature atomic clocks and magnetometers' at the 2012 IEEE 18th international symposium for design and technology in packaging conference.

8.1 Summary

The motivation behind pushing the double-resonance technique towards miniature and chip-scale clock applications was described, and this necessitates a low-power consuming easily-integrable chip-scale Rb light source for efficient optical pumping. The exact power, stability and performance requirements of the light source were stated and all the necessary background information, including the current state-of-the-art Rb lamps and atomic clocks, were studied for the light source development. This whole study was part of the MACQS (Miniature Atomic Clocks and Quantum Sensors) project, funded by the Swiss National Science Foundation (SNSF), which involved a multi-disciplinary task force with an objective to realize and study the physics package of a chip-scale DR clock and other quantum sensors.

An external and parallel electrode geometry (dielectric barrier discharge or DBD design) to ignite a RF-AC capacitively-coupled plasma (CCP) discharge was chosen for the planar mm-scale gap cell fabrication and characterization. This design allowed for **(1)** the electrodes to be placed outside the discharge gap hence avoiding electrode erosion and a longer device lifetime, **(2)** lower breakdown power by maximizing the number of electron momentum transfer collisions in the discharge gap. The conceptually ideal frequency was identified to be 1-50 MHz based on kinetic theory calculations, as it was in the range when the transit time of electrons in the applied alternating electric field starts to get higher than half the time period of the applied field cycle.

A low-pressure buffer gas inert to Rb - Argon, was chosen to enable a low-power breakdown power, and other suitable gases and pressure ranges were reported. A novel low-temperature (<140 °C with 58Bi42Sn) Rb dispensing and solder-sealing technique was reported, and it was developed in collaboration with Dr. Thomas Maeder and Mr. Fabrizio Vecchio at LPM, EPFL for producing mm-scale planar Rb vapor cells. In the current state of development, the solder-sealed cells stayed hermetically sealed for not more than two weeks. However, with further studies, especially on metallization and soldering materials for minimum leaching, enhanced metallization-solder wetting and elimination of contamination by solder flux residues, a long-term hermetic cell can be potentially achieved through this novel technique. Rb lamp-cells for this research were microfabricated by Dr. Yves Pétremand, using a state-of-the-art chip-scale anodic bonding setup developed by EPFL-SAMLAB and UniNE-LTF.

A series LC resonant rf drive circuit was developed for the various capacitive-load lamp-cells for high voltage amplification at the desired drive frequencies. The lamp-cell load was impedance matched to 50 Ω at the desired drive frequency for maximum power transfer to the discharge gap. Plasma discharges could be ignited down with less than 200 mW of total electrical power at drive frequencies between 2-4 MHz where the power consumed by the lamp-cell was less than few mW. At higher drive frequencies, significant amount of power was dissipated by the LC matching components, mainly because of the huge mismatch between the source impedance (50 Ω) and the lamp-cell load impedance (~80 kΩ at tens of MHz). A significant improvement in the power consumption can be achieved by developing a custom drive circuitry for the light source, rather than using standard commercially-available components. The drive circuits developed in this research were successful in demonstrating the first capacitively-coupled Rb discharge light source and were used for observing the lamp performance for a wide drive range between 2-500 MHz.

One of the primary objectives of this research is to evaluate the feasibility of a miniature Rb discharge light source in a potential portable clock application. The Rb lamp-cells were experimentally characterized in terms of power consumption, optical power and optical stability for a wide range of the relevant input parameters and reported in the fifth chapter. Two distinct operation modes, dependent on the electron oscillation amplitude (A_e), were identified and were named the DBD (drift-dominated breakdown, $A_e>d/2$) and the rf-discharge (diffusion controlled breakdown, $A_e<d/2$) regions. The main characteristics of these regions were observed to be: DBD – lower breakdown power, higher optical instability and rf-discharge – higher breakdown power, lower optical instability. The suitable region for the light source operation was found to be when $A_e \approx d/2$, where a power-efficient emission of Rb D line power was possible with an acceptable amount of optical fluctuations. DBD observations have never been reported for Rb discharge light sources and these experiments helped establish the different operating regimes and the preferred range of parameter values for miniature light sources.

The best electrode configuration had to be determined for an optically stable and low sustaining-power operation of the light source for which different electrode geometries and materials (In, Al, ITO) were tested. The EL6 configuration with Al and the EL8 configuration with Al-ITO electrodes were experimentally observed to yield the lowest sustaining power and highest optical stability for a given p.d cell. The effect of cell temperature on the light source performance and the red-mode transition was demonstrated. More than 70% improvement in the Rb D line output power was possible in the red mode when compared to the normal operation mode for a given input power. Hence, if optical pumping in the red mode can give an acceptable clock performance, it can make way for a highly power-efficient and compact light source. The microfabricated Rb light source also functioned continuously for 6 months without any significant degradation in its performance, showing its high potential for a new class of portable DR clocks and quantum sensors. These experiments report on the previously unexplored area of microfabricated Rb discharge lamps and the experimentally verified input conditions suitable for a low-power consuming, optically stable and long-term operation.

Very high power efficiency and output optical stability is required from the Rb DBD lamp and this requires a rigorous optimization of the lamp-cell parameters to meet the optical pumping performance requirements. However, a sufficient range of cell parameters could not be tested using the microfabricated cells (only one buffer gas: Argon with a limited number of gas pressure values and an almost constant discharge gap length of 2 mm were tested) for a complete performance evaluation, as such a large number of cells could not be microfabricated with the available resources in the time-frame of this research. Also, while the developed Rb DBD light source is promising for a miniature atomic clock, there is high interest to understand if it could be potentially scaled down to a chip-scale atomic clock application. To comprehensively characterize and evaluate the lamp performance for such a wide range of parameters, two sets of experiments were performed:

(1) A discharge gap experimental setup, reported in the sixth chapter, was developed to study the effect of different buffer gas types, wider range of pressures and discharge lengths and surface area on the DBD lamp performance. These experiments helped identify that Argon, with lower ionization energy than helium and lower atomic diameter than N_2, had a lower breakdown field at the preferred diffusion-controlled operating regime of the Rb lamp. It was also observed that

the best drive frequency for the mm-scale light source is when the electron oscillation amplitude is just lesser than half the gap length (8-15 MHz for a 2 mm gap) for a low breakdown power, with low p.d conditions (~2 mbar.cm here for Argon) to enable a very stable (<0.1% sub-second fluctuations) diffuse discharge output. This set of experiments helped establishing the suitable operating conditions for the current mm-scale Rb DBD light source.

(2) A plasma model of the Rb and Argon discharge in a Rb DBD light source, using the impact collisions kinetics of Rb and Argon atoms, was simulated using COMSOL to understand the electron properties and the expected Rb output at different cell and frequency conditions. The light source performances after wall-coating the inner dielectric layers with a secondary electron coefficient and after further miniaturization were estimated. The model was validated by comparing it to the experimentally measured Rb spectral data from a light source with the same input conditions. This is the first reported simulation model that can estimate the optical power of the Rb D light from a light source for a given set of operating conditions. The results from both these experiments help identifying the next steps that could to be taken to further optimize the light source performance in terms of size and power consumption and potentially engineer it for even smaller chip-scale atomic clock applications.

An understanding of the optical pumping performance of the Rb DBD lamp would give a better insight on the possible steps that could be taken towards improving its pumping efficiency. In order to get this information, the lamp was tested in a DR atomic clock test setup at LTF, University of Neuchâtel. However, due to the unavoidable high working distance between the lamp and the resonance cell (10 cm), enough light could not be coupled for a measurable signal even after several improvements in the lamp's operation. A compact DR magnetometer test setup using the M_z-technique was built to reduce the working distance to less than few cm and the setup was successfully demonstrated to be functional after observing pumping signals from a Rb D1 laser and conventional Rb ICP lamps. Optical pumping tests were conducted using the Rb DBD lamp but a pumping signal could not be demonstrated possibly because of electromagnetic interferences from the electrodes or due to inadequate optimization of the frequency modulation parameters.

8.2 Thesis contributions

A summary of the key thesis contributions include:

1. This research successfully demonstrated the first ever capacitively-coupled miniature Rb discharge light source.

2. This research is also the first to report on a microfabricated Rb DBD light source, showing high potential for use in an integrated miniature DR atomic clock or magnetometer.

3. A stable output of 10 μW of Rb D2 with less than 0.2% sub-second fluctuations could be achieved from the Rb DBD light source for a discharge gap power consumption of less than 20 mW.

4. The optimum operating conditions, including the drive frequency range and buffer gas pressure range for a mm-scale planar Rb light source were reported.

5. The best lamp-electrode configurations for a low-power consumption and high optical stability operation were identified and reported.

6. A novel low-temperature Rb dispensing and solder-sealing technique was developed for producing mm-scale planar Rb vapor cells.

7. An electrical model of the light source and matching circuit was developed using MATLAB and PSPICE to calculate the discharge gap voltage and power consumption, whose values cannot be reliably measured using high-frequency voltage probes.

8. A plasma simulation model, that can calculate the electron properties and estimate the Rb D line power from a light source for a given set of input conditions, was developed in COMSOL.

9. A compact optical pumping test setup using a microfabricated Rb cell, following the principles of atomic magnetometry was developed.

10. An LTCC packaged Rb discharge lamp module, including the drive circuit and heater, was developed for portable optical pumping applications.

8.3 Outlook

Future work aimed at improving and industrializing the Rb DBD light sources developed in this research should focus on the following key points:

1. The rf drive circuitry needs to be improved, which can be done by custom-building a drive circuitry with a characteristic impedance equal to the cell impedance. This also requires the amplifier to have an output impedance that is the complex conjugate of the cell impedance, to allow for a significant reduction in power dissipation losses, pushing the device closer to the desired power consumption levels of portable applications.

2. For potential chip-scale clock applications, a novel, highly compact (<0.5 mm discharge gap length) and high Rb D line power emitting device with very low power consumption (possibly 10 μW of Rb D2 with less than 1/10th of the power consumption levels reported in this thesis) is possible to develop but the lamp will be operating in the 'red-mode'. Optical pumping has been demonstrated when the lamp was operating in the red-mode by past researchers but it was never used as the timing uncertainty was much worse than when the lamp was in the normal mode (or ring-mode in the case of ICP lamps). If such a higher timing uncertainty is acceptable, the red-mode operation might be useful and a novel way to consider for a miniature DR clock design.

By having a very small discharge gap (0.2-0.5 mm with the Rb DBD cell or possibly even lower), filling with a suitable higher buffer gas pressure (80-200 mbar) and a high volume of Rb (enough to cover a good proportion of the inner dielectric surface), a very low breakdown field can be achieved and by having appropriate electrodes, the fields can be maximized for electron bombardment on the liquid Rb surface which leads to localized heating and a high output of Rb D lines. However, this also usually leads to a higher probability of Rb self-absorption leading to the red-mode transition, Doppler broadening of Rb lines and a lower contrast in the pumping signal (and probably a slightly higher Rb diffusion into the walls with time). But this method

would avoid the necessity of an external heater, can allow much smaller devices, low drive frequencies and much lower input powers.

3. A Fabry-perot interferometer or an optical instrument with a similar capacity, that can help measure the hyperfine line spectra that are of interest for optical pumping, is required for improving the light source parameters and for efficient troubleshooting. This would help understand the hyperfine frequency shifts induced due to the buffer gases and the Doppler broadening effects due to Rb self-absorption and hence is crucial for performance evaluation and product development.

4. The glass used for the microfabrication could be changed from Pyrex to a more alkali resistant glass such as SCHOTT 8436 [191] to increase the lifetime and reliability of the light source.

5. One of the spectral lines of Argon coincides with the Rb D1 wavelength. Neon and mixtures of Xenon-Neon have been reported to yield slightly lower breakdown fields compared to Argon [83]. Hence, changing the buffer gas to such a mixture might improve both the device power consumption and the contrast of the emitted Rb D1 line.

6. A miniature DBD light source, without the addition of Rb, can also be used as an excimer lamp for several applications in the fields of microbiology, skin treatments and photochemistry [192]. By using high-pressure (several hundreds of mbar) Xenon - a suitable choice for high density UV radiation [72], local skin treatments [193] would be possible when they require a power-efficient high UV output on mm-scale precision surfaces.

Appendix: COMSOL simulation data

Here, the necessary atomic data required as inputs for simulating a Rb discharge (with Argon buffer gas) using COMSOL are mentioned. The collision cross-section data, the excited levels of Rubidium and Argon and the necessary reaction rate constants for all the considered reactions are specified. Some important data references for Rubidium and Argon: [194], [195], [196], [197].

I. Species considered in the plasma region

Electrons, **e;** Neutral Argon atoms, **Ar;** Argon ions, **Ar+;** Argon excited states, **Ars1-Ars12;** Neutral Rubidium atoms, **Rb;** Rubidium excited states, **Rb1-Rb5;** Rubidium ions, **Rb+**

II. Rubidium excited states

Excited state notation	Excited level	Energy of level
Rb1	$5^2P_{1/2}$	1.56 eV
Rb2	$5^2P_{3/2}$	1.59 eV
Rb3	5D	3.19 eV
Rb4	7S	3.26 eV
Rb5	6D	3.56 eV

III. Argon excited states

Excited state notation	Energy of level	Excited state notation	Energy of level
Ars1	11.54 eV	Ars7	13.15 eV
Ars2	11.623 eV	Ars8	13.17 eV
Ars3	11.72 eV	Ars9	13.28 eV
Ars4	11.82 eV	Ars10	13.30 eV
Ars5	13.07 eV	Ars11	13.32 eV
Ars6	13.09 eV	Ars12	13.47 eV

IV. Elastic collisions

Collision cross-section data is necessary for these reactions. The data for Argon is given in COMSOL. The data for Rb can be found here [198].

e+Rb=>e+Rb	e+Ars4=>e+Ars4
e+Rb1=>e+Rb1	e+Ars5=>e+Ars5
e+Rb2=>e+Rb2	e+Ars6=>e+Ars6
e+Rb3=>e+Rb3	e+Ars7=>e+Ars7
e+Rb4=>e+Rb4	e+Ar8=>e+Ar8
e+Rb5=>e+Rb5	e+Ars9=>e+Ars9
e+Ar=>e+Ar	e+Ars10=>e+Ars10
e+Ars1=>e+Ars1	e+Ars11=>e+Ars11
e+Ars2=>e+Ars2	e+Ars12=>e+Ars12
e+Ars3=>e+Ars3	

V. Electron impact collisions leading to Ar and Rb excitations

e+Ar=>e+Ars1	11.54 (eV)	e+Rb=>e+Rb1	1.56 (eV)
e+Ars1=>e+Ars2	0.083	e+Rb=>e+Rb2	1.59
e+Ars1=>e+Ars3	0.18	e+Rb=>e+Rb3	3.19
e+Ars1=>e+Ars4	0.28	e+Rb=>e+Rb4	3.26
e+Ars1=>e+Ars5	1.53	e+Rb=>e+Rb5	3.56
e+Ars1=>e+Ars6	1.55	e+Rb1=>e+Rb2	0.03
e+Ars1=>e+Ars7	1.61	e+Rb1=>e+Rb3	1.63
e+Ars1=>e+Ars8	1.63	e+Rb1=>e+Rb4	1.7
e+Ars1=>e+Ars9	1.74	e+Rb1=>e+Rb5	2
e+Ars1=>e+Ars10	1.76		
e+Ars1=>e+Ars11	1.78		
e+Ars1=>e+Ars12	1.847		

V. Rb discharge emissions between 400-1000 nm

Rb de-excitations to lower states	**Rate constant (s^{-1})**	**Wavelength in spectrum (nm)**
Rb1=>Rb	3.61e7	795 (D1)
Rb2=>Rb	3.8e7	780 (D2)
Rb3=>Rb1	1.17e7	761
Rb3=>Rb2	1.29e7	775
Rb4=>Rb1	3.62e6	728
Rb4=>Rb2	3.5e6	741
Rb5=>Rb1	1.19e6	620
Rb5=>Rb2	1.24e6	630

VI. Strong Ar emissions between 400-1000 nm

Ar de-excitations to lower states	**Wavelength in spectrum (nm)**
Ars11=>Ars1	696.5
Ars10=>Ars1	706.7
Ars12=>Ars4	750.3
Ars8=>Ars1	763.5
Ars9=>Ars3	794.8
Ars6=>Ars1	801.4
Ars7=>Ars2	810.3
Ars5=>Ars1	811.5
Ars10=>Ars4	840.5
Ars11=>Ars2	912.4

Bibliography

1. Kitching, J., *Microfabricated atomic clocks*. 2005: Neuchatel.
2. Droz, F., et al. *On-board Galileo RAFS, current status and performances*. in *Proceedings of the 2003 IEEE International Frequency Control Symposium and PDA Exhibition Jointly with the 17th European Frequency and Time Forum*. 2003.
3. Camparo, J., *The rubidium atomic clock and basic research*. Physics Today, 2007. **60**(11): p. 33-39.
4. Knappe, S., *MEMS atomic clocks* Comprehensive Microsystems, 2007. **3**: p. 571-612.
5. Bell, W.E., A.L. Bloom, and J. Lynch, *Alkali metal vapor spectral lamps*. Review of Scientific Instruments, 1961. **32**(6): p. 688-692.
6. Lutwak, R., et al. *The chip-scale atomic clock–coherent population trapping vs. conventional interrogation*. in *34th Annual Precision Time and Time Interval Meeting*. 2002.
7. Knappe, S., et al., *A microfabricated atomic clock*. Applied Physics Letters, 2004. **85**(9): p. 1460-1462.
8. Vanier, J., *Atomic clocks based on coherent population trapping: a review*. Applied Physics B: Lasers and Optics, 2005. **81**(4): p. 421-442.
9. Youngner, D., et al. *A manufacturable chip-scale atomic clock*. in *2007 Solid-State Sensors, Actuators and Microsystems Conference*. 2007.
10. Serkland, D.K., et al. *VCSELs for atomic clocks*. in *Proceedings of the SPIE conference*. 2006.
11. Cyr, N., M. Tˆetu, and M. Breton, *All-optical microwave frequency standard: a proposal*. IEEE Transactions on Instrumentation and Measurement, 1993. **42**(2): p. 640-649.
12. Pellaton, M., et al., *Study of laser-pumped double-resonance clock signals using a microfabricated cell*. Physica Scripta, 2012. **2012**(T149): p. 014013.
13. Braun, A., et al. *RF-interrogated end-state chip-scale atomic clock*. in *39th Annual Precise Time and Time Interval Meeting*. 2007.
14. Hawkins, B.M., et al. *Reliability of various size oxide aperture VCSELs*. in *Proceedings of the 52nd Electronic Components and Technology Conference*. 2002.
15. Camparo, J., *Does the light shift drive frequency aging in the rubidium atomic clock?* IEEE Transactions on Ultrasonics, Ferroelectrics and Frequency Control, 2005. **52**(7): p. 1075-1078.
16. Spectratime, *iSync+ Lifetime and MTBF performance*. 2008.
17. Arditi, M. and T.R. Carver, *The principles of the double resonance method applied to gas cell frequency standards*. Proceedings of the IEEE, 1963. **51**(1): p. 190-202.
18. Lutwak, R., et al. *The MAC - a miniature atomic clock*. in *Proceedings of the 2005 IEEE International Frequency Control Symposium and Exposition* 2005.
19. Knappe, S., et al., *A chip-scale atomic clock based on 87Rb with improved frequency stability*. Optics Express, 2005. **13**(4): p. 1249-1253.
20. MATLAB, *The Mathworks Inc., Natick, MA*. 1998. **5**.
21. PSpice, O.C., *Electronic Design Software*. EMA, Design Automation. **225**.
22. Multiphysics, C., *COMSOL Inc*. 2011.
23. Francis, G., *Ionization phenomena in gases*. 1960: Academic Press.
24. Brown, S.C., *Basic data of plasma physics: The fundamental data on electrical discharges in gases*. 1967: American Institute of Physics.
25. Florez, D., et al. *DBD excimer lamp power supply with fully controlled operating conditions*. in *2012 13th International Conference on Optimization of Electrical and Electronic Equipment (OPTIM)*. 2012.
26. Mukhovatov, V. and V. Shafranov, *Plasma equilibrium in a tokamak*. Nuclear Fusion, 2011. **11**(6): p. 605-633.
27. Eckert, E. and E. Pfender, *Advances in plasma heat transfer*. Advances in heat transfer, 1967. **4**: p. 229-313.

28. Hasegawa, A. and L. Chen, *Kinetic processes in plasma heating by resonant mode conversion of Alfvén wave.* Physics of Fluids, 1976. **19**(12): p. 1924-1934.
29. Lister, G., et al., *The physics of discharge lamps.* Reviews of modern physics, 2004. **76**(2): p. 541-598.
30. Raizer, Y.P., V.I. Kisin, and J.E. Allen, *Gas discharge physics.* Vol. 1. 1991: Springer-Verlag Berlin.
31. Baars-Hibbe, L., *Characterization and applications of high frequency discharges in the near-atmospheric rressure range using micro-structured electrode arrays.* 2005: Cuvillier Verlag.
32. Von Engel, A., *John Sealy Edward Townsend. 1868-1957.* Biographical Memoirs of Fellows of the Royal Society, 1957. **3**: p. 257-272.
33. Chang, J.S., P.A. Lawless, and T. Yamamoto, *Corona discharge processes.* Plasma Science, IEEE Transactions on, 1991. **19**(6): p. 1152-1166.
34. Bogaerts, A., et al., *Gas discharge plasmas and their applications.* Spectrochimica Acta Part B: Atomic Spectroscopy, 2002. **57**(4): p. 609-658.
35. Roth, J.R., *Industrial plasma engineering volume 1: principles.* 1995: Institute of Physics Press.
36. Paschen, F., *On sparking over in air, hydrogen, carbon dioxide under the potentials corresponding to various pressures.* Wiedemann Annalen der Physik und Chemie, 1889. **37**: p. 69-96.
37. Longwitz, R.G., *Study of gas ionization in a glow discharge and development of a micro gas ionizer for gas detection and analysis.* 2004, PhD thesis, Ecole Polytechnique Fédérale de Lausanne, Switzerland.
38. Ledernez, P., et al. *A modification of Paschen law for argon.* in *34th ICPIG conference.* 2009.
39. Duckworth, D.C., C.M. Barshick, and D.H. Smith, *Analysis of soils by glow discharge mass spectrometry.* Journal of Analytical Atomic Spectrometry, 1993. **8**(6): p. 875-879.
40. Beer, T.A., J. Laimer, and H. Stori, *Study of the ignition behavior of a pulsed dc discharge used for plasma-assisted chemical-vapor deposition.* Journal of Vacuum Science & Technology A: Vacuum, Surfaces, and Films, 2000. **18**(2): p. 423-434.
41. Eijkel, J.C.T., H. Stoeri, and A. Manz, *A dc microplasma on a chip employed as an optical emission detector for gas chromatography.* Analytical Chemistry, 2000. **72**(11): p. 2547-2552.
42. Davis, W.C. and R.K. Marcus, *An atmospheric pressure glow discharge optical emission source for the direct sampling of liquid media.* Journal of Analytical Atomic Spectrometry, 2001. **16**(9): p. 931-937.
43. Carazzetti, P., P. Renaud, and H. Shea. *Experimental study of electrical breakdown in MEMS devices with micrometer scale gaps.* in *Proceedings of SPIE.* 2008.
44. Kher, V. and V. Ayachit, *Increase of breakdown voltage of a low pressure AC discharge in air with frequencies from 20 to 15000 Hz.* Physica, 1964. **30**(4): p. 702-712.
45. Brown, S.C., *High-frequency gas-discharge breakdown.* Proceedings of the IRE, 1951. **39**(12): p. 1493-1501.
46. Pim, J., *The electrical breakdown strength of air at ultra-high frequencies.* Proceedings of the IEE-Part III: Radio and Communication Engineering, 1949. **96**(40): p. 117-129.
47. Piejak, R., V. Godyak, and B. Alexandrovich, *A simple analysis of an inductive RF discharge.* Plasma sources science and technology, 1999. **1**(3): p. 179-186.
48. Brewer, R.G., *High intensity low noise rubidium light source.* Review of Scientific Instruments, 1961. **32**(12): p. 1356-1358.
49. Hopwood, J., *Review of inductively coupled plasmas for plasma processing.* Plasma sources science and technology, 1999. **1**(2): p. 109-116.
50. Montaser, A., S.K. Chan, and D.W. Koppenaal, *Inductively coupled helium plasma as an ion source for mass spectrometry.* Analytical Chemistry, 1987. **59**(8): p. 1240-1242.
51. Waggoner, J.W., et al., *Novel low power/reduced pressure inductively coupled plasma ionization source for mass spectrometric detection of organotin species.* Journal of Analytical Atomic Spectrometry, 1998. **13**(9): p. 879-883.

52. Allemand, C.D. and R.M. Barnes, *A study of inductively coupled plasma torch configurations.* Applied Spectroscopy, 1977. **31**(5): p. 434-443.
53. Wharmby, D., *Electrodeless lamps for lighting: a review.* Science, Measurement and Technology, IEE Proceedings A, 1993. **140**(6): p. 465-473.
54. Shinomiya, M., et al., *Development of the electrodeless fluorescent lamp.* Journal of the Illuminating Engineering Society, 1991. **20**(1): p. 44-49.
55. Jonkers, J., M. Bakker, and J. Van der Mullen, *Absorption measurements on a low-pressure, inductively coupled, argon-mercury discharge for lighting purposes: 1. The gas temperature and argon metastable states density.* Journal of Physics D: Applied Physics, 1999. **30**(13): p. 1928.
56. Lieberman, M.A. and A. Lichtenberg, *Principles of Plasma Discharges.* Materials Processing ed Wiley (New York), 1994.
57. Hopwood, J.A., *A microfabricated inductively coupled plasma generator.* Journal of Microelectromechanical Systems, 2000. **9**(3): p. 309-313.
58. Kolobov, V. and D. Economou, *The anomalous skin effect in gas discharge plasmas.* Plasma sources science and technology, 1999. **6**(2): p. R1-R17.
59. Park, J., et al., *Discharge phenomena of an atmospheric pressure radio-frequency capacitive plasma source.* Journal of Applied Physics, 2001. **89**(1): p. 20-28.
60. Puač, N., et al. *Low pressure RF capacitively coupled plasma reactor for modification of seeds, polymers and textile fabrics.* in *Materials Science Forum*. 2005.
61. Moravej, M. and R.F. Hicks, *Atmospheric plasma deposition of coatings using a capacitive discharge source.* Chemical vapor deposition, 2005. **11**(11-12): p. 469-476.
62. Anghel, S.D., et al., *Atmospheric pressure capacitively coupled plasma source for the direct analysis of non-conductive solid samples.* J. Anal. At. Spectrom., 1999. **14**(4): p. 541-545.
63. Carazzetti, P., P. Renaud, and H. Shea, *Micromachined chip-scale plasma light source.* Sensors and Actuators A: Physical, 2009. **154**(2): p. 275-280.
64. Bass, A., C. Chevalier, and M. Blades, *A capacitively coupled microplasma (CCμP) formed in a channel in a quartz wafer.* J. Anal. At. Spectrom., 2001. **16**(9): p. 919-921.
65. Franzke, J., et al., *Microplasmas for analytical spectrometry.* J. Anal. At. Spectrom., 2003. **18**(7): p. 802-807.
66. Ferreira, C.M. and M. Moisan, *Microwave discharges(fundamentals and applications).* NATO Advanced Study Institute series. Series B, Physics. 1993: Plenum Press.
67. Moisan, M., et al., *The development and use of surface-wave sustained discharges for applications*, in *NATO ASI Series 3 High Technology*. 1999. p. 23-64.
68. Gordiets, B., et al., *A travelling wave sustained hydrogen discharge: modelling and experiment.* Plasma sources science and technology, 2000. **9**(3): p. 295-303.
69. Kogelschatz, U., *Dielectric-barrier discharges: their history, discharge physics, and industrial applications.* Plasma chemistry and plasma processing, 2003. **23**(1): p. 1-46.
70. Kogelschatz, U., B. Eliasson, and W. Egli, *From ozone generators to flat television screens: history and future potential of dielectric-barrier discharges.* Pure and Applied Chemistry, 1999. **71**(10): p. 1819-1828.
71. Eliasson, B., M. Hirth, and U. Kogelschatz, *Ozone synthesis from oxygen in dielectric barrier discharges.* Journal of Physics D: Applied Physics, 2000. **20**(11): p. 1421-1437.
72. Eliasson, B. and U. Kogelschatz, *UV excimer radiation from dielectric-barrier discharges.* Applied Physics B: Lasers and Optics, 1988. **46**(4): p. 299-303.
73. Boeuf, J., *Plasma display panels: physics, recent developments and key issues.* Journal of Physics D: Applied Physics, 2003. **36**(6): p. R53-R79.
74. Callegari, T., R. Ganter, and J. Boeuf, *Diagnostics and modeling of a macroscopic plasma display panel cell.* Journal of Applied Physics, 2000. **88**(7): p. 3905-3913.
75. Meunier, J., P. Belenguer, and J. Boeuf, *Numerical model of an ac plasma display panel cell in neon-xenon mixtures.* Journal of Applied Physics, 1995. **78**(2): p. 731-745.

76. Zhang, J.Y. and I.W. Boyd, *Efficient excimer ultraviolet sources from a dielectric barrier discharge in rare-gas/halogen mixtures.* Journal of Applied Physics, 1996. **80**(2): p. 633-638.
77. Urakabe, T., et al., *A flat fluorescent lamp with Xe dielectric barrier discharges.* Journal of Light & Visual Environment, 1996. **20**(2): p. 20-25.
78. Sonnenfeld, A., et al., *Deposition process based on organosilicon precursors in dielectric barrier discharges at atmospheric pressure—a comparison.* Plasmas and polymers, 2001. **6**(4): p. 237-266.
79. Borcia, G., C. Anderson, and N. Brown, *Dielectric barrier discharge for surface treatment: application to selected polymers in film and fibre form.* Plasma sources science and technology, 2003. **12**(3): p. 335-344.
80. Heise, M., et al., *Sterilization of polymer foils with dielectric barrier discharges at atmospheric pressure.* Plasmas and polymers, 2004. **9**(1): p. 23-33.
81. Zhang, J.Y. and I.W. Boyd, *Efficient XeI excimer ultraviolet sources from a dielectric barrier discharge.* Journal of Applied Physics, 1998. **84**: p. 1174-1178.
82. Na, N., et al., *Development of a dielectric barrier discharge ion source for ambient mass spectrometry.* Journal of the American Society for Mass Spectrometry, 2007. **18**(10): p. 1859-1862.
83. Veronis, G., U.S. Inan, and V.P. Pasko, *Fundamental properties of inert gas mixtures for plasma display panels.* IEEE Transactions on Plasma Science, 2000. **28**(4): p. 1271-1279.
84. Siliprandi, R., et al., *Characterization of the streamer regime in dielectric barrier discharges.* Journal of Applied Physics, 2008. **104**(6): p. 063309-9.
85. Gellert, B. and U. Kogelschatz, *Generation of excimer emission in dielectric barrier discharges.* Applied Physics B: Lasers and Optics, 1991. **52**(1): p. 14-21.
86. Vecchio, F., et al., *Dispensing and hermetic sealing Rb in a miniature reference cell for integrated atomic clocks.* Sensors and Actuators A: Physical, 2011. **172**(1): p. 330-335.
87. Vecchio, F., et al., *Dispensing and hermetic sealing Rb in a miniature reference cell for integrated atomic clocks.* Procedia Engineering, 2010. **5**: p. 367-370.
88. Tako, T., Y. Koga, and I. Hirano, *Spectral profiles of Rb-D lines.* Japanese Journal of Applied Physics, 1975. **14**(5).
89. Kuramochi, N., et al., *Spectral profiles of the 87 Rb D 1 line emitted from a spherical electrodeless lamp.* Japanese Journal of Applied Physics, 1977. **16**(5): p. 673-679.
90. Camparo, J. and R. Frueholz, *Linewidths of the 0-0 hyperfine transition in optically pumped alkali-metal vapors.* Physical Review A, 1985. **31**(3): p. 1440-1448.
91. Kuramochi, N., I. Matsuda, and H. Fukuyo, *Analysis of the effect of foreign gases in the filtering action of a 85Rb cell.* Journal of the Optical Society of America, 1978. **68**(8): p. 1087-1092.
92. Arditi, M. and T.R. Carver, *Pressure, light, and temperature shifts in optical detection of 0-0 hyperfine resonance of alkali metals.* Physical Review, 1961. **124**(3): p. 800-809.
93. Andrews, L., *Matrix reactions of K and Rb atoms with oxygen molecules.* The Journal of Chemical Physics, 1971. **54**: p. 4935.
94. Liew, L.A., J. Moreland, and V. Gerginov, *Wafer-level filling of microfabricated atomic vapor cells based on thin-film deposition and photolysis of cesium azide.* Applied Physics Letters, 2007. **90**(11): p. 114106-3.
95. Woetzel, S., et al., *Microfabricated atomic vapor cell arrays for magnetic field measurements.* Review of Scientific Instruments, 2011. **82**(3): p. 033111.
96. Steck, D.A., *Rubidium 87 D line data*. 2001.
97. Choi, K.C., *Microdischarge in microbridge plasma display with holes in the cathode.* IEEE Electron Device Letters, 1998. **19**(6): p. 186-188.
98. Akiyama, T. *Evaluation of discharge cell structure for color AC plasma display panels*. in *Proceedings of the 15th International Display Resolution Conference*. 1995.
99. Atkinson, R., G. Chapman, and L. Krause, *Light sources for the excitation of atomic resonance fluorescence in potassium and rubidium.* Journal of the Optical Society of America, 1965. **55**(10): p. 1269-1274.

100. Dushman, S., *Low Pressure Gaseous Discharge Lamps--Part I*. Transactions of the American Institute of Electrical Engineers, 1934. **53**(8): p. 1204-1212.
101. Rosenberry, M., et al., *Radiation trapping in rubidium optical pumping at low buffer-gas pressures*. Physical Review A, 2007. **75**(2): p. 023401.
102. Camparo, J.C. and R. MacKay, *Spectral mode changes in an alkali rf discharge*. Journal of Applied Physics, 2007. **101**(5): p. 053303-6.
103. Pétremand, Y., et al., *Microfabricated rubidium vapour cell with a thick glass core for small-scale atomic clock applications*. Journal of Micromechanics and Microengineering, 2012. **22**(2): p. 025013.
104. Wei, J., et al., *Glass-to-glass anodic bonding process and electrostatic force*. Thin solid films, 2004. **462**: p. 487-491.
105. Mack, S., H. Baumann, and U. Gosele. *Gas tightness of cavities sealed by silicon wafer bonding*. in *Proceedings of the 1997 IEEE Tenth Annual International Workshop on Micro Electro Mechanical Systems*. 1997.
106. Deng, J., et al. *A commercial CPT rubidium clock*. in *Proceedings of the European Frequency and Time Forum conference*. 2008.
107. Ma, J., et al., *Modification of glass cell walls by rubidium vapor*. Physical Review A, 2009. **79**(4): p. 042905.
108. Tudryn, C.D., *Characterization of anodic bonding*. 2004, Massachusetts Institute of Technology.
109. Wallis, G. and D.I. Pomerantz, *Field assisted glass-metal sealing*. Journal of Applied Physics, 1969. **40**(10): p. 3946-3949.
110. Ko, W., J. Suminto, and G. Yeh, *Bonding techniques for microsensors*. Micromachining and Micropackaging of Transducers, 1985. **20**: p. 41-61.
111. Kwakernaak, M., et al. *Components for batch-fabricated chip-scale atomic clocks*. in *36th Annual Precision Time and Time Interval Meeting*. 2004.
112. Eklund, E.J. and A.M. Shkel, *Glass blowing on a wafer level*. Microelectromechanical Systems, Journal of, 2007. **16**(2): p. 232-239.
113. Gong, F., et al., *Electrolytic fabrication of atomic clock cells*. Review of Scientific Instruments, 2006. **77**: p. 076101.
114. Douahi, A., et al., *Vapour microcell for chip scale atomic frequency standard*. Electronics Letters, 2007. **43**(5): p. 33-34.
115. Tsujimoto, K., et al. *Sacrificial microchannel sealing by glass-frit reflow for chip scale atomic magnetometer*. in *IEEE 24th International Conference on Micro Electro Mechanical Systems (MEMS)*. 2011.
116. Hasegawa, M., et al. *Fabrication of wall-coated Cs vapor cells for a chip-scale atomic clock*. in *2008 IEEE/LEOS Internationall Conference on Optical MEMs and Nanophotonics*. 2008.
117. Radhakrishnan, S. and A. Lal. *Alkali metal-wax micropackets for chip-scale atomic clocks*. in *The 13th International Conference on Solid-State Sensors, Actuators and Microsystems, 2005, TRANSDUCERS'05 Technical Digest Papers*. 2005.
118. Liew, L.A., et al., *Microfabricated alkali atom vapor cells*. Applied Physics Letters, 2004. **84**(14): p. 2694-2696.
119. Espe, W., *Materials of high vacuum technology*. 1968: Pergamon Press.
120. Lee, C., W.F. Huang, and J.S. Shie, *Wafer bonding by low-temperature soldering*. Sensors and Actuators A: Physical, 2000. **85**(1): p. 330-334.
121. Knechtel, R., *Glass frit bonding: an universal technology for wafer level encapsulation and packaging*. Microsystem technologies, 2005. **12**(1): p. 63-68.
122. Straessle, R., et al. *Low-temperature indium hermetic sealing of alkali vapor-cells for chip-scale atomic clocks*. in *2012 IEEE 25th International Conference on Micro Electro Mechanical Systems (MEMS)*. 2012.

123. Sangster, J. and C. Bale, *The Rb-Sn (rubidium-tin) system*. Journal of Phase Equilibria and Diffusion, 1998. **19**(1): p. 82-85.
124. Cook, R.A. and R.P. Frueholz. *An improved rubidium consumption model for discharge lamps used in rubidium frequency standards*. in *Proceedings of the 42nd Annual Frequency Control Symposium, .* 1988.
125. Volk, C., et al. *Lifetime and reliability of rubidium discharge lamps for use in atomic frequency standards*. in *38th Annual Symposium on Frequency Control*. 1984.
126. Prudenziati, M., *Thick film sensors*. 1994: Elsevier Amsterdam, The Netherlands.
127. Leibfried, W., *Wetting, leaching and solder adhesion of copper thick film conductors on alumina and multilayer glasses*. Microelectronics International, 1986. **3**(2): p. 24-37.
128. Venkatraman, V., et al., *Microfabricated chip-scale rubidium plasma light source for miniature atomic clocks*. IEEE Transactions on Ultrasonics, Ferroelectrics and Frequency Control, 2012. **59**(3): p. 448-456.
129. Venkatraman, V., et al., *Characterization and modelling of low-pressure rf discharges at 2–500 MHz for miniature alkali vapour dielectric barrier discharge lamps*. Journal of Physics D: Applied Physics, 2012. **45**(50): p. 505205.
130. Reitz, J.R., F.J. Milford, and R.W. Christy, *Foundations of electromagnetic theory*. 2008: Addison-Wesley Publishing Company.
131. Reinhold, L. and B. Pavel, *RF circuit design: theory and applications*. 2000, Pearson Education International.
132. Heald, M.A. and J.B. Marion, *Classical electromagnetic radiation*. Fort Worth: Saunders College Publishing, 3rd ed., 1995.
133. Chabert, P. and N. Braithwaite, *Physics of radio-frequency plasmas*. 2011: Cambridge University Press.
134. Babat, G.I., *Electrodeless discharges and some allied problems*. Journal of the Institution of Electrical Engineers-Part III: Radio and Communication Engineering, 1947. **94**(27): p. 27-37.
135. Sowa, W. and R. Lecheler. *Lamp driver concepts for dielectric barrier discharge lamps and evaluation of a 110 W ballast*. in *Record of the 2004 IEEE Industry Applications Conference*. 2004.
136. Díez, R., et al. *Current mode converter for dielectric barrier discharge lamp*. in *Power Electronics Specialists Conference, 2008*. 2008.
137. El-Deib, A., et al., *Simulation of dielectric barrier discharge lamp coupled to the external electrical circuit*. Proceedings of the COMSOL Conference, 2008.
138. Smith, H., C. Charles, and R. Boswell, *Breakdown behavior in radio-frequency argon discharges*. Physics of Plasmas, 2003. **10**: p. 875-881.
139. Park, J., et al., *Gas breakdown in an atmospheric pressure radio-frequency capacitive plasma source*. Journal of Applied Physics, 2001. **89**(1): p. 15-19.
140. Lisovsky, V. and V. Yegorenkov, *Low-pressure gas breakdown in combined fields*. Journal of Physics D: Applied Physics, 1999. **27**(11): p. 2340-2348.
141. Kohler, K., et al., *Plasma potentials of 13.56-MHz rf argon glow discharges in a planar system*. Journal of Applied Physics, 1985. **57**(1): p. 59-66.
142. Walls, F.L. and J.R. Vig, *Fundamental limits on the frequency stabilities of crystal oscillators*. IEEE Transactions on Ultrasonics, Ferroelectrics and Frequency Control, 1995. **42**(4): p. 576-589.
143. Cagdaser, B. and B.E. Boser. *Resonant drive: sense and high voltage electrostatic drive using single MEMS capacitor and low voltage electronics*. in *18th IEEE International Conference on Micro Electro Mechanical Systems*. 2005: IEEE.
144. Jeremy, E., *Fundamentals of RF circuit design with low noise oscillators*. Wiley. 2002.
145. Kothari, D.P. and I.J. Nagrath, *Basic Electrical Engineering*. 2 ed. 2007: Tata Mcgraw Hill.
146. 16.3, O.P., *Cadence Design Systems Inc. San Jose, U.S.A.* 2009.

147. Nakahara, S., N. Shiiba, and K. Itoyama. *The characteristics of the starting potential of barrier discharge*. in *Digest of Technical Papers in 2001 Pulsed Power Plasma Science*. 2001.
148. Valdivia-Barrientos, R., et al., *Analysis and electrical modelling of a cylindrical DBD configuration at different operating frequencies*. Plasma sources science and technology, 2006. **15**(2): p. 237-245.
149. Manual, L.U., *National Instruments*. Austin, TX, 1998.
150. Hickman, I., *Practical radio-frequency handbook*. 2007: Newnes.
151. Nair, K. and S. Priya, *Advances in electroceramic materials II: ceramic transactions*. 2010: Wiley-American Ceramic Society.
152. Liu, S. and M. Neiger, *Electrical modelling of homogeneous dielectric barrier discharges under an arbitrary excitation voltage*. Journal of Physics D: Applied Physics, 2003. **36**(24): p. 3144-3150.
153. Zhi, F., et al., *Electrical model and experimental analysis of the atmospheric-pressure homogeneous dielectric barrier discharge in He*. IEEE Transactions on Plasma Science, 2012. **40**(3): p. 883-891.
154. Beleznai, S., et al., *High-efficiency dielectric barrier Xe discharge lamp: theoretical and experimental investigations*. Journal of Physics D: Applied Physics, 2006. **39**(17): p. 3777-3787.
155. Flores-Fuentes, A., et al., *Electrical model of an atmospheric pressure dielectric barrier discharge cell*. IEEE Transactions on Plasma Science, 2009. **37**(1): p. 128-134.
156. Dıez, R., et al., *Predictive model of a DBD lamp for power supply design and method for the automatic identification of its parameters*. European Physics Journal Applied Physics, 2007. **37**(3): p. 307-313.
157. Alcock, C., V. Itkin, and M. Horrigan, *Vapour pressure equations for the metallic elements: 298–2500K*. Canadian Metallurgical Quarterly, 1984. **23**(3): p. 309-313.
158. Venkatraman, V., et al. *Low-Power chip-scale Rubidium plasma light source for miniature atomic clocks*. in *2011 Joint Conference of the IEEE International Frequency Control and the European Frequency and Time Forum*. 2011.
159. Venkatraman, V., et al. *Microfabrication and packaging of a Rubidium vapor cell as a plasma light source for MEMS atomic clocks*. in *2011 16th International Solid-State Sensors, Actuators and Microsystems Conference (TRANSDUCERS)*. 2011.
160. Venkatraman, V., et al. *LTCC integrated miniature Rb discharge lamp module for stable optical pumping in miniature atomic clocks and magnetometers*. in *2012 IEEE 18th International Symposium for Design and Technology in Electronic Packaging (SIITME)*. 2012.
161. Fukuyo, H., et al., *Temperature dependence of hyperfine spectrum of Rb D1 line*. Japanese Journal of Applied Physics, 1970. **9**: p. 729-734.
162. Kulagin, E., et al., *Dependence of optical density of rubidium vapor on buffer gas pressure*. Journal of Applied Spectroscopy, 1980. **33**(1): p. 772-775.
163. Mueller, C., *The secondary electron emission of pyrex glass*. Journal of Applied Physics, 1945. **16**(8): p. 453-458.
164. Walsh, J.L., et al., *Atmospheric-pressure gas breakdown from 2 to 100 MHz*. Applied Physics Letters, 2008. **93**(22): p. 221505-3.
165. Camparo, J. and G. Fathi, *Effects of rf power on electron density and temperature, neutral temperature, and Te fluctuations in an inductively coupled plasma*. Journal of Applied Physics, 2009. **105**(10): p. 103302.
166. Massines, F., et al., *Experimental and theoretical study of a glow discharge at atmospheric pressure controlled by dielectric barrier*. Journal of Applied Physics, 1998. **83**(6): p. 2950-2957.
167. Camparo, J. and R. Mackay. *A mechanism of rubidium atomic clock degradation: Ring-mode to red-mode transition in rf-discharge lamps*. in *2007 IEEE International Frequency Control Symposium joint with the 21st European Frequency and Time Forum*. 2007.

168. Venkatraman, V., et al. *Reliability characteristics of microfabricated Rb mini-lamps for optical pumping in miniature atomic clocks and magnetometers*. in *SPIE MOEMS-MEMS*. 2013: International Society for Optics and Photonics.
169. Quan, S. and P.H. Kvam, *Multi-cause degradation path model: a case study on rubidium lamp degradation*. Quality and Reliability Engineering International, 2011. **27**(6): p. 781-793.
170. Zhong, J. and H. Bau, *Thick-film thermistors printed on low temperature co-fired ceramic tapes*. American Ceramic Society Bulletin, 2001. **80**(10): p. 39-42.
171. Vecchio, F., et al., *Effects of thermal losses on the heating of a multifunctional LTCC module for atomic clock packaging*. Solid State Phenomena, 2012. **188**: p. 244-249.
172. Imanaka, Y., *Multilayered low temperature cofired ceramics (LTCC) technology*. 2004: Springer.
173. Wagenaars, E., et al., *Experimental and modelling investigations of a dielectric barrier discharge in low-pressure argon*. Journal of Physics D: Applied Physics, 2006. **39**(4): p. 700-711.
174. Khatun, H., A. Sharma, and P. Barhai, *Experimental study of low-pressure nitrogen dielectric barrier discharge*. Brazilian Journal of Physics, 2010. **40**(4): p. 450-453.
175. Choi, K.C., G.F. Saville, and S.C. Lee, *Microbridge plasma display panel with high gas pressure*. IEEE Transactions on Electron Devices, 1998. **45**(6): p. 1356-1360.
176. Ishikawa, S., et al., *The surface modification of poly (tetrafluoroethylene) film using dielectric barrier discharge of intermittent pulse voltage*. Surface and Coatings Technology, 2000. **130**(1): p. 52-56.
177. Boeuf, J. and L. Pitchford, *Calculated characteristics of an ac plasma display panel cell*. IEEE Transactions on Plasma Science, 1996. **24**(1): p. 95-96.
178. Vink, T., et al., *Materials with a high secondary-electron yield for use in plasma displays*. Applied Physics Letters, 2002. **80**(12): p. 2216-2218.
179. Choi, E.H., et al., *Measurement of secondary electron emission coefficient (gamma) of MgO protective layer with various crystallinities*. Japanese Journal of Applied Physics, 1998. **37**: p. 7015.
180. Schwindt, P.D.D., et al., *Chip-scale atomic magnetometer with improved sensitivity by use of the Mx technique*. Applied Physics Letters, 2007. **90**: p. 081102.
181. Sarma, B., B. Verma, and S. Satyanarayana, *Magnetic mapping of Majhgawan diamond pipe of central India*. Geophysics, 1999. **64**(6): p. 1735-1739.
182. Bison, G., R. Wynands, and A. Weis, *A laser-pumped magnetometer for the mapping of human cardiomagnetic fields*. Applied Physics B: Lasers and Optics, 2003. **76**(3): p. 325-328.
183. Sander, T., et al., *Magnetoencephalography with a chip-scale atomic magnetometer*. Biomedical Optics Express, 2012. **3**(5): p. 981-990.
184. Klein, J.R.W., *Optical pumping of Rb*. University of Wisconsin Madison, 2005.
185. Zibold, T., *Active magnetic shielding and optical magnetometry*, in *Faculty of Physics and Astronomy*. 2007, University of Heidelberg.
186. Weis, A. and R. Wynands, *Laser-based precision magnetometry in fundamental and applied research*. Optics and lasers in engineering, 2005. **43**(3): p. 387-401.
187. Bell, W.E. and A.L. Bloom, *Optical magnetometers*. 1966, US Patent 3,257,608.
188. Groeger, S., A.S. Pazgalev, and A. Weis, *Comparison of discharge lamp and laser pumped cesium magnetometers*. Applied Physics B: Lasers and Optics, 2005. **80**(6): p. 645-654.
189. Farr, W. and E.W. Otten, *A Rb-magnetometer for a wide range and high sensitivity*. Applied Physics A: Materials Science & Processing, 1974. **3**(5): p. 367-378.
190. Bjorklund, G., et al., *Frequency modulation (FM) spectroscopy*. Applied Physics B: Lasers and Optics, 1983. **32**(3): p. 145-152.
191. Volk, C. *For use in atomic frequency standards*. in *38th Annual Frequency Control Symposium*. 1984.
192. Erofeev, M., E. Sosnin, and V. Tarasenko, *Miniature KrCl and XeBr Excimer Lamps*. Journal of Applied Spectroscopy, 2003. **70**(5): p. 807-810.
193. Seme, B., et al., *Light for treating skin diseases*. Optik & Photonik, 2010. **5**(4): p. 44-46.

194. Sansonetti, J., *Wavelengths, Transition Probabilities, and Energy Levels for the Spectra of Rubidium (Rb I through Rb XXXVII).* Journal of Physical and Chemical Reference Data, 2006. **35**: p. 301-421.
195. Minnhagen, L., *Spectrum and the energy levels of neutral argon, Ar I.* Journal of the Optical Society of America, 1973. **63**(10): p. 1185-1198.
196. De Galan, L., *Some considerations on the excitation mechanism in the inductively coupled argon plasma.* Spectrochimica Acta Part B: Atomic Spectroscopy, 1984. **39**(4): p. 537-550.
197. Norlén, G., *Wavelengths and energy levels of Ar I and Ar II based on New Interferometric Measurements in the Region 3 400-9 800 Å.* Physica Scripta, 2007. **8**(6): p. 249-268.
198. Nakamura, Y. and M. Sakai, *Rb collision cross-section data.* IEE Transactions of Japan, 1982. **102**(A): p. 397-404.

Curriculum Vitae

Vinu L. Venkatraman

Indian, born **April 12, 1984**

EDUCATION

Ph.D. Microsystems and Microelectronics **07/2009 – 03/2013**
École Polytechnique Fédérale de Lausanne (EPFL), Lausanne, Switzerland

Research topic: Microfabricated rubidium dielectric barrier discharge light sources for portable atomic clocks

Master of Science in Electrical Engineering **09/2006 – 01/2009**
Portland State University, Portland, OR, U.S.A

Thesis: Iridium oxide nanomonitors for health monitoring systems

Master of Science (Honors) in Chemistry **08/2001 – 07/2006**
Birla Institute of Technology & Science, Pilani, India

Bachelor of Engineering (Honors) in Electrical & Electronics **08/2001 – 07/2006**
Birla Institute of Technology & Science, Pilani, India

WORK EXPERIENCE

Doctoral Research Assistant **07/2009 – present**
Microsystems for Space Technologies Laboratory (LMTS), EPFL, Neuchâtel

- Developed a mm-scale rubidium plasma light source for optical pumping in portable atomic clocks and magnetometers, as part of the MACQS research project collaboration.

Graduate Research Assistant **09/2006 – 12/2008**
Biomedical Microdevices & Nanotechnology Laboratory, Portland State University, Portland

- Developed a novel lab-on-a-chip 'point-of-care' biosensor using iridium oxide nanowires for real-time electrical detection of multiple protein biomarkers, as part of a project collaboration with SHARP labs Inc.

Intern **01/2006 – 06/2006**
Cisco Systems India Pvt. Ltd., Bangalore, India

- Trained in RADIUS network security protocols and AAA APIs

Intern **05/2003 – 07/2003**
Central Leather Research Institute, Chennai, India

- Worked on improving the electronic architecture of the sensor interface of a 300 MHz FT Nuclear Magnetic Resonance (NMR) spectrometer

List of publications

PEER-REVIEWED JOURNAL PUBLICATIONS

1. V Venkatraman, Y Pétremand, N de Rooij and H Shea, "Characterization and modeling of low-pressure rf discharges at 2-500 MHz for miniature alkali vapor dielectric barrier discharge lamps", *Journal of Physics D: Applied Physics*, Vol. 45, No. 50, 505205, Dec 2012.
2. V Venkatraman, Y Pétremand, C Affolderbach, G Mileti, N de Rooij and H Shea, "Microfabricated chip-scale rubidium plasma light source for miniature atomic clocks", *IEEE Transactions on Ultrasonics, Ferroelectrics and Frequency Control*, Vol. 59, No. 3, pp. 448-456, Mar 2012.
3. F Vecchio, V Venkatraman, H Shea, T Maeder and P Ryser, "Dispensing and hermetic sealing Rb in a miniature resonance cell for integrated atomic clocks", *Sensors and Actuators A: Physical*, Vol. 172, No. 1, pp. 330-335, Dec 2011.
4. V Venkatraman, F Zhang, D Evans, B Ulrich and S Prasad, "Iridium oxide nanomonitors for real-time health monitoring systems", *Journal of Laboratory Automation*, Vol. 14, No. 6, pp. 400-406, Dec 2009.
5. V Venkatraman, RK Reddy, F Zhang, D Evans, B Ulrich and S Prasad, "Iridium oxide nanomonitors: clinical diagnostic devices for health monitoring systems", *Biosensors and Bioelectronics*, Vol. 24, No. 10, pp. 3078-3083, Jun 2009.
6. M Bothara, V Venkatraman, RK Reddy, T Barrett, J Carruthers and S Prasad, "Nanomonitors: electrical immunoasssays for protein biomarker profiling", *Nanomedicine*, Vol. 3, No. 4, pp. 423-436, Aug 2008.
7. F Zhang, B Ulrich, RK Reddy, V Venkatraman, S Prasad, TQ Vu and ST Hsu, "Fabrication of submicron IrO_2 nanowire array biosensor platform by conventional complementary metal-oxide semiconductor process", *Japanese Journal of Applied Physics*, Vol. 47, No. 2, pp. 1147-1151, Feb 2008.

CONFERENCE PROCEEDINGS

8. V Venkatraman, F Vecchio, T Maeder, P Ryser and H Shea, "LTCC integrated rubidium discharge lamp module for stable optical pumping in miniature atomic clocks and magnetometers", *Proceedings of the 2012 IEEE SIITME conference*, pp. 111-114, Oct 2012.
9. V Venkatraman, Y Pétremand, N De Rooij, C Affolderbach, G Mileti and H Shea, "Optimization of a Chip-Scale Rb Plasma Discharge Light Source: Effects of RF Drive Frequency and Cell Impedance", *Proceedings of the European Frequency and Time Forum (EFTF)*, Apr 2012.
10. V Venkatraman, Y Pétremand, C Affolderbach, G Mileti, N de Rooij, and H Shea, "Microfabrication and packaging of a rubidium vapor cell as a plasma light source", *Transducers 2011 Technical Digest*, pp. 1907-1910, Jun 2011.
11. V Venkatraman, Y Pétremand, C Affolderbach, G Mileti, N de Rooij and H Shea, "Low-power chip-Scale rubidium plasma light source for miniature atomic clocks", *Proceedings of the 2011 Joint IFCS-EFTF Conference*, May 2011.
12. F Vecchio, V Venkatraman, H Shea, T Maeder and P Ryser, "Dispensing and hermetic sealing Rb in a miniature resonance cell for integrated atomic clocks", *Procedia Engineering*, Vol. 5, pp. 367-370, Sep 2010.
13. V Venkatraman, RK Reddy, F Zhang, D Evans, S-T Hsu, B Ulrich and S Prasad, "A comparative analysis of iridium oxide nanowires in electrical detection of biochemical reactions", *Materials Research Society Symposium Proceedings*, Vol. 1095, No. EE08-22, Mar 2008.
14. V Venkatraman, RK Reddy and S Prasad, "Iridium oxide nanomonitors for protein detection", *NSTI-Nanotech Conference Proceedings*, Vol. 2, ISBN 978-1-4200-8504-4, pp. 649-652, Jun 2008.